Volume 1

OAR 607-2

Proceedings of the OAR RESEARCH APPLICATIONS CONFERENCE

14 March 1967

STATE DEPARTMENT ★ Main Conference Room ★ Washington, D.C.

Volume 1

OAR 607-2

Proceedings of the OAR RESEARCH APPLICATIONS CONFERENCE

14 March 1967

OFFICE OF AEROSPACE RESEARCH

UNITED STATES AIR FORCE, WASHINGTON, D. C.

FOREWORD

The Second Research Applications Conference of the Office of Aerospace Research (OAR), like the first, illustrates some of the valuable applications that have resulted from basic research by the United States Air Force.

Scientific information is the principal product of OAR, the prime research agency of the U. S. Air Force. From research within its own laboratories, and from sponsored research in universities and technical institutions, come new and unique ideas that contribute directly to a wide range of present and future Air Force needs. The long-range value of these ideas, and the usefulness of OAR-produced scientific information, will ultimately be judged by their use in advancing technology. However, some unique applications of OAR research are evident now, and are the subject of these Proceedings.

Ernest A. Pinson

ERNEST A. PINSON
Brigadier General, USAF
Commander

CONTENTS

INTRODUCTION

The object of the OAR Research Applications Conference is to present and demonstrate, by specific examples, how proven results of OAR research may be applied, to solve Air Force or Department of Defense problems -- and how research is contributing to new concepts and technologies. This second Conference was scheduled as a result of the very fine reception given the first, which was held in Washington, D. C. in the spring of 1966.

The papers published in these Proceedings include those submitted by OAR in-house scientists as well as by contractors or grantees. One is representative of OAR research conducted at foreign institutions.

The research applications presented in these Proceedings cover a broad spectrum of Air Force interests. They are not intended to represent a review of the total program, but are examples of the many applications, or potential applications, which have resulted from OAR research.

These papers, therefore, demonstrate the vital importance of maintaining a fundamental-research effort in the Department of Defense.

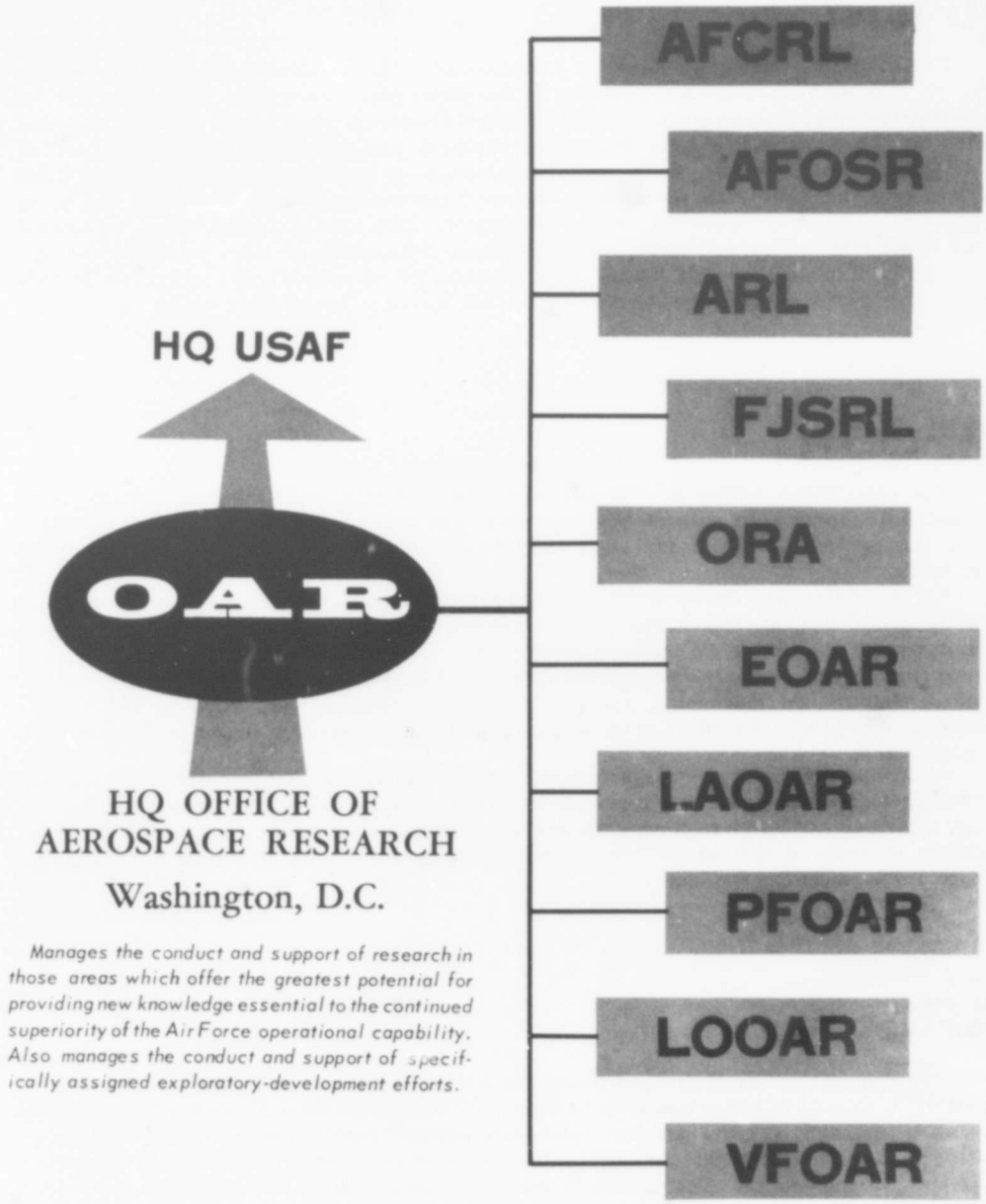

HQ OFFICE OF
AEROSPACE RESEARCH

Washington, D.C.

Manages the conduct and support of research in those areas which offer the greatest potential for providing new knowledge essential to the continued superiority of the Air Force operational capability. Also manages the conduct and support of specifically assigned exploratory-development efforts.

AFCRL

The Air Force Cambridge Research Laboratories, L.G. Hanscom Field, Mass., constitute the Air Force focal point for research in the environmental sciences. These nine AFCRL laboratories also provide a major in-house facility for research in the physical and engineering sciences. They conduct a large and varied research program, including research in all of the environmental sciences, in the physical sciences--primarily radio physics, gaseous and plasma physics, solid-state electronics, quantum electronics, and mathematics; and in the engineering sciences--primarily energy conversion. They also do exploratory-development work in the environment and aerospace environment. Although the primary function of AFCRL is to conduct research within its in-house laboratories, research under contract to outside agencies is used to support the research being carried out by the AFCRL scientists.

AFOSR

The Air Force Office of Scientific Research, located in Washington, D.C., supports extramural research to provide new knowledge and understanding in those sciences which offer the greatest potential for improving the Air Force's present and future operational capability.

As the major Air Force activity for sponsoring fundamental research in the sciences, AFOSR plans, directs, and carries out its research program through more than 1,200 grants and contracts with about 200 colleges, universities, and research organizations in the United States and abroad. Research is supported in nuclear and general physics, chemistry, mathematics, electronics, mechanics, energy conversion, astronomy-astrophysics, and the behavioral, biological, and information sciences. The kind of research sought is fundamentally a quality item.

AFOSR programs may be thought of as supporting research in areas keyed to recognized Air Force problems, as pioneering research which may lead to new technologies or concepts to meet unforseen Air Force requirements, and as providing a window for looking into world-wide science in order to enable the Air Force to draw upon scientific knowledge and ability for future development and application.

ARL

The Aerospace Research Laboratories at Wright-Patterson Air Force Base, Ohio, form a major Air Force in-house research facility in the following areas: physical and engineering sciences, including general physics; solid-state physics; general chemistry; physical chemistry; fluid dynamics; flight mechanics; mechanics of solids and energetics; and theoretical and applied mathematics. Although the primary function of ARL is to conduct research within its in-house laboratories, research under contract with outside agencies is used to support the research being carried out by ARL scientists.

FJSRL

The Frank J. Seiler Research Laboratory at the U.S. Air Force Academy, Colo., is an in-house facility in an academic setting engaged in research in the physical and engineering sciences--primarily general chemistry, physical chemistry, mathematics, fluid dynamics, and flight mechanics.

ORA

At Holloman Air Force Base, N. Mex., the Office of Research Analyses performs analysis and evaluation of future Air Force systems. Under OAR direction, these technically complex studies are made for any Air Force activity. Particularly significant is the fact that they are independent studies. Through this study activity, OAR is provided with critical technology needs which are incorporated into the research program.

EOAR

Since the pursuit of knowledge transcends national boundaries and geographical divisions, the OAR sponsorship of research extends throughout the free world. The purpose of this sponsorship is to capitalize on the free world's best brainpower with its fresh ideas and unique R&D capabilities.

The European Office of Aerospace Research, located in Brussels, Belgium, is responsible for the administration of contracts and grants in Free Europe, the Near East, and Africa. All funds for the support of foreign R. & D. come from stateside laboratories as a part of their total programs.

LAOAR

The Latin American Office of Aerospace Research, located in Rio de Janeiro, Brazil, administers the research efforts in South America.

Proposals from researchers located either in Europe or Latin America should be sent to EOAR or LAOAR, respectively.

PFOAR VFOAR LOOAR

Other supporting aerospace-research organizations are the field offices located at Patrick Air Force Base, Fla.; Vandenberg Air Force Base, Calif.; and the Los Angeles offices. These field offices maintain liaison among the scientist, the launch team, and the contractors. As a result, small scientific experiments are installed on rockets fired for other purposes, thus insuring that the Air Force receives maximum pay-load utilization.

BLANK PAGE

Conference Papers

Mrs. Rita C. Sagalyn is a physicist with the Upper Atmosphere Physics Laboratory, Air Force Cambridge Research Laboratories. She is currently engaged in experimental and theoretical studies of electrical phenomena in the upper atmosphere, including measurement of the properties of the ionospheric, exospheric and magnetospheric plasma, and the physical processes responsible for spatial and temporal variations in these regions. Her earlier work involved studies of atmospheric electrification in the troposphere and stratosphere, and its relation to meteorological processes in fair and disturbed weather. Mrs. Sagalyn obtained her B.S. in Physics from the University of Michigan, Ann Arbor, and her M.A. in Physics from Harvard University. She has over 40 publications in scientific journals and symposia proceedings, and has presented invited lectures before national and international societies.

Dr. Michael Smiddy is a research physicist with the Upper Atmosphere Physics Laboratory, Air Force Cambridge Research Laboratories. He is presently doing research on the electrical properties of the upper atmosphere and interplanetary plasma. This work includes the analysis and study of experimental data taken aboard rockets and satellites, in addition to the concept and design of the experimental equipment. Prior to joining AFCRL in 1958, Dr. Smiddy studied at Durham University in England, earning his B.S.C. degree in Honours Physics, and his Ph. D. He has been project scientist on numerous space launching expeditions in the United States, and was a member of the NASA mobile launch expedition to the South Pacific in 1965.

POSITIVE ION-SENSING SYSTEM FOR THE MEASUREMENT OF SPACECRAFT ATTITUDE

by

R.C. Sagalyn and M. Smiddy
Upper Atmosphere Physics Laboratory
Air Force Cambridge Research Laboratories (OAR)
L.G. Hanscom Field, Bedford, Massachusetts

ABSTRACT

An attitude sensing system utilizing the properties of ambient positive ions was successfully flown on Gemini Spacecraft 10 and 12. The outputs of two planar electrostatic analyzers mounted symmetrically about the appropriate axis are combined to give directly pitch and yaw angles. The system could be readily adapted for automatic control of manned or unmanned rockets, satellites, or supersonic aircraft. In-flight and post-flight comparison with the inertial guidance system on Gemini spacecraft shows that the ion system functions extremely well. Significant reductions in required power, weight, warm-up time, cost, and a greatly improved response time make this a potentially valuable technique for future space navigation.

INTRODUCTION

The principal objective of the experiments flown on Gemini Spacecraft 10 and 12, which are referred to as Air Force Experiment D-10, was to investigate the feasibility of using environmental positive ions with appropriate electrostatic detection methods to measure spacecraft pitch and yaw. A secondary objective was to measure the spatial and temporal variations of the positively charged particles along the satellite orbit. The flight plan also included spacecraft maneuvers to obtain

accurate measurements as a function of angle of positively charged particles in the wake of the vehicle.

In the altitude range 60 miles to 10 earth radii, positive ions and electrons produced primarily by photoionization exist in equal concentrations. The number density varies greatly in space and with time; for example, the charge density reaches a maximum of the order of 5×10^5 per cubic centimeter in the vicinity of the F region maximum at approximately 350 km and decreases to approxir ıtely 100 per cubic centimeter at about 10 earth radii. There are also great variations in the number densities on the day and night side of the earth, in the vicinity of the geomagnetic equator, and in the lower ionosphere below approximately 1000 km. Very rapid increases in ion and electron concentrations occur at sunrise due to photoionization and dissociation of the neutral atmosphere constituents with more gradual decreases in density occurring at local sunset when charged particle recombination and diffusion become important. This is illustrated in Figure 1 which gives the results of positive ion measurements obtained with spherical electrostatic analyzers on a Discoverer satellite as a minimum interference experiment.[1] The average energy of the particles varies from about 0.01 eV at 100 km to approximately 0.4 eV at 10 earth radii. The kinetic temperature of the charged particles in the altitude range covered by the Gemini spacecraft varies from approximately 250°K to about 3000°K.[1, 2] It has been demonstrated by the authors and other experimenters that the charged particles in the upper atmosphere have an essentially Maxwellian velocity distribution. The average thermal velocity of the particles may then be given by the relation:

$$v = \frac{8\,kT}{\pi\, m}\,, \qquad (1)$$

where k = Boltzmann constant,
T = temperature in degrees Kelvin,
m = mass in grams,
v = velocity in centimeters per second.

Substituting in Eq. (1) representative values for temperature and mass of the positive ions, one finds that their random thermal velocity varies between 0.8 km/sec and 1 km/sec in the altitude regions covered by the Gemini spacecraft. Satellites flying in the upper ionosphere have varying average velocities depending upon the nature of the orbit; however typical satellite speeds vary between 7 km/sec and 11 km/sec. The spacecraft velocity is therefore approximately 10 times greater than the average thermal velocity of the positive ions. Relative to the spacecraft the positive ions possess negligible velocity.[3] The fact that positive ions may be considered stationary with respect to the spacecraft velocity is used in the ion attitude sensing system.

EXPERIMENT DESCRIPTION

Multi-electrode electrostatic analyzers of varying sensor geometry, usually spherical, planar, or cylindrically shaped to simplify data interpretation, have been utilized in the study of the physical properties and the spatial and temporal variations of ambient charged particles in the upper atmosphere for several years.[4-7] One of the simpler configurations consists of a three-electrode sensor consisting of an aperture grid, a photo-emission suppressor grid and a charged-particle collector. A planar electrostatic analyzer of this type is illustrated in Figure 2.

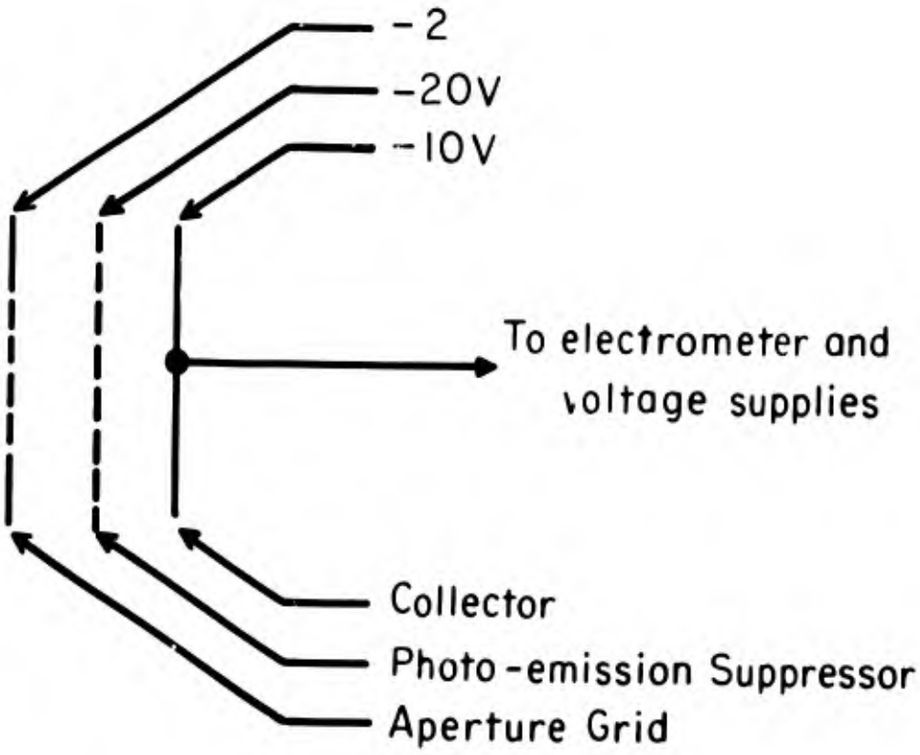

Figure 2. Example of Electrode Arrangement and Voltages Applied to the Planar Electrostatic Analyzer

When the ratio of the satellite velocity to the random velocity of the ions is greater than or equal to 2, with the grid and collector voltages as indicated in Figure 2, the current i to the collector is given by:

(2)

where A = aperture area,
N = charged particle density,
$f(v)$ = a function of the vehicle potential with respect to the undisturbed plasma,
α = experimentally determined transmission factor for the grid electrodes,
e = particle charge.

Under the experimental conditions discussed, the ions may be considered fixed and the magnitude of the velocity $|V|$ is equal to $v_s \cos \theta$, where v_s is the spacecraft velocity and θ is the angle between the direction of motion of the vehicle and normal to the plane of the sensor. Equation (2) then becomes:

$$i = A N e v_s \cos \theta f(v) \alpha. \tag{3}$$

It is seen from Eq. (3) that the planar sensor current is highly dependent on its orientation with respect to the direction of motion. This characteristic of the planar sensor is utilized in the attitude control system with the sensor configuration shown in Figure 3. For example, for the yaw measurement, two identical sensors are aligned at 45° with respect to the plane of zero yaw. An identical sensor system, mounted symmetrically about the zero pitch plane, is used for the measurement of pitch angles. These two independent systems are mounted on booms approximately three feet in length which are located in the aft section of the spacecraft. They are extended on command by the astronaut at the appropriate time after orbital injection is accomplished. The location of the booms and sensors on Gemini Spacecraft 10 and 12 is shown in Figure 4. The location of the sensors and the boom lengths are set to minimize the influence of spacecraft wake, contamination, and space-charge effects.

The principle of operation of the experiment may be understood by considering first the measurement of pitch. Except for the change in alignment as indicated above, the analysis of the yaw measurement is identical. With two sensors aligned symmetrically about the pitch axis as shown in Figure 3, the current to the collector of each sensor is given by:

$$i_1 = N e v_s \alpha A \cos (45 - \theta), \tag{4}$$

$$i_2 = N e v_s \alpha A \cos (45 + \theta), \tag{5}$$

where i_1 = current to sensor 1,
i_2 = current to sensor 2,
θ = pitch angle (in degrees).

Solving Eqs. (4) and (5) for θ one obtains:

$$\text{Tan } \theta = \frac{i_1 - i_2}{i_1 + i_2}, \tag{6}$$

For θ less than or equal to 20°, tangent θ is equal to θ, in radians.

From Eq. (6) it is seen that the output of the sensors may be displayed on a meter calibrated directly in degrees, and that changes in charge density N or satellite velocity v_s do not affect the angular measurement.

A block diagram of the pitch or yaw system is shown in Figure 5. The output of each sensor is amplified by electrometers 1 and 2. In order to obtain the desired accuracy over the current range 10^{-6} to 10^{-11} amperes, linear amplifiers with range switching covering five current decades are employed. The outputs of electrometers 1 and 2 are then electronically added, subtracted, integrated, and compared. The final output tangent θ, referred to as the compared output, is sent to the flight director's indicator, to an on-board magnetic tape which is periodically transmitted to ground stations, and is also transmitted in real time to a few ground stations.

In order to fully evaluate the experimental system, to obtain information on the ambient ion densities and on the variation of positive ions in the wake of the vehicle, the direct outputs of electrometers 1 and 2, the range analog indicator, and calibrate monitors are also transmitted through telemetry. These latter outputs would not be required in an operational system. It should be noted that while the Gemini D-10 experiment was designed for precise pitch and yaw angular measurements over the range ± 20°, there is no basic limitation to the magnitude of the angle to be measured. The required resolution, response time, and so forth, vary with the specific application of the system. A simple engineering modification of the ratio circuits would be involved for varying systems requirements. Comparison of certain characteristics of the ion attitude sensor with the inertial system is given in Table 1.

Table 1. Comparison of Ion Attitude Sensor and the Inertial System Characteristics

	Inertial System	D-10 System	Improvement Factor
Response time	1 sec	1 msec	1,000
Weight	750 lb	15 lb	50
Power	150 watts	3.0	50
Lifetime	≈ 14 days (mechanical)	> 1 year	infinite
Volume	3 cu ft	.2 cu ft	15
Cost	1,500,000	30,000	50

The output of this experiment could be sent to a servo system to control thruster firings for automatic control of spacecraft pitch and yaw angles. With the addition of a horizon sensor and a spacecraft roll monitor, a completely self-contained navigational system would be obtained. A view of the D-10 sensors is shown in Figure 6. A photograph of the total unit consisting of the electronics package and the sensor is given in Figure 7.

DISCUSSION OF RESULTS

The ion attitude sensing experiments were flown on Gemini Spacecraft 10 and 12 in August and November 1966, respectively. The experiment functioned very well on both flights. The system was operated for approximately twelve hours on Gemini 10, including three and one-half hours when the inertial platform was also operating. On Gemini 12 power was applied to the experiment for about thirty hours, during thirteen hours of which the inertial guidance system was also operative. Thus, a great deal of data was obtained on the ambient environmental positive ions, on the properties of the vehicle wake, and on direct comparison of the ion system angular measurements with the inertial guidance unit.

Specific in-flight maneuvers included:

1. Yaw angle study, which consisted of maintaining roll and pitch fixed and varying yaw from 0 to 360° at a rate determined by the bandwidth of the telemetry system and the ability of the astronaut to control the spacecraft motion.

2. Pitch study.

3. Roll study.

4. Rotation of the position of the spacecraft through 360° in turn, in pitch, yaw, and roll to determine the properties of the vehicle wake and its effect on the instrument outputs.

5. Determination of the effects of spacecraft thruster firings on the experiment outputs.

6. Determination of the influence of environmental factors such as the photo-emission which can best be determined near a local sunrise and sunset.

7. Ambient positive ion data: with the spacecraft in a fixed position with respect to pitch, roll, and yaw, the sensor output was monitored during several complete orbital periods.

Both the post-flight analysis of the transmitted data and the astronauts' in-flight comparison of the ion-sensing system with the inertial guidance system showed that the two systems agreed in absolute magnitude very well in the measurement of both pitch and yaw angles. The response of the Air Force D-10 experiment to variations in angular position was extremely rapid, of the order of milliseconds.

An example of the simultaneous measurement of the ion yaw sensor output and the inertial yaw data during a controlled maneuver is shown in Figure 8. The magnitudes of the angles at a given time agree within the experimental error of the systems. The inertial yaw measurement accuracy is of the order of two degrees. The ion yaw accuracy for the Gemini spacecraft is ±0.25°. The inertial data given in Figure 8 illustrates certain characteristics which introduce difficulties in the manual control of the spacecraft. That is, when the yaw angle is varied, a lag in the response time of the order of 8 seconds occurs. The step-like variations in yaw angle, giving jumps of the order of one and one-half degrees in the inertial measurement, are partly due to the synchronous detectors used in the inertial guidance system, but also partly due to the manner in which the data is digitized through the telemetry system. The addition of an ion yaw sensor alone would therefore be a significant improvement in existing attitude systems.

The existing inertial system requires about 40 minutes to stabilize and warm up after power turn-on. This is partly due to the electronic

circuits used and the adjustment of the gyroscopes on the unit; however, the astronauts have found that the use of the ion yaw angular measurements significantly decreases the time for platform alignment.

An example of the simultaneous measurement of pitch angles with the ion sensor and inertial systems is given in Figure 9. It is seen that the absolute values of the angles agree within a fraction of a degree over the angular range of ±20°. A good illustration of the response time of the two systems is seen in Figure 9 between 66 hours, 0 minutes and 66 hours, 5 minutes. While individual maxima and minima in pitch agree very well, the faster response of the ion sensor makes it easier to detect angular changes. Operationally, this should be of particular importance in conserving thruster fuel and under conditions where very precise angular positioning is desired.

The experimental results also demonstrate that variations in roll do not affect the yaw or pitch measurements. It was also shown during controlled maneuvers on the Gemini 12 mission that the ion attitude sensor operates both in the forward and in the reverse direction. Ion attitude measurements may therefore be obtained from 0 to 360°.

An unexpected opportunity for the in-flight operation of the ion system occurred during the flight of Gemini 12. Shortly after experiment turn-on, Mission Control turned the spacecraft on-board computer to the angular measurement mode. Real-time comparison of the two systems was carried out. The outputs of the ion sensor unit and of the inertial computer agreed to within a fraction of a degree. When fuel cells degradation occurred late in the flight, the inertial system was turned off to conserve fuel and the ion sensor system was used by Mission Control as a check on the spacecraft attitude and for up-dating the flight plan.

On Gemini 12 it was also demonstrated that firing the spacecraft thrusters in the direction of the sensors did not affect their operation. Very accurate measurements of the charged particle distribution in the shadow or wake of the vehicle and of the sensors were also obtained. This is an important measurement for the utilization of charged particles systems for docking and maneuvering in space.

SUMMARY AND RECOMMENDATIONS

Several of the potential applications of the ion-sensing system are summarized in Table 2.

Table 2. Potential Applications

1. Yaw measurement for rockets and satellites (accuracy: fraction of a degree).
2. Complete attitude system including pitch, roll, yaw, with addition of horizon scanner

   for: { manned spacecraft, unmanned spacecraft, manual control, automatic control.
3. Attitude sensing for supersonic transport vehicles.
4. Space maneuvering applications: docking, re-entry, photography, and so forth.

The ion-sensing system would be particularly useful on long-lived satellites where low power consumption, weight, and reliability are important. The yaw system could be added immediately to decrease the time required to align the inertial platform by 10 to 20 minutes.

ACKNOWLEDGMENTS

This work was carried out as an in-house AFCRL experiment. In addition to the authors, the members of the Space Electricity Group who contributed to the development of the unit were: D. DeCourcy, A. Romanelli, and S. Cleaves. The authors are particularly grateful to Astronauts Young, Collins, Lovell, and Aldrin for their cooperation and excellent performance in carrying out the maneuvers required to properly test this system. We also gratefully acknowledge the financial support of SSD-Los Angeles and the liaison assistance of SSD Detachment 2 personnel at the Manned Space Flight Center.

REFERENCES

1. Sagalyn, R.C., Smiddy, M., and Bhargava, Y.N., Satellite measurements of the diurnal variation of electron temperatures in the F region, Space Research V:189-206 (1964).

2. Spencer, N.W., Brace, L.H., and Carignan, G.R., J. Geophys. Res. 67(1):157 (1962).

3. Sagalyn, R.C., Smiddy, M., Charged Particle Measurements by Means of Electrostatic Probes, Techniques Manual, COSPAR (1966).

4. Bourdeau, R.E., Space Research II:554 (1961).

5. Hinteregger, H.E., Space Research I:304 (1960).

6. Brace, L., Spencer, N., and Dalgarno, A., Results Explorer 17, AGU, Wash., D.C. meeting (1964).

7. Sagalyn, R.C., Smiddy, M., and Wisnia, J., J. Geophys. Res. 68(1):199 (1963).

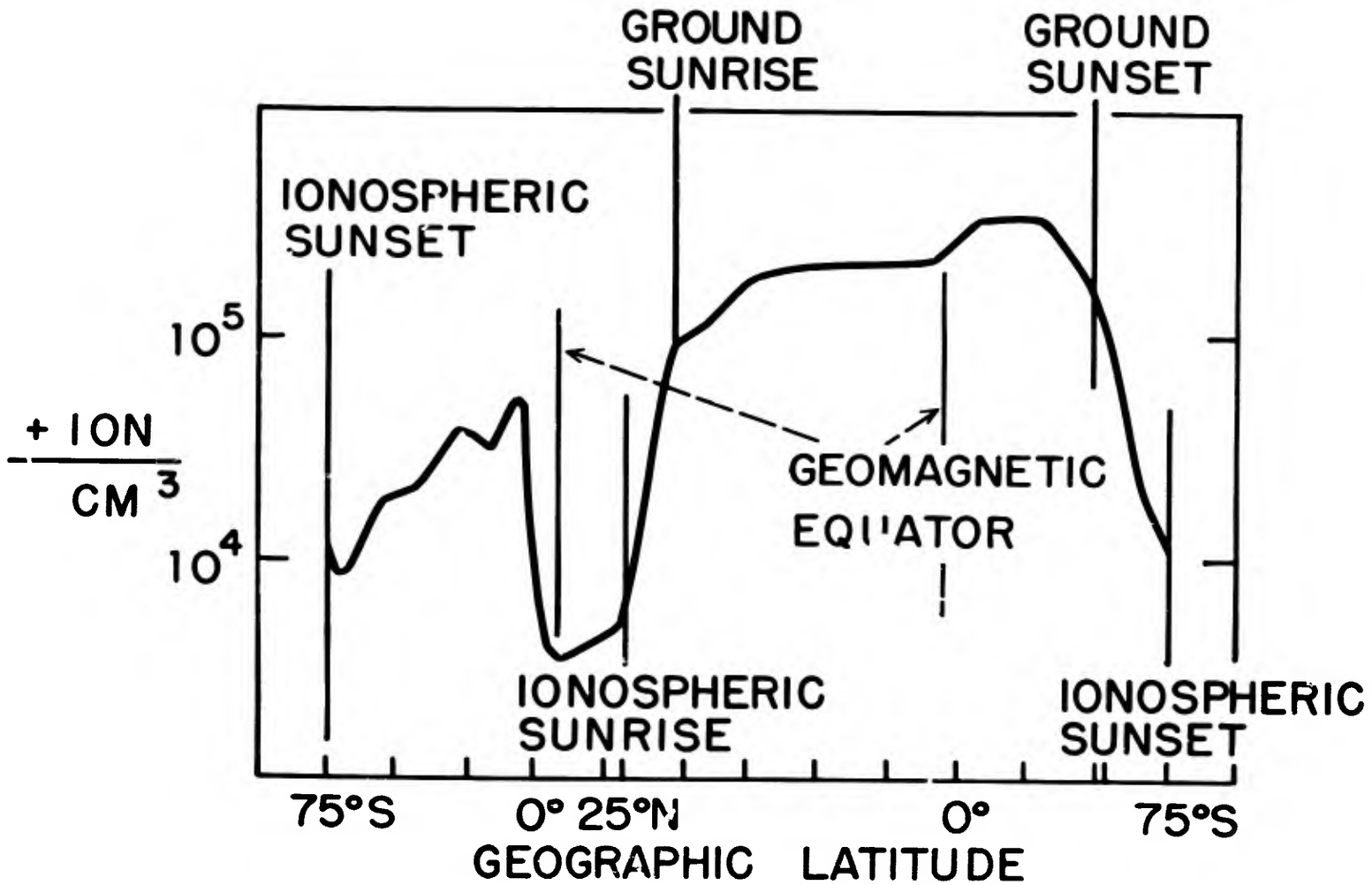

Figure 1. Variation of Positive Ions in the F Region on One Complete Orbit

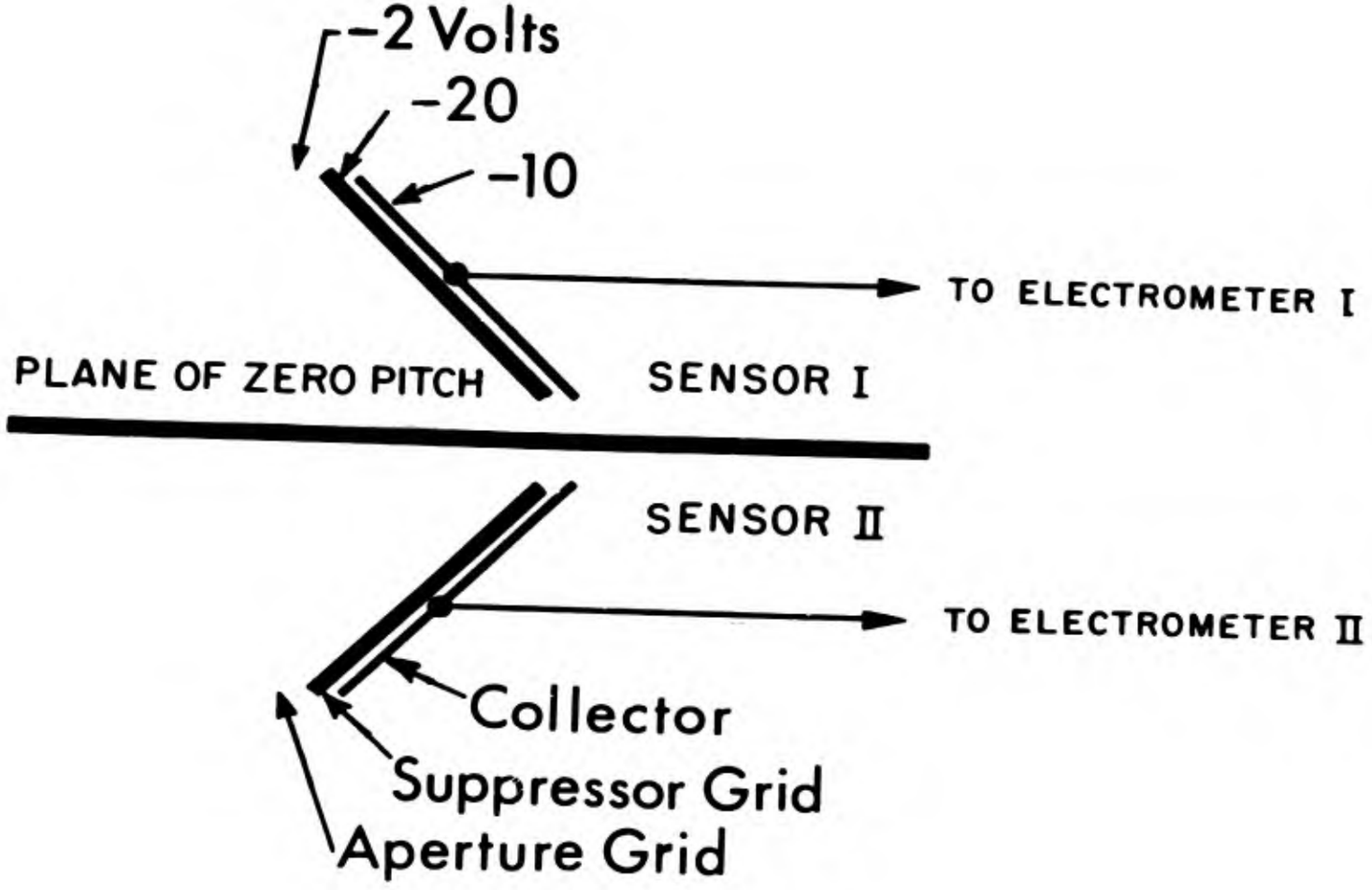

Figure 3. Pitch System Sensor Arrangement and Applied Voltages

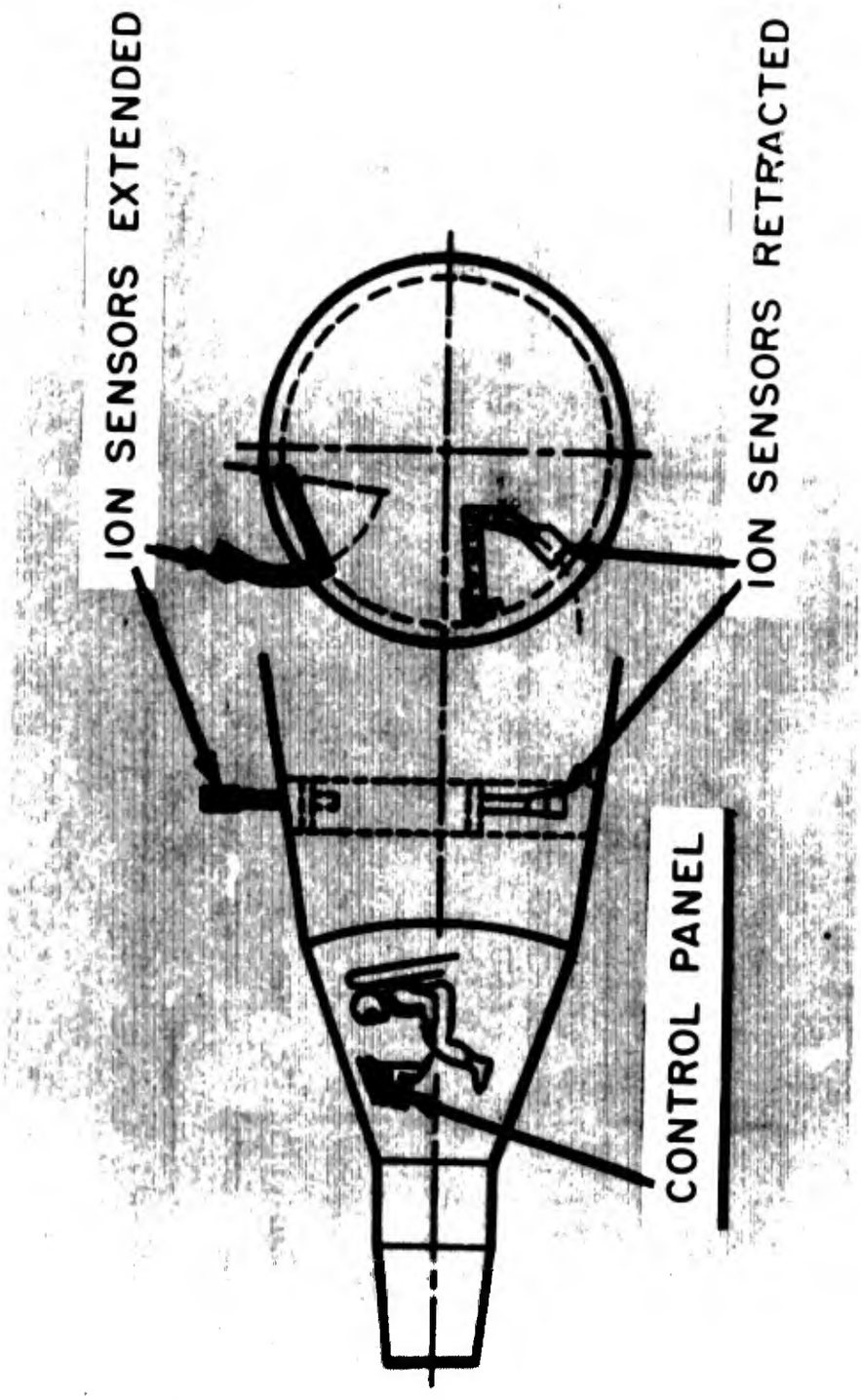

Figure 4. Location of Experiment D-10 Pitch and Yaw Experiment on Gemini Spacecraft

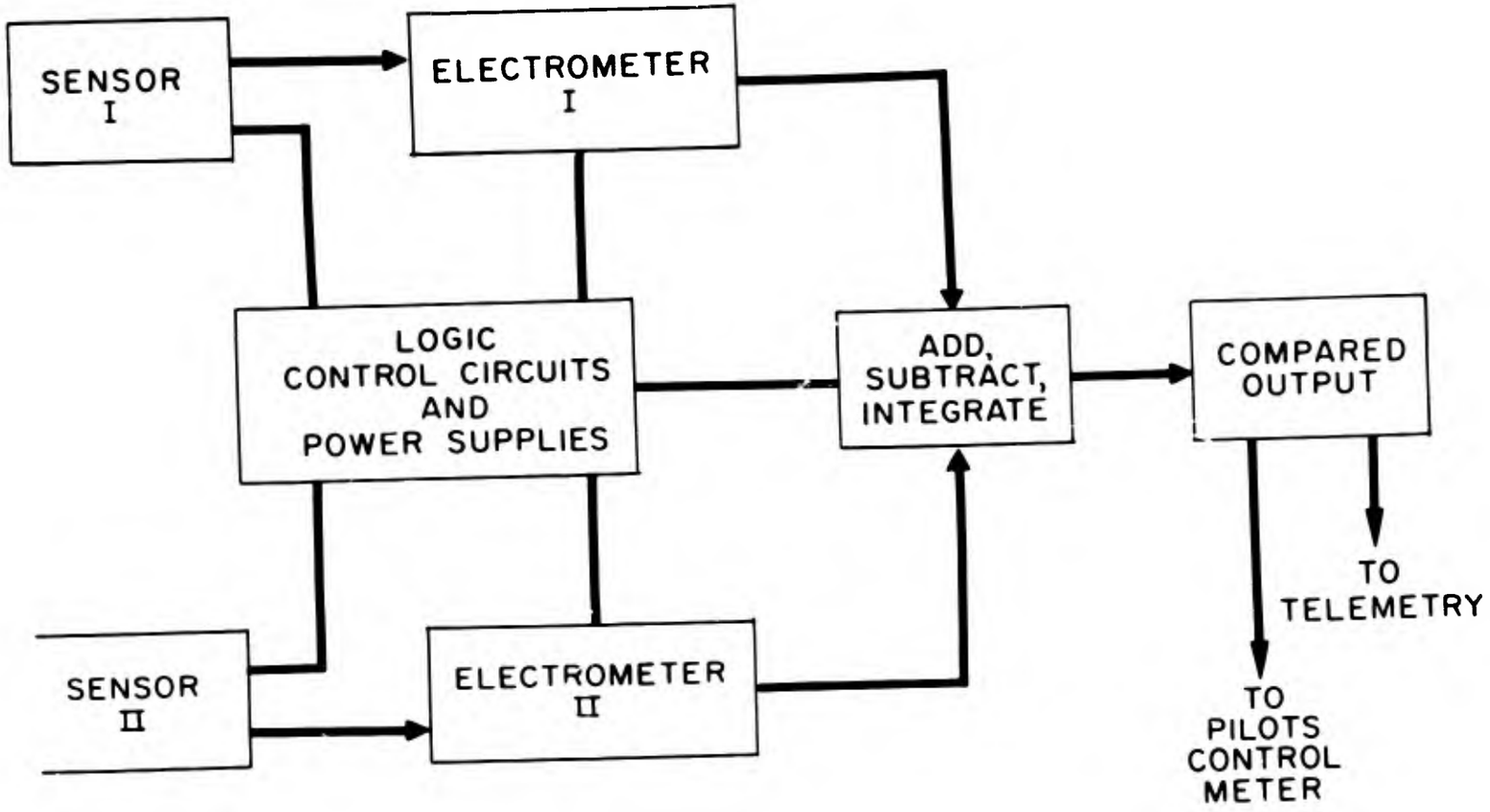

Figure 5. Block Diagram of Ion Yaw/Pitch Sensing System

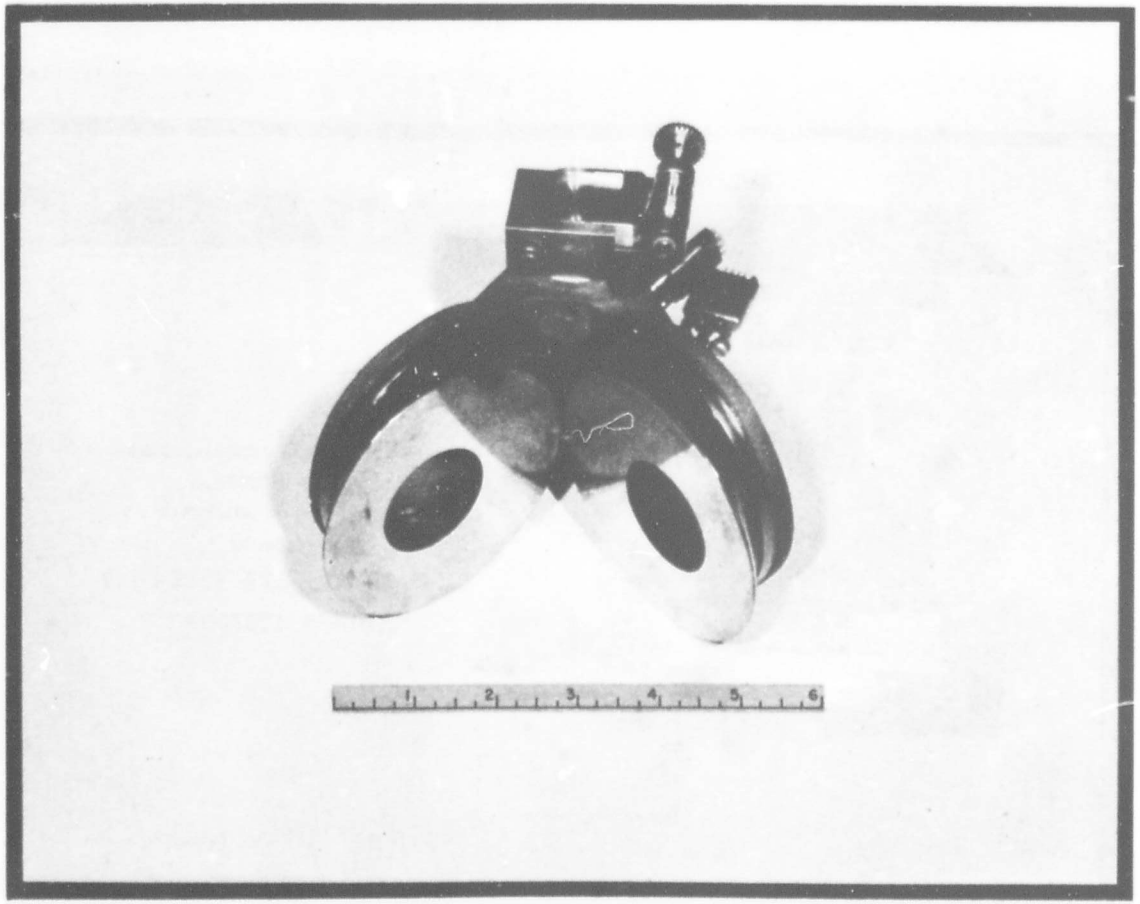

Figure 6. Ion Attitude Sensor With Alignment Fixture

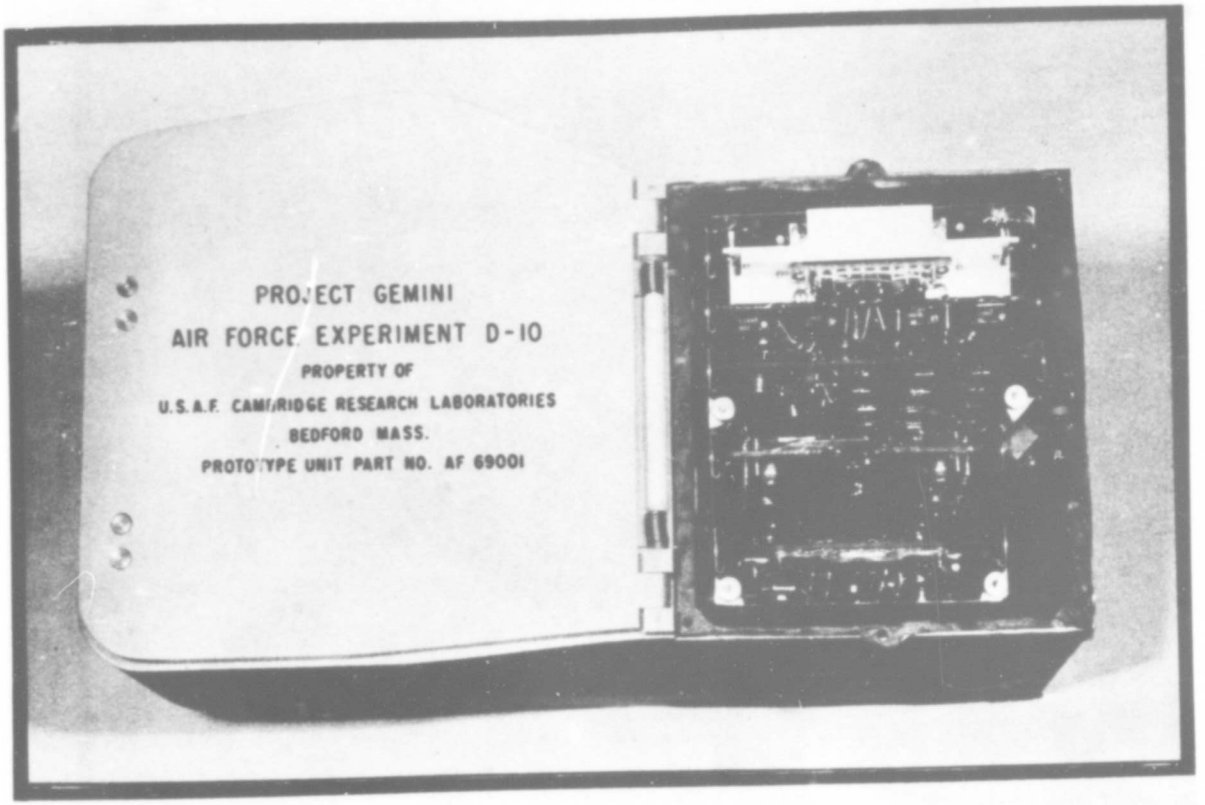

Figure 7. Positive Ion Attitude Sensor Package With View of Electronics Section

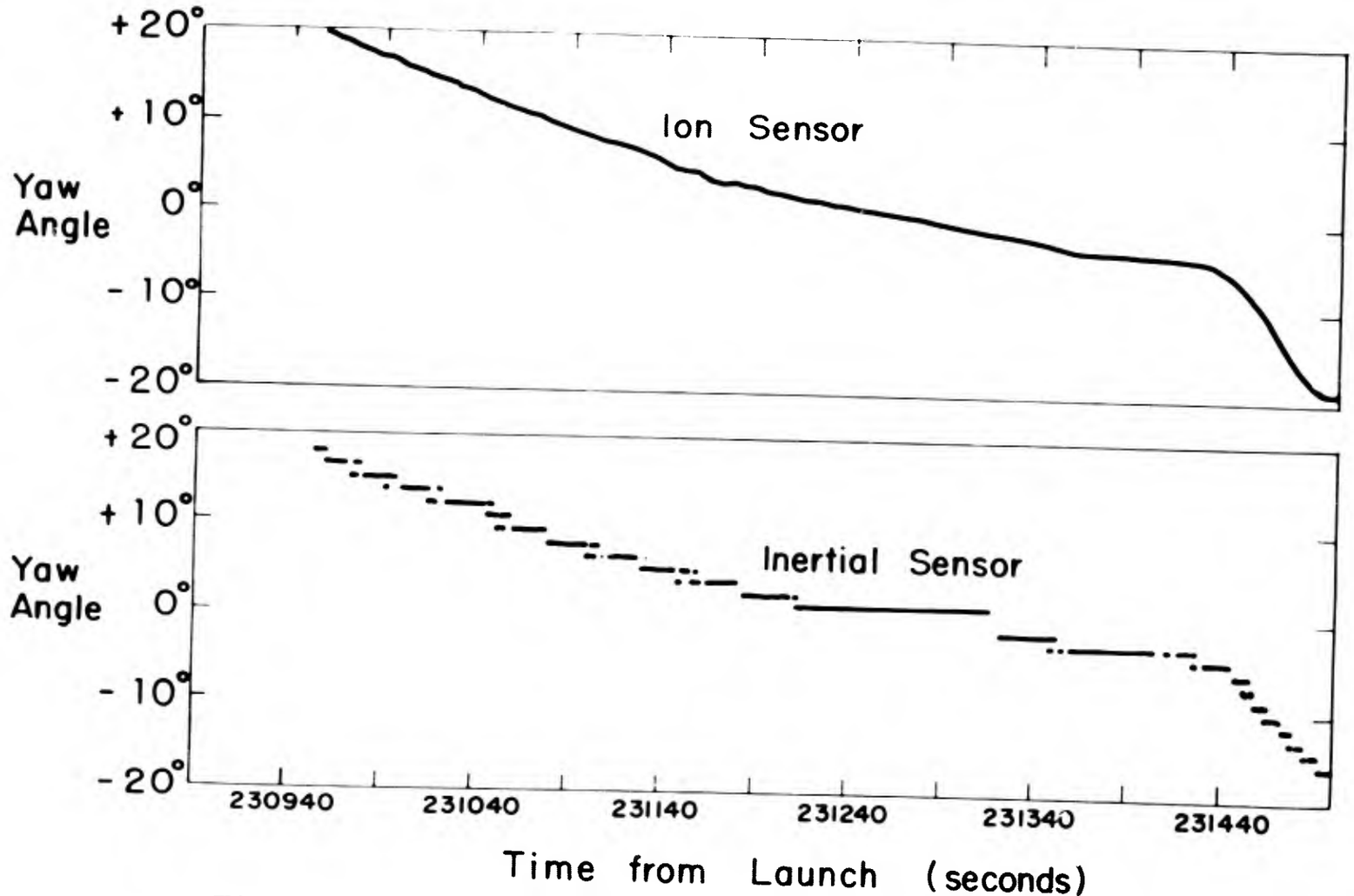

Figure 8. Comparison of Ion Attitude Yaw Angle Measurements With Inertial System - Gemini 10

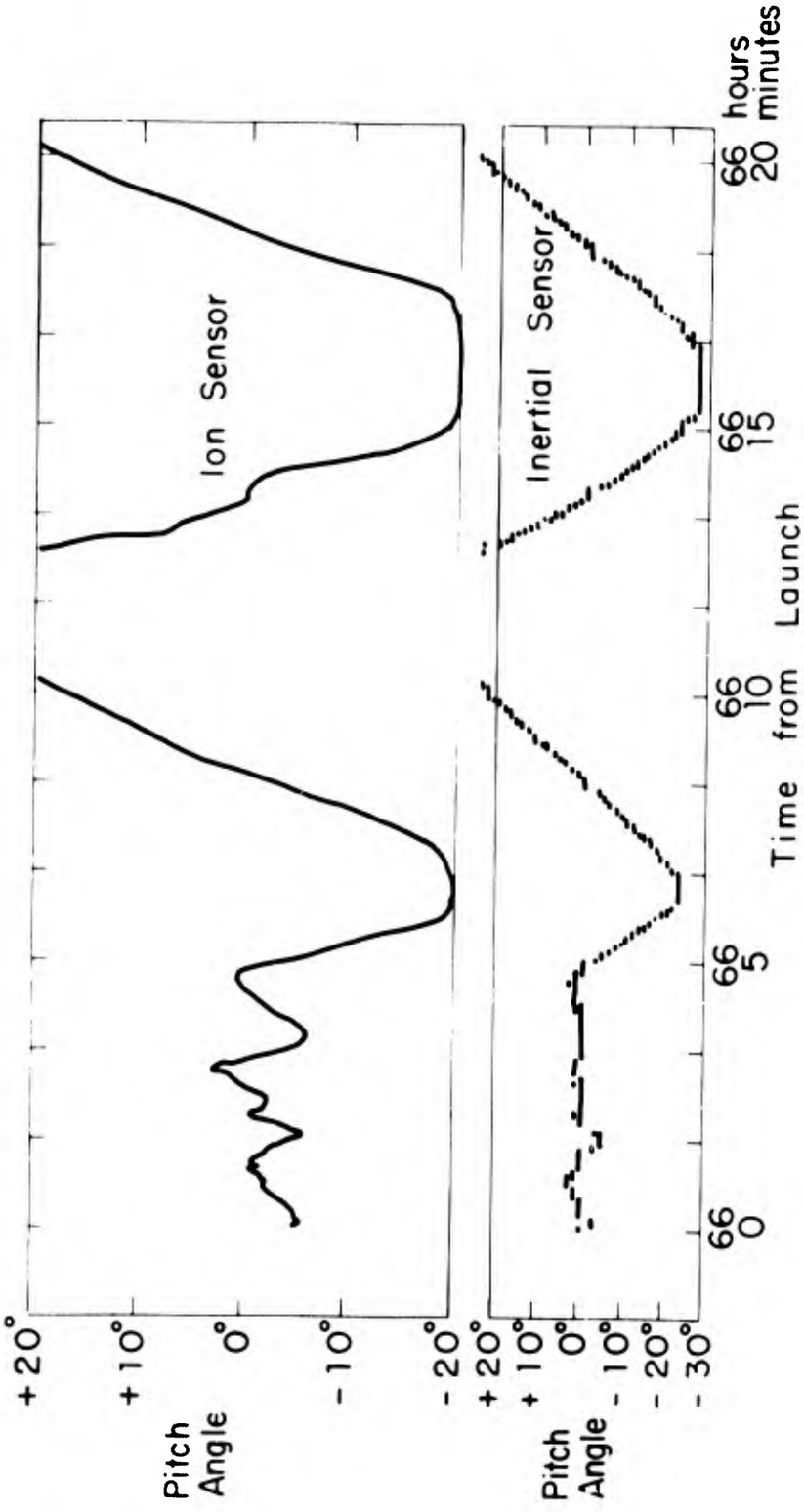

Figure 9. Comparison of Ion Attitude Pitch Angle Measurements With Inertial System - Gemini 10

Dr. Wilbur L. Hankey is an aerospace research engineer with the Hypersonic Research Laboratory, Aerospace Research Laboratories, where he is conducting theoretical studies in the optimization of hypersonic configurations. He received his B.S. degree in Engineering from Pennsylvania State University in 1951, and his M.S. degree in Aeronautical Engineering from the Massachusetts Institute of Technology in 1953. In 1962, he received his Ph. D. degree in Aeronautical and Astronautical Engineering from Ohio State University. Before joining ARL in 1960, Dr. Hankey worked in the Aero Systems Division's Wind Tunnel Branch and Hypersonic Flight Section, and served as Chief of the aerodynamics branch, Dyna-Soar Office. He is a member of Sigma Xi, Sigma Tau, Tau Beta Pi, Chi Epsilon, Parmi Nous, Alpha Phi Omega, Phi Kappa Phi, and the American Institute of Aeronautics and Astronautics. He is also a registered professional engineer in Ohio.

BLANK PAGE

INVESTIGATION OF OPTIMUM LIFTING BODIES

by

WILBUR L. HANKEY*

INTRODUCTION

The USAF is interested in extending the flight of lifting aircraft to hypersonic speeds (i.e. Projects such as ASSET, PRIME, Scramjet etc). Experience in the past decade has shown that it is difficult to design an efficient lifting vehicle. For example, the Dyna-Soar, upon cancellation weighed about five times as much as Mercury to perform a similar space mission. Therefore, in order for hypersonic lifting vehicles to become competitive as useful space systems, optimization is necessary.

Optimization studies of lifting bodies are being conducted at the Aerospace Research Laboratories. These investigations are for the purpose of establishing classical optimum configurations and for the determination of the severity of various practical constraints to furnish the designer general guidelines for achieving an efficient aerospace system.

Historically the aircraft industry has evolved a vehicle by the inverse method in which a configuration is determined first by intuition and then the performance computed. The direct method employed in this optimization first establishes the mission requirement and then determines the optimum configuration to accomplish this objective.

The primary objective of a lifting body is to enclose a prescribed payload (volume requirement) with minimum structural weight (wetted area limitation) and produce the highest possible hypersonic lift-to-drag ratio. A geometric quantity which represents this payload to structural weight ratio is volumetric efficiency (η). This is a dimensionless ratio of a volume-area parameter referenced to that of a sphere.

$$\eta = \frac{\forall\, 6\sqrt{\pi}}{A_w^{3/2}}$$

*Dr. Wilbur L. Hankey, Hypersonic Research Laboratory, Aerospace Research Laboratories, Wright-Patterson Air Force Base, Ohio.

A sphere then possesses an η of unity and all other closed geometric shapes have values of η less than one (unfortunately a sphere possesses an L/ D of zero).

In addition to consideration of the primary objective of a lifting body (i. e. L/ D and volumetric efficiency), there is the awareness of the requirement for the vehicle to survive the aerodynamic heating, be trimable and possess adequate stability, tolerate the aerodynamic skin friction, and provide safe terminal landing. These latter items are additional constraints which must be considered in the optimization.

To better understand the importance of these constraints, each was examined sequentially rather than simultaneously in this investigation. Previous work performed by the author (Ref. 1) reports results of the simultaneous effect of these multiple constraints.

The cases under investigation which shall be reported here are as follows:

(1) Maximize L/ D for fixed volumetric efficiency.

(2) Maximize L/ D for fixed volumetric efficiency with a heating constraint.

(3) Maximize L/ D for fixed volumetric efficiency with a skin friction constraint.

ANALYSIS

To ascertain the configurations which achieve these objectives, several mathematical approaches were taken. It was soon apparent that greater success was possible by employing crude numerical techniques on elaborate computers than by use of the classical calculus of variations. The procedure utilized was to express a general closed geometric shape by a finite number of degrees of freedom, program the geometric relationships and aerodynamic characteristic equations and employ a numerical searching technique to find the optimum. The details of this operation are presented in the following paragraphs.

To determine the optimum lifting body configuration, the generalized shape (Figure 1) was established with ten degrees of geometric freedom.

The general equations for lift, drag, volume and area are required.

$$\frac{L}{q} = \iint \left[C_p (\underline{k} \cdot \underline{n}) - C_f (\underline{k} \cdot \underline{t}) \right] dA$$

$$\frac{D}{q} = \iint \left[C_p (\underline{i} \cdot \underline{n}) - C_f (\underline{i} \cdot \underline{t}) \right] dA$$

$$\forall = \frac{1}{3} \iint (\underline{r} \cdot \underline{n}) \, dA$$

$$A_w = \iint dA$$

Newtonian pressure distribution is assumed,

$$C_p = k (\underline{n} \cdot \underline{i})^2$$

and laminar skin friction is considered.

$$C_f = C_{f_c} \sqrt{\frac{c}{x}}$$

where

$$\underline{n} = \frac{-\underline{i} z_x - \underline{j} z_y + \underline{k}}{\sqrt{1 + z_x^2 + z_y^2}}$$

$$r = \underline{i} x + \underline{j} y + \underline{k} z$$

$$\underline{t} \approx -\underline{i}$$

Since directional stability requirements dictate symmetry about the x-z plane, the resulting hemiconfiguration is composed of two conical and four prismoidal sections plus nose and base sections.

Placing these relationships into the equations for lift, drag, volume and area and integrating these for the geometry of Figure 1

produces the following ($R^2 / c^2 << 1$):

$$\frac{L}{qRck\left(\frac{R}{c}\right)^2} = 1 + m + \frac{1}{3}m^2 + \frac{2n}{3}\left(\frac{3\pi}{4} + m + n\right) + \left(\frac{b_2}{R} + m\right)(1+n)^2$$

$$- \left(\frac{R_1}{R}\right)^3 \left[1 + m_1 + \frac{1}{3}m_1^2 + \frac{2n_1}{3}\left(\frac{3\pi}{4} + m_1 + n_1\right)\right]$$

$$- \left(\frac{R_1}{R}\right)^2 \left(\frac{b_2}{R} + m_1 \frac{R_1}{R}\right)\left(1 + n_1\right)^2$$

$$\frac{D}{qRck\left(\frac{R}{c}\right)^3} = \frac{\pi}{2} + 3(m+n) + \frac{3\pi}{4}(m^2 + n^2) + \frac{2}{3}(m^3 + n^3)$$

$$+ mn(3 + m + n) + \left(\frac{R_1}{R}\right)^4 \left[\frac{\pi}{2} + 3(m_1 + n_1) + \frac{3\pi}{4}(m_1^2 + n_1^2)\right.$$

$$\left. + \frac{2}{3}(m_1^3 + n_1^3) + m_1 n_1 (3 + m_1 + n_1)\right]$$

$$+ \left(\frac{b_2}{R} + m\right)\left(1 + n\right)^3 + \left(\frac{R_1}{R}\right)^3 \left(\frac{b_2}{R} + m_1 \frac{R_1}{R}\right)\left(1 + n_1\right)^3$$

$$+ \left(\frac{2h_2}{R} + n + n_1 \frac{R_1}{R}\right)\left(1 + m\right)^3 + \frac{C_{D_N}}{k} \frac{h_2}{R} \frac{b_2}{R}\left(\frac{c}{R}\right)^2$$

$$+ \frac{4 C_{f_c}}{3k\left(\frac{R}{c}\right)^3}\left[\frac{\pi}{2} + m + n + \frac{R_1}{R}\left(\frac{\pi}{2} + m_1 + n_1\right) + \frac{3b_2}{R} + \frac{3h_2}{R}\right]$$

$$\frac{3\forall}{R^2 c} = \frac{\pi}{2} + m + n + \left(\frac{R_1}{R}\right)^2 \left(\frac{\pi}{2} + m_1 + n_1\right) + \frac{R_1}{R}\left(1 + n_1\right)\left(\frac{3b_2}{2R} + m_1 \frac{R_1}{R}\right)$$

$$+ \left(1 + n\right)\left(\frac{3b_2}{2R} + m\right) + \left(1 + m\right)\left(\frac{3h_2}{R} + n + n_1 \frac{R_1}{R}\right) + \frac{3h_2}{R} \frac{b_2}{R}$$

$$+ \frac{3(\forall_N + \forall_B)}{R^2 c}$$

$$\frac{A_w}{Rc} = \frac{\pi}{2} + m + n + \frac{R_1}{R}\left(\frac{\pi}{2} + m_1 + n_1\right) + \frac{2b_2}{R} + \frac{2h_2}{R} + \frac{A_{w_N} + A_{w_B}}{Rc}$$

where

$$\frac{R_1}{R} = \frac{1 + m}{1 + m_1}$$

$$1 + m = \frac{b_1 - b_2}{2R}$$

$$1 + n = \frac{h_1 - h_2}{R} - \frac{R_1}{R}(1 + n_1)$$

The nose and base sections are treated as ellipsoids.

$$\frac{3(\forall_N + \forall_B)}{R_2 c} = \pi \frac{R}{c}\left[\frac{3}{8}\frac{b_2}{R}\left(\frac{h_2}{R}\right)^2 + 2\left(\frac{R_1}{R}\right)^2\sqrt{1 - e^2}\right]$$

$$\frac{A_{w_N} + A_{w_B}}{R c} = \pi \frac{R}{c}\left[\frac{1}{2}\frac{b_2}{R}\left(\frac{h_2}{R}\right) + \left(\frac{R_1}{R}\right)^2\left(1 + \frac{1 - e^2}{2e}\ln\frac{1 + e}{1 - e}\right)\right]$$

where

$$e^2 = 1 - \left(\frac{\Delta c}{R_1}\right)^2$$

and from Reference 2,

$$\frac{h_2}{R} = 10.53\,\frac{\gamma_w}{\dot{q}_{max}^2}\left(\frac{c}{R}\right)^2\left(\frac{3\forall}{R^2 c}\right)\left(\frac{qR^3K}{Lc}\right)$$

With the generalized equations developed, we are ready to proceed to maximize L/ D for various constraints by examining the influence of the various degrees of freedom. Three cases shall be presented herein.

Case I. Maximum L/ D with Constant Volumetric Efficiency

For this case L/ D and η are functions of eight geometric variables.

$$\frac{L}{D} = \frac{L}{D}\left(m,\ n,\ m_1,\ n_1,\ \frac{b_2}{R},\ \frac{h_2}{R},\ \frac{R}{c}\right)$$

$$\eta = \eta\left(m,\ n,\ m_1,\ n_1,\ \frac{b_2}{R},\ \frac{h_2}{R},\ \frac{R}{c},\ \frac{\Delta c}{R_1}\right)$$

An iteration procedure (Ref. 3) was employed to determine the combination of these eight geometric quantities which produces maximum L/ D for fixed volumetric efficiency (η).

The results of this optimization are tabulated below for $(R/c)^2 << 1$.

$$\frac{h_2}{R} = 0$$

$$\frac{R_1}{R} = 1.0$$

$$n + n_1 \frac{R_1}{R} = 0$$

$$\frac{b_2}{R} + 2m = 0$$

$$n = 0.59$$

$$\frac{b_2}{R} = 0.81$$

$$\frac{\Delta c}{R_1} = 1.0$$

One of these optimum configurations is shown in Figure 2 for an L/ D of 4. A summary of these "classically" optimized configurations is shown in Figure 3 as L/ D versus η. These configurations achieve the ultimate hypersonic L/ D for a specified volumetric efficiency in the absence of heating, skin friction, stability or landing constraints. Also shown on Figure 3 for comparison are the X-20, ASSET and GEMINI configurations. Note the substantial gains that are potentially available for high L/ D vehicles.

Case II. Maximum L/ D with Constant Volumetric Efficiency and a Heating Rate Limitation

The most obvious limitation in the previous configuration was the sharp leading edge which could not sustain the heat transfer during reentry. Another optimization was performed which limited the heat transfer ($\dot{q}$) to the leading edge (thus requiring blunting of the nose) in addition to the requirement of fixed volumetric efficiency. Only minor changes in the configuration resulted with substantial reductions in L/ D, i. e., minor bluntness and width reduction of the nose occurred with no other configuration change.

The results of this optimization are tabulated below for $(R/c)^2 << 1$.

$$\frac{R_1}{R} = 1.0$$

$$n + n_1 \frac{R_1}{R} = 0$$

$$\frac{b_2}{R} + 2m = 0$$

$$\frac{\Delta c}{R_1} = 1.0$$

$$\frac{b_2}{2R} = \text{(See Fig. 4)}$$

The characteristics of a typical configuration are shown in Fig. 4. Note that the $(L/D)_{max}$ asymptote is nearly attained for values of the heating rate parameter of $\dot{q}/\sqrt{\gamma_w} = 1000$ Btu/ ft^2 sec lb$^{1/2}$/ft$^{3/2}$ indicating that it is probably possible by using advanced cooling techniques to essentially eliminate heat transfer as a severe constraint on vehicle performance.

Case III. Maximum L/ D with Constant Volumetric Efficiency and Prescribed Skin Friction

The optimization procedure was repeated for the addition of a skin friction coefficient to the computation of maximum L/ D with fixed volumetric efficiency.

The results of this optimization are tabulated below for $(R/c)^2 << 1$.

$$\frac{R_1}{R} = 1.0$$

$$n + n_1 \frac{R_1}{R} = 0$$

$$\frac{\Delta c}{R_1} = 1.0$$

$$\frac{h_2}{R} = 0$$

$$\frac{b_1}{2R} = \text{(See Fig. 5)}$$

The addition of a skin friction coefficient to the computation of L/D resulted in a flattening of the configuration and a reduction in L/D (Fig. 5). Since it is not likely that skin friction coefficients less than 0.001 shall be experienced in flight, therefore skin friction greatly limits the maximum L/D that can be achieved. Even for a volumetric efficiency of zero, an L/D limit of four exists.

EXPERIMENTAL RESULTS

Since the configurations evolved are unusual, the application of the Newtonian pressure and laminar skin friction relationships require experimental confirmation. An experimental program was conducted in the ARL 20-Inch Hypersonic Wind Tunnel (Ref. 4) to examine the accuracy of the assumed aerodynamic characteristics. A force model of the configuration shown in Fig. 2 was constructed and tested at Mach number 14 to ascertain the L/D. The experimental results are shown in Fig. 6 with the theoretical prediction. Agreement is considered excellent thereby substantiating the assumed pressure and skin friction relationships for this application.

SUMMARY

Hypersonic lifting configurations were optimized to produce maximum lift-to-drag ratios for constraints of volumetric efficiency, heating and skin friction. Geometric details of these configurations are presented which show them to be wedge-nosed shapes with conical

afterbodies and hemispherical bases. Although the hypersonic L/ D is appreciably reduced by a heating limitation, it is the skin friction which severely limits the maximum value L/ D to less than four for flight application. Correlation of these results with wind tunnel data are shown to verify the aerodynamic characteristics. The resulting optimized configurations of this investigation are shown to be substantially superior to any previous developmental flight vehicle.

REFERENCES

1. Hankey, W. L.,"Optimization of Lifting Re-entry Vehicles," ASD-TDR-62-1102, WPAFB, Ohio, 1963.

2. Hankey, W. L., Neumann, R. D., Flinn, E. V., "Design Procedures for Computing Aerodynamic Heating at Hypersonic Speeds," WADC TR-59-610, WPAFB, Ohio, 1960.

3. Hankey, W. L., Schroeder, L. J., "Optimization of Lifting Re-Entry Bodies," Proceedings 12th Annual Air Force Science and Engineering Symposium, 1965.

4. Gregorek, G. M. and Lee, J. D., "Design Performance and Operating Characteristics of the ARL Twenty-Inch Hypersonic Wind Tunnel," ARL 62-392, 1962.

NOMENCLATURE

A	Surface area (ft^2)
b	Width (ft)
c	Root chord (ft)
C_f	Skin friction coefficient
C_p	Pressure coefficient
D	Drag (lb)
h	Height (ft)
k	Newtonian modifier
L	Lift (lb)
$\underline{n}$	Surface unit normal vector
q	Dynamic pressure (lb/ft^2)
$\dot{q}$	Heating rate (Btu/ft^2 sec)
R	Body radius (ft)
Re	Reynolds numbers
R_N	Nose radius (ft)
$\forall$	Volume (ft^3)
α	Angle of attack (degrees)
γ_w	Vehicle density (lb/ft^3)
η	Volumetric efficiency

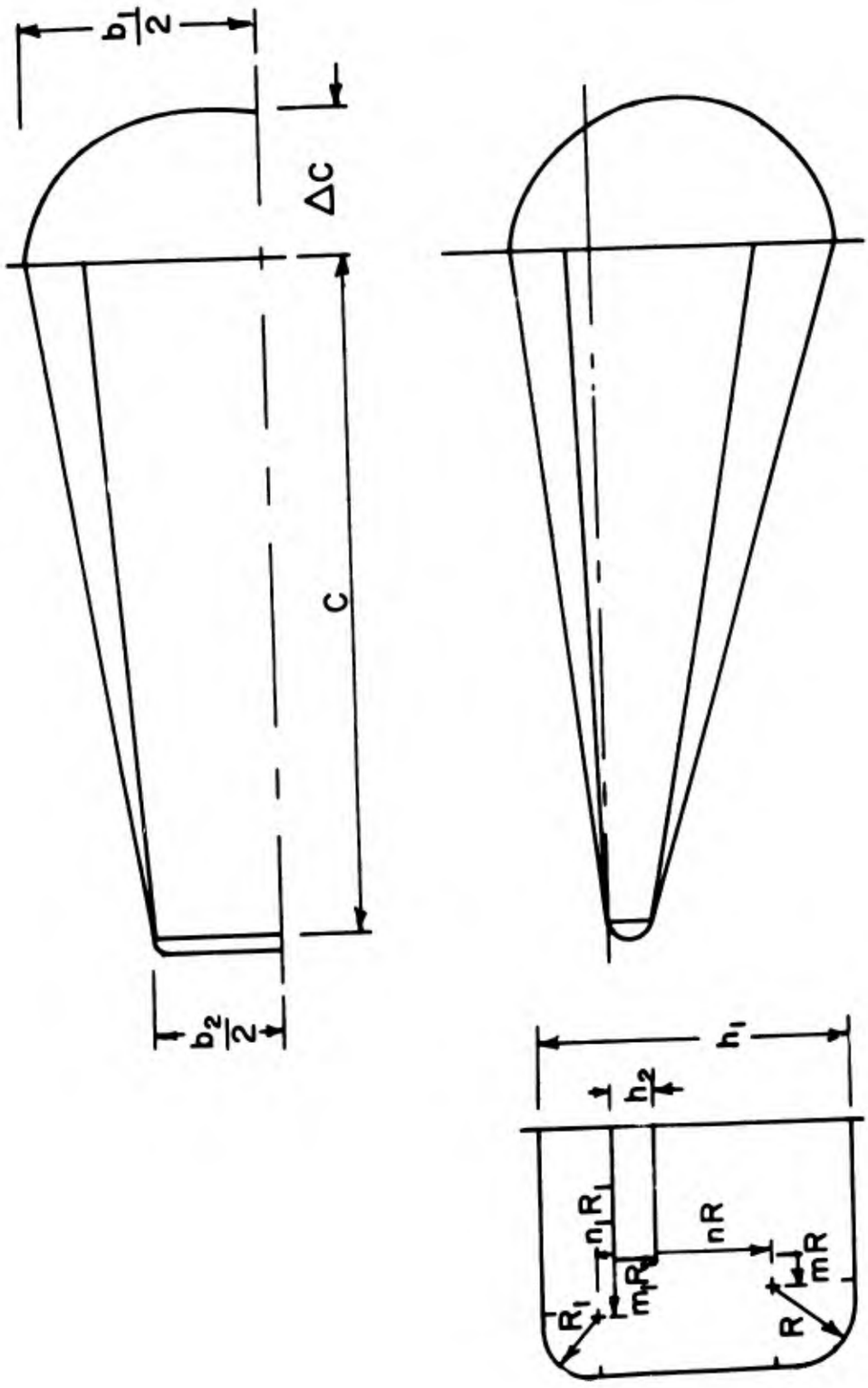

GENERALIZED LIFTING BODY GEOMETRY

FIGURE 1

$\frac{L}{D} = 4$

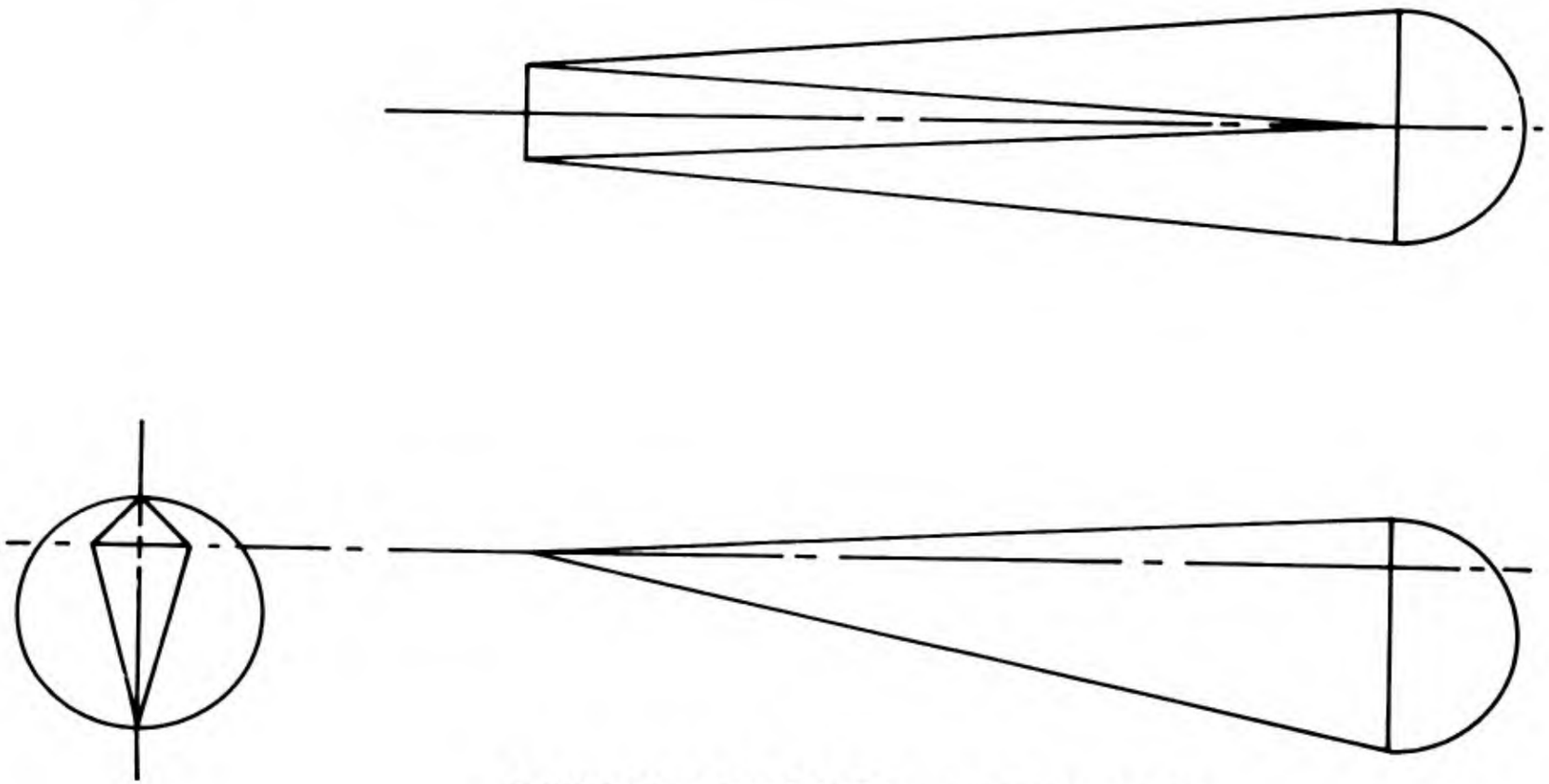

TYPICAL OPTIMIZED LIFTING BODY

FIGURE 2

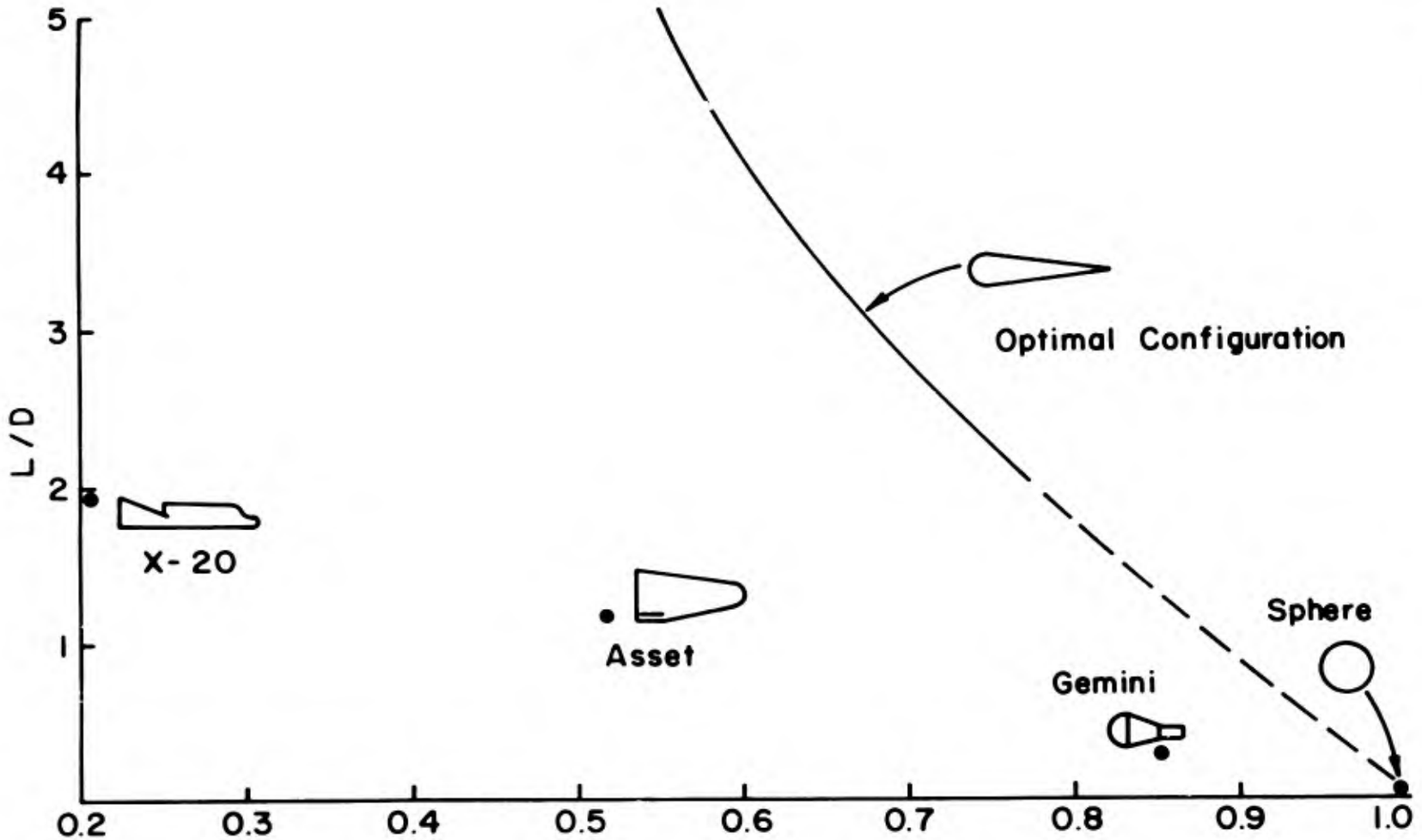

HYPERSONIC LIFT/DRAG RATIOS VERSUS VOLUMETRIC EFFICIENCY

FIGURE 3

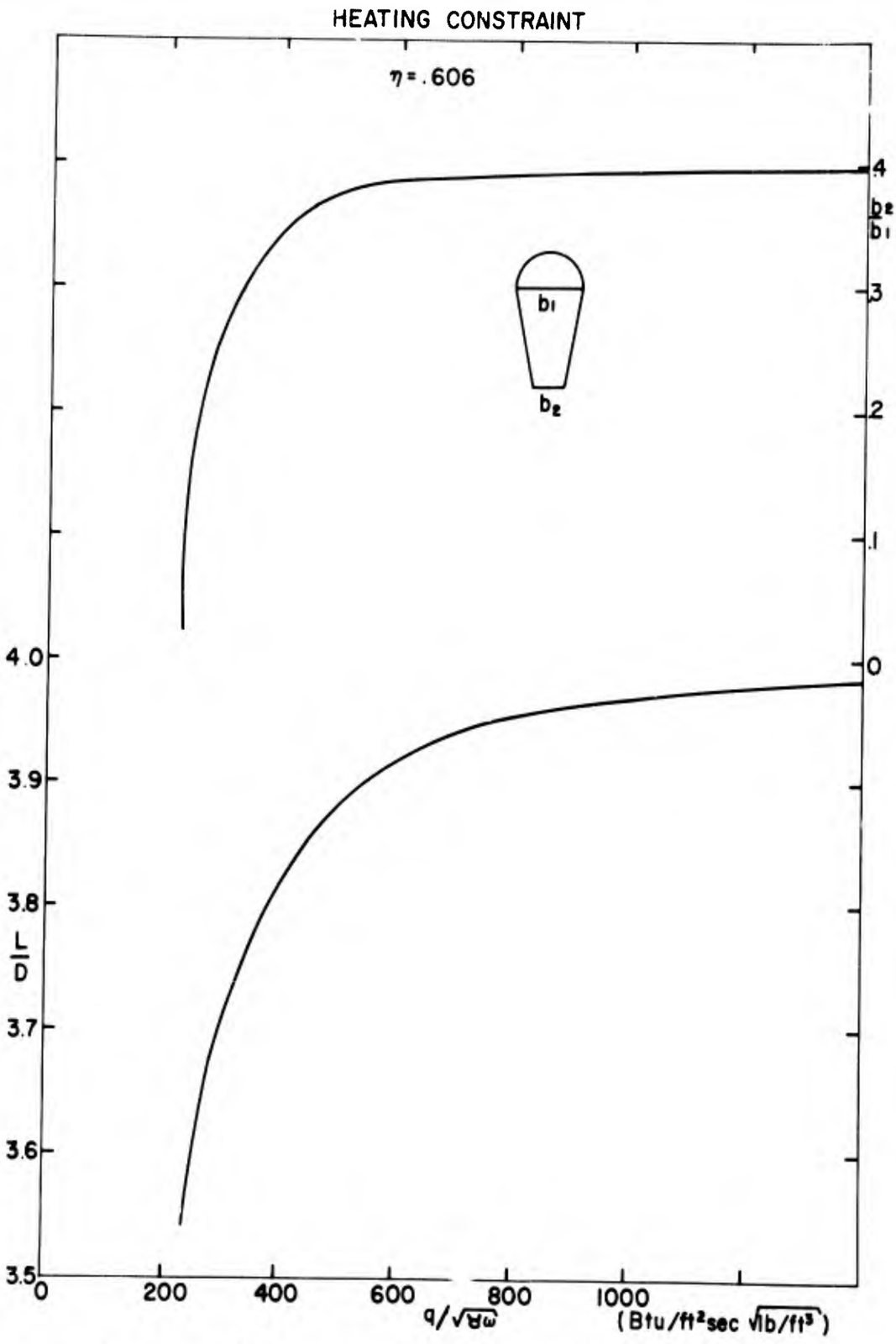

Fig 4. Optimum Configuration with Heating Constraint

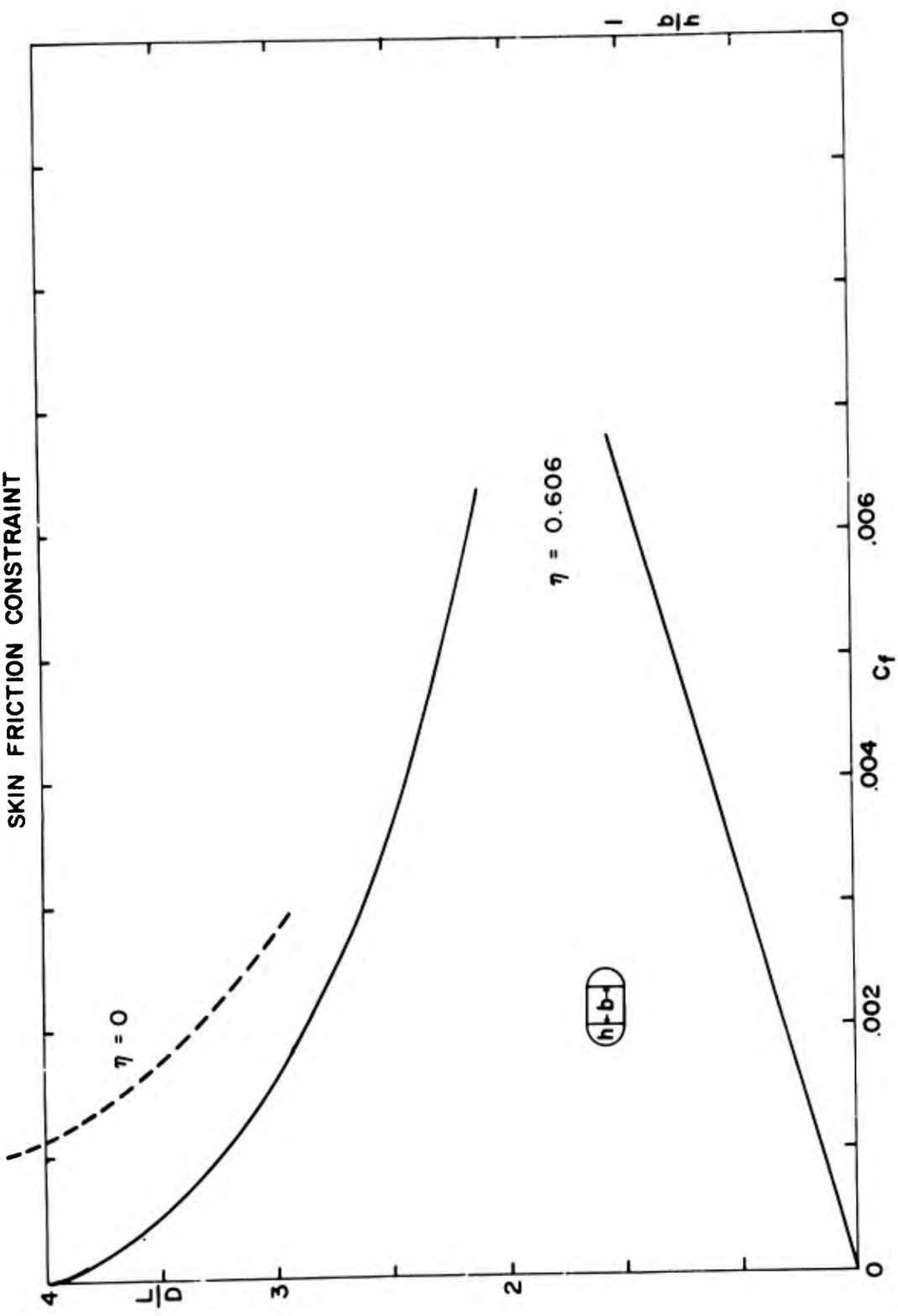

Fig 5. Optimum Configuration with Skin Friction Constraint

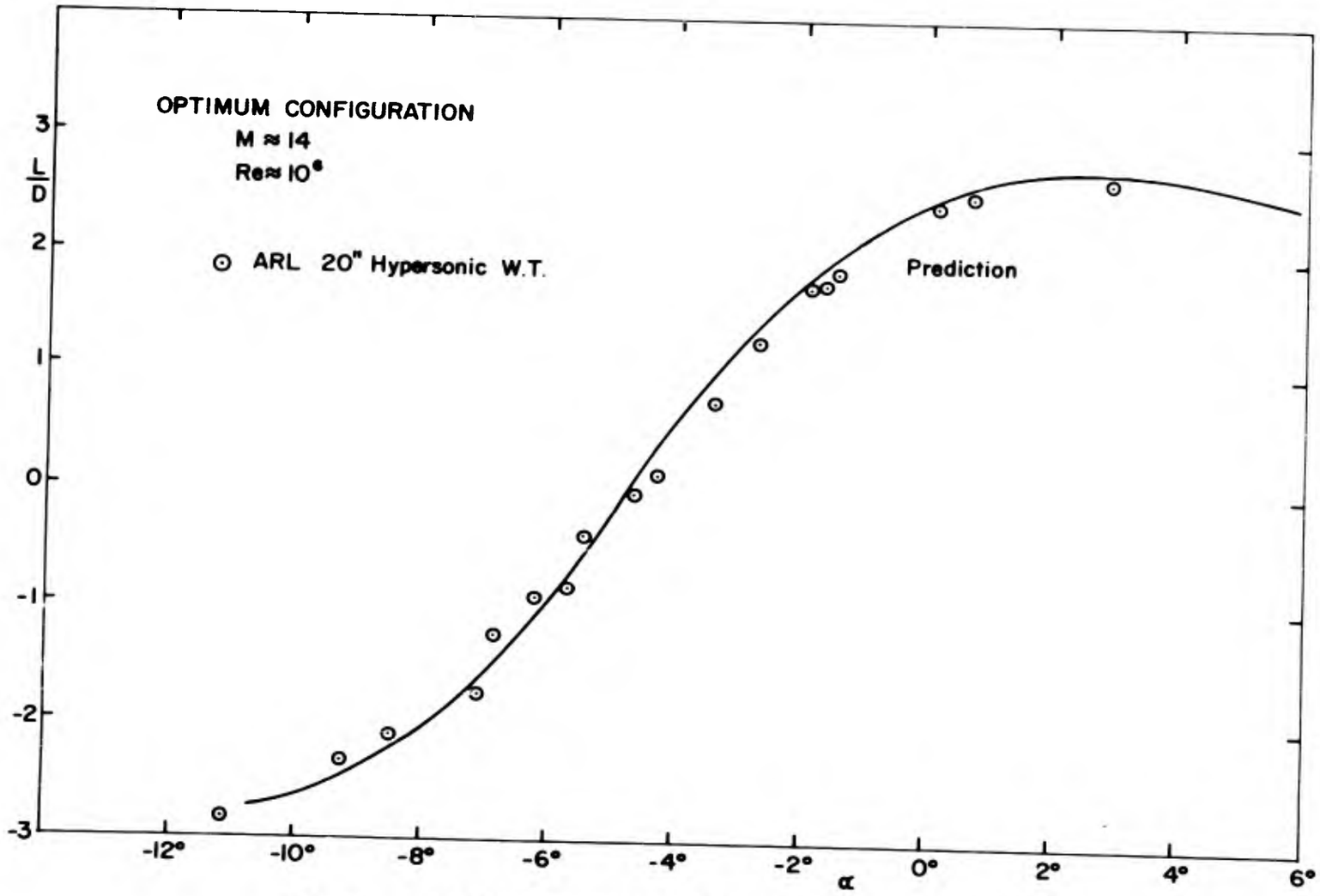

Fig 6. L/D Comparison of Theory and Experiment

Dr. Anthony K. Oppenheim is Professor of Aeronautical Sciences at the University of California, Berkeley. He received his Dipl. Ing. from the Warsaw Institute of Technology in 1943, and his Ph. D. from the University of London and the Imperial College in 1945. Before joining the staff of the University of California, he served on the faculties of City and Guilds College in London from 1945 to 1948, and Stanford University from 1948 to 1950. Dr. Oppenheim spent the 1960–61 academic year in Paris as a visiting professor at the Sorbonne, and has been serving on the National Aeronautics and Space Administration's Research Advisory Committee on Fluid Mechanics since 1963. He is the author of numerous journal articles and technical papers.

GASDYNAMICS OF EXPLOSIONS AND ITS RELEVANCE TO PROPULSION

A. K. OPPENHEIM
University of California, Berkeley

ABSTRACT

The subject of Gasdynamics of Explosions concerns the interrelationship between molecular processes resulting in the deposition of a significant amount of power in the working substance and tne continuum mechanics of its concomitant, non-steady motion. It is demonstrated that acquisition of knowledge in this field should be instrumental in extending the performance range of rocket propulsion systems, and recent advances in the subject are reviewed. These were due primarily to novel insight into gaseous detonation phenomena that has been achieved by the use of a variety of modern experimental techniques, such as laser-schlieren photography yielding a multi-frame sequence of records, each with an effective exposure of about a nanosecond,produced at a megacycle frequency; pressure transducers with sub-microsecond rise-time; as well as direct recording of the traces of the multi-wave intersections that are typical of the gasdynamic processes associated with the deposition of high power in a compressible medium.

INTRODUCTION

The involvement of the Air Force in the basic aspects of explosion on one hand, and propulsion on the other,does not need any justification. The novel feature of this paper is the suggestion that the two interests can be combined in a program of research, offering a promise for a profitable pay-off in the future. It should be pointed out at the outset that this does not exclude the possibility of using the results of such a study directly for the improvement of explosive devices. In fact,some of the findings of the described here research program have been already utilized for the development of a novel weapon for insurgent warfare. These achievements are, however, left out completely from present considerations, in favor of the argument that the study under question can have a much more profound influence on the progress of those aspects of technology that are of the most crucial importance to the Air Force, namely propulsion for aircraft and rockets.

The justification for a program of basic research in engineering requires special argumentation. If it is demonstrated that the pay-off is in the form of a device or an instrument, the research is not basic. In order to be basic, such a program must support industrial research, that is needed for the design, which leads to the development, yielding eventually the desired product. How then can one devise a rational justification for a program of basic research? In the opinion of the author

this can be accomplished only by an extrapolation, on a sufficiently broad spectrum, of the progress of technology that one desires to promote.

This is exactly how the subject of our research program is introduced here. From the synthesis of the progress of propulsion, covering the full spectrum from the steam engine up to modern booster rocket, it is demonstrated that the next step must be based on the exploitation of explosive processes. This,in turn,demands a better understanding of the Gasdynamics of Explosions -- a subject concerned with the interrelationship between kinetic processes that result in the deposition of a significant amount of power in the working substance,and the continuum mechanics of its concomitant, non-steady motion. The significance of power deposition is manifested by the acceleration it imparts on the medium, or, what amounts to the same thing, by the pressure wave it generates.

Recent advances in this subject are then described. They are based primarily on novel insights into gaseous detonation phenomena that have been attained as a consequence of a successful exploitation of modern high-frequency response instrumentation. This includes a schlieren-rotating mirror camera system, equipped with a pulsating, high-power laser light source, capable of frame photography with nanosecond exposures at megacycle frequency; pressure transducers with submicrosecond rise time; pulse spectrometric measurements; fast response heat transfer gauges; and direct recording of the traces of the multi-wave interaction phenomena that are characteristic of the gasdynamic processes associated with the deposition of energy at a high power density in a compressible medium.

TECHNOLOGICAL ASPECTS

Evolution of propulsion is characterized by the strive to pack more and more power into less and less space, or, in other words, to achieve higher power density of energy deposition in the working substance. Although this sense of development is quite evident from the fact that today's gigawatt rocket booster engine is not much larger than the considerably weaker powerplant of John Stevenson, it might be of interest to have this notion expressed specifically.

Fig. 1 displays the spectrum of power density of energy deposition in combustion chambers of prime-movers. It covers the complete range of operating conditions, from the steam boiler, whose power density is about 1 kilowatt per liter, through an I.C. engine, where it may reach a level of 100 kilowatts per liter, followed by a turbojet combustor, where it can achieve the magnitude of 1 megawatt per liter, to a high output rocket thrust chamber, where it can be as high as 100 megawatts per liter, attainable in hydrogen-oxygen systems. The higher levels of power deposition can be easily reproduced for study in the laboratory, under equivalent flow conditions, by experiments involving gasdynamic explosions, covering a

range in power density from at least 10 megawatts per liter to over 10 gigawatts per liter.

For example Fig. 2 shows a stroboscopic laser-schlieren record of a detonation wave in a hydrogen-oxygen mixture, where the effects of energy deposition at a power density of almost 1 gigawatt per liter (1) are manifested by the multi-wave structure of the front that, at the same time, extends over a convenient width of nearly half a centimeter,which is quite sufficient for experimental insight into some of its most prominent gasdynamic features. A photograph of the traces, scraped on a soot-covered side wall of the detonation tube by the multi-wave intersections (5, 6, 7) that are associated with such a front, is displayed to scale above the schlieren record. Information provided by the soot imprint permits a qualitative insight into the gasdynamic flow field of the detonation wave.

It should be noted that reproduction of the value of power density alone is not sufficient for the simulation of gasdynamic conditions existing in high output thrust chambers. The process must be also dynamic in nature, that is,it must be capable of generating a high intensity flow field. This is indeed the case in detonation experiments where the high velocity of the wave is associated with an appreciable motion of the products. As it can be easily ascertained from Fig. 2, the wave propagated at a velocity of 2.5 km/sec into the reactants which were at rest. Since the local velocity of sound immediately behind the wave was about 1.5 km/sec, it follows from the Chapman-Jouguet condition that the process generated a flow field in the products with an effective particle velocity of an order of 1 km/sec.

How realistic are such observations with respect to technological operating conditions? Performance range of rocket propulsion systems is usually described by means of a vehicle acceleration - specific impulse map, as shown in Fig. 3. Of particular interest to our theme are the lines of constant specific power that evidently impose a limit,at a level of about 100 hp/lb,on the attainable performance, according to current technology. An equivalent map can be constructed to describe the performance range of just the thrust chambers, as shown in Fig. 4, where reference unit of mass is that of the working substance,rather than of the vehicle, as in Fig. 3. Such a map describes,in effect,all the mechanical parameters associated with the acceleration of the substance due to the deposition of power. This is reflected in the new set of lines, namely those of the "effective reaction time" which is understood here to represent the average time interval required for acceleration to final jet velocity under the action of a constant force to mass ratio. The values of the various parameters in Fig. 4 are, of course, orders of magnitude larger than those of Fig. 3, except for the jet velocity and specific impulse which, it should be noted, cover on both maps the full range, up to the velocity of light.

The range of operating conditions characteristic of CURRENT TECHNOLOGY has been sketched out on the basis of performance parameters of the F1, H1 and J2 engines,and the estimated capability of an advanced arc-jet thrustor (2). The field

of ADVANCED CONCEPTS corresponds to operating conditions of such projects as Orian, and is culminated by the performance characteristics of explosive accelerators that, as it has been experimentally demonstrated (3, 4), are capable of producing high density jets at a velocity of up to 100 km/sec. The coordinates of the point marked DETONATION in Fig. 4 are those of the wave depicted by Fig. 2.

The REGIME OF GASDYNAMICS OF EXPLOSIONS covers the range of operating conditions from those corresponding to current booster engines up to the specific powers of the most advanced concepts,and the effective time of a nanosecond whose significance to our subject lies in the fact that it represents the characteristic chemical time (local density divided by the overall reaction rate) of a high intensity combustion process.

The map of Fig. 4 suggests that the study of Gasdynamics of Explosions should be certainly of benefit to the progress of propulsion technology. This conclusion is confirmed by the fact that upper bounds of specific power attainable in chemical propulsion systems are, as a rule, imposed by the stability limits, beyond which the process of energy conversion becomes explosive in character. In this respect it is significant to note that the more recently identified modes of combustion instability, such as surge and Pe-pops, are associated with the action of high frequency pressure pulses. Study of the generation of such pulses should be therefore considered of prime importance to further evolution of propulsion, irrespectively whether it is associated with the actual exploitation of the detonation process or not.

Summing up the foregoing arguments, we can be either satisfied with the performance range of propulsion systems according to current technological standards, or we may wish to promote further progress. The latter can be accomplished only by basic research. Should this be indeed our choice, then the proper direction to proceed is that towards the advances of our knowledge in the field of Gasdynamics of Explosions.

PHENOMENOLOGICAL ASPECTS

The most convenient way to study experimentally the subject of Gasdynamics of Explosions is, as it has been already inferred, by the observation of detonative processes in gaseous media. Great progress has been made over the last few years in this field, especially as a result of contributions from the Soviet Union (5, 6, 7). A review of the literature on this subject has been presented recently (8), so that, references to the numerous contributions of others can be omitted from here, and - not, of course, without the unavoidable restriction in scope - our attention can be concentrated instead on the phenomenological implications of just the experimental records obtained in the Propulsion Dynamics laboratory at Berkeley.

In order to understand how the gasdynamic flow field is developed, one must probe first into the initiation of flow, following ignition of a detonative gas mixture. This process is demonstrated by Fig. 5, which presents,in its main portion, a streak schlieren photograph of an accelerating flame in a stoichiometric hydrogen-oxygen mixture, maintained in a 1" x 1 1/2" cross-section tube initially at NTP, immediately upon ignition produced by a weak spark located at the closed end. Displayed as inserts are pressure records obtained in three locations along the path of the accelerating flame. One of them is shown replotted to the time scale of the streak photograph,to demonstrate the relationship between the pressure and the flow field. The latter is manifested by a representative particle path denoted by the broken white line. As clearly manifested by pressure records and by the wave streaks ahead of the flame, its acceleration is associated intimately with the generation of a pressure pulse which propagates into the reactive mixture in form of a simple compression wave that later coalesces into a shock wave. The coupling between molecular processes of energy deposition and gasdynamics of fluid motion is illustrated here by the interrelationship between the flame trace and the particle path. This can be described as a non-linear feed-back system in the course of a bootstrap operation, in that the accelerating flame generates a pressure wave, which precompresses the reactants before they are engulfed by the flame, reinforcing thereby its acceleration. In the case at hand the temperature increase corresponding to the maximum pressure ratio is about 200°F,and the maximum flame acceleration is 10^5 g's.

The origin of the pressure pulse is believed today to be well understood (9,10), as stemming primarily from the increase in the rate of energy release per unit frontal area which, in turn, can be, at this stage, ascribed entirely to the rate of growth of the flame kernel. Thus, at the initial phase of explosion, the only effect of the kinetic processes of energy release inducing the gasdynamic flow field,is the relative propagation velocity of the flame front. The rest can be accounted for by the geometry of the flame kernel in relation to the cross-section of the enclosure that confines the flow field.

Streaks which are observed behind the accelerating flame front are due to its cellular, or wrinkled-laminar, structure, as shown by the laser-schlieren photograph taken across the whole width of the tube and displayed below the main record of Fig. 5. Later, due to wall effects, the flame and the flow deccelerate, while the pressure drops down and the flame surface area decreases. At the top of the flame trace a new system of streaks appears. This is associated with the transition to turbulent structure, as demonstrated by the laser-schlieren photograph displayed above the main record of Fig. 5. Especially noteworthy here is the complete change in the character of the flame front, as its surface caves in when it becomes turbulent.

The transition to turbulence promotes an increase in the rate of molecular processes of energy release, that is,it results in higher power density of energy deposition. This leads to further acceleration of the flame, and to the concomitant

generation of additional pressure waves. As a consequence of this process, a system of shock fronts is generated ahead of the flame, as illustrated by Figs. 6 and 7, representing,respectively,the streak schlieren (11) and the multi-frame laser-schlieren records (12) of the onset of detonation. In order to establish proper relationship between these two sets of records, one should perceive that in Fig. 6, as in Fig. 5, the time increases upwards, while in Fig. 7, as in Fig. 2, it increases downwards. The reason for this is the fact that, since for streak records the orientation of the print is factually immaterial, it has been selected for Figs. 5 and 6 so as to conform with the generally accepted practice of wave diagrams. In the case of frame photographs, orientation is of factual significance, and printing upside down, in order to comply with convention, would produce unnecessary confusion.

The shocks merge, creating a high temperature regime between the transmitted shock and the contact discontinuity, where pre-ignition, in form of a point explosion, takes place (11). The front of this secondary explosion in the exploding gas appears at first as a spherical kernel (visible in the frame at 20μsec. in Fig. 7) and, upon collision with the walls, it is transformed into a wave system consisting of three fronts:

(1) the reactive detonation moving into the unburned mixture,
(2) the retonation - an inert shock - moving into the burned gas, and
(3) the decaying blast waves oscillating between the walls of the enclosure.

All this is associated with the generation of an intense pressure pulse, as manifested by the transducer records displayed in the insert, and demonstrated by the pressure profile drawn on the basis of one of these records in Fig. 6. The multi-wave structure of the detonation front, which was so clearly apparent in Fig. 2, is evident also from the streaks behind the detonation front in Fig. 7, in contrast to their complete absence behind the retonation front,as well as behind the transverse blast waves. Similarly as in Fig. 2, displayed on top of Fig. 7 is a soot imprint recorded on a side wall and inserted in proper orientation,as well as to scale, with frame photographs.

In reference to this record it should be observed that the property of "writing on the wall" is indeed typical of the detonation wave, since neither the highly turbulent flame nor the system of shocks ahead of it left any trace on the soot film. Study of the exact nature of the multi-wave intersection processes that take place in detonation are of prime significance to our subject, since they offer an attractive promise of being instrumental in bridging the gap between the molecular processes of energy deposition at a high power density under intense flow conditions,and the concomitant gasdynamic wave phenomena. This is the reason why observation and analysis of multi-wave intersections (13) became one of the principal objectives of our current research effort.

The bridge has been already established in some cases. For example, it has been demonstrated recently (14) that the time delay between the instant of shock

merging and the onset of detonative ignition corresponds exactly to that deduced from the kinetic theory of chemical induction times. Experimentally this theory is based on shock tube data obtained at conditions of negligibly small power density of energy deposition.

This brief sketch of the development of detonation points out four distinct gasdynamic phases of the explosion process, each associated with a progressively higher level of power density of energy deposition in the substance:

(1) initial generation of the flow field by an accelerating flame following ignition,
(2) subsequent intensification of the flow due to transition to turbulence,
(3) wave interaction processes associated with transition to detonation and the concomitant generation of a high intensity pressure pulse, and
(4) establishment and maintenance of the multi-wave structure of the detonation wave.

The fluid-mechanic features of each of these phases are quite different, but all are basically governed by the interaction between the molecular processes of energy release and the gasdynamic properties of the flow field. It is the theory of such phenomena that constitutes in essence the Gasdynamics of Explosions. In this respect the evolution of the subject has just been barely started, notwithstanding the almost hundred years of detonation research.

CONCLUSIONS

From the survey of propulsion technology it appears that the next step in its evolution, if we wish to make it, must be based on basic research in Gasdynamics of Explosions. Recent advances in this subject helped to reveal a good deal of novel phenomenological facts. This should be followed now by a period of painstaking research into the precise nature of these phenomena and their analytical interpretation, as well as into the effects of various operating conditions, with the objective of developing suitable means for their control.

The most important tool for further experimental research is the ultra-high frequency response instrumentation. Since the most prominent feature of explosive phenomena is the pressure pulse they produce, the most important of such instruments is the pressure transducer. A reasonable goal here should be a frequency response in gigacycles per second,or a rise-time of a nanosecond - the typical characteristic chemical time of the explosion process.

Future pay-off from such a research program should be quite rewarding, not only in its contribution to the science of explosion processes and gasdynamics, but also directly to such technological objectives as the observation, control and rating of combustion instability in combustors and augmentors, as well as the development of propulsion and energy conversion systems utilizing fuels whose explosive

(referred to in the trade as "energetic") properties are beyond the limits of today's technology.

To sum it all up, we have just learned what is it all about, but we are still far from knowing how much, let alone how to get the best bargain out of it. Only when we reach the last of these three stages, can we claim a real contribution in an engineering sense, since it is just the last step that implies optimization - the earmark of engineering. In order to do so, we must have specific knowledge of the facts, and this can be obtained solely by a basic research program,as described in this paper.

ACKNOWLEDGEMENT

The accomplishments of the described here research program, carried out at the Propulsion Dynamics laboratory in Berkeley, would not have been possible without the sustained support it received right from the outset and throughout its duration from the Air Force Office of Scientific Research. For continuation of this program acknowledgement is also due to the National Aeronautic and Space Administration which today contributes an almost equal share of support. The results of our work cannot be presented without giving proper credit to the invaluable assistance the author received from his students and staff, especially Dr. P. A. Urtiew whose association with the laboratory dates from its inception in 1957.

REFERENCES

1. Oppenheim, A. K., "Evolution of Propulsion Systems and the Detonation Process", Proceedings of the Third Annual Meeting of the Society of Engineering Science, Davis, November, 1965.

2. Stuhlinger, E., Ion Propulsion for Space Flight, McGraw-Hill Book Co., First Edition, Table 2-1, p. 16, 1964.

3. Voytenko, A. Ye., "Producing High-Velocity Gas Jets", A. N. SSR Doklady 158, G, 1278-1280, 1964.

4. Lunc, M., Nowak, H. and Smolenski, D., "Accelerators for Jets Formed by Shaped Charges", Bulletin de l'Academie Pononaise des Sciences, Serie des Sciences Techniques, XII, 5, 295-297. 1964.

5. Shchelkin, K. I. and Troshin, Ya. K., Gazodinamika Goreniya (Gasdynamics of Combustion), Izd. Akad. Nauk SSSR, 255 pp., Moscow, 1963; Transl. NASA TTF-231, 1964, or Mono Book Corp., Baltimore, 1965.

6. Soloukhin, R. I., Udarnye Volny i Detonatsii v Gazakh (Shock Waves and Detonation in Gases), Gos. Izd. Fiz. Mat. Literatury, 175 pp., Moscow, 1963; (Transl. by B. W. Kuvshinoff, Mono Book Corp., Baltimore, 1966).

7. Voitsekhovsky, B. V., Mitrofanov, V. V. and Topchian, M. E., Struktura Fronta Detonatsii v Gazakh (Structure of Detonation Fronts in Gases), Izd. Sib. Otd. A. N. SSSR, 168 pp., Novosibirsk, 1963.

8. Oppenheim, A. K., "Novel Insight into the Structure and Development of Detonation", Astronautica Acta, 11, 6, 391-400, 1965.

9. Laderman, A. J. and Oppenheim, A. K., "Initial Flame Acceleration in an Explosive Gas", Proc. Roy. Soc., A, 268, 153-180, 1962.

10. Urtiew, P. A., Laderman, A. J. and Oppenheim, A. K., "Dynamics of the Generation of Pressure Waves by Accelerating Flames", Tenth Symposium (International) on Combustion, pp. 797-804, The Combustion Institute, Pittsburg, 1965.

11. Urtiew, P. A. and Oppenheim, A. K., "Experimental Observations of the Transition to Detonation in an Explosive Gas", Proc. Roy. Soc., A, 295, 13-28, 1966.

12. Oppenheim, A. K. and Urtiew, P. A., "On the Genesis of Gaseous Detonation", XXXVI International Congress of Industrial Chemistry, Brussels, September 10-21, 1966.

13. Oppenheim, A. K. and Smolen, J. J., "Vector Polar Method for the Analysis of Wave Intersections", University of California, College of Engineering, Tech. Note No. 1-67, Berkeley, November 1966.

14. Urtiew, P. A. and Oppenheim, A. K., "Detonative Ignition Induced by Shock Merging", Eleventh Symposium (International) on Combustion, Berkeley, August 15-21, 1966.

FIGURE CAPTIONS

Figure 1. Power Density Spectrum of Energy Deposition in Prime-Mover Combustion Chambers including the extent of conditions attainable by experiments involving gasdynamic explosions.

Figure 2. Stroboscopic Laser-Schlieren Records of a Detonation Wave and Matching Soot Imprint on Side Wall. The medium is a $4H_2 + 3O_2$ mixture maintained in a 1" x 1 1/2" cross-section tube, initially at a pressure of 87.3 mmHg and room temperature (1).

Figure 3. Performance Range of Rocket Propulsion Systems on the vehicle acceleration -- specific impulse plane.

Figure 4. Performance Range of Thrust Chambers on the effective force to mass ratio -- specific impulse plane.

Figure 5. Streak Schlieren Photograph of Accelerating Flame and the Concomitant Flow Field (9) in a stoichiometric hydrogen-oxygen mixture maintained initially in a 1" x 1 1/2" cross-section tube at NTP. Displayed as inserts are pressure records at positions 1, 2 and 3. Vertical scale: 5.2 psia/cm for record (1), 10.4 psi/cm for records (2) and (3); horizontal sweep from left to right: 100 μsec/cm for record (1) and (2) 200 μsec/cm for record (3). Depicted by white broken line is a representative particle path, while the continuous line presents pressure record (3) replotted to the time scale of the streak photograph. Immediately below and above the streak record are flash laser-schlieren photographs,taken across the whole width of the tube. Streaks were taken through a slit along the center line of the tube. Time instances corresponding to flash records are denoted by appropriate white horizontal lines, demonstrating the relationship between the recorded streaks and the actual flame structure.

Figure 6. Streak Schlieren Record of Transition to Detonation and Matching Flash Photograph of the Flow Field (11). Stoichiometric hydrogen-oxygen mixture in a 1" x 1 1/2" cross-section tube initially at NTP. Pressure record displayed as insert is shown replotted to the time scale of the streak. Vertical scale: 260 psia/cm; horizontal scale: 50 μsec/cm. Oscilloscope sweep leads the streak record by 18 μsec.

Figure 7. Stroboscopic Laser-Schlieren Record of Transition to Detonation and the Matching Soot Imprint on Side Wall (12). Stoichiometric hydrogen-oxygen mixture in a 1" x 1 1/2" cross-section tube initially at a pressure of 696 mmHg and room temperature. Pressure records displayed as insert. Vertical scale 200 psia/cm; horizontal scale 50 μsec/cm. Oscilloscope sweep leads the photographic record by 115 μsec.

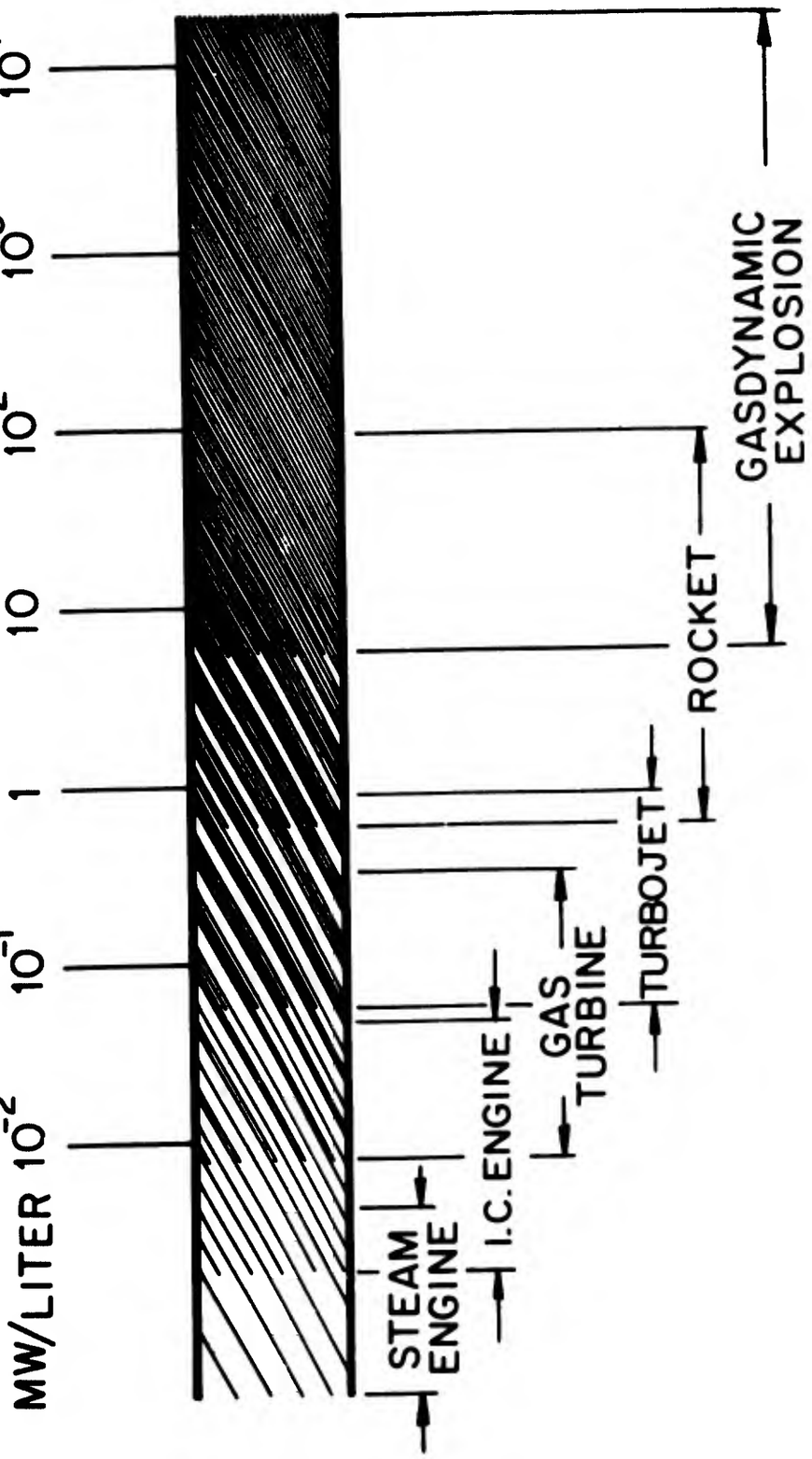
MW/LITER
10^{-2}
10^{-1}
1
10
10^{2}
10^{3}
10^{4}
STEAM ENGINE
I.C. ENGINE
GAS TURBINE
TURBOJET
ROCKET
GASDYNAMIC EXPLOSION

FIGURE 1.

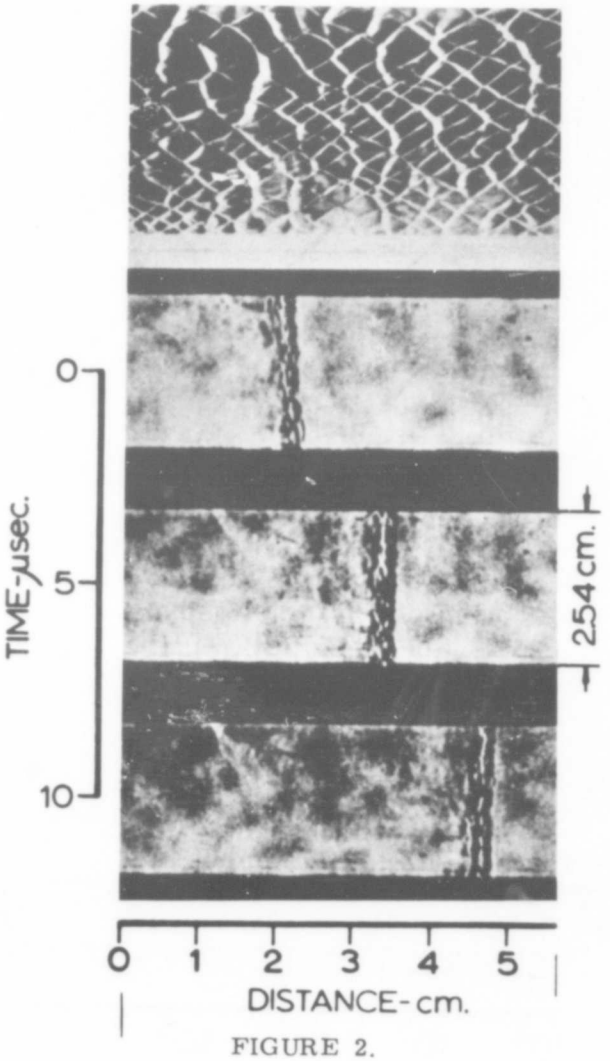

FIGURE 2.

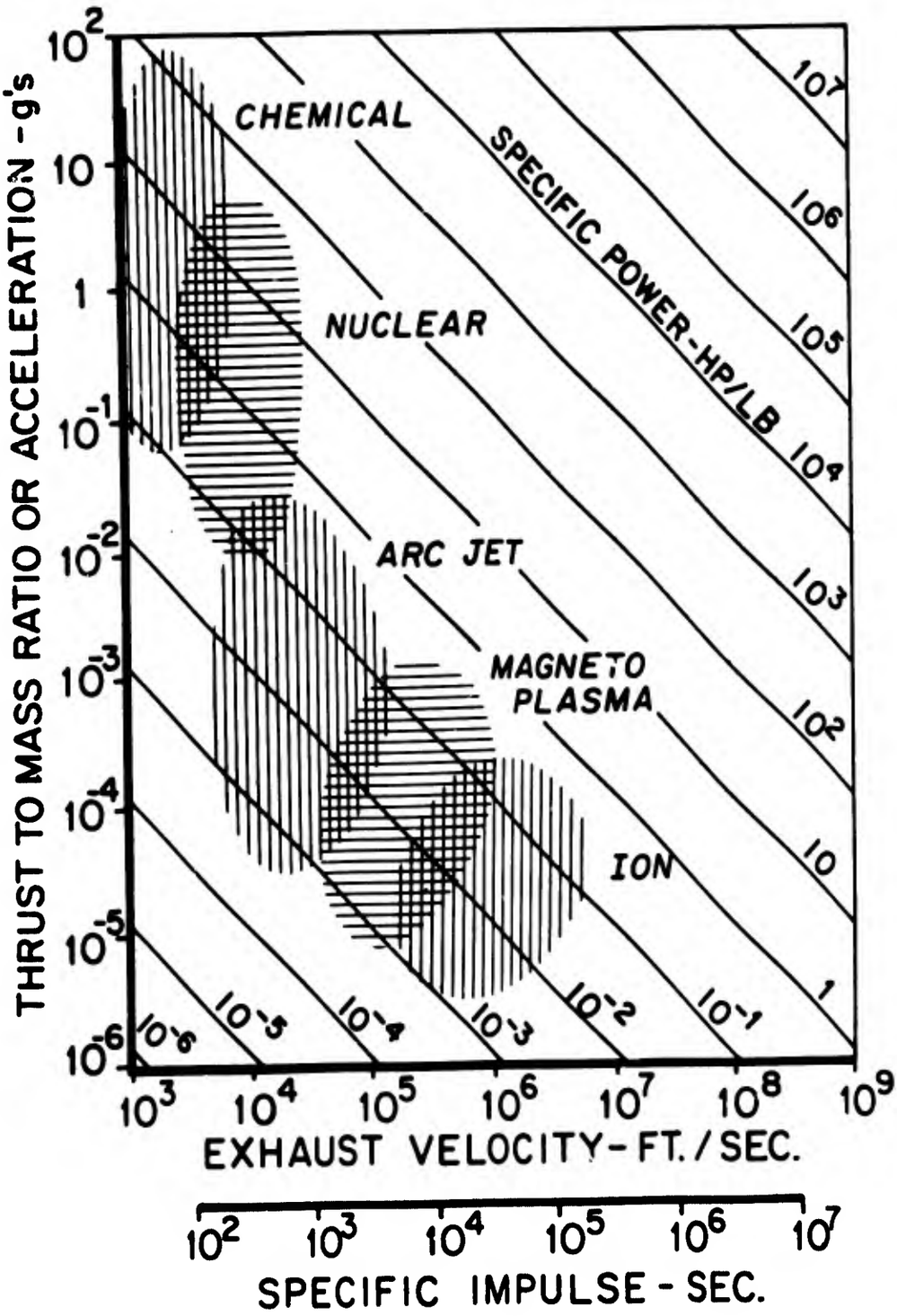
THRUST TO MASS RATIO OR ACCELERATION - g's
10^2
10
1
10^{-1}
10^{-2}
10^{-3}
10^{-4}
10^{-5}
10^{-6}
CHEMICAL
NUCLEAR
ARC JET
MAGNETO PLASMA
ION
SPECIFIC POWER - HP/LB
10^7
10^6
10^5
10^4
10^3
10^2
10
1
10^{-1}
10^{-2}
10^{-3}
10^{-4}
10^{-5}
10^{-6}
10^3 10^4 10^5 10^6 10^7 10^8 10^9
EXHAUST VELOCITY - FT./SEC.
10^2 10^3 10^4 10^5 10^6 10^7
SPECIFIC IMPULSE - SEC.

FIGURE 3.

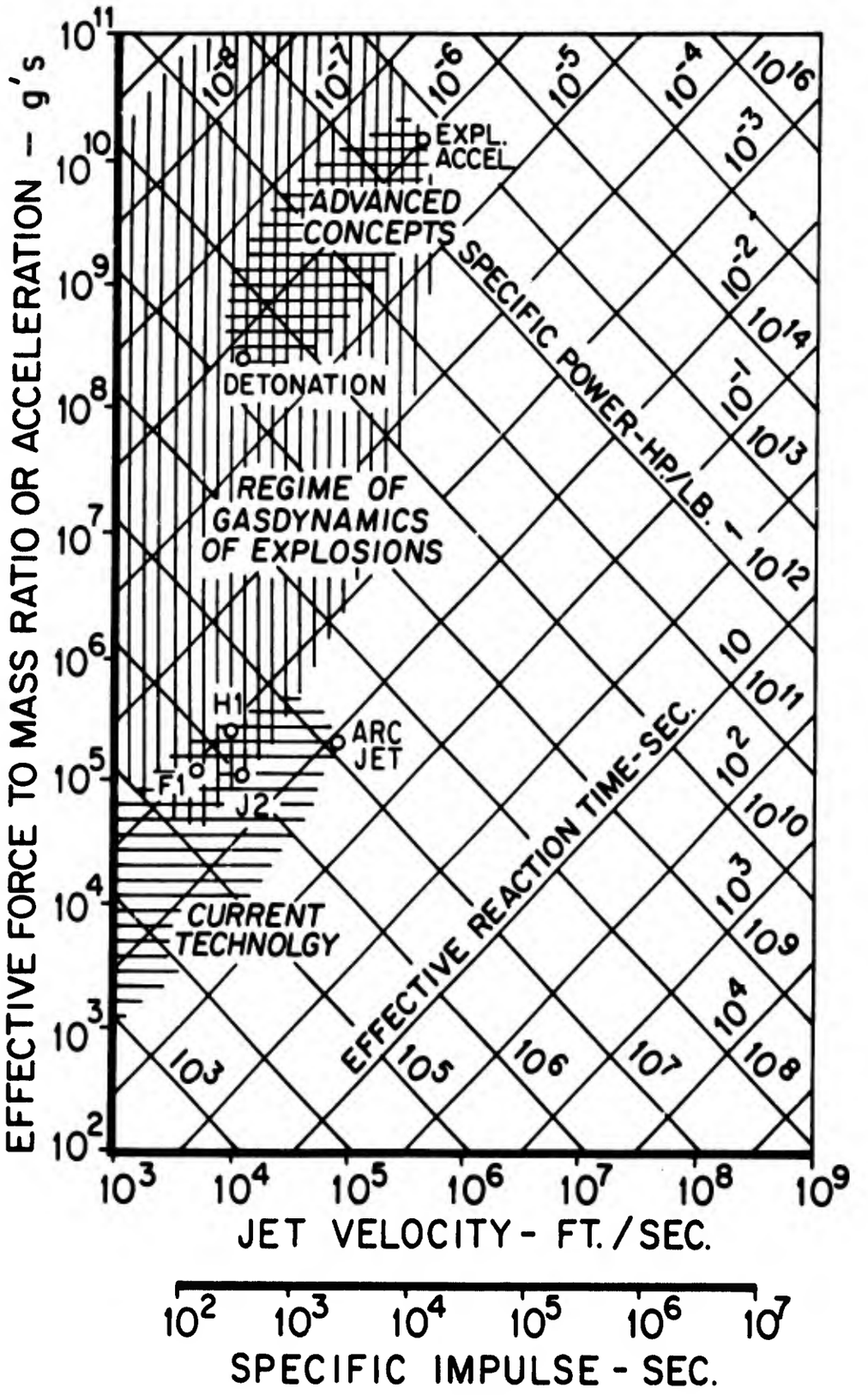
EFFECTIVE FORCE TO MASS RATIO OR ACCELERATION - g's
JET VELOCITY - FT./SEC.
SPECIFIC IMPULSE - SEC.
EXPL. ACCEL
ADVANCED CONCEPTS
DETONATION
REGIME OF GASDYNAMICS OF EXPLOSIONS
H1
ARC JET
F1
J2
CURRENT TECHNOLGY
SPECIFIC POWER-HP/LB.
EFFECTIVE REACTION TIME-SEC.

FIGURE 4.

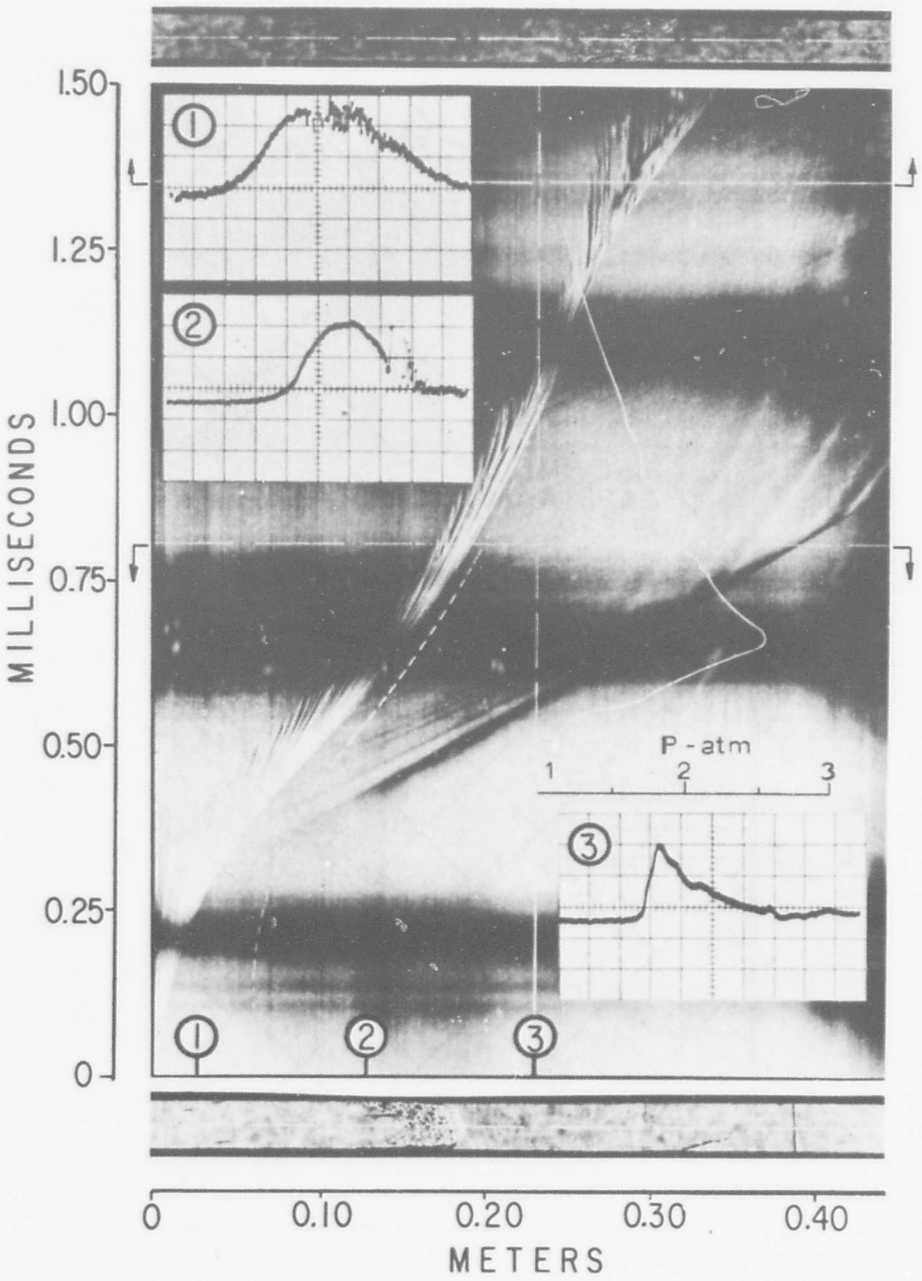
1.50
1.25
1.00
0.75
0.50
0.25
0
MILLISECONDS
P - atm
1
2
3
0
0.10
0.20
0.30
0.40
METERS

FIGURE 5.

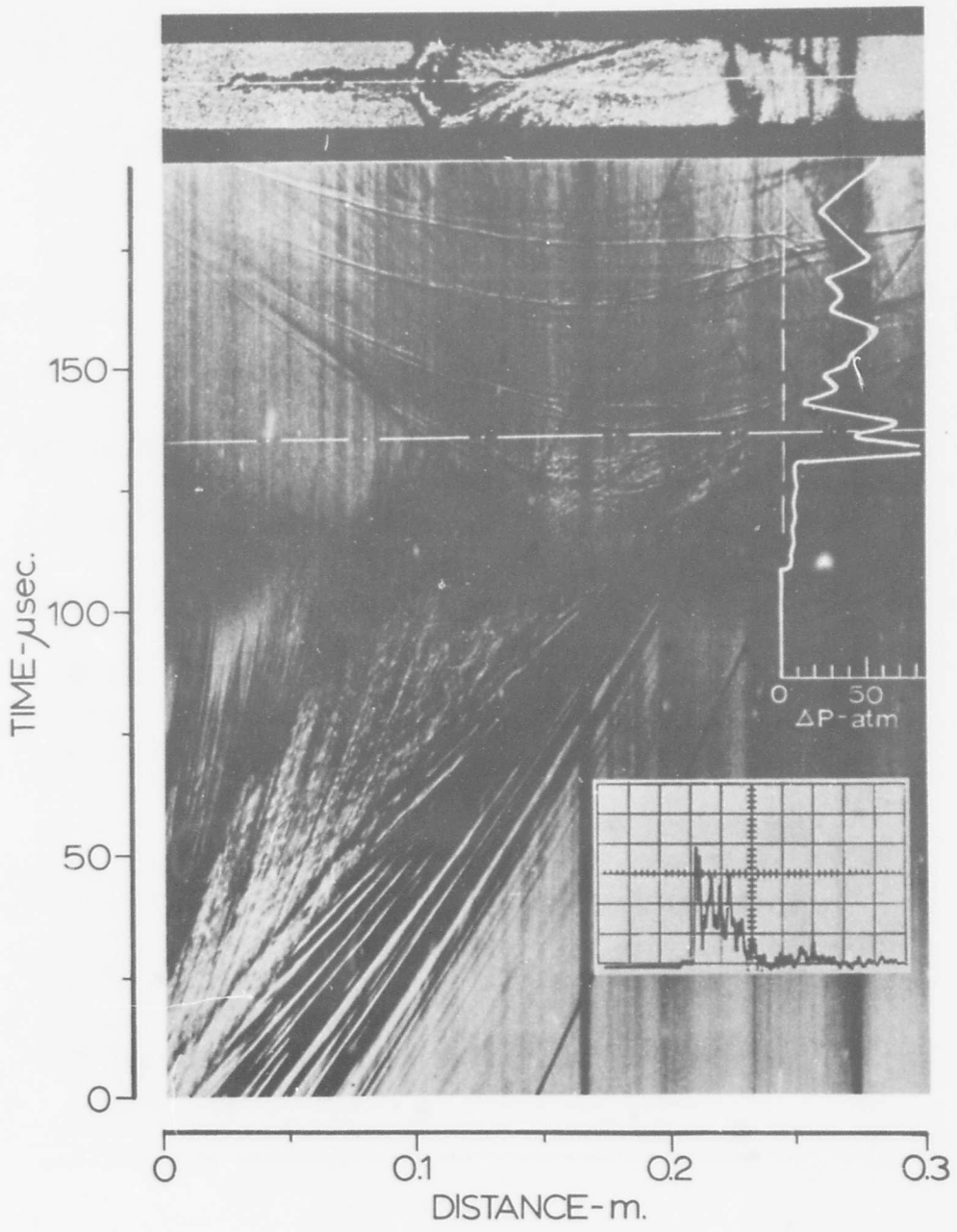

FIGURE 6.

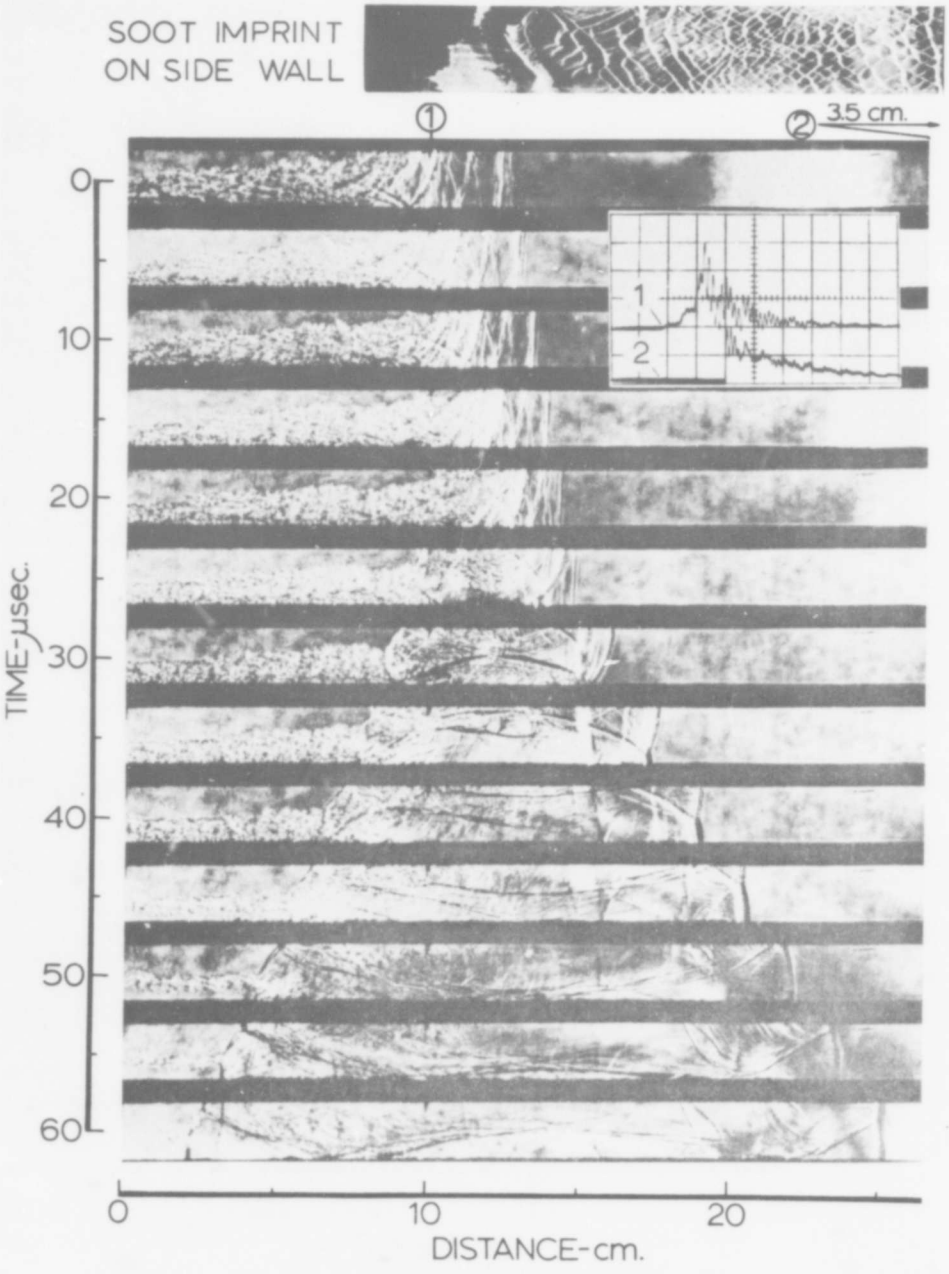
SOOT IMPRINT
ON SIDE WALL
①
②
3.5 cm.
1
2
0
10
20
30
40
50
60
TIME-μsec.
0
10
20
DISTANCE-cm.

FIGURE 7.

BLANK PAGE

Lt. Col. Clyde A. Northcott, Jr., is Program Manager for the OV1 (Orbital Vehicle One) research satellite and Deputy Commander of Detachment 6, Office of Aerospace Research, in Los Angeles, Calif. He received his B.S. degree in Aeronautical Engineering through a resident course of the Air Force Institute of Technology, Dayton, Ohio, in 1952, and his M.A. degree in Business Administration from the University of Chicago in 1962. He has been Chief of the Tactical Bomber Station, Air Force Armament Center at Eglin AFB, Fla., and exchange officer with the Royal Canadian Air Force Central Experimental and Proving Establishment at Fort Churchill, Canada. Col. Northcott has been associated with the Aerospace Research Support Program ever since its establishment in 1960.

THE OV1 - PROMOTER OF TIMELY SPACE RESEARCH

Several years ago the space researcher faced the apparently insurmountable problem of getting his instruments to their selected space environment and then recovering the data. Recognizing this, in 1960 General Schriever established the Probes Program. Now known as the Aerospace Research Support Program or Project 7043, and considerably larger in scope, this program still has the same objective it had then: to meet the requirements of the experimenter economically and on a timely basis. This paper describes an important element of this program: the Orbital Vehicle, Type One (OV1).

In the early stages of the Probes Program two types of vehicles supported the experimenters. The first type, called probes, were such self-propelled vehicles as Aerobees, Spearobees, and Black Brants. The second type was the Scientific Passenger Pod (SPP), which was conceived when a survey of Air Force resources showed that many R&D ICBMs launched were carrying less than their maximum payload. This led to the "piggyback" concept of an auxiliary payload device being flown as a secondary payload. Development of this concept was contracted to the Convair division of General Dynamics (then known as Astronautics) and by late 1960 the Scientific Passenger Pod was a reality.

Twenty-nine of these pods, representing 85 experiments have been flown without degradation of the primary mission of the launch vehicle. Agencies supported by these flights included Air Force Cambridge Research Laboratories, Air Force Special Weapons Center, Naval Research Laboratories, Aero Medical Laboratories, Aeronautical Systems Division, and National Aeronautics and Space Administration. The Scientific Passenger Pod program proved to be successful, but its capability was limited to ballistic trajectories which precluded support of prolonged weightless (in orbit) flights.

The original concept of a vehicle to support the new requirement was an orbital pod. The SPP configuration was elongated to accommodate a solid propellant motor and an attitude control system. The Atlas interface was again limited to mechanical attachment and the SPP 30-inch diameter was retained to avoid additional wind tunnel testing of the missile. Having established the feasibility and cost effectiveness of the concept, OAR contracted with Convair for the development of the orbital vehicle, or as it became known, the OV1. The vehicle, shown in Figure 1, was capable of placing a 300-pound satellite into a 500-nautical mile orbit. The Ballistic Systems Division's Advanced Ballistic Re-entry Systems (ABRES) Office, which had so ably supported the SPP program, agreed to support at least five OV1 launches as secondary payloads. Operationally the OV1 was

designed to ride in an enclosure, called the Atlas Retained Structure (ARS), until after Atlas Sustainer Engine Cut Off (SECO) at which time the ARS door opened and the OV1 vehicle was separated from Atlas. The OV1 attitude control system positioned the OV1 and the programmer fired the motor, placing the satellite into orbit. This is basically the same design and procedure that is followed in the present day vehicles. Except for the autopilot, only previously-developed components and subsystems were used in the design. This reduced development risk and total cost, and also allowed earlier support of orbital requirements. In fact, the first OV1 was flown with a full payload of experiments.

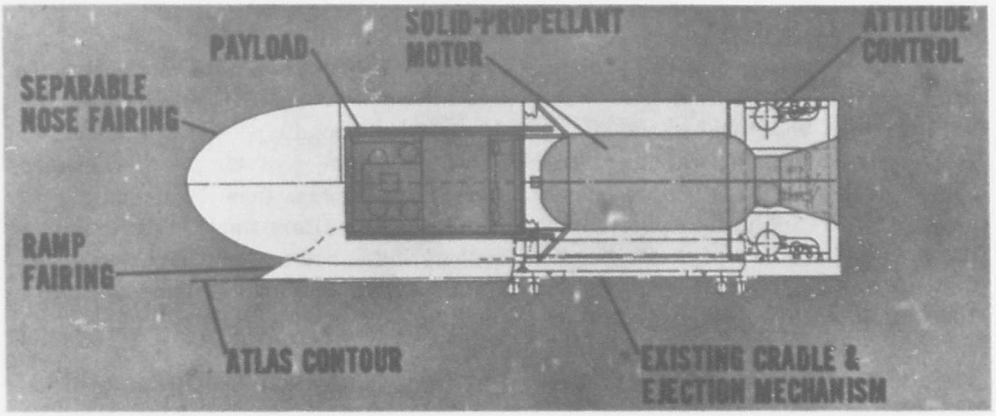

Figure 1. Orbital Pod Concept

In 1964 a series of planning changes by the ABRES program impacted the OV1 program. First, transferring launch location from the East coast to the West coast lowered OV1's orbital capability because of the earth's rotational effect. Second, ABRES requirements for higher lofted launches had additional degrading effects. These circumstances prompted a review of the total OV1 program and resulted in a one year slip in the program.

Fortunately, at this time, the Atlas D missiles were being phased out of the operational inventory. Analyses indicated that it was economically feasible to refurbish them for use as the first propulsive stage for two OV1 vehicles installed on the nose. This configuration uses the existing OV1 assemblies by attaching two ARS's back-to-back as shown in Figure 2, with essentially no change to the flight vehicle. A proven adapter was combined with fairings to mount this dual assembly on the nose of the Atlas. Staging of the two vehicles occurred in the same manner as the original side installation. These old missiles have proven to be very reliable, with 20 successes out of 21 launches. The next launch in May 1967 will be the last with a Series D.

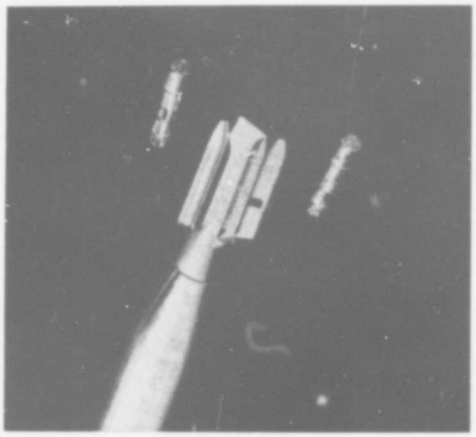

Figure 2. OV1 Staging

The original design imposed contraints on experiment integration because of the minimum cross section of the ARS. This size limitation required costly deployment devices and fairing modification to support peculiar experiment requirements. Modifications such as these required extensive engineering analysis and design time with added risk of degrading basic system reliability.

With the depletion of the Series D, support for the OV1 program will come from Series E and F Atlas missiles as they are released from inventory. Assessment of all factors associated with this change indicated a conventional nose fairing offered the most flexible configuration. This change as shown in Figure 3 has been made and will be flown on the first E/F launch in September 1967. The fairing, sized to match an existing missile adapter will use a previously developed separation system. The 84-inch diameter provides ample clearance around the flight vehicle and satellite and eliminates this as a significant constraint. Provision was made for longitudinal growth of the satellite without changing the rest of the system.

The orbital requirements of the scientists are about equally divided between circular and elliptical with an increasing demand for higher and higher apogees. The OV1 capability has been regularly improved in support of these requirements.

The growth in OV1 orbit performance is shown in Figure 4. A significant improvement is realized between secondary and primary OV1 status since in the latter, the booster trajectory is optimized for the space mission. Primary status

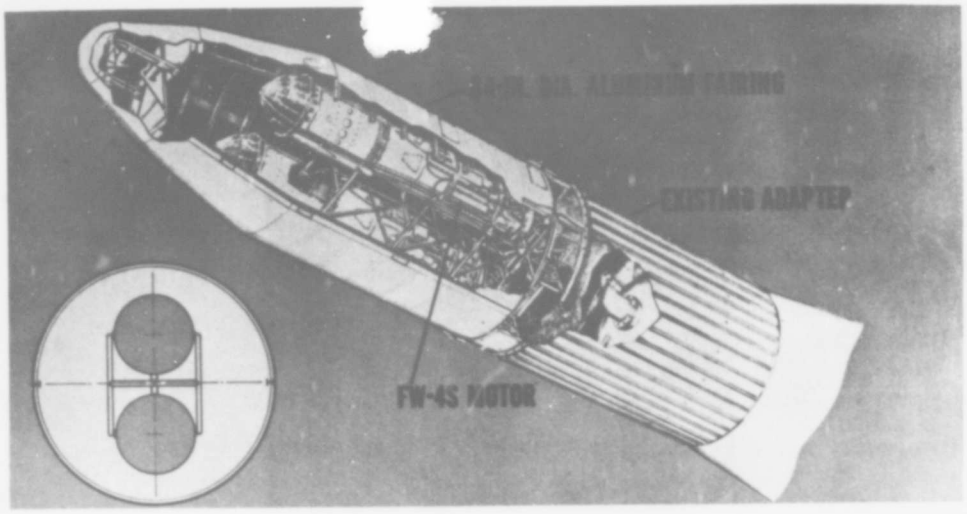

Figure 3. 84-inch Fairing Configuration

also enabled the program to support experiments requiring a polar orbit. By replacing the ABL-258 motor with the FW-4S further performance improvement was realized. OV1-2 weighed 190 pounds and, using the full capability of Atlas on a westerly trajectory, was only able to achieve 1,860 nautical miles of apogee, while OV1-9, weighing 230 pounds, achieved 2,600 nautical miles on a near polar trajectory. It is important to note that OV1-10 was launched into a circular 375-mile orbit and OV1-9 into the elliptical orbit from the same Atlas booster. This flexibility of the system is a significant advantage in supporting scientific payloads. Although the 2,600 nautical mile apogee is a substantial improvement, it is not the maximum capability of the system. For example, OV1-13 and -14 will be launched into orbit having 5,000 and 6,000-nautical mile apogee.

While extended performance is very important, orbit accuracy is a must. Accumulative tolerances in launch vehicle guidance and propulsion systems produce variations in final orbital parameters. Perigee of a highly elliptical orbit must be chosen as low as practical to get maximum apogee altitude. Dispersions can lead to satellite re-entry at perigee which, of course, would be catastrophic and requires careful analysis to preclude its happening. The high degree of accuracy demonstrated by the Atlas/OV1 system to date increases the probability that the OV1 will provide the necessary injection accuracy for the future highly elliptical orbits.

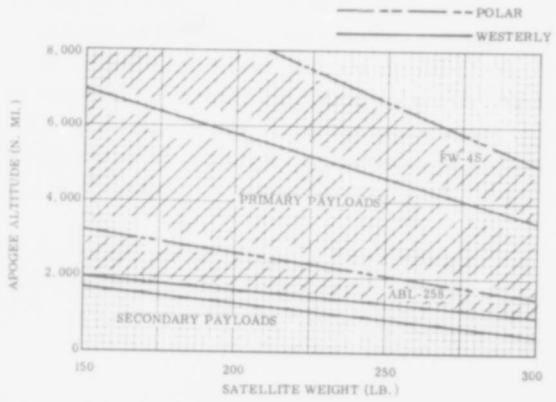

Figure 4. Elliptical Orbit Capability - WTR Atlas Launch

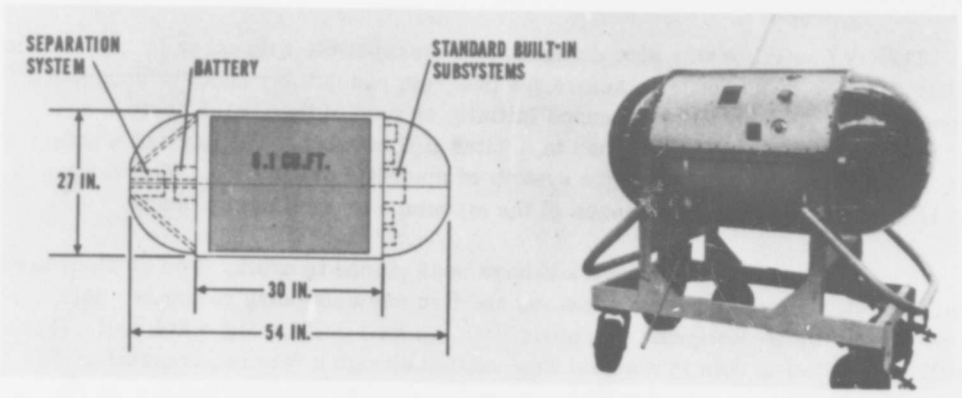

Figure 5. OV1 Satellite Components

The OV1 satellite was conceived as a general purpose vehicle to support the requirements of the space scientists. The mechanical and electrical interfaces are so configured that the application of widely diversified payloads can be accomplished with minimum change. The concept has proven successful in minimizing the lead time requirements which are imposed on the user. Basically, the satellite is designed with three sections as shown in Figure 5. The two areas covered by the domes house all of the support subsystems, which are the power subsystem, command, data storage, and telemetry. The center area is reserved for the experiments and is the only non-standard part of the satellite.

Figure 6 shows the wide spectrum of exploratory endeavor that is being supported by the OV1. The OV1-9/-10 payload, placed into orbit in December, is an example of the typical dual payload, each satellite being integrated with a mixed group of experiments submitted by five different organizations.

The OV1 propulsion module is a self-contained booster stage easily adapted to other payloads. For example, OV1-8 was launched with a special ASD payload (Figure 7). A simple interface adapter was provided to mount a package containing a 30-ft balloon that was placed in orbit for passive radar studies. The balloon was constructed of wire mesh covered by a material that ablated away in sunlight after inflation. The big advantage to this design is low drag for increased orbital life at low orbits and no change in rigidity if the sphere is penetrated since it is not pressure stabilized.

The OV1 satellite was also designed to be compatible with other launch vehicles without major redesign. Therefore the program can quickly react to launches of opportunity. The satellite procured initially as part of the OV1-8 system was launched with a classified payload in a Titan IIIC booster. The payload weighed 450 pounds and required a unique system of magnetic orientation. The increased weight caused only minor changes in the structure to meet design loads.

Seven OV1 satellites or payloads have been placed in orbit. Two of these have successfully completed their missions and five are continuing to acquire data. The first of these launched in October 1965, is still performing quite well. It is still accumulating data in the real time mode although a failure occurred in the data storage system. Having this pre-positioned data source available during periods of high solar activity has been very advantageous.

One of the greatest advantages of the OV1 program is the timeliness of the support accorded the experimenter. All aspects of flight preparation, launch support, and orbital support are accomplished with a minimum of inconvenience to him. Necessary interface meetings are held to acquire experiment details and

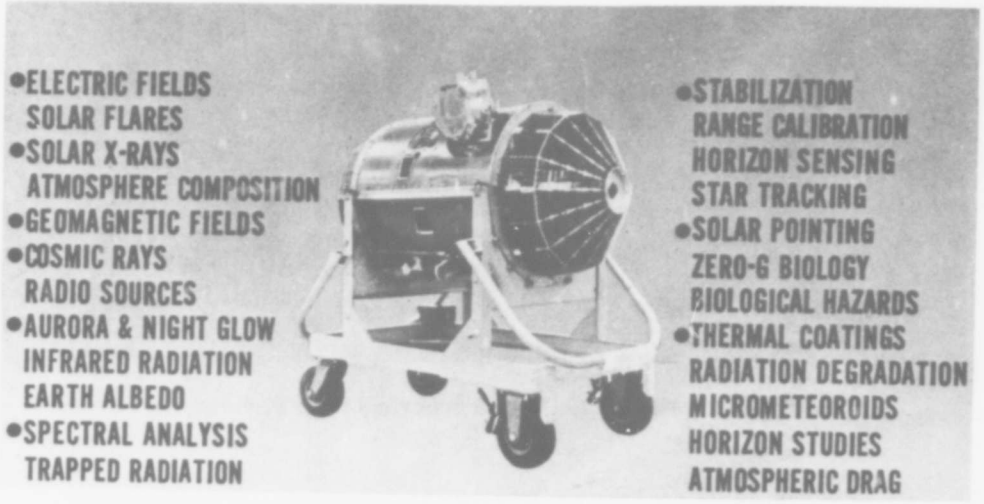

• Indicates Experiments Integrated on OV1-9 and -10

Figure 6. Experiment Integration

to familiarize the scientist with the OV1 capabilities and the existing range facilities. His experiments are prepared for space flight and installed in the satellite. Range documentation is prepared specifying both launch and orbital support details. Necessary testing is accomplished and, finally, the integrated OV1 vehicle is shipped to the launch site for thirty days of launch preparation. Lapsed time from support approval, through integration, to launch is approximately fifteen months, with orbital support and data services provided for the useful life of the satellite.

The 15-month schedule has proven realistic. Delays have occurred in only two instances. The only significant delay was on OV1-4/5 and this was to accommodate the experiment on OV1-4. The payload consisted of a Zero G experiment on algae and Duck Weed. The experimenter experienced some difficulty in sustaining growth in the space laboratory. However, with the delay he worked out his difficulties and acquired his data. Adherence to schedule is not to imply that the experimenters' requirements are in any way subordinated. Schedules are established initially based on experimenters' commitments. When unforeseen problems develop they are resolved on an individual basis.

The OV1 vehicle configuration permits a logical extension of existing capabilities as the needs of the scientist expand and the state of the art permits. One example is the current development of a nose fairing which will accommodate

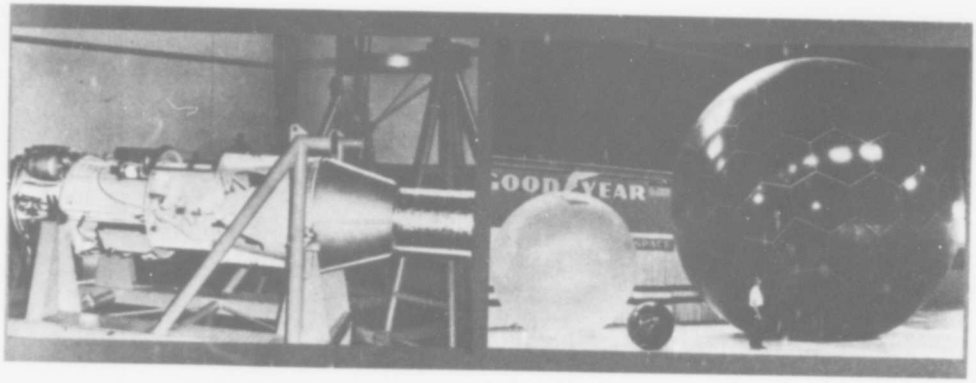

Figure 7. OV1-8 Spherical Grid Payload

various flight vehicle configurations without change to the envelope. Further, the program is sensitive to the needs of the researcher in orbital performance flexibility and adequacy of the spacecraft supporting systems. Studies indicate a potential performance gain can be achieved by spinning the entire vehicle prior to motor ignition and separating the propulsion module structure and subsystems so that only the motor and payload are accelerated to orbital velocity. This will permit the satellite weight to be increased to 500 pounds for currently achievable orbits or injecting the existing 300-pound satellite into elliptical orbits with an apogee of 8,000 nautical miles. Another growth potential of the design is the incorporation of a developed higher thrust motor. For example the Alcor 1B could achieve an apogee altitude of 10,000 nautical miles with the 300-pound satellite, or 5,000 nautical miles with a 450-pound satellite. In conjunction with this study we are investigating the addition of a kick-stage motor. This would give us the added flexibility of placing payloads in a higher circular orbit or achieving escape velocity.

In summary, a total of 7 OV1 satellites supporting 43 different experiments for 7 different organizations have been orbited to date. This amounts to 1,690 pounds of payload weight. In May we will accomplish another first by putting three satellites into three different orbits from the same Atlas booster. In September we will launch OV1-13/14 and this will complete the support of the 50 experiments submitted for Fiscal Year 1967.

The OV1 is OAR's answer to the Air Force Researcher's request for timely space support.

BLANK PAGE

Dr. Donald A. Calahan is Professor of Electrical Engineering at the University of Michigan, and has been a grantee with the Applied Mathematics Division, AFOSR, for 4 years. He was graduated from the University of Notre Dame in 1957, and received his doctorate from the University of Illinois in 1960. Dr. Calahan has made significant contributions to mathematical circuit theory through his extensive research with the Air Force, and as a consultant to industry on computerized design and optimization of electronic circuits. He has taught at the University of Kentucky, the University of Illinois, the University of California at Berkeley, and the Ballistic Research Laboratories, Aberdeen Proving Ground.

COMPUTER-AIDED CIRCUIT DESIGN

D. A. CALAHAN
Electrical Engineering Department
University of Michigan

The complexity of micro-electronic circuits and the attendant requirement for maximum reliability has forced the circuit designer to turn to computer-aided approaches to design. As an elementary example, consider the problem of designing a computer logic circuit with prescribed worst-case limits on the operating point, assuming all circuit components may depart some known per cent from their nominal values. With ten elements, a designer would have to construct $2^{10} = 1034$ such circuits to determine the extreme element variations which most severely effect operation. At worst, a computer could perform the same 1034 analyses; more realistically, a highly reliable guess of the worst case could be made with only a single computer analysis.

Over the past four years, this investigator has been concerned with the development of computational algorithms for the analysis and design of electrical networks. The research has been concentrated particularly on methods of computer synthesis of rather arbitrary forms of linear networks. Before discussing synthesis, however, it is well to review the principal methods of network analysis.

Matrix Methods

By writing the Kirchoff voltage law equations around independent meshes or the Kirchoff current law equations at every node in matrix form and then using standard matrix inversion techniques, a frequency response for the network can be calculated. There is a considerable accuracy problem here because of subtraction in the matrix inversion; also, a matrix inversion is required for each frequency.

Topological Methods

If the elements in a network are regarded as branches in a graph, then a network function (i.e., a rational function of s, the Laplace Transform variable) may be calculated from linear graph theory. From this, either the network frequency or transient response follows directly. An advantage over the matrix is that the effect of each network element on the response may be trivially calculated. Such derivative information is fundamental to any formal computer synthesis procedure. However, the original evaluation of the network function is time-consuming, which in turn places restrictions on the size network which can be analyzed in reasonable computing times.

State Variable Methods

A hybrid form of mesh and node analysis, this procedure yields first order differential equations describing network response. Derivative information concerning the effect of elements on response is available indirectly. The method is efficient in computing time compared with the previous.

The programming of any of the above methods is a straightforward and laborious task. By coupling such a program to a circuit designer via a means of optical computer output (such as CRT display), the designer can apply his natural talent for cut-and-try design. Thus, he presents the computer with an initial design; the corresponding network response is then optically displayed; he makes an adjustment in the circuit and the latter is analyzed again. Such man-machine iterations are continued until some design criterion is optimized.

From a formal viewpoint, it is obvious that the above design cycle is most efficient. In fact, for most modern design criteria (especially in filter applications) the procedure is totally inadequate. The manner in which the network elements must be adjusted to optimize a design is typically far too complicated to be directed by intuition. What is required is a completely automatic method of iteration which will accept common network design criteria. This was recognized in the early stages of our research and a search was made for a method of iteration compatible with one of the general methods of analysis discussed above. The topological method was chosen because it yields derivative information directly. (It should be emphasized that the procedures to be proposed are successful because the networks considered are linear. The synthesis of non-linear systems of any type is obviously a much harder problem.)

Among the design criteria encountered in linear network design, frequency response and the sensitivity of that response to element variation are the most common specifications. Our research has shown it has been possible to incorporate both of these criteria in a general circuit optimization program. The remaining discussion is a summary of this investigation, principally in the form of examples which point out its utility.

If a frequency response is specified, this may be converted to a corresponding network function in terms of $\underline{s}$. The coefficients of this rational function, together with an initial design, form the input data to the program. The designer's initial guess is then analyzed, yielding an initial transfer function. These rational functions (the prescribed and the calculated) are then matched, coefficient by coefficient, using a modified form of Newton-Raphson iteration. At this point, derivative information is required from the topological analysis program to establish the effect of every adjustable element

on every coefficient. Iteration continues until the coefficients are matched to a prescribed accuracy. This algorithm may be readily extended to the case when only a subset of the coefficients are specified - the so-called dominant frequency case-as happens frequently in active network design.

The power of the above procedure lies in its range and speed of convergence. Although it was originally developed to allow relatively small changes in element values, it became obvious in testing it convergence that the initial network supplied by the designer did little more than establish the form or topology, and that the same final design resulted from a wide range of "poor" initial guesses. In particular, large classes of active networks, previously immune to any precise design because of the constraints imposed by parasitic, could now be accurately synthesized.

Two examples showing the rather unusual application of this program to circuit design problems are now given. The generality of the program will be noted by observing the different classes of networks considered.

The low-pass (Butterworth) filter of Figure 1 is to be designed for various source resistances (R_s). A classical network synthesis procedure[1] exists for such networks, derived from reasonably involved and elegant theory. However, if the element values for a single value of source resistance are known, then these constitute an initial guess for iteration with any source resistance. Thus, Table 1 can be obtained from the known design with $R_s = 1$ without any recourse to formal network theory.

As a graphic demonstration of the range of convergence, the active network of Figure 2 (which was "academically" chosen to have unit element values initially) is required to behave as an oscillator with a specified frequency of oscillation. In contrast, the initial network design is quite stable. After iteration the element values of the oscillator are given in parentheses in Figure 2, showing a range of convergence of 100:1.[2]

Particularly in the design of active networks, the problem of sensitivity of the network response to component variation is most acute. At the same time, most active networks have sufficient redundancy that specifying the frequency response alone as above leaves degrees of freedom in the network design. Hence, we considered introducing some measure of sensitivity for minimization while maintaining the desired response. Among the common network sensitivity criteria, the change in network natural frequencies per fractional change in element is directly related to frequency and Q stability of tuned amplifiers and oscillators. In addition, this sensitivity and its gradient as a function of the network elements are readily obtained from a general topologically-based analysis program. Therefore, it was felt a computer program would be developed for the minimization of sensitivity in quite arbitrary forms of linear, frequency-selective

networks.[3]

The effect of minimizing sensitivity in a typical active filter (Figure 3) is shown in Figure 4. From Figure 4, it is clear that a large change in the active element results in catstrophic change in the original filter response but affects the desensitized filter very slightly. The element values are given in Table 2.

The above definition of sensitivity was then generalized to correspond to the observed fact that like elements tend to change the same per cent as a function of environment.[+] The important criterion is now the algebraic sum of the element sensitivities, and is therefore linearly related to individual element sensitivities. This fact makes multiparameter sensitivity quite amenable to minimization using the same general approach as for single element sensitivity.

As a final example,[4] a state-of-the-art problem in the area of active filter synthesis is considered.[5] The filter of Figure 5 is first designed by iteration from an initial guess to have a prescribed bandpass response. All resistances increase with temperature by 10000 ppm/°C and all transistor betas increase by 30000 ppm/°C; it is required to redesign the filter so that the network response is independent of temperature while maintaining the prescribed frequency response. Such a problem is routinely solved by the computer program developed, resulting in the values shown in parentheses in Figure 5. Figure 6 shows the effect of actual simultaneous variation of parameters on the response,[++] demonstrating a significant desensitization in the final design.

In conclusion, by insisting on a formal and general approach to the design of linear electrical networks in place of cut and try procedures, we have developed a powerful iterative computer technique. Both classical problems in passive network synthesis and modern problems in active networks and micro-electronics may be readily solved. One indication of the utility of the programs is that over 120 program decks have been requested by industries and institutions, including most of the major electronics and aerospace companies. These programs have been in the hands of their designers for over three years, and have been used in the design of circuits ranging from video amplifiers for T.V. receivers to amplifiers for space missions. As previously mentioned, for many circuits which are operating near the frequency limit of the device characteristics, this unique combination of a

---

[+] This is especially true in micro-electronic circuits.

[++] Due to the differential definition of sensitivity, complete cancellation will in fact not occur.

general network analysis program and a rapidly-convergent iteration algorithm offers the only method of design which includes the parasitics of the device. Some users have coupled the program into a time-shared system which provides t..eir engineers with a desk-top capability of computerized circuit design.

REFERENCES

1. M. E. Van Valkenburg, Introduction to Modern Network Synthesis, John Wiley and Sons; 1960.

2. D. A. Calahan, "Computer Design of Linear Frequency Selective Networks," Proceedings of the IEEE, vol. 53, pp 1701-6; November, 1965.

3. D. A. Calahan, "A Numerical Algorithm for the Minimization of Sensitivity, "Proceedings of the Third Allerton Conference (University of Illinois), pp 394-406; October, 1965

4. D. A. Calahan, "Linear Network Sensitivity Minimization Procedure," AFOSR Report AFOSR 65-1931; February, 1966.

5. A. A. Gaash, and R. S. Pepper, "Design of Integrable Desensitized Frequency Selective Amplifier", Digest of the ISSCC; February, 1966.

R_s	L_1	C_1	L_2	C_2
1.	.7654	1.848	1.848	.7654
.75	.3552	1.771	1.400	1.986
.5	.2688	2.103	1.083	2.613
.25	.1017	4.603	.4181	6.384
.1	.0392	11.09	.1616	15.64

Table 1

	C_1	R_1	R_2	C_2
Original Design	.3	297.	.33	.0643
After Sen. Min.	.692	61.7	.775	.0462

Table 2

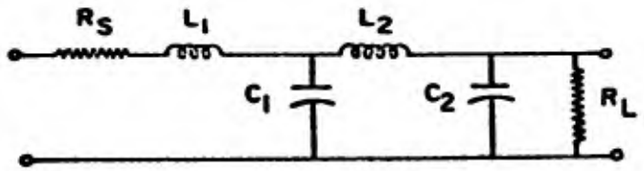

Figure 1.

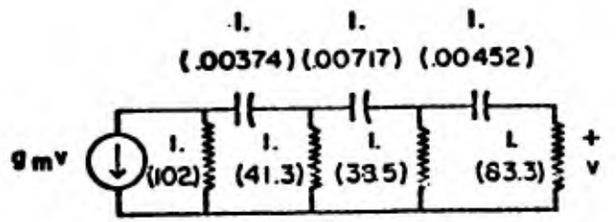

Figure 2.

g_m = 1 mho
other values in
ohms, farads

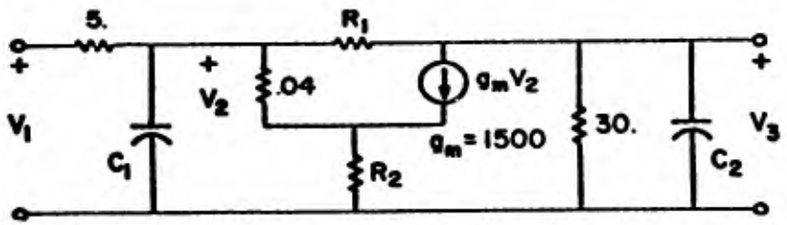

Figure 3.

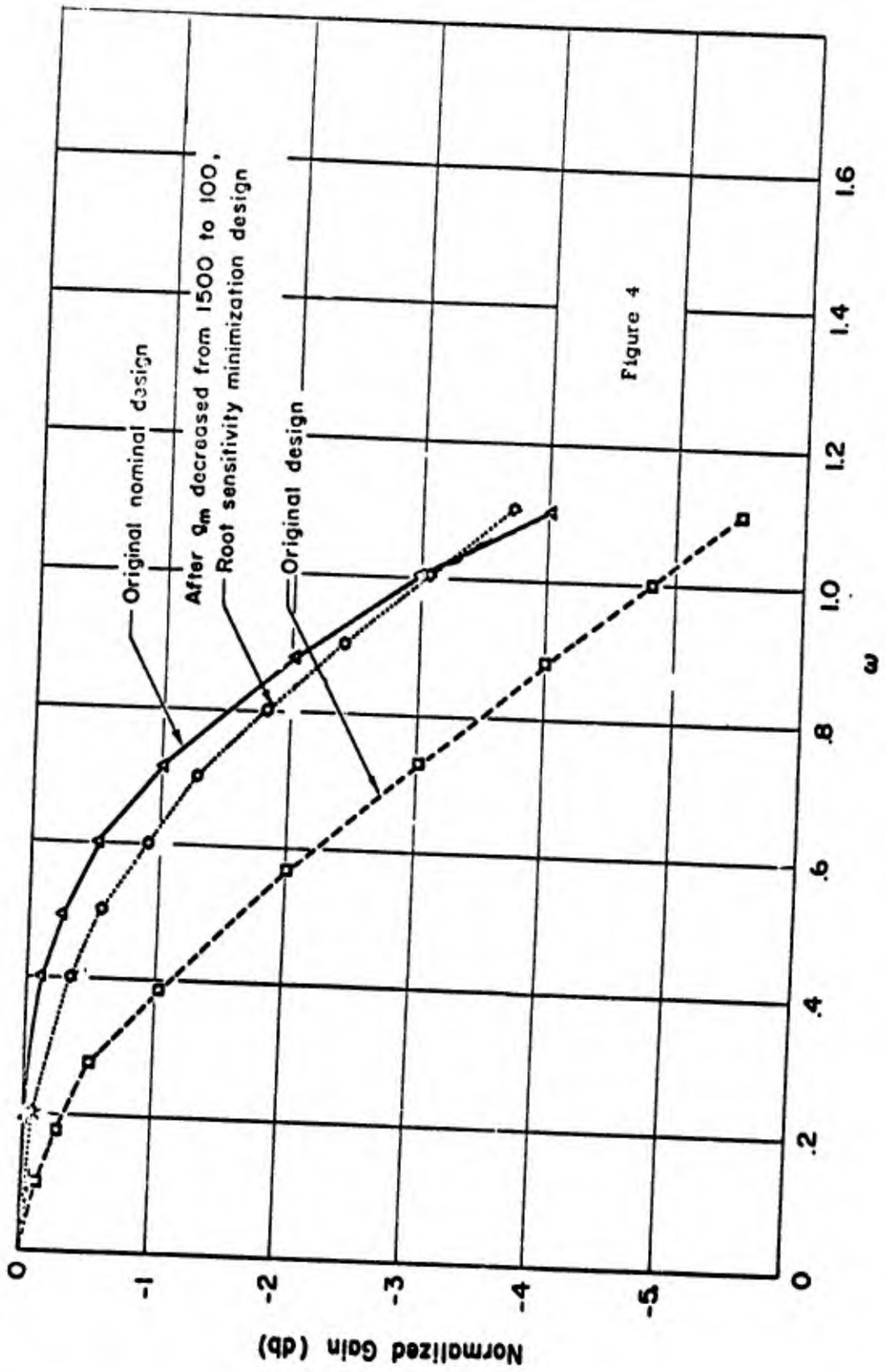
Original nominal design
After g_m decreased from 1500 to 100,
Root sensitivity minimization design
Original design
Figure 4
Normalized Gain (db)
0
-1
-2
-3
-4
-5
0
.2
.4
.6
.8
1.0
1.2
1.4
1.6
ω

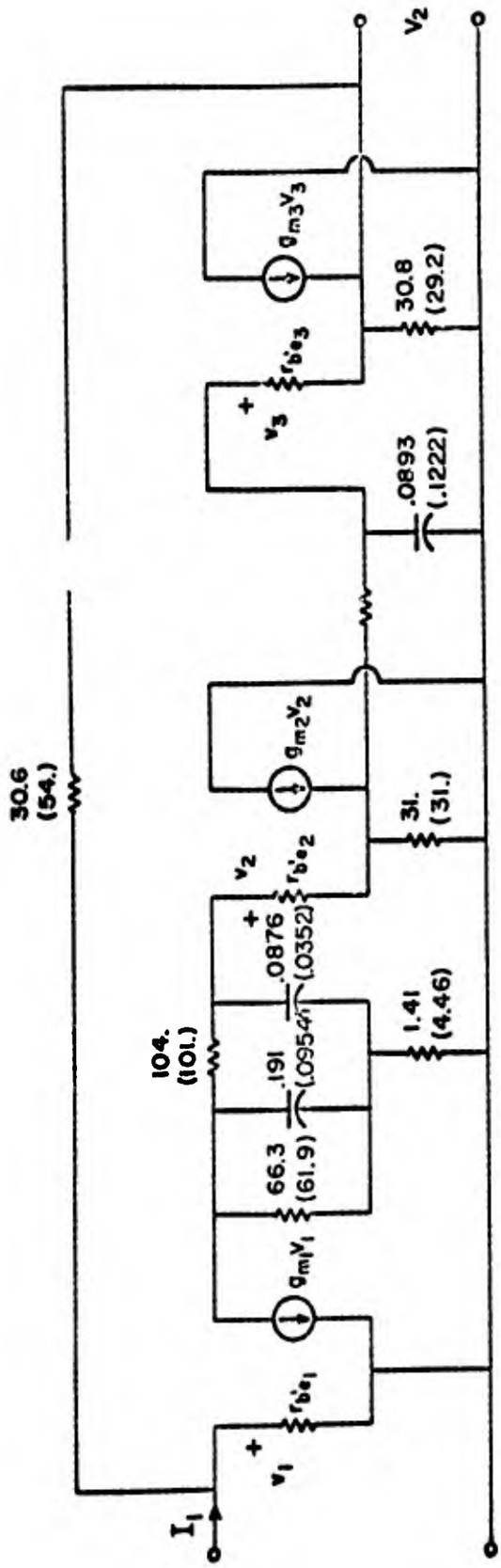
I_1
V_1
$r_{b'e_1}$
$g_{m_1}V_1$
66.3
(61.9)
.191
(.0954)
104.
(101.)
V_2
.0876
(.0352)
$r_{b'e_2}$
$g_{m_2}V_2$
30.6
(54.)
31.
(31.)
1.41
(4.46)
V_3
$r_{b'e_3}$
$g_{m_3}V_3$
30.8
(29.2)
.0893
(.1222)
V_2

Figure 5.

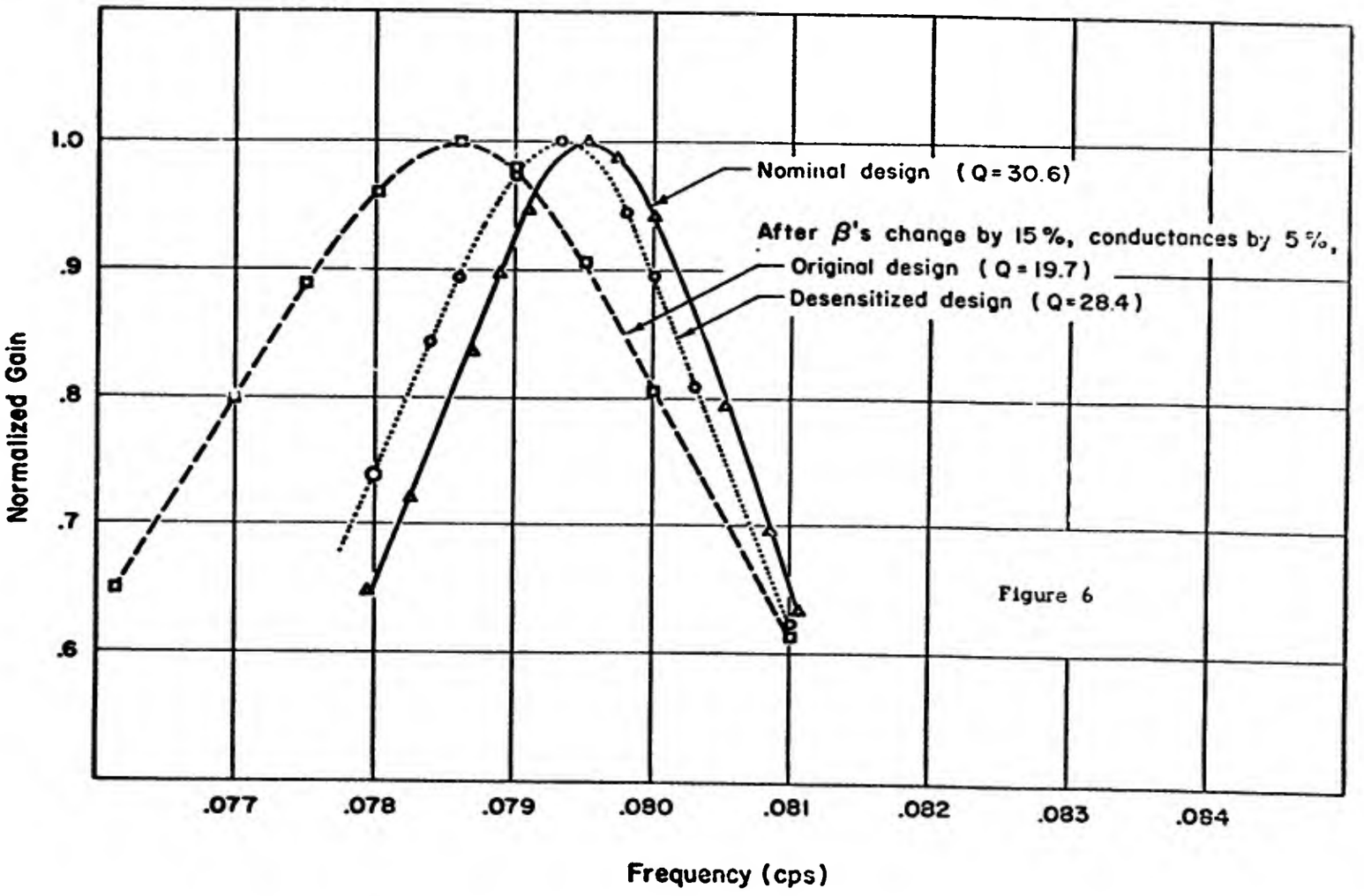
Normalized Gain
1.0
.9
.8
.7
.6
.077
.078
.079
.080
.081
.082
.083
.084
Frequency (cps)
Nominal design (Q = 30.6)
After β's change by 15%, conductances by 5%,
Original design (Q = 19.7)
Desensitized design (Q = 28.4)

Figure 6

Dr. Hermann W. Ehrenspeck is a research physicist in the Microwave Physics Laboratory, Air Force Cambridge Research Laboratories. He is presently engaged primarily in work on surface-wave antennas and related problems. Dr. Ehrenspeck received his B.S. and M.S. degrees in Physics and Engineering from the Institute of Technology, Munich, Germany, in 1935 and 1937, respectively, and his Ph. D. degree from the same institute in 1947. From 1937 to 1945, he worked on directional antennas, on the propagation of electromagnetic waves, and on antennas for direction-finding for the Airborne Research Institute in Germany. From 1946 until 1953, when he joined AFCRL, he was in charge of the research laboratory of an electrical component company. Dr. Ehrenspeck is the author of a number of professional papers and holder of several patents.

A FAMILY OF NOVEL ANTENNAS: THE "BACKFIRE" ANTENNA

by

H.W. Ehrenspeck
Microwave Physics Laboratory
Air Force Cambridge Research Laboratories (OAR)
L.G. Hanscom Field, Bedford, Massachusetts

ABSTRACT

The "backfire" antenna, a new antenna element that produces gains ranging from 15 to 30 dB, operates on a combination of surface-wave and open-cavity principles. Its side- and backlobes in both planes are much lower than those of conventional antennas in that gain range, and its construction is far more compact. It can be arrayed for pencil or fan beam as well as monopulse applications. Models have been tested inhouse and by NASA in the frequency range from 100 MHz to 10 GHz, with good results. The antenna is ideal for ground-to-ground and ground-to-air communications, telemetry and satellite-tracking, and lends itself to flush installation in aircraft, missiles, and space vehicles.

1. INTRODUCTION

The invention of the backfire antenna is a direct outgrowth of AFCRL inhouse research on slow-wave antennas.[1,2] During the course of this work it was discovered that the gain of an endfire antenna like a Yagi can be markedly increased by using a large plane reflector at the end of the antenna opposite the feed to reflect the incoming energy back toward the feed and the aperture from which it is finally radiated into space. The resulting antenna, called the "backfire" obviously because the main beam fires backwards, has since become the progenitor of a large family of new antennas[3-9] with principal applications in the gain range between 15 and 30 dB.

Ordinary endfire antenna structures for this gain range become impractically long; paraboloids of the size required are too costly to construct and not usually attempted since geometric optics is not fully applicable to such cases. To date, most of the antennas used for this gain range have been multielement arrays consisting of a large number of single dipoles, slot radiators, or Yagis. Because they need very complicated feed systems (each element must have its own feed) they are expensive as well as insufficiently reliable in operation.

Backfire antennas offer remarkable advantages over these antennas. They perform optimally in the gain range between 15 and 30 dB. They have extremely low side- and backlobes. Their reflectors are planar rather than paraboloidal. Their feed system is much simpler and their construction costs much lower than those of any other antenna in this gain range. They can be arrayed as pencil- or fan-beam antennas. They can be flush-mounted into the bodies of airplanes or space vehicles. They can be used as efficient feeds for large paraboloidal antennas.

Backfire antennas should therefore be especially suitable as replacements for most of the bulky and costly multielement arrays for telemetry and satellite-tracking; they should be useful for air-to-ground and ground-to-ground applications, for plane-to-satellite communications, for microwave relay links, and for mobile satellite relay stations.

2. GAIN OF BACKFIRE ANTENNAS

A typical example of the backfire antenna, developed by converting a Yagi type of endfire antenna, [3] is shown in Figure 1, where R, F, and D mark the reflector, feed, and directors of the basic Yagi, M is the plane reflector necessary to convert the Yagi into a backfire, and B is a rim about $\lambda/4$ wide, which improves the overall performance. Whereas an ordinary Yagi would radiate the energy only to the right, the backfire radiates it to the left, as from an aperture formed in the plane of R. The spacing L between M and R is the total axial length of the backfire. It should be mentioned that the slow-wave structure of the Yagi need not be a row of dipoles but may also be a dielectric rod, a helix, or a disk-on-rod structure; the reflectors M and R may consist of a row of properly spaced metal rods, or they may be formed of metal or wire mesh.

The gain of a Yagi type of endfire antenna is roughly proportional to its axial length, provided that the height and spacing of the directors are adjusted to their optimal values for the specific length chosen. The gain increase of a backfire antenna, although obtained without a

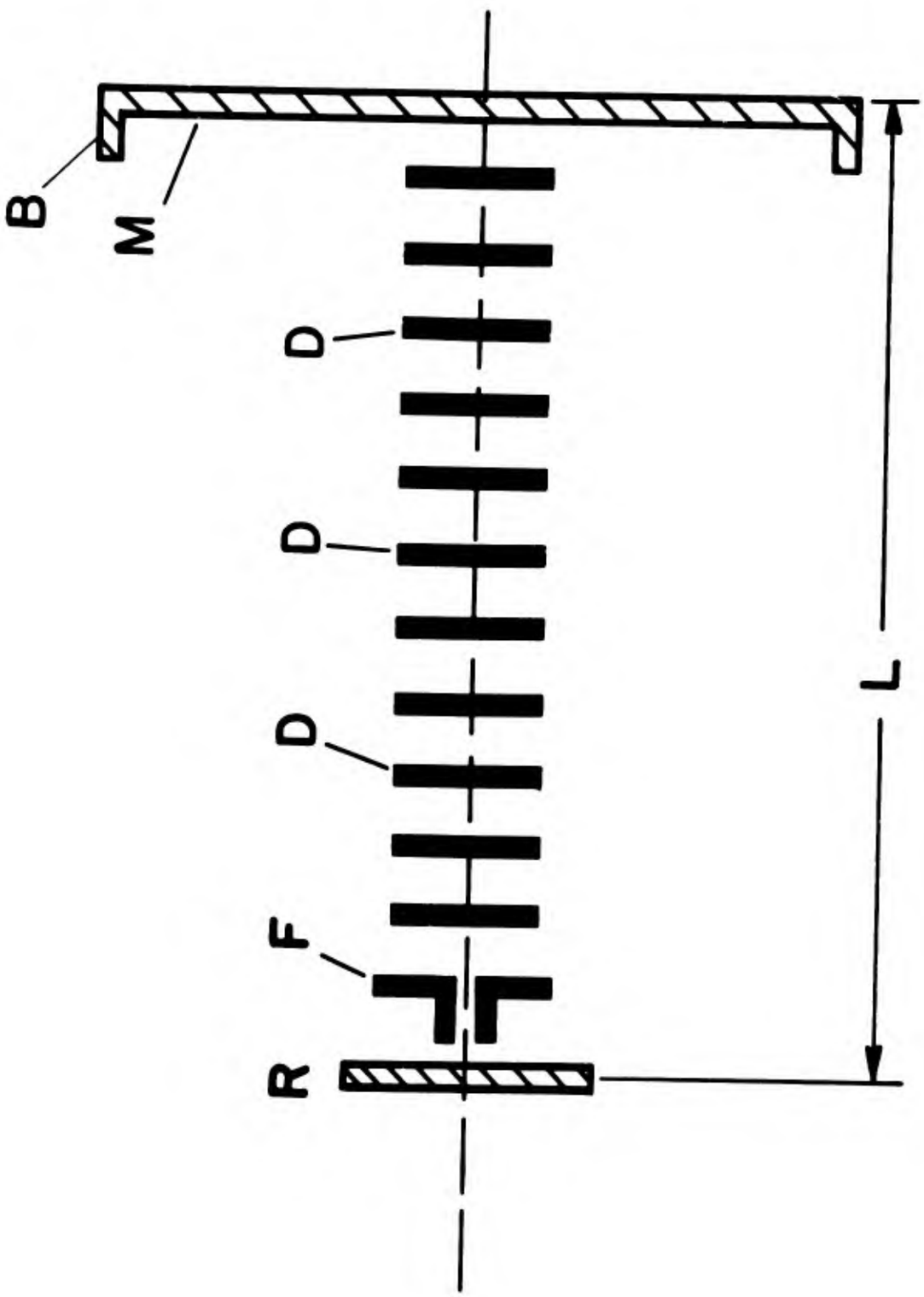

Figure 1. Principle of Backfire Antenna

corresponding physical increase in length was first explained as due to an effective doubling of the length of the endfire since the slow wave travels twice the entire length of the endfire. Gain measurements showed a higher gain increase, however, than could be attributed to any doubling of the length. A much better insight into the radiation mechanism of the backfire has since been obtained by studying the amplitude and phase distribution in the nearfield. It has led to the more appropriate analysis of the backfire as a cavity antenna, the space between M and R having a configuration similar to that of a laser (Fabry-Perot) cavity.

The gain G_B of backfire antennas is approximately:[7]

$$G_B \cong 60 \frac{L}{\lambda},$$

compared with the gain G_E of ordinary endfire antennas, which is

$$G_E \cong 10 \frac{L}{\lambda}.$$

Thus, the backfire has a gain increase of about 8 dB over an endfire antenna of equal length. In addition, its side- and backlobe levels are typically 8 to 12 dB lower than those of the endfire antenna.

The progress achieved with the new antenna structure can best be demonstrated by comparing it with the Yagi, which is the most frequently used endfire antenna. Figure 2 compares the physical structures of the shortest possible backfire antenna (a) and a Yagi antenna (b), both having the same gain and approximately the same patterns in the E and H planes. Both are drawn to the same scale so that they can be directly compared in size and material requirements. Although the backfire has a reflector area larger than that of the Yagi, and in addition, requires a second smaller reflector, its length is less than one-tenth that of the Yagi; and the number of dipole elements is only 1 in contrast to 27 elements for the Yagi (including 5 transverse reflector dipoles not shown).

3. RADIATION MECHANISM OF BACKFIRE ANTENNA

Experimental studies of the nearfield of backfire antennas have disclosed that optimum performance depends on obtaining an extremely high VSWR over the entire antenna length, and that this condition can be fulfilled only when the distance between the plane reflectors M and R is a multiple of $\lambda/2$. These observations suggest that backfire antennas[3-9] are characterized by the multiple reflection of

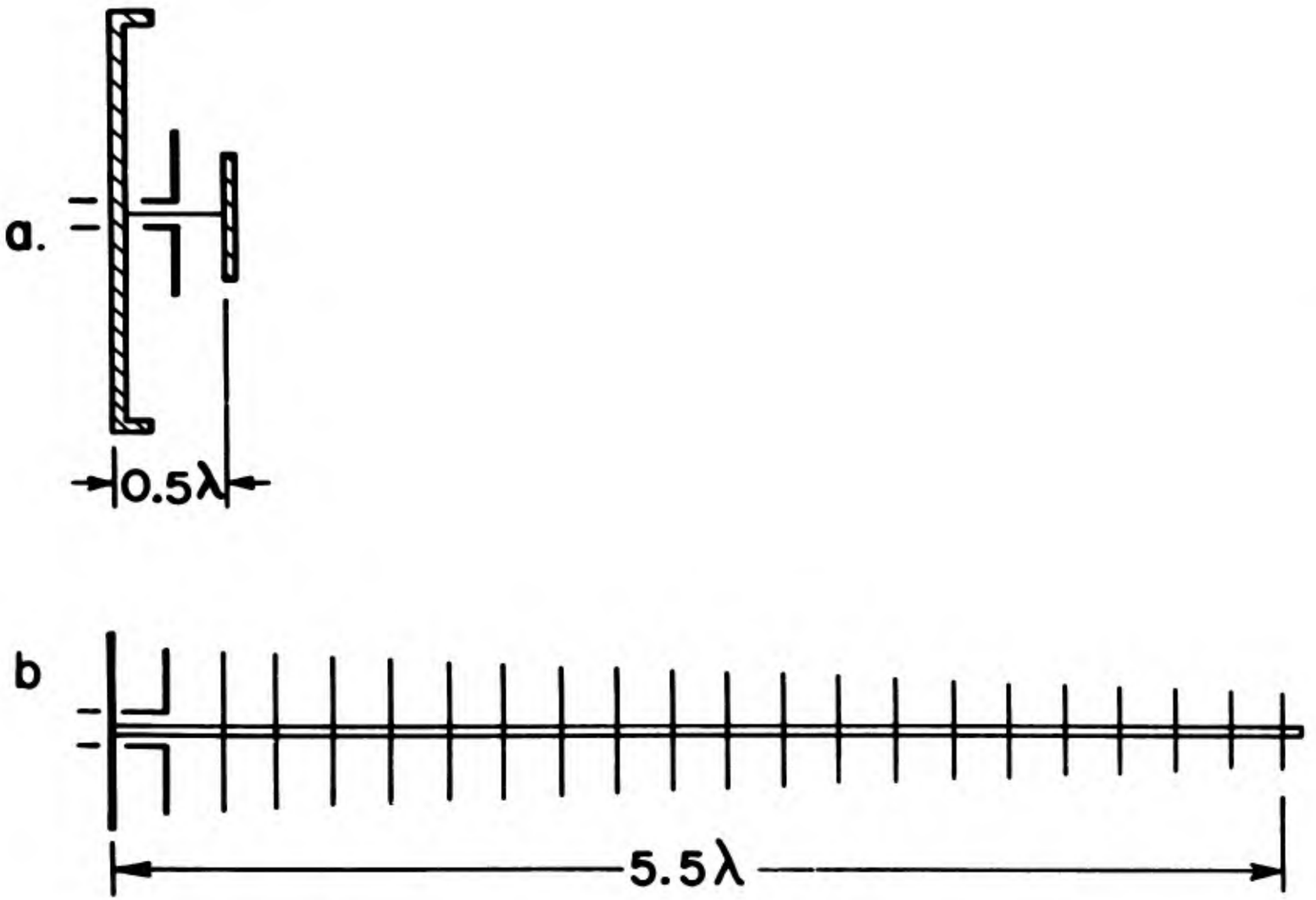

Figure 2. Comparison of Physical Structures of Short-Backfire and Yagi of Same Gain

electromagnetic waves between two plane reflectors of different size (M and R in Figure 1), and that the space between these reflectors acts like an open resonant cavity whose basic configuration resembles a Fabry-Perot laser cavity except that is is filled with air rather than with an active medium. While the larger reflector (M) plays the role of the perfectly reflecting mirror in the conventional laser structure, the smaller reflector (R) plays that of the partially transparent end mirror, its size corresponding to the degree of transparency. A certain percentage of the cavity energy is radiated into space from the virtual aperture, which is located in the open area surrounding the smaller reflector (R). Gain and radiation patterns are functions of the amplitude-phase distribution in this aperture. Cavities that are several wavelengths in axial length require loading by a slow-wave structure (D, D, D... in Figure 1) to concentrate the energy along the backfire axis and thus prevent its radiation before it reaches the aperture. The structure of a shorter backfire antenna, however, is so compact that practically all of the energy contained in the cavity is intercepted by reflector M and R, and therefore no slow-wave structure is needed.

4. BACKFIRE ANTENNAS AND ARRAYS

Two types of backfire antennas will be discussed: (1) the "short-backfire," and (2) the "long-backfire."

(1) A short-backfire antenna — in fact, the shortest one conceivable — approximately $\lambda/2$ long, is shown in Figure 3(a). It consists of only two plane reflectors — the larger one with a rim — and the feed between them. The feed may be a single as well as a crossed dipole. The reflector diameters are 2λ and $\lambda/2$ respectively. This antenna develops a gain of 15 dB above an isotropic source. Its patterns, measured with an S-band model, are shown for the E and H planes in Figures 3(b) and (c). All sidelobes are at least 20 dB, and the backlobe is at least 30 dB, below the maximum. The patterns retain their quality over a bandwidth of about 1.5:1, and the gain is approximately proportional to the area of the larger reflector. Special low-sidelobe adjustment can reduce the side- and backlobe level to 27 dB and far below 30 dB, respectively [as shown later in Figure 9(c)], but at the cost of some gain and bandwidth; special broadband adjustment can increase the bandwidth to over 2:1, but at the cost of some gain. Short backfires can be used to advantage as transmitting and receiving antennas for 2:1 bandwidth, as flush-mounted antennas, as feeds for paraboloids, and as elements for large telemetry and satellite-tracking arrays.

(2) A long-backfire antenna, several wavelengths long, is shown in Figure 4(a). Besides reflectors M and R, it requires a slow-wave

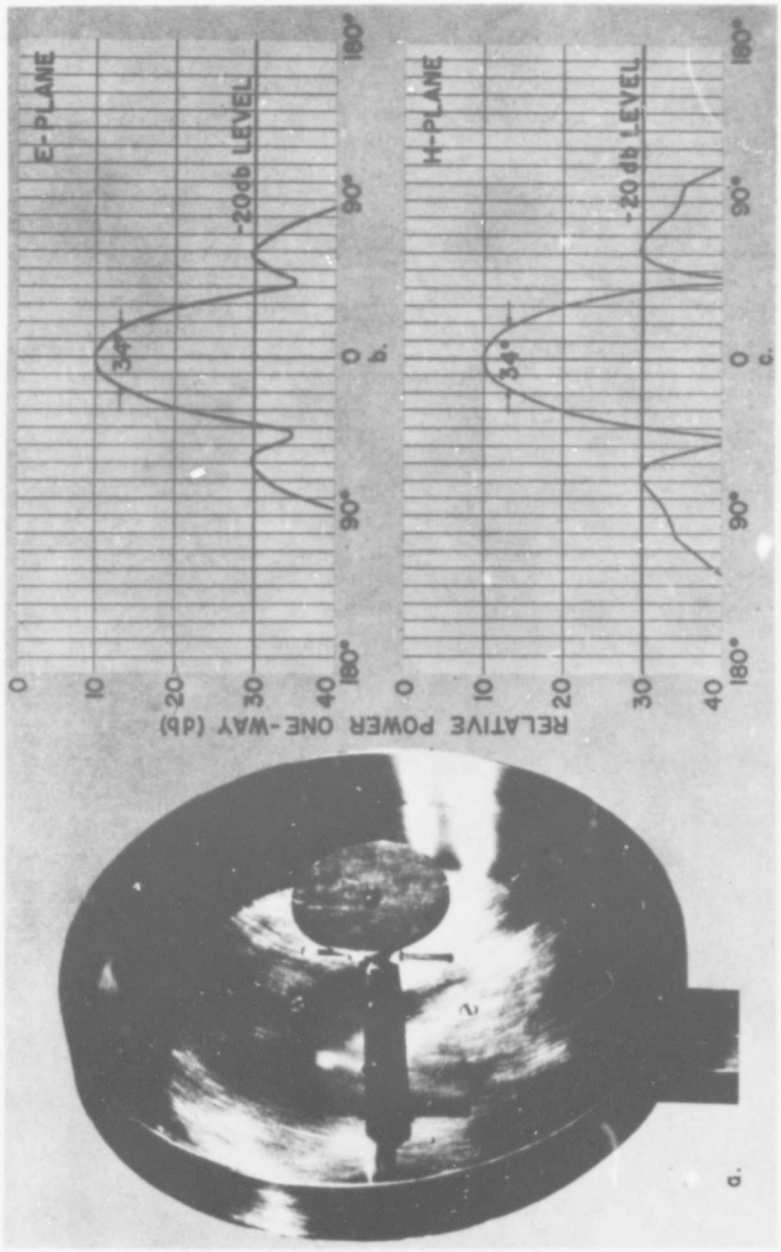

Figure 3. Typical Short-Backfire and Its Radiation Patterns

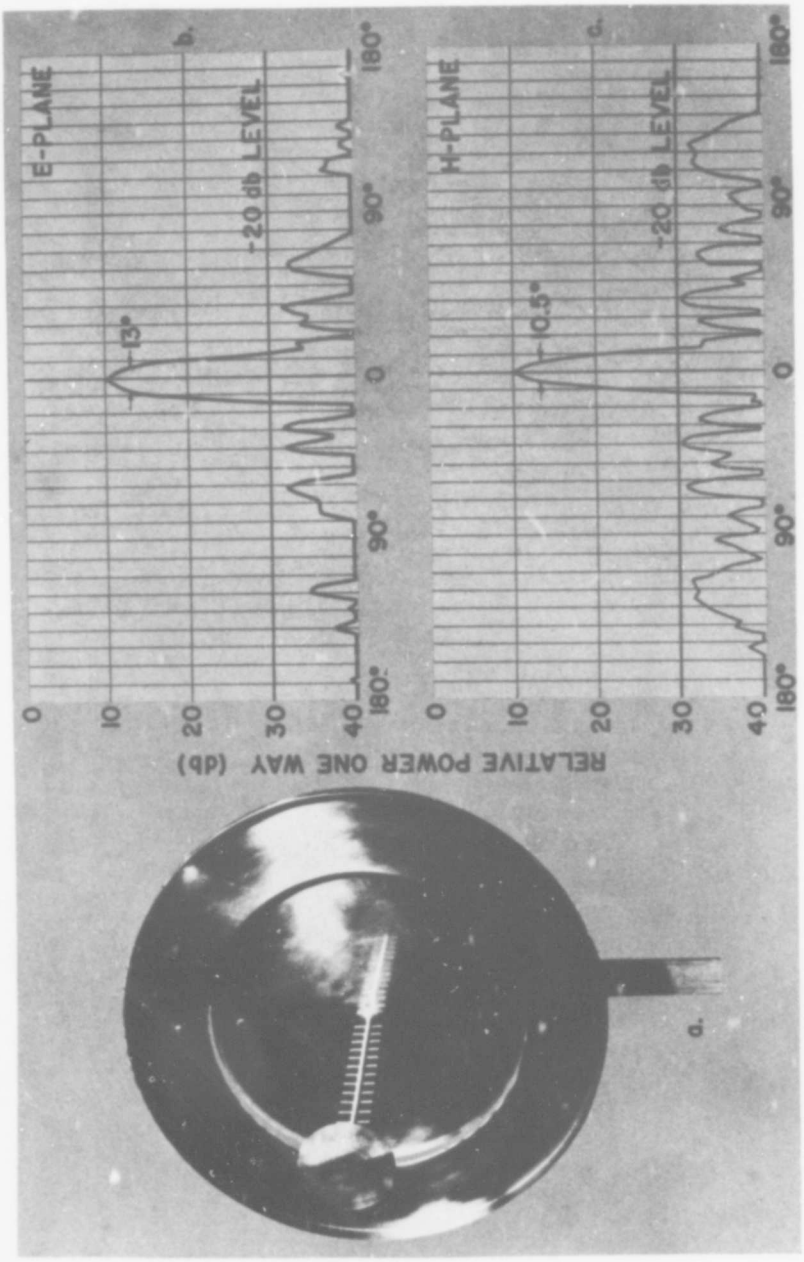

Figure 4. Typical Long-Backfire and Its Patterns

structure, which in Figure 4(a) is a row of dipoles, extending along the antenna axis. Its gain depends mainly on the size of the larger reflector and on the length L of the structure. For an antenna more than 3λ long, a stacked reflector M will give better performance. The S-band antenna in Figure 4(a) is a 4λ long-backfire model; its E- and H-plane patterns are shown in Figures 4(b) and (c). The antenna has a gain of 23.5 dB and a pattern bandwidth of about 1.4:1. All sidelobes are more than 20 dB, and the backlobe is more than 30 dB, below the maximum. Long-backfires can be built for gains of up to 25 dB before their dimensions become impractically large. For higher gains, it is better to array several in front of a large common reflector than to lengthen the single-element long-backfire antenna any further. The difference between an array of short-backfires and one of long-backfires is that the former allows tighter pattern control and is mechanically easier to construct, whereas the latter requires fewer backfire elements and therefore has a simpler feed system.

5. PRACTICAL MODELS OF BACKFIRE ANTENNAS

5.1 Short-Backfire Antenna for 400 to 800 MHz

Figure 5 is a photograph of a short-backfire antenna for the frequency range from 400 to 800 MHz. It has a circular metal disk as its smaller reflector which, like the larger plane reflector, is made of expanded aluminum sheet material. The feed is a bow-tie, used for its well-known broadband characteristics. Both dipoles are directly connected to the terminals of an impedance transformer with a primary input impedance of 50 Ω.

Since the backfire antenna operates, as previously mentioned, through a combination of surface-wave and open-cavity principles, a much smaller frequency range might be expected. The proper dimensions, however, chosen to give optimum backfire performance at the highest frequency, will yield a certain type of combination antenna that acts as a short-backfire at the higher frequencies (as long as the diameter of the reflector disk remains in the neighborhood of λ/2), and gradually changes over into a reflector antenna at the lower frequencies (when the effect of the reflector disk has become too small to cause any backfire action at all). The gain of this antenna, highest at the highest frequency, decreases proportionally with decreasing frequency.

Figure 6 shows E- and H-plane patterns for the frequencies 500, 600, 700, and 800 MHz. The low side- and backlobe levels typical of the short-backfire antenna are maintained over the entire frequency

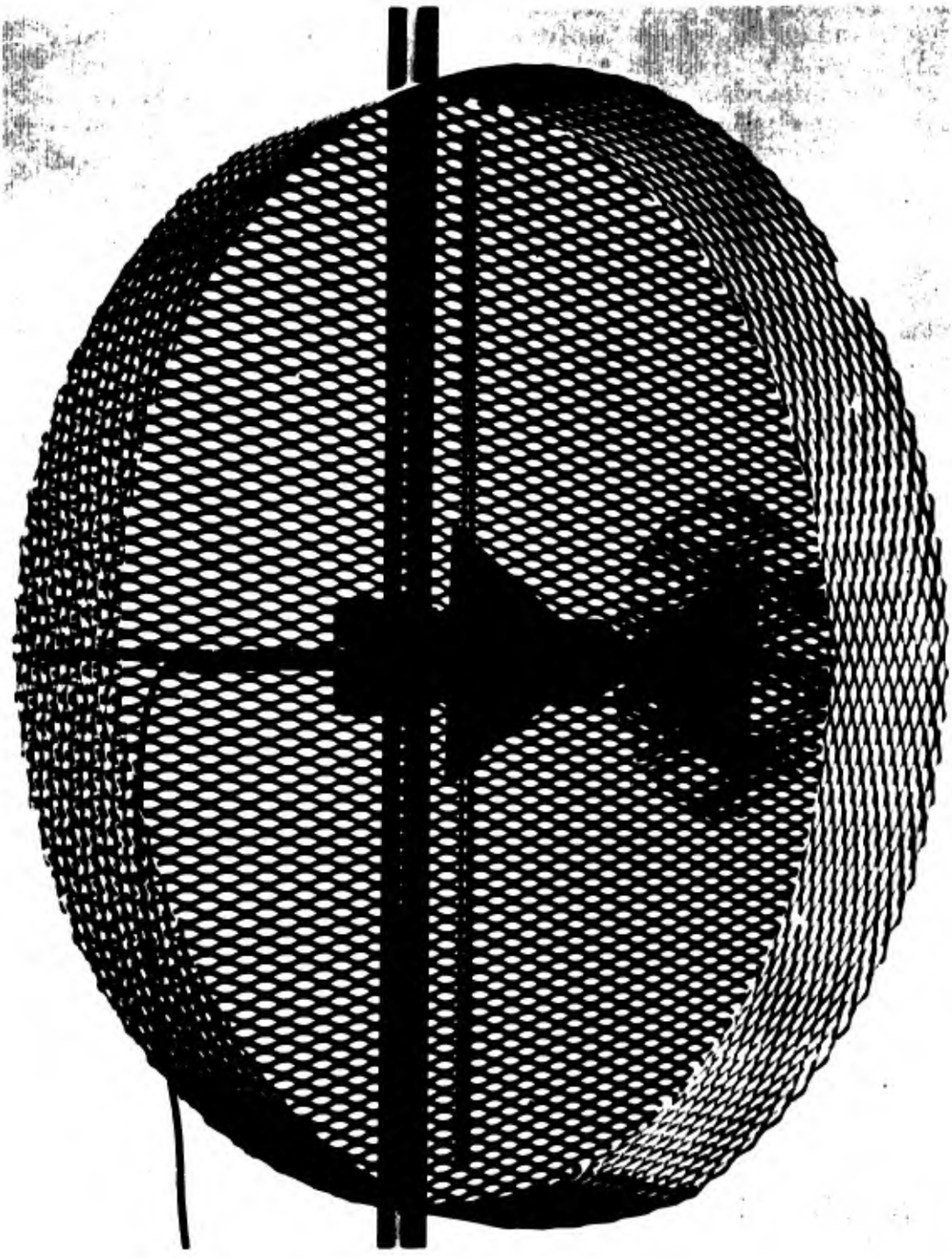

Figure 5. UHF Short-Backfire Antenna for 2:1 Frequency Range

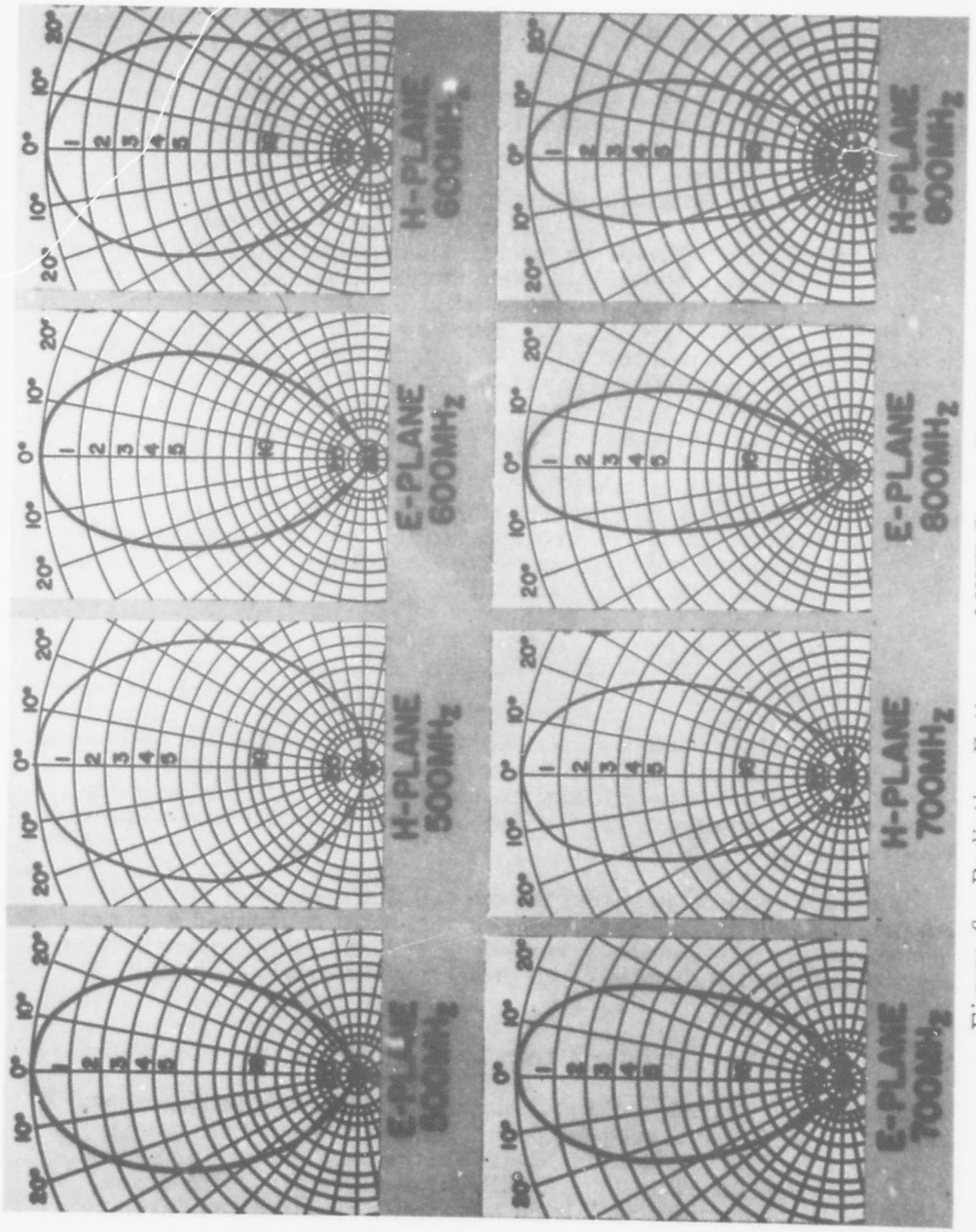

Figure 6. Radiation Patterns of UHF Short-Backfire Antenna

range from 400 to 800 MHz. As already shown in Figure 2, to demonstrate approximately the same gain and pattern quality, a Yagi would have to be 11 times as long as this short-backfire and have 27 dipole elements, 6 of them acting as reflectors, compared with the single feed dipole and two plane reflectors of the short-backfire.

5.2 Flush-Mounted Short-Backfire Antenna

A study of the amplitude and phase distribution in the nearfield of backfire antennas has shown that even complete enclosure of the structure by a metal cylinder of the diameter of the larger plane reflector (M in Figure 1) and long enough to extend over the entire length L of the backfire does not degrade antenna performance. Instead, the resulting closed cavity of circular cross section, with the partly open end as the antenna aperture, constitutes a backfire antenna that is especially useful in flush-mounted high-gain applications for airplanes and space vehicles. Most important, the short-backfire extends only about $\lambda/2$ into the skin of the vehicle body, and still produces gains of more than 16 dB with a single feed; even much higher gain figures can be reached if short-backfires are arrayed in front of a common reflector. As an example, the short-backfire ground antenna array shown later in Figure 11(a) could just as well be flush-mounted.

A photograph of a short-backfire antenna flush-mounted into a metal sheet 10λ by 10λ is shown in Figure 7(a). A close-up view of this 3000-MHz antenna, which is covered with a dielectric plate, is shown in Figure 7(b). The reflector disk is simply glued to the plate. The E- and H-plane patterns for 3000 MHz [Figures 8(a) and (b)] indicate a gain of about 15 dB, which increases to about 16.5 dB for 3500 MHz. The extremely low side- and backlobe levels inherent in the backfire principle are readily apparent. The usable bandwidth is about 1.5:1.

It should be mentioned that the overall dimensions of the short-backfire element in Figure 7(b) can be somewhat decreased — but at a penalty of some reduction in bandwidth — if the entire space between reflectors M and R is filled with dielectric material.

5.3 Short-Backfire Feed for Paraboloidal Antennas

The patterns in Figure 3(b) indicate the feasibility of the short-backfire as an efficient feed for paraboloidal antennas. Of special importance for this application are the extremely low side- and backlobe levels, and the almost identical shapes in the E- and H-plane patterns. An experimental S-band model of a backfire-fed paraboloid 6 ft in diameter is shown in Figure 9(a), with its secondary and primary patterns for 3000 MHz given in Figures 9(b) and (c), respectively.

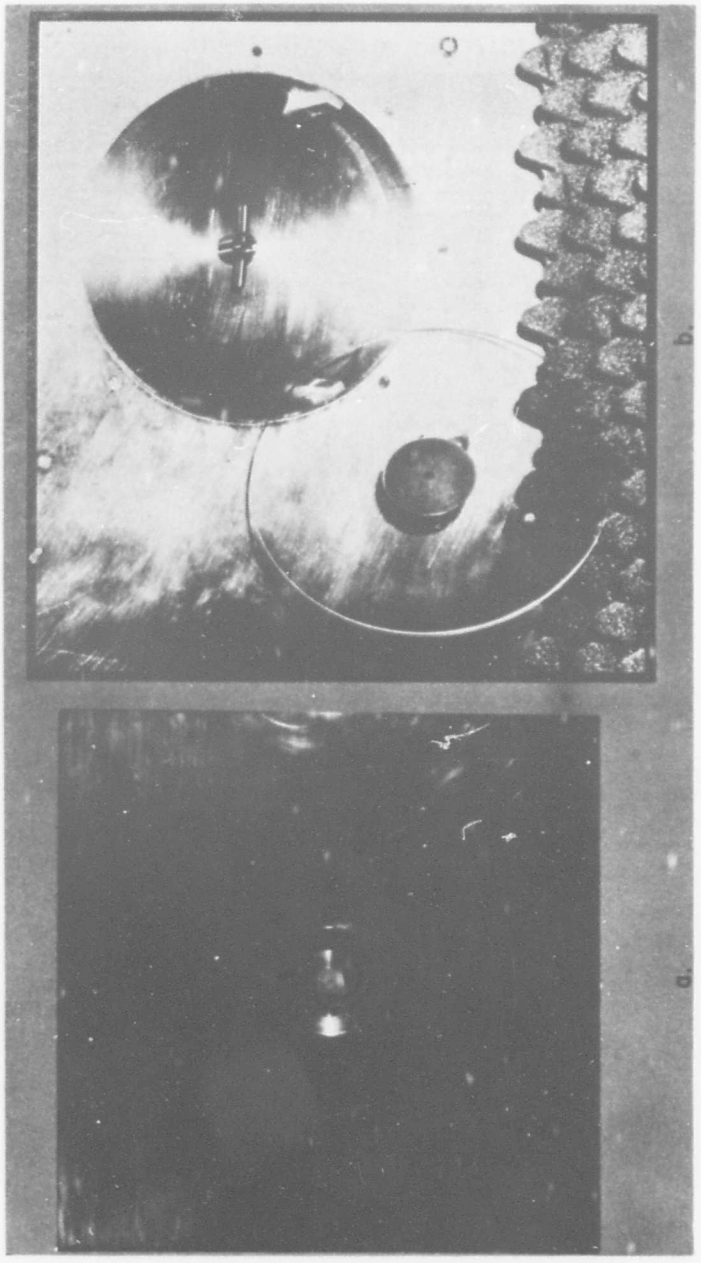

Figure 7. Flush-Mounted Short-Backfire Antenna

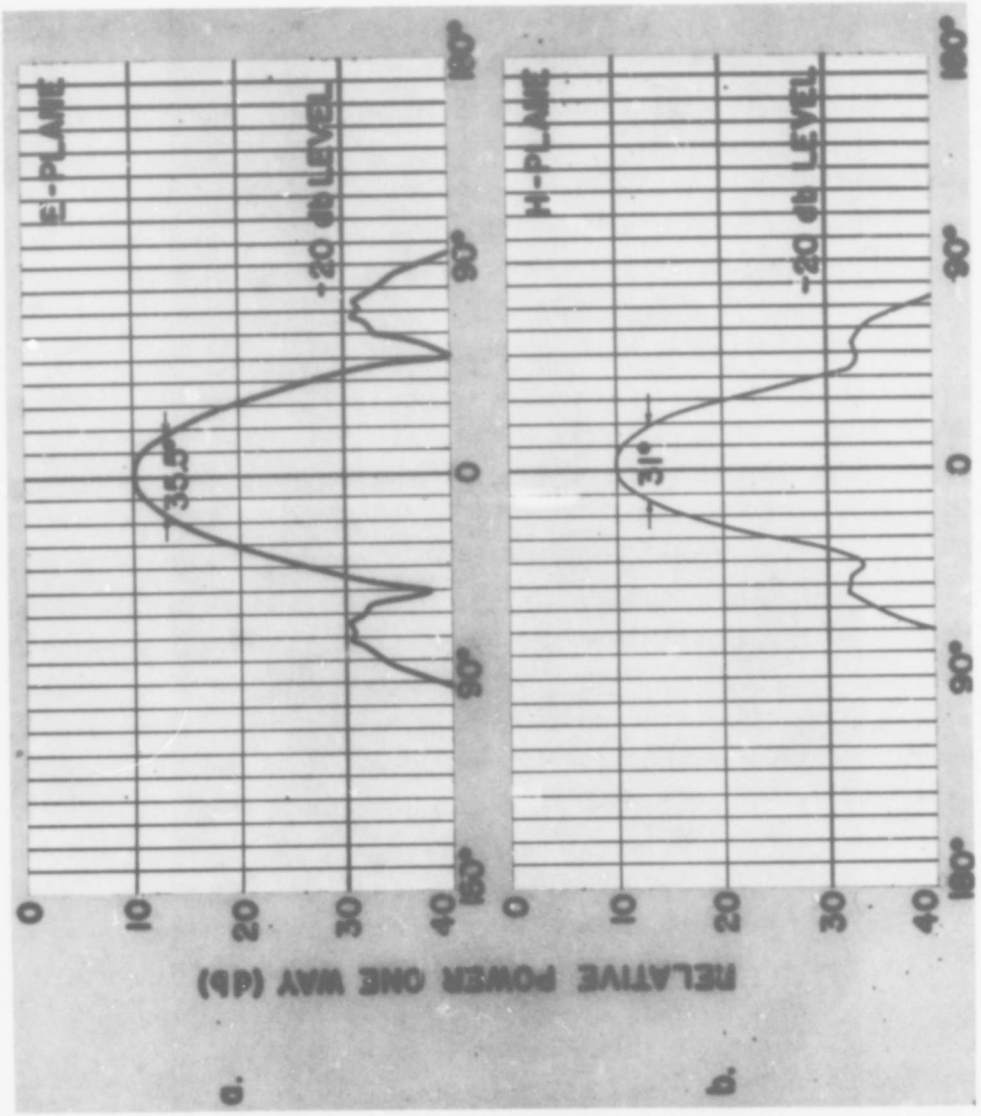

Figure 8. Radiation Patterns of Flush-Mounted Short-Backfire Antenna

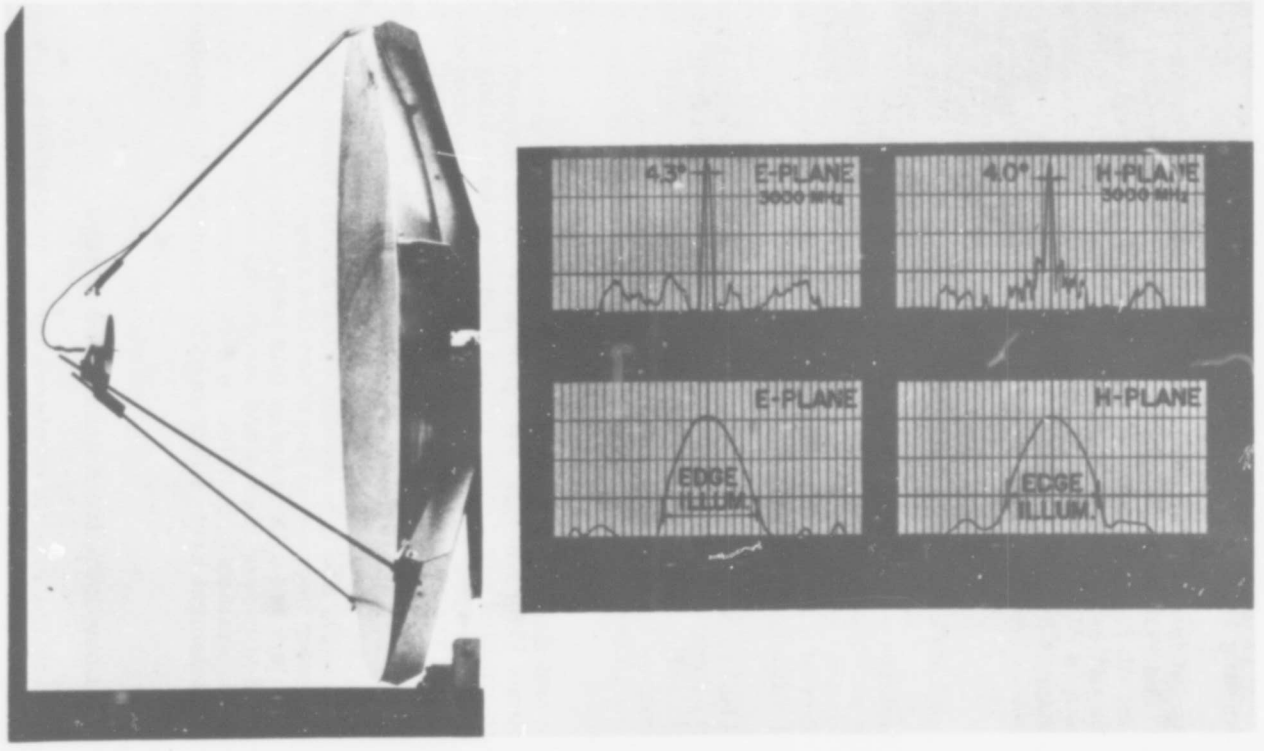

Figure 9. Short-Backfire-Fed Paraboloid With Primary and Secondary Patterns

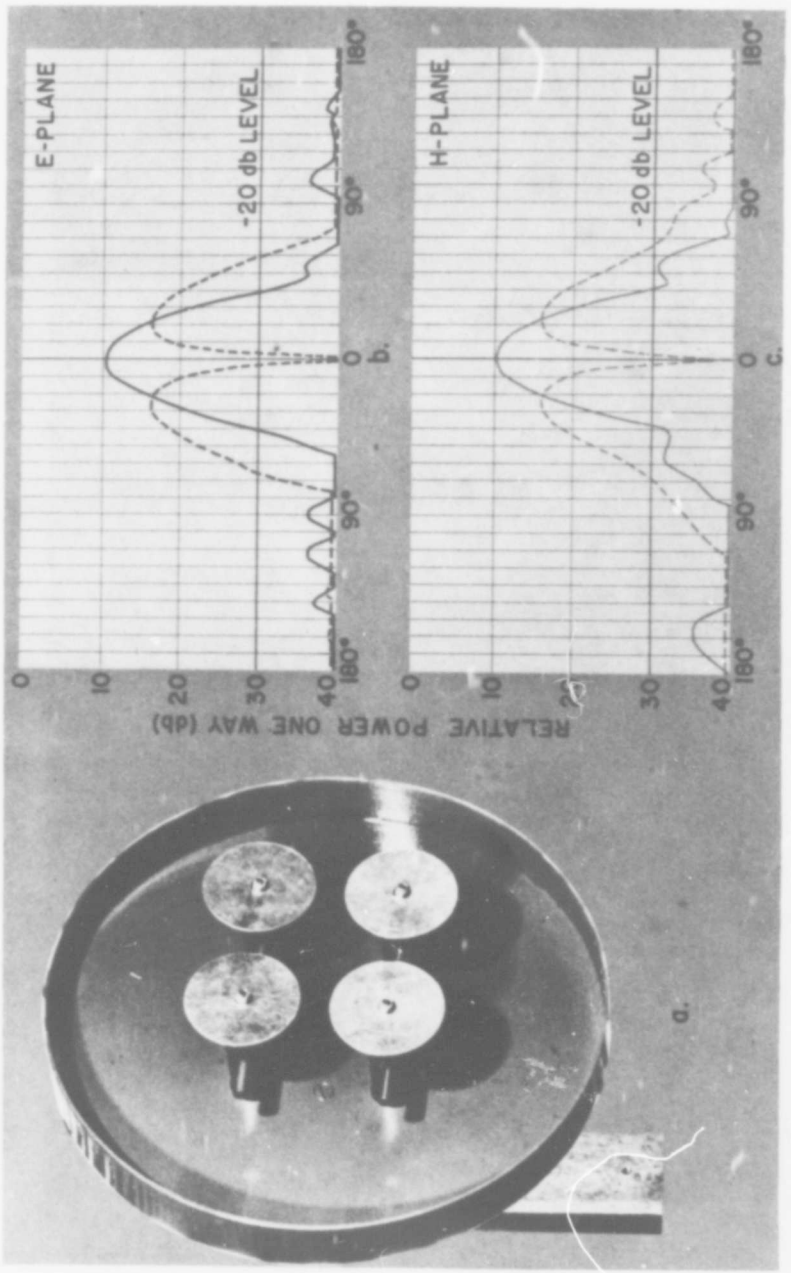

Figure 10. Monopulse Feed for Paraboloids and Its Sum and Difference Patterns

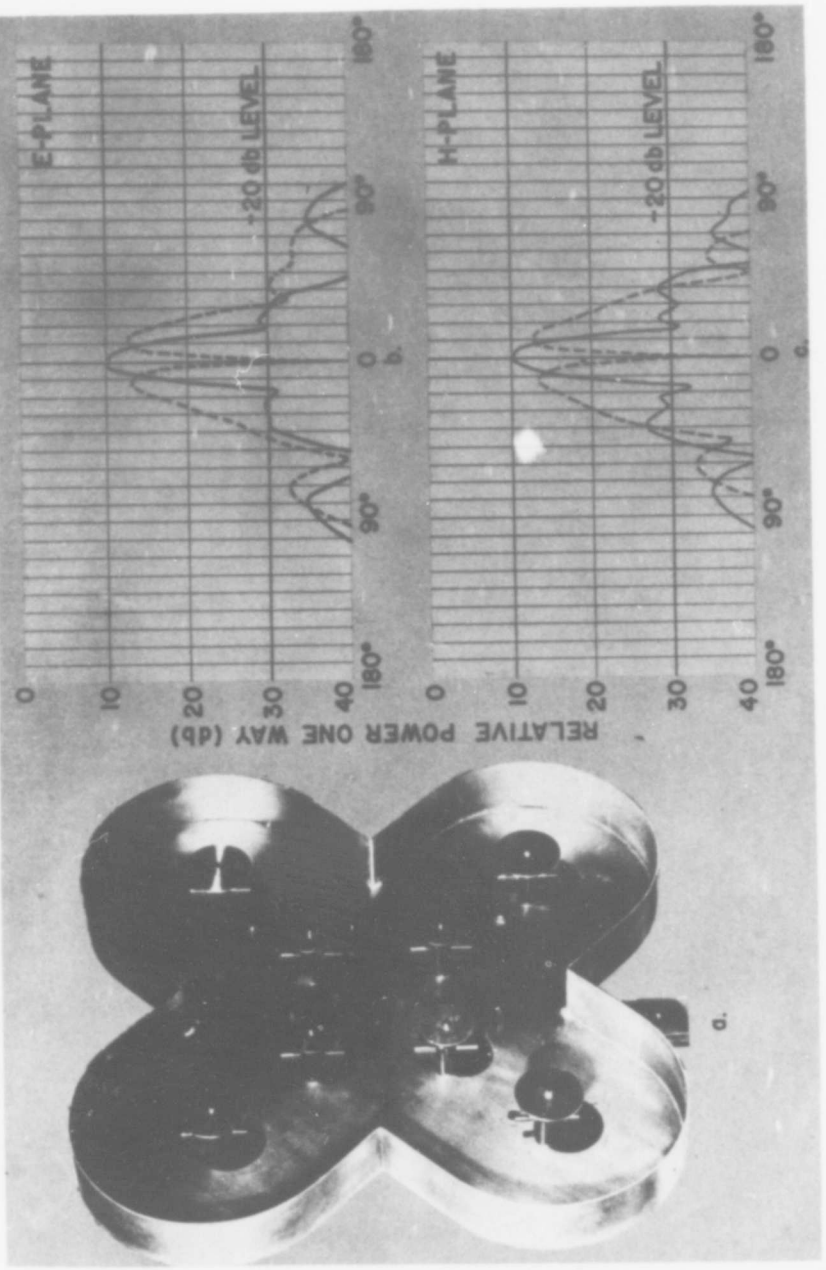

Figure 11. Short-Backfire Monopulse Array With Its Sum and Difference Patterns

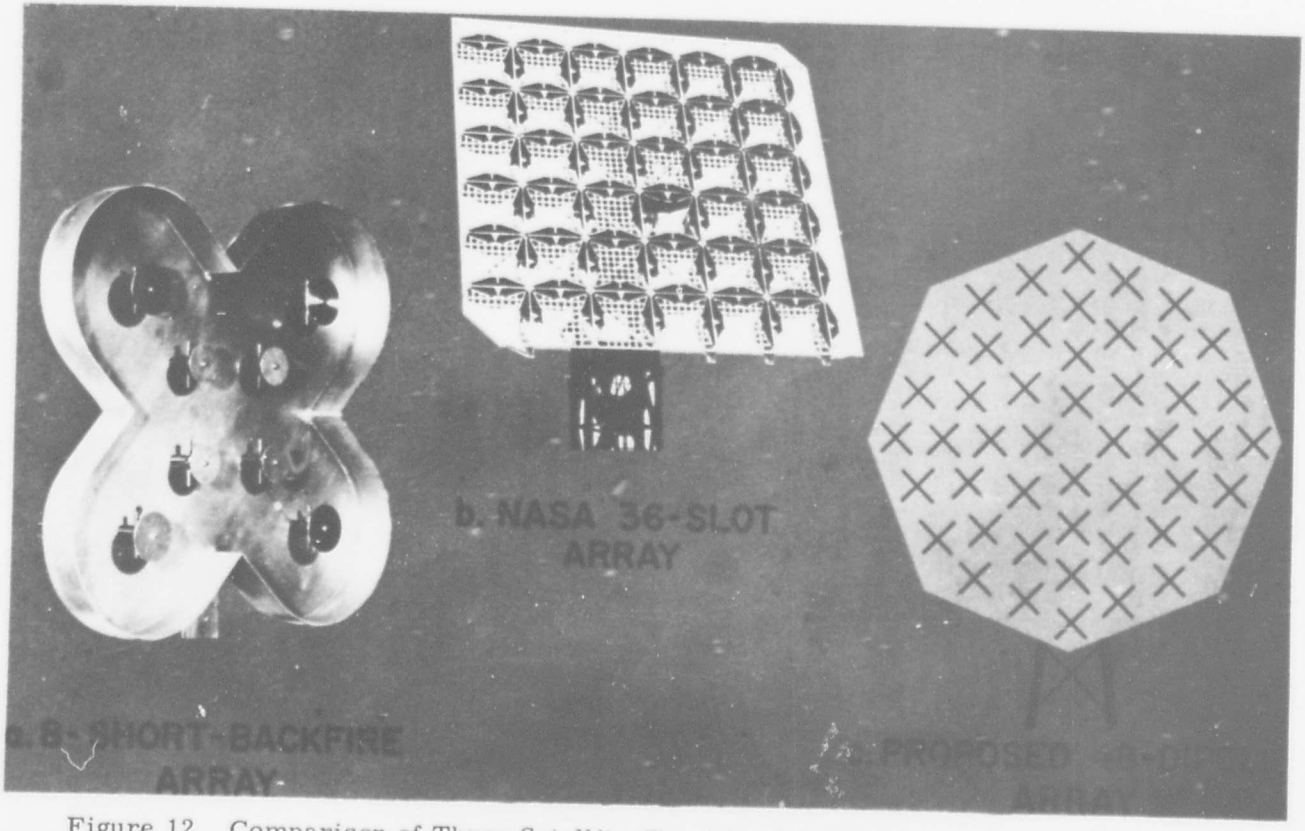

Figure 12. Comparison of Three Satellite-Tracking Antennas: (a) 8-short-backfire array; (b) NASA 36-slot array; (c) proposed 48-dipole array

The secondaries [Figure 9(b)] have very low side- and backlobe levels, corresponding favorably to the primary patterns.

Also of great interest for paraboloid applications is the model of a monopulse feed that consists of a group of four short-backfires in front of a common 2λ-reflector. It is shown in Figure 10(a); its sum and difference patterns for the E plane are given in Figure 10(b), and for the H plane in Figure 10(c). It can be seen that both the sum and difference patterns have approximately the same shape within the 0 to 20-dB energy levels in both planes.

5.4 Arrays of Short-Backfire Antennas

Short-backfire antennas are suitable array elements for constructing high-gain antennas for the gain range from 20 to over 30 dB. Because the radiating aperture of each short-backfire element is much larger than that of a dipole, a much smaller number of short-backfires is needed for illuminating the same area.

Figure 11(a) is a photograph of an S-band model of a high-gain short-backfire array consisting of 8 elements arranged in front of a common plane reflector in such a way that for monopulse applications, the sum as well as the difference patterns can be obtained. The reflector area was kept as small as possible by means of the four-leaf clover design.

The sum and difference patterns for the E and H planes are shown in Figures 11(b) and (c). The gain is 21 dB for the sum pattern. The progress attained can best be demonstrated by comparing the short-backfire cloverleaf array in Figure 11(a) with arrays of slot elements [Figure 11(b)] or conventional dipoles [Figure 11(c)]. To achieve the same magnitude of gain as the cloverleaf, a recently built satellite-tracking antenna[10] uses 36 cavity-backed slots; another, proposed elsewhere, uses 48 dipoles. Of the three antennas compared in Figures 12(a), (b), and (c), the cloverleaf has the much less complicated feed system because in the other two arrays, each element has to be separately fed. Because of this advantage and those accruing from the reduction in feed losses and structural weight, this short-backfire array is eminently suitable as a replacement for the bulky and costly multielement arrays now used in telemetry and satellite-tracking.

5.5 High-Gain Long-Backfire Antennas and Arrays

The long-backfire antenna combines the structural advantages of a single endfire with the high gain of a reflector antenna. Its principal applications lie in the field of telemetry and satellite-tracking, especially for frequencies below 500 MHz. A single slow-wave structure

yields gains of up to 25 dB. Higher gains (and monopulse patterns) can be obtained by using an array of such structures placed in front of one common plane reflector, whose construction costs are far less than those of a paraboloidal reflector.

The 4-λ S-band model of a long-backfire with stacked reflectors shown in Figure 4(a) yields patterns [Figures 4(b) and (c)] that demonstrate a gain of 23.5 dB. The diameters of the two reflectors are 6λ and 1λ. The slow-wave structure consists of 14 dipoles. For higher frequencies (f > 1000 MHz) it may also be a dielectric rod, as shown in the 2000-MHz model in Figure 13, but for lower frequencies the rod dimensions would become impractically large. The dielectric-rod short-backfire, like a crossed-dipole structure, offers the advantage of being applicable to any polarization the feed is capable of.

Figure 14 compares a long-backfire (gain 23.5 dB) with a recently designed array of Yagis[10] (gain 22.4 dB). Both antennas have approximately the same physical area. To approach the same gain, the array in Figure 14(b) needs 16 Yagis, each 2λ long, consisting altogether of 128 crossed dipoles, whereas the long-backfire in Figure 14(a) needs only a single Yagi-like structure 4λ long, consisting of 14 crossed dipoles.

The E-plane patterns of both antennas are compared in Figure 14(c). The 16-Yagi array pattern has a first sidelobe of about 11.5 dB below the maximum, contrasting sharply with the long-backfire pattern, where all sidelobes are below 20 dB and the backlobe is below 30 dB. The Yagi half-power beamwidth is 13° in the E and H planes, compared with 13° and 10.5° respectively, for the long-backfire E and H planes, thus indicating the somewhat higher gain of the backfire structure.

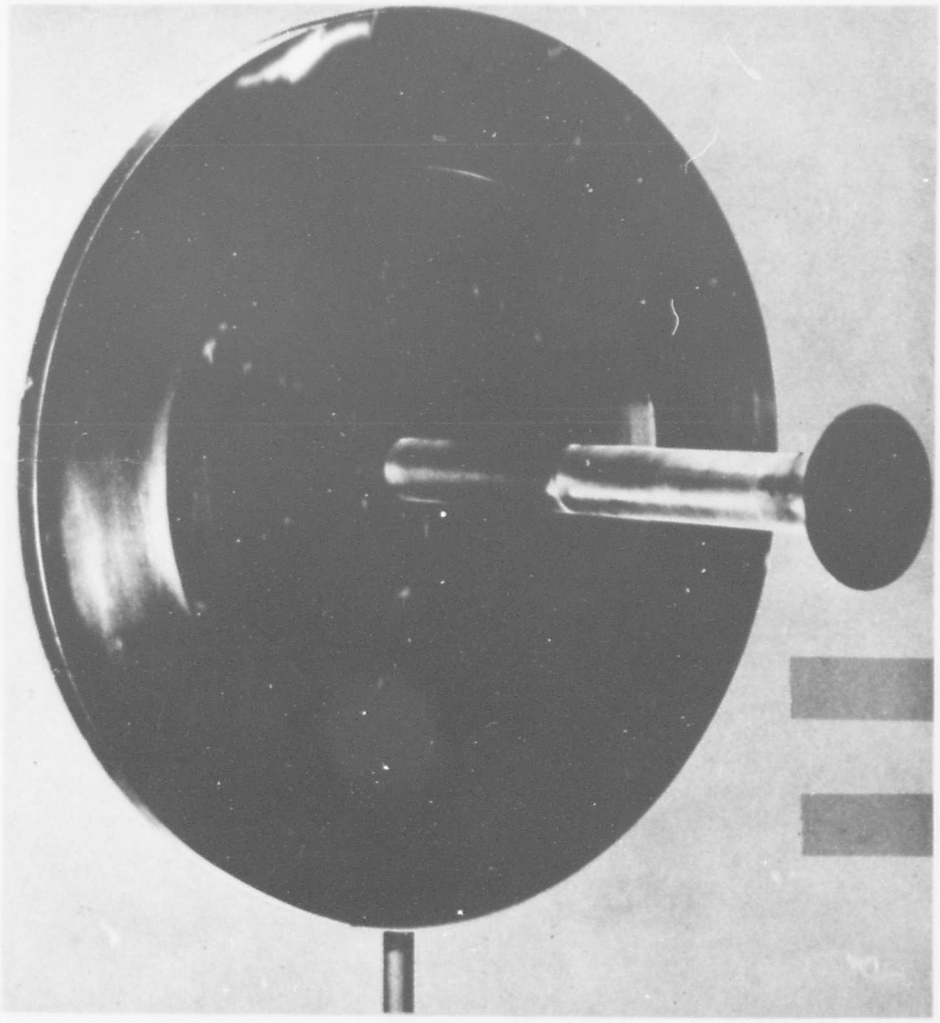

Figure 13. 4-λ Long-Backfire With Dielectric Rod

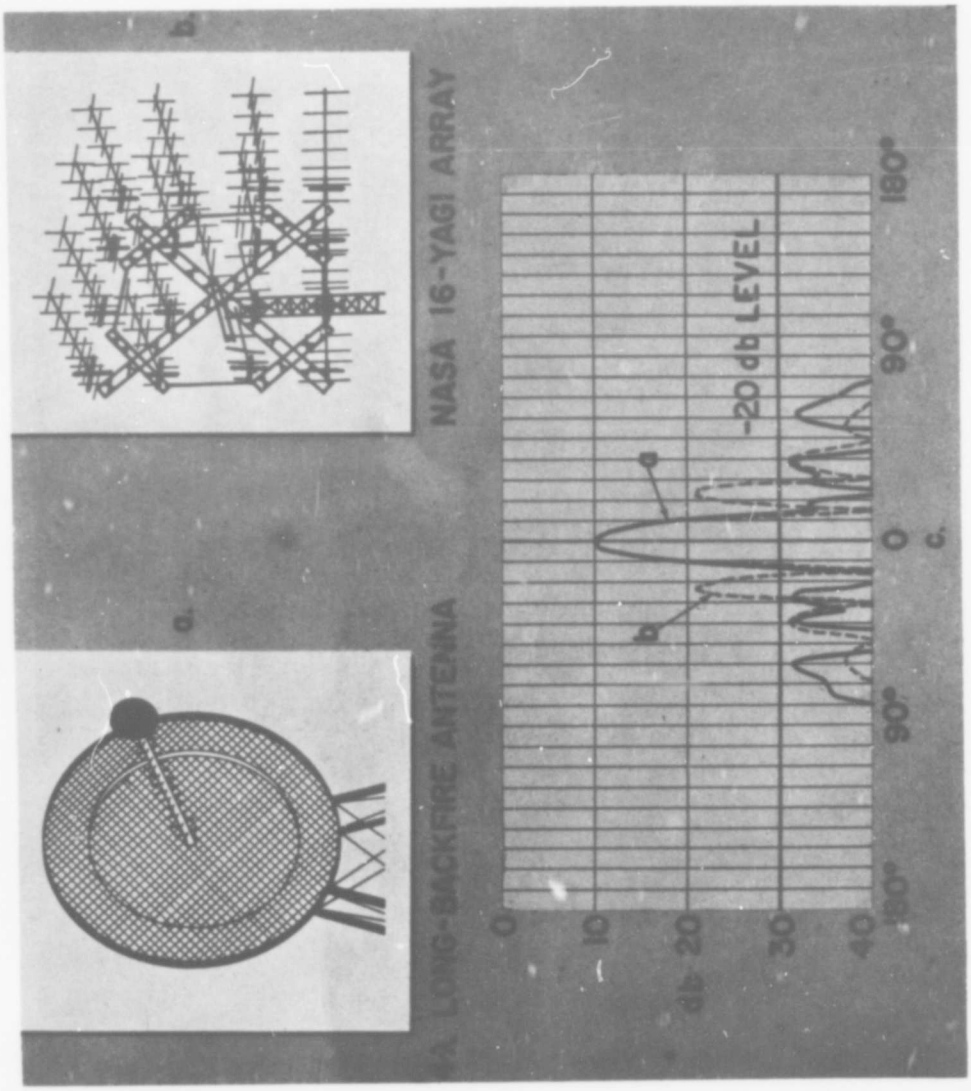

Figure 14. Comparison of Telemetry Antennas and Their E-Plane Patterns

6. SUMMARY

A short-backfire $\lambda/2$ long can now replace a 27-element Yagi that is 5.5λ long.

A flush-mounted short-backfire (or an array of these) extending only $\lambda/2$ into the skin of an airplane or space vehicle can now be constructed for a gain range from 15 dB to 30 dB.

An array of 8 short-backfires or 4 long-backfires can now replace a monopulse array of 36 slot elements or 48 dipoles.

A long-backfire with a single Yagi-like structure of 14 crossed dipoles can now replace a telemetry antenna with 16 single Yagis consisting of a total of 128 crossed dipoles.

Our discussion has thus far been restricted to technical data directly related to the radiation patterns of the antenna models. If construction data and cost are examined, an equally favorable picture emerges:

The reduction in the amount of material, and therefore in the weight of the antenna structure, results in a smaller and less expensive mount.

The simpler feed system needed for connecting the single-element long-backfire — instead of an array of 16 single Yagis — with the receiver, or for connecting the 8 short-backfires — instead of an array of 36 or 48 single elements — with the monopulse network, greatly reduces costs and insertion losses of the array.

From all standpoints — gain, bandwidth, reliability, size, ease of construction, and cost — the family of backfire antennas and arrays have shown their superiority over the multielement arrays in the same gain range. Only a few of the possible applications have been explored in this paper. More are being developed.

ACKNOWLEDGMENTS

This work was done under the general direction of Mr. F. J. Zucker, Chief of the Waves and Circuits Branch, and Mr. C. J. Sletten, Chief of the AFCRL Microwave Physics Laboratory. The author is indebted to Mr. F. J. Zucker for many stimulating discussions, to Mr. J. A. Strom for assistance in performing the extensive experimental program, and to B. S. Karasik for editorial advice.

REFERENCES

1. Ehrenspeck, H.W., and Poehler, H., A new method for obtaining maximum gain from Yagi antennas, AFCRC Rpt No. ERD-CRRDA-TM-56-123, Aug. 1956; also, IRE Tr. PGAP AP-7: 379-386, Oct. 1959.

2. Ehrenspeck, H.W., and Kearns, W.J., Two-dimensional endfire array with increased gain and sidelobe reduction, 1957 IRE Wescon Conv. Record (Pt. 1), 1957, p. 217.

3. Ehrenspeck, H.W., Reflection Antenna Employing Multiple Director Elements and Multiple Reflection of Energy to Effect Increased Gain, U.S. Patent applied for 1959, granted Feb. 1964. Additional patents applied for.

4. Strom, J.A., and Ehrenspeck, H.W., Backfire Antennas for SHF, UHF, and VHF Bands, AFCRL-63-114, Apr. 1963.

5. Zucker, F.J., Surface and leaky-wave antennas, Chapter 16 in Antenna Engineering Handbook, H. Jasik, Ed, McGraw-Hill, 1961.

6. Ehrenspeck, H.W., The backfire antenna: new results, Proc. IEEE (Correspondence) 53 (No. 6):639-641, June 1965.

7. Zucker, F.J., The backfire antenna: a qualitative approach to its design, Proc. IEEE (Correspondence) 53 (No. 7):746-747, July 1965.

8. Ehrenspeck, H.W., The short-backfire antenna, Proc. IEEE (Correspondence) 53 (No. 8):1138-1140, Aug. 1965.

9. Ehrenspeck, H.W., The "Backfire," A High-Gain Cavity Antenna, Proceedings of the Symposium on Electromagnetic Wave Theory, Delft, 1965, Pergamon Press Ltd., Oxford, 1966.

10. Lantz, P.A., Handbook of NASA/GSFC Tracking, Data-Acquisition, and Communication Antennas, Tech Rpt X-525-64-222, Goddard Space Flight Center, Greenbelt, Md., Oct. 1964.

BLANK PAGE

Dr. William A. Tiller is Executive Head of the Department of Materials Science at Stanford University, and has been an AFOSR grantee for 6 years. He was graduated from the University of Toronto in Engineering Physics in 1952, and received his M.A. Sc. and his Ph. D. in Physical Metallurgy from the same university. Dr. Tiller teaches courses on surfaces and phase transformations, and is continuing and extending his quantitative studies of the crystallization process. Before joining Stanford University in 1964, he was with the Westinghouse Research Laboratory in Pittsburgh. While there, he investigated the basic physics of the freezing process on a wide range of materials, through which new processes for ingot casting, material purification, single-crystal growth and chemical crystallizers have been generated. As manager of a research team in this effort, he authored or coauthored more than 75 publications on crystallization.

The Generation of Science-Based Technology in the Field of Crystallization

by

W. A. Tiller

ABSTRACT

AFOSR co-sponsored research at Stanford and formerly at Westinghouse in the area of basic research on "Crystallogenics" has produced a sufficiently strong base of scientific understanding that the field of crystallization, which has been very dependent on "art", is rapidly becoming an engineering science. Attendant technological applications have begun to appear in three areas: (i) single crystal growth, (ii) materials purification and (iii) structure control of ingots and castings.

The following examples serve to illustrate this advance.

(i) By studying the crystallization of selenium at high pressures, a technique and control criteria were generated for preparing large single crystals. Besides its potentially interesting electronic and optical properties, selenium is a polymeric material in the liquid state, and thus does not crystallize readily. The experimental procedure should be useful for the controlled crystallization of a host of other materials consisting of associated molecules.

(ii) From interface stability studies, it has been possible to quantitatively describe the freezing conditions that must be maintained for effective purification of a material by the freezing process. For a material like water, purification by a factor of 2 or 10^3 per freezing

cycle can occur depending upon the freezing conditions. Simple devices can be designed for effective saline water purification or for producing ultra-pure water.

(iii) The investigation of crystal multiplication phenomena during crystallization under the influence of moving electromagnetic fields has led to the generation of extremely fine-grained and chemically homogeneous cast metals. Simple electromagnetic devices may be developed which are capable of improving ingot structure and yield. This type of technology is expected to have a significant impact upon the foundry industry.

The Generation of Science-Based Technology in the Field of Crystallization

by

W. A. Tiller

Introduction

The field of crystallization has been an art rather than a science for a very long time. Only in the past 20-30 years have we begun to look at it in its entirety from a sufficiently quantitative point of view that we can recognize the sophisticated insights and techniques needed for controlling the crystallization process to such a degree that we can tailor-make solids of the state of aggregation most suited to our particular needs. It is well known that many important properties of a material are controlled by its structure, both micro and macro. In recent years, it has also become well known that the structure of a material is influenced by the manner in which it was crystallized.

In the past, the majority of workers in the crystal growth and crystal characterization area have been primarily interested in crystal preparation from the point of view of the end product and have largely adopted the distinctly empirical approach of relating the gross perfection of the material to the macroscopic variables of the process. This is a straightforward procedure and is one that has been adopted by investigators for centuries. However, the efforts expended in determining an empirical solution to one specific example in this area make only a very small contribution to enhancing the efficiency

of and the capabilities for determining a solution to a different example in this area. Such an approach leads to an Art-Based Technology.

This strongly empirical approach to crystal preparation is no longer suited to satisfy the technological needs of a nation such as ours which requires highly specialized and sophisticated materials reliably manufactured. Recognizing that detailed scientific insight and reliable engineering specification was needed in this important area of materials preparation to fill the present and future needs of our technical society, AFOSR helped to pioneer the more enlightened "Crystallogenics" approach to materials preparation. The word "Crystallogenics" means, literally, crystal genesis or the birth and growth of crystals and it was initially selected to stand for a basic comprehension of and a high degree of control over this important process. Because of AFOSR co-sponsored research at Stanford and formerly at Westinghouse, the word crystallogenics has now become synonymous with scientific understanding of the crystallization process.

At present, basic research on "Crystallogenics" has materially helped to produce a sufficiently strong base of scientific understanding that the field of crystallization which has been an art is rapidly becoming an engineering science. Attendant technological applications have begun to appear in three areas: (i) materials purification, (ii) single crystal growth and (iii) structure control of ingots and castings. In recognition of the awareness that important innovations are imminent in this area, the number of investigators in industrial companies that are working on crystallization problems has increased by an order of magnitude in the last few years. This trend has

undoubtedly been further stimulated by the recent Pratt & Whitney breakthrough in making turbine components using controlled crystallization knowledge and techniques[1]. They now cast turbine blades by directional solidification and single crystal methods. Though processing of turbine parts in this way takes longer than conventional casting, it is worthwhile because of the superior strength, ductility and oxidation resistance of the resulting material.

In this paper, we shall first gain a perspective on what elements of knowledge are necessary to reliably engineer a crystallization application. Next, the Crystallogenics approach and successes will be briefly discussed. Finally, a discussion of the present exploitation opportunities in the crystallization area is presented.

The Science of Crystallization

To illustrate what fields of science and what general knowledge must be brought to bear upon the reliable analysis of a crystal growth problem, let us say that we wish to control the structure of a solid by isothermally freezing a small volume of liquid alloy. By structure, we shall mean grain size and shape, degree of microscopic and macroscopic chemical segregation, etc. Thus, we shall be concerned with understanding the growth characteristics and morphology of dendritic crystals.

The name "dendrite", which comes to us from the early Greeks, has been given to that particular "tree-like" crystal morphology so often observed in nature and familiar to us all in the patterns of snowflakes, geological formations and the development of ice on neighborhood ponds. Comparing such shapes

generated by crystals of several different materials as illustrated in Fig. 1 with the drawing of Nakaya's 8 prime snowflake patterns given in Fig. 2, one begins to get a hint of the amazing variety of form that can be generated even in a single material. It is little wonder that the singular beauty and complexity of such dendritic forms have fascinated both the casual and the perceptive observer for centuries. Experimental studies on this crystal form have served to illustrate how a slight change in environmental conditions may cause a growing crystal to change from the dendritic form to an entirely different morphology and how vastly different morphologies can be generated by only slight differences in some of the important material parameters that control the crystal growth process.

For this "overview" we will be satisfied with a phenomenological description of the important processes in terms of "lumped" parameters. The conventional macroscopic variables that we either set or control are (1) bath composition, C_∞, (2) bath cooling rate, $\dot{T}$, and (3) the shape of the container holding the liquid. Let us proceed with the process description by stages.

(a) As the liquid is being cooled, we need to know the magnitude of the driving force for solid formation, ΔG, at any bath temperature T. This can be expressed as

$$\Delta G = f_1 [\Delta H, T_L (C_\infty)] \qquad (1)$$

where f_1 refers to the appropriate functional relationship between the latent heat of fusion, ΔH, and the liquidus temperature, $T_L(C_\infty)$. Thus, we see that

phase equilibria data is one prerequisite. The material parameters needed for this area of study are listed and defined in Table I.

(b) As the bath undercooling, ΔT, increases with time, t, we need to know the undercooling at which particles of solid begin to form and also their density. Thus, we must evaluate the nucleati n frequency, I, which can be most simply expressed as

$$I = f_2 [N_o, \Delta T_C, \dot{T}, t, C_\infty] \tag{2}$$

where f_2 represents the appropriate functional realtionship, N_o is the number of atoms in conact with the foreign substrate that catalyzes the nucleation event and ΔT_C is a parameter which defines the potency of the catalyst.

(c) When the crystals illustrated in Fig. 3 begin to grow at some velocity, V, solute partitioning will occur at the interface since the equilibrium concentration of solute in the solid, C_S, is different than the concentration in the liquid at the interface. Thus, the concentration of solute in the liquid at the interface, C_i, must be determined and can be represented by a functional relationship of the form

$$\frac{C_i}{C_\infty} = f_3 [V, k_i, D, \delta_C, S, t] \tag{3}$$

where k_i refers to an interface solute partition coefficient which is generally different from k_o, D is the solute diffusion coefficient, δ_C refers to the solute boundary layer thickness at the crystal surface and S refers to the shape of the crystal.

(d) In order to evaluate δ_C in eq. 3, it is necessary to consider the hydrodynamics of the fluid. The fluid will generally exist in some state of motion whether the driving force is applied by external means or arises naturally due to density variations in the fluid. We can consider the fluid far from the crystal/liquid interface to be moving with some relative stream velocity, u_∞, due to the average fluid body forces. The fluid motion will aid in the matter transport of solute away from the crystal into the bulk liquid and cause a lowering of C_i. We find that δ_C can be expressed as

$$\delta_C = f_4 [V,\nu,D,S,u_\infty,t] \tag{4}$$

where ν is the kinematic viscosity of the fluid.

That portion of the total undercooling consumed in driving the solute transport, ΔT_S, is given by

$$\Delta T_S = T_L(C_\infty) - T_L(C_i) \tag{5}$$

(e) Because the growing crystal is small in size, has curved surfaces and often contains non-equilibrium defects, the solid contains a higher free energy than the solid which is considered in generating a phase diagram which we use as our standard state in the overall treatment. Thus, the equilibrium melting temperature for such a solid is lowered by an amount, ΔT_E, compared to that for the equilibrium solid. We find that the portion of the total undercooling consumed in the production of non-equilibrium solid, ΔT_E, can be expressed as

$$\Delta T_E = T_L(C_i) - T_E(C_i) = f_5 \left[\gamma, \Delta S, S, \sum_i \gamma_i^f, \sum_i N_i^f\right] \quad (6)$$

where $T_E(C_i)$ is the equilibrium interface temperature for interface liquid concentration C_i, γ is the solid/liquid interfacial energy, ΔS is the entropy of fusion, γ_i^f is the fault energy for defects of type i and N_i^f is the number of faults of type i.

(f) Next, because the crystal is growing, a departure from the equilibrium temperature, ΔT_K, must exist at the interface in order to produce a net driving force for molecular attachment to the growing solid. At sufficiently large departures from equilibrium, the molecules can attach at any interface site and lower the free energy of the system. However, at small departures from equilibrium, molecular attachment at random interface sites generally leads to an increase in the free energy of the system and thus such interface attachment will not occur as a spontaneous process. Rather, in such an instance, molecules become a part of the solid only by attachment at layer edge sites on the interface and one must consider the various mechanisms of layer generation on the crystal surface. The portion of the total undercooling consumed in driving this interface process, ΔT_K, can be expressed as

$$\Delta T_K = T_E(C_i) - T_i = f_6 \left[V, \mu_1, \mu_2, S, t\right] \quad (7)$$

where T_i is the actual interface temperature and where μ_1 and μ_2 are lumped parameters needed to specify the interface attachment kinetics for the various attachment mechanisms.

(g) Finally, since the crystal is growing, it must be evolving latent heat and the interface temperature, T_i, must be sufficiently far above the bath temperature, T_∞, to provide the potential for heat dissipation to the bath. That portion of the total undercooling consumed in driving the heat dissipation, ΔT_H, can be expressed as

$$\Delta T_H = T_i - T_\infty = f_7 [K,\alpha,\Delta H,V,S,t] \tag{8}$$

where K refers to the thermal conductivity and α refers to the thermal diffusivity.

The foregoing has been a description of the subdivision of the total bath undercooling, ΔT, into its four component parts; i.e.,

$$\Delta T = \Delta T_S + \Delta T_E + \Delta T_K + \Delta T_H \tag{9}$$

Equation 9 is called the "Coupling Equation" and illustrates the fact that these four basic elements of physics enter every crystal growth situation and are intimately coupled through this constraint. However, for different materials, certain of the components of eq. 9 tend to dominate the phase transformation. In the growth of metal crystals from a relatively pure melt, $\Delta T_H \sim \Delta T$ so that this case is largely controlled by heat flow. During the growth of an oxide crystal from a melt of steel, for example, $\Delta T_S \sim \Delta T$ so that the growth is largely diffusion controlled. During the growth of a polymer cyrstal from a well-fractionated polymeric melt, $\Delta T_K \sim \Delta T$ and the growth is largely controlled

by the kinetics of interface attachment. Finally, during the growth of a lamellar eutectic crystal, $\Delta T_E \sim \Delta T/2$ and the growth is to a large degree controlled by the excess free energy of the solid (due to the formation of α/β phase boundaries). By considering Fig. 4, which is a plot of crystal growth velocity as a function of time, we find that, at small times, ΔT_E in eq. 9 dominates the crystal's growth and thus plays an overriding role in its morphology. At large times, ΔT_S and ΔT_H in eq. 9 dominates the crystal's growth and leads to very different morphologies. At intermediate times, all of the four factors play significant roles in the shape adopted by the crystal.

From Table I, we can begin to see why the field of crystallization has remained an art for so long. To have maintained a clear understanding of the problem to this point would have required (i) the specification of at least 20 material parameters, (ii) the solution of at least 3 boundary value problems and (iii) the correlation of at least 6/interface variables (independent) with 4/macroscopic field variables (independent). Changing one of the parameters without a change in the macroscopic field variables can lead to a major change in structure as can the changing of one of the field variables without changing any of the material parameters.

There is little doubt that crystal morphology plays a significant role in the resultant crystal perfection and that this morphology is largely determined by the subtle interplay of the factors already discussed. However, the prediction of crystal shape with time is a problem that we have been unable to solve in any general way. This arises because the problem thus far stated is, in general, not completely specified. Knowing V and S, C_i and T_i can be completely determined in terms of C_∞ and T_∞ respectively, and also ΔT_S, ΔT_E, ΔT_K and ΔT_H are completely determined in the general mathematical sense. However, we do

not know either V or S. If S(t) is specified, eq. 9 can be used to determine V(t). We are in need of an additional condition to completely specify the problem and thus provide simultaneous prediction of both V(S) and S(t).

We shall find that our extra condition is generated by considering the response of the growing crystal to shape perturbations. It can be easily shown that the various elements of the interface will always be subjected to fluctuations in ΔT and in its component ΔT_i's. Thus, given sufficient time, we should always expect that shape distortions will have a finite probability of forming on the crystal surface and that the crystal will evolve to that shape which is most stable in the environment that allows such perturbations. With the addition of our perturbation response equation in the general form

$$V^*(S) = f_8 [S^*, \Delta T_S, \Delta T_E, \Delta T_K, \Delta T_H] \quad , \tag{10}$$

the most stable crystal shape, S^*, and the corresponding growth velocity at various points on the crystal surface, V^*, may be evaluated from eqs. 9 and 10.

At this point in the problem we can, in principle, specify the solute, temperature and fluid velocity fields throughout the system. We thus have the potential to specify the chemical inhomogeneity of the final solid and the types of compound formation that should occur in the highly solute-enriched liquid that is last to freeze. The stress distribution due to both constitutional and thermal variations in the as-solidified alloy should also be specifiable and thus, the defect generation in the solid as it cools to a particular temperature may be predicted.

It is to be hoped that the reader now sees that we are no longer treading through a blind maze in the crystallization area and that we have developed a logical and orderly framework of understanding from which a Science-Based Technology can be generated. The main thrust of the "Crystallogenics" investigations has been the explicit determination of the f - functions in eqs. 1 - 10 which are the important "subroutines" of the overall systems analysis of our crystallization problem.

BLANK PAGE

Crystallogenics Research

The basic physics of most of the phenomena we encounter in crystallization are fairly well understood; however, in the majority of real crystallization situations, there are so many variables and parameter interactions to be considered, understanding of experimental observations most often requires a variety of mathematical linkages to separate the important interactions and correlate them with the field variables. In many cases we are dealing with very complicated boundary-value problems and we need mathematical solutions largely guided by physical insight. The Crystallogenics approach for generating a Science-Based Technology in this area is idealized in the following:

1. Develop a quantitative understanding of the relationships between crystal morphology and perfection and the interface variables both as to (a) a phenomenological description for day-to-day utilization and (b) an eventual atomic process description; i.e., some of the f_n in eqs. 1 to 10.

2. Develop quantitative relationships between the interface variables and the macroscopic variables. These are generally determined by solving a series of particular boundary-value problems and, as such, represent the application of classical field theory to the crystallization process; i.e., determine some of the f_n in eqs. 1 to 10.

3. Control the macroscopic variables of a particular crystallization device in such a way as to control the spatial and time-dependence of the macroscopic variables (through 2) to produce the desired structure (through 1). In many cases, a particular crystallization device may not allow the necessary degree

of macroscopic variability to generate the desired structure. Such an approach allows one to recognize what is needed and to design a new device or process which provides one with the desired degree of variability.

4. Attack the problem area on a broad front with sufficient effort to be truly effective in accomplishing item 3 above.

The emphasis of this study was primarily directed towards generating detailed understanding and control of the freezing process. To achieve this end, both theoretical and experimental investigations of all of the important elements of the freezing process enumerated in Table I were carried out. The experiments were carried out on a broad range of materials (metals, elemental and compound semiconductors, ionic materials, oxides and polymers) to elucidate the essential physics of the problem. Most strikingly, it was found that the phenomena differed only in degree and not in kind as one moved from material to material. This pioneering study of Crystallogenics, which is in its 6th year of AFOSR sponsorship, has led to the generation of much new understanding and documentation by over 70 scientific publications in the open literature. Since it is not possible to illuminate the impact of this work on the general area by discussing one or two highlights, let us proceed to consider some immediate applications of these studies.

At this point we must recognize that it is often necessary to depart from a well defined and purely analytical path when we are involved in generating technology. This is because, in the interesting areas of science, we never have all the relevant facts to put into our systems analysis and, for these items of knowledge, we must use empirical insight and educated guesses.

The technology problem can be likened to a golf game where one's science gets him off the tee and onto the green near the hole. If the science is very good, one finds himself very close to the hole. If it is not too good, one may find himself in the rough! However, that is as far as science takes one - it is enlightened empiricism that takes one the last step of sinking the ball in the cup (or getting a successful solution to a practical problem). In what follows, we shall see that it is often the control of the dendrite morphology that leads to a successful application.

Present Exploitation Opportunities

Technical understanding in the crystallization area nourishes at least 5 separate industries: (1) Foundry, (2) Chemical Purification, (3) Chemical Crystallizer, (4) Single Crystal and (5) Frozen Food. In this section, we

shall consider application potentials in the areas of (A) materials purification, (B) single crystal growth and (C) structure control of ingots and castings.

A. Materials Purification

From basic interface stability studies, it has become possible to quantitatively describe the freezing conditions that must be maintained for effective purification of a material by the freezing process. The interface morphologies that are of primary concern are (i) a smooth interface which leads to the minimum solute incorporation (greatest purification) and (ii) a cellular or dendritic interface (see Fig. 6) which leads to a greatly enhanced solute incorporation (greatly diminished purification).

The concentration of the solid freezing with a smooth interface is given by kC_∞ where C_∞ is the concentration of the bulk liquid and k is the effective solute partition coefficient which is related to k_o by the relationship[2]

$$k = \frac{k_o}{k_o + (1-k_o) \exp(-V\delta_C/D)} \qquad (11)$$

As $V\delta_C/D \to 0$, $k \to k_o$ and the maximum purification occurs; as $V\delta_C/D \to \infty$, $k \to 1$ and no purification occurs. Thus, in purification applications such as zone refining, one needs to stir the liquid and reduce δ_C to small values so that $k < 1$. The purification factor per pass, P, will then be given by 1/k so that $P_{max} = 1/k_o$.

The above analysis, however, applies only when the solid-liquid interface

is smooth. When the interface becomes cellular, k changes abruptly to a value close to unity (see Fig. 5). This can be understood by considering Figs. 6 and 7. The cells are like small pencils stacked together and separated from each other by a thin layer of solute-rich material. From the cross section of the cells in Fig. 7, we can anticipate that, as the radius of curvature, ρ, of the cell tip decreases, the amount of solute rejected laterally increases. This lateral solute transport is relatively uninfluenced by stirring of the bulk liquid and solute diffuses into the groove regions between the cells. Thus, although the centers of the cells are much purer than the liquid from which they freeze, the cell boundaries are much more impure. The net effect is that the total aggregate is only slightly purer than the bulk liquid from which it freezes. Thus, in many purification applications, the device design criterion must be that the freezing conditions never intrude upon that domain where the cellular interface morphology is stable.

Theoretical predictions, which have been substantiated by experiments on several metallic systems[3][4], state that a smooth interface will be stable only if the following inequality is satisfied.

$$\xi \geq -\frac{m C_\infty (1-k_o) V k}{k_o D G_L} \qquad (12)$$

where G_L is the temperature gradient in the liquid at the interface and ξ is defined as the constitutional supercooling parameter[5]. When the temperature gradient in the solid is the same as in the liquid, the interface attachment kinetics are infinitely fast and the solid-liquid interfacial energy is

zero, $\xi = 1$. In general, $\frac{1}{2} < \xi < 2$ except for optically transparent materials or for systems with very sluggish interface attachment kinetics. As the ratio of the heat transport in the solid due to radiative versus non-radiative processes increases, ξ decreases. As the interface attachment kinetics become more sluggish, ξ increases. Thus, for effective purification, one must never let P fall below

$$P^* = - \frac{m C_\infty (1-k_o) V}{\xi k_o D G_L} \qquad (13)$$

If $P < P^*$, a cellular interface will exist and P will drop to extremely small values ($\delta_C > \delta_C^*$, $k > k^*$); i.e., the design criterion must be such that $P^* < P \lesssim 1/k_o$.

Controlled freezing experiments were carried out on distilled water, tap water, $K_2C_rO_4$ solutions, NaCl solutions, milk and natural sea water at freezing rates up to $V = 10^{-3}$cm/sec. The interface was observed directly and photographed during the growth of ice via a stereomicroscope and k was found by analyzing samples of the solution and the ice. For ice grown from these solutions with a smooth interface, we found $k \sim 10^{-3} - 10^{-4}$; for ice grown from the same solutions with a cellular or dendritic interface, we found $k \sim 0.5$. In fact, a very small change in δ_C in the vicinity of δ_C^*, leads to a change in purification by a factor of 10^3 or more.

With respect to water treatment, the application areas of interest can be itemized as follows:

(a) Purification

(i) Desalination of sea water from 35,000 ppm to less than 500 ppm

(ii) Water softening of well or tap water

(iii) Demineralizing water for laboratory and industrial use

(iv) Treatment of municipal water and waste

(v) Purification of human waste as required in space travel.

(b) Concentration

(i) Removing water from aqueous solutions of volatile solutes in competition with stills

(ii) Food processing - concentrating food products without loss of vitamin content or flavor (e.g., milk, orange juice, beer)

(iii) Production of minerals such as salt, gold, etc. from sea water.

With respect to the purification of metals or chemicals, we need not limit ourselves to the small volume production of zone refining but may consider processes for the purification of these materials in tonnage quantities. Such application has already been made to the purification of aluminum and it is only a matter of equipment engineering and sufficient industrial or military interest that keeps us from extending the application to other important materials like iron, nickel, chromium, etc.

B. Single Crystal Growth

Most people realize that the science of single crystal preparation is one

of the mainstays of our materials-research effort. Our present-day electronics and space technology, with its wide spectrum of semiconductor products, depends ultimately upon the preparation of single-crystal semiconductor material. The immense effort that has been expended in developing the quality of silicon boules to their present stage of utility is well known. In less than 15 years, this silicon achievement has become standard technology in the crystal growing industry.

In this section, three crystal growing achievements that significantly extend this crystal growing technology will be discussed. Although successful single-crystal growth in these areas is intimately related to interface stability and dendrite formation, our scientific understanding only brought us close to the solution - ultimate success, as always, was a consequence of enlightened empiricism.

1. Silicon Web: an exercise in controlled dendritic growth.

Suppose we asked "How can our knowledge of dendritic growth be utilized to help build a greater materials technology than we have today?".

The first category of answers that one develops to this question is in the nature of "preventative medicine"; i.e., we can see that many material properties will be deteriorated if we allow a filamentary interface to form; thus, one's energies are expended in eliminating the environmental conditions that stabilize this morphology. This point of view applies whether we are considering semiconductor or laser crystal formation, chemical crystallizers or saline water conversion apparati. Recently, we took a more positive approach to this phenomenon and considered how it might be utilized to produce materials

in a more desirable form than hitherto possible. One great stride in this direction has been the utilization of the unconstrained crystal growth technique to produce long filaments of semiconductor crystals.

Consider the experimental set-up illustrated in Fig. 8. Here, a graphite container filled with germanium is heated with an induction coil until the Ge melts, the power input is then controlled until the liquid is supercooled by an amount ΔT. If we allowed a seed crystal of the dendrite orientation to be aligned perpendicular to the upper surface and then brought into contact with this surface, a dendrite would grow into this bath colinear with the seed crystal at a velocity V. If the seed crystal were withdrawn from the bath at a velocity V, a long continuous filament of the material having a predictable thickness could be pulled from the bath. Such a filament of Ge is being pulled from the melt in Fig. 8. For a bath supercooled by $\Delta T = 10^{o}C$, filaments of metals, semiconductors, oxides and polymers must be withdrawn at velocities of $V \sim 10$ cm/sec, $1\text{-}10^{-1}$ cm/sec, $10^{-1}\text{-}10^{-2}$ cm/sec and $10^{-2}\text{-}10^{-4}$ cm/sec respectively. The most convenient pulling velocity, in present practice, is about 10^{-1}-1 cm/sec so that the bath supercooling, ΔT, must be adjusted accordingly in order to have stable filaments of the various materials pulled from the melt in this velocity range.

Dendritic ribbons of Ge, Si and several of the III-V compounds have been pulled from the melt and some of them have been wound on large reels to lengths of several hundred feet. The surfaces of the filaments appear to be very perfect and to make ideal surfaces for semiconductor device fabrication. Electronic devices made upon such dendritic ribbons have been found to exhibit

very satisfactory electrical characteristics.

Often during the pulling of semiconductor dendritic ribbons it was observed that two ribbons would grow side by side and, at the lower pulling velocities, a sheet of liquid was pulled from the melt and held between the dendrites by surface tension forces. In the beginning, this was a nuisance for those studying ribbon formation; however, soon certain application-minded individuals recognized the potential of using the dendritic ribbons only as guiding edges for the formation of a sheet of semiconductor between these ribbons. It then seemed possible to pull sheets of semiconductor of controlled thickness with widths of 1-2 cm rather than widths of about 0.1 cm as obtained for the dendritic ribbons.

In Fig. 9, it is illustrated that the edge dendrites grow below the surface of the supercooled melt while the sheet grows above the normal melt surface. As the dendrites are pulled upward, molten material is drawn up by surface tension, the height of the freezing interface depending upon the furnace parameters (ΔT and pull rate). Surface features and the internal structure of sheets suggest that freezing at the interface takes place by a process similar to normal crystal growth. The edge dendrites, besides being necessary for growth of sheets of constant thickness, serve also to give stability to very thin sheets. Flat sheets can be pulled much thinner than dendrites and, as the pull rate decreases, the sheet thickness increases towards the dendrite thickness. Actually, they can be grown thicker than the dendrites but with more rounded surfaces.

After a suitable development study, extremely long continuous sheets

of Ge and Si with widths up to 2 cm at thicknesses of 0.5-35 mils were grown. This material was single crystal in structure with extremely low dislocation content normal to the surface and the surfaces were of such perfect character that they could be used without further treatment for device fabrication. On both Ge and Si, diodes, transistors and PNPN devices have been fabricated and on Si, unique large area solar cells have been constructed. The solar cell application affords a unique opportunity for the use of such silicon web.

2. Large Selenium Single Crystals: an exercise in high pressure technology.

Selenium is an elemental semiconductor that has heretofore been available in crystalline form only as extremely small single crystals. This is because, at one atmosphere pressure, the Se molecule is a polymer in the liquid state and the molecules in the medium ahead of the growing crystal are in the form of chains of varying lengths which exhibit various degrees of entanglement with other molecules. The equilibrium chain length at 217°C (melting point for 1 atm pressure) is greater than 5000 Se atoms long. Such long chain materials generally exist as solids only in the glassy state or in the form of small spherulite crystals (see Fig. 1). These states of aggregation are not desirable for utilization of selenium's semiconducting properties.

One basic requirement to be satisfied before one can grow large Se crystals is that the environmental conditions must be such as to reduce the interface attachment kinetic and transport problems. This may be achieved by either growing the crystals under conditions of much reduced chain length or by growing the crystals from a dilute solution in simple solvents. In either case, the chain entanglements are greatly reduced. A second basic requirement is that

the crystal must be grown under conditions of V and G_L such that a smooth interface morphology is stable (see eq. 12).

Knowing that the chain length of liquid Se is strongly reduced as the temperature is increased, and that the crystallization temperature increases with increase of pressure, we chose the former method for growing our crystals. Increasing the pressure of argon over a Se melt to 6000 atmospheres increases the melting temperature from 217°C to 338°C and reduces the chain length by about an order of magnitude. This decrease in chain length is such that Se crystals can be grown 3 orders of magnitude faster than at 1 atmosphere pressure.

Single crystals of Se, 1 cm in diameter and 10 cm long were grown in an open quartz vial within a stellite pressure bomb[6]. Both the temperature and pressure were controlled in such a way that the rate of freezing was typically 10^{-5}cm/sec, with an essentially smooth interface. These crystals have now been made widely available for property studies in the U. S. and Europe.

From this study on the growth of selenium crystals, it seems likely that a new dimension has been added to our crystal growing technology; i.e., the pressure field. It seems very likely that the pressure variable may be useful in obtaining crystals of other materials with polymeric melts. Of course, the chain length in typical polymers like polyethylene and related compounds is considerably greater than that of selenium and the problem of growing large single organic crystals is thus much more formidable. However, it does appear that the use of elevated pressures is a step in the right direction even for these materials.

3. Large Sapphire Single Crystals: an exercise in high temperature technology.

In the past, sapphire and ruby crystals have been grown by the flame fusion technique; however, we felt that this technique was basically limited in

capability. We thus proceeded to develop the more difficult but ultimately more controllable technique of Czochralski crystal pulling which has been so successfully used for growing large silicon crystals.

Crystal pulling of silicon occurs at an interesting temperature level; i.e., thermal radiation is just beginning to become important as a heat transport mechanism. However, the dominant heat transfer mechanisms are still conduction and convection and the controlling technology of the crystal's growth are consistent with the previous experience. The experiments with sapphire moved us into a new domain of experience where the dominant heat transport mechanism is by radiation. Further, the crystal is largely transparent to this thermal radiation so that surface distortions and reflections begin to play a significant role in the attainment of successful crystal growth.

A variety of unexpected difficulties beset our efforts largely because our idealized theoretical and empirical understanding were significantly stretched by working in this new environment (2100°C - 2300°C). We found unanticipated natural convection phenomena occurring in our melts, dileterious chemical reactions between the various components of the system and severe temperature instabilities due to the fast thermal response between the crystal-crucible-heater-radiation shield system. More fundamentally, we began to appreciate the importance of the temperature distribution in the crystal upon the interface instability phenomenom. Because of the crystal's transparency and our method of growth, only shallow temperature gradients existed in the crystal. This decreased ξ in eq. 12 by a large factor and made it more difficult to get smooth interface growth.

Continued effort, however, finally allowed us to resolve the difficulties of this new thermal environment and large single crystals of

sapphire and ruby have been produced. From optical examination, these crystals appear to be of the best quality ever produced in these materials (comparable to that of interferometric quality glass) to date/and they will find an immediate utility in semiconductor substrate, acoustical delay line and laser applications. The presence of only a single fringe in a 3 inch length of ruby indicates a degree of chemical and strain homogeneity which is almost unheard of in such materials. Finally, having overcome the challenge of the thermal radiation environment opens the door to extending this single crystal technology above the 2150°C operating temperature for Al_2O_3 to the 3000°C range - and beyond.

C. Structure Control of Ingots and Castings

In the recent past, new devices have appeared on the industrial scene which control the chemistry of the melting and casting processes, i.e., vacuum arc melting, vacuum freezing, etc. Today, as a result of our detailed understanding of the freezing process, we are ready to take the next logical step of developing devices and processes for the control of the structure of ingots and castings.

To gain a satisfactory measure of ingot structure control, we will need the invention of devices which may be imposed on a mold and which are capable of (i) dominating the existing macroscopic variables and fulfilling their function and (ii) allowing a continuous range of variability and controllability of the new "effective" macroscopic variables. Only then can we control the microscopic or interface variables in such a way as to control the ingot structure.

The physical principles upon which such devices may be based have been available for a long time; however, it is only recently that our fundamental experiments have allowed this fact to be recognized. From our experiments, one

class of devices can be conceived which consists of suitably arranged coils for the application of electromagnetic power to the liquid metal. By the intelligent application of electromagnetic power, it is possible to generate eddy currents both in the outer skin of the metal and deep within the mold. In this way, it is possible to control the rate of heat flow in the mold, the effective superheat of the melt and the fluid motion in the melt in a continuous fashion. Being essentially electronic in nature, such devices would be ideally suited for automation.

In order to appreciate the benefits to the structure and homogeniety of ingots and castings that derive from proper electromagnetic stirring, let us consider some simple experiments carried out on tin-lead alloys and our theoretical understanding of the results.

The first direct laboratory experiment was carried out about 5 years ago on 250 gram samples of Sn - 1.35 wt% Pb alloys in the apparatus of fig. 10 [7]. The samples were contained in a quartz tube, heated to above the melting temperature, electromagnetically stirred with 3 Ø-400 cycle power by the coil indicated and cooled in place until the onset of freezing was recorded by the thermocouple at which time, the sample was rapidly quenched. The mode of stirring was such as to cause the fluid to move vertically upwards along the outside of the sample and vertically downwards along the center line of the sample or vice versa. The major effect of the stirring was to produce a greatly refined grain size in the cast sample. This is illustrated in fig. 11. The following important observations were made with respect to this grain refinement: (i) it was only necessary to stir the liquid during that portion of the cooling curve associated with recalescence of the melt ; ie. just after the first nucleus of solid had formed,

(ii) for a particular bath undercooling, ΔT, at which nucleation of the solid occurs, a critical magnetic stirring field strength, H_c, exists for which the number of grains per unit volume increases abruptly by factors of 10^4 - 10^5 (see figs. 12 and 13) and (iii) one finds that H_c and ΔT are related in the following way

$$H_c \, \Delta T \approx \text{constant} \qquad (14)$$

It was first thought that the stirring was somehow influencing the nucleation process; however, further experiments in a modified apparatus of fig 10, showed that we were dealing with a crystal multiplication phenomena.[8] This modified apparatus was designed to introduce one or a number of tiny crystals of tin to the bath at a particular ΔT. By operating at values of ΔT less than that at which the bath would normally nucleate and introducing only one crystal of Sn, we were able to produce the identical results found in the earlier experiments. Thus, the introduction of 1 seed crystal into an electromagnetically stirred bath, leads to a shower of individual growth centers that originated from the initial seed. This is why the effect has been termed the "Shower Effect".

These experiments have been extended to larger samples (2 lbs) with identical results except that H_c decreases in magnitude by a factor of 4-5. On unstirred melts, a small crystal multiplication effect is present suggesting that some natural convection is present in the melt. On pure melts, stirring leads to some grain refinement but the grain size is limited by recrystallization and grain growth. Finally, high temperature stirring devices have been operated on Fe and Ni base alloys with molybdenum as the prime alloying constituent. Here, the heating is by R.F. power and the stirring is by 400 cycle power. The shower effect has been found in these systems also.

Our theoretical understanding of this "shower effect" phenomena is based upon the analysis of the growth of a crystal in this supercooled bath of liquid as discussed in the early portion of this paper. The crystal develops the dendritic morphology very early in its growth period and a network of primary, secondary and tertiary branches ensues so that a dendrite raft structure like that illustrated in fig 14 should be found. The questions that we ask are (1) what is the effect of recalescence upon the integrity of this raft structure, (2) what is the effect of fluid motion on this raft structure and (3) in the fresh, hot-worked solid (by fluid convection), what are the kinetics of recrystallization and grain growth?

The generation of multiple grains from one seed can occur via two separate paths both depending upon the operation of two sequential events. On the first path the separation or segmentation of an enlarging dendritic array into several pieces occurs by a natural recalescence phenomenon and the misaligning of these segments with respect to crystallographic orientation of the primary stalk occurs by fluid body forces. On the second path, no segmentation occurs but the array collapses into a bent and distorted raft by the action of fluid body forces. and new grains are formed in this hot-worked material by recrystallization. Thus, the probability, P_G, of obtaining a new grain by each of these paths is given by the product of two probabilities; (a) Path I - the probability, P_s, of segment formation and the probability, P_R, of segment rotation by a significant amount, (b) Path II - the probability, P_R of significant raft distortion and the probability, P_r, of recrystallization occurring during the cooling path; i.e.,

$$P_G = P_s P_R + P_B P_r \qquad (15)$$

Semi-quantitative evaluation of each of these factors has been carried out

and the results are found to be in good qualitative agreement with the experimental observations. We now are in a position to make intelligent guesses concerning the material systems that should exhibit this phenomenon plus the relationships between the number of grains formed per unit volume and the constitutional, thermal and hydrodynamic conditions in the system. The stage is thus set for intelligent engineering application of this phenomenon and this knowledge.

In conclusion, the results of our crystallogenics studies reinforce the postulate that a well-organized base of scientific understanding in an area leads to the most efficient and probably the most effective engineering application in the area. Further, in the crystallization area, a sufficiently strong base of scientific understanding now exists that the next ten years will produce many significant technological applications of this science.

TABLE I

Crystallization Variables and Parameters

Areas of Study	Boundary-Value Problems	Material Parameters	Interface Variables	Macroscopic Variables	Constraints
Phase Equilibria		ΔH, T_o, k_o, m_L		$T_L(C_\infty)$	
Nucleation		N_o, ΔT_c		t	
Solute Partitioning	Diffusion Eq. (C)	D_S, D_L, k_i	C_i, $T_L(C_i)$ V, S	C_∞	
Fluid Motion	Hydrodynamic Eq. (u)	ν	δ_C	u_∞	C_∞
Excess Solid Free Energy		γ, ΔS, $\sum_i \gamma_i^f$, $\sum_i N_i^f$	T_E		$\dot{T}$
Interface Attachment Kinetics		μ_1, μ_2			
Heat Transport	Heat Eq. (T)	K_S, K_L, α_S, α_L	T_i	T_∞	
Interface Morphology	Perturbation Response and Coupling Eqs.				
Defect Generation	Stress Eq.				

ΔH - latent heat of fusion; T_o - melting temperature of solvent; k_o - solute distribution coefficient; m_L - liquidus slope; N_o - parameter related to area of nucleation catalyst surface; ΔT_c - parameter related to potency of nucleation catalyst; k_i - interface partition coefficient; D - solute diffusivity; ν - kinematic viscosity; γ - solid/liquid interfacial energy; ΔS - entropy of fusion; γ_i^f - fault energy; N_i^f - number of faults of type i; μ - parameter related to interface attachment kinetics; K - thermal conducitivity; α - heat diffusivity.

BLANK PAGE

References

1. B. J. Piearcey and F. L. Versnyder; "A Breakthrough in Making Turbine Components - Directional Solidification and Single Crystals", Metal Progress, November 1966, p 66.
2. W. G. Pfann; "Zone Melting" (John Wiley and Sons, Inc., 1958).
3. W. A. Tiller, K. A. Jackson, J. W. Rutter and B. Chalmers; Acta Met. 1, 428 (1953).
4. W. A. Tiller; "Solidification" in "Physical Metallurgy, North-Holland Publishing Co., 1965 (edited by R. W. Cahn).
5. L. Tarshis and W. A. Tiller; J. Phys. Chem. Solids, 1967 (the 1966 I.C.C.G. Proceedings Issue).
6. D. E. Harrison and W. A. Tiller; J. App. Phys. 36, 1680 (1965).
7. W. C. Johnston, G. R. Kotler and W. A. Tiller; Trans. AIME 227, 890 (1963).
8. W. C. Johnston, G. R. Kotler, S. O'Hara, H. V. Ashcom and W. A. Tiller; Trans. AIME 233, 1856 (1965).

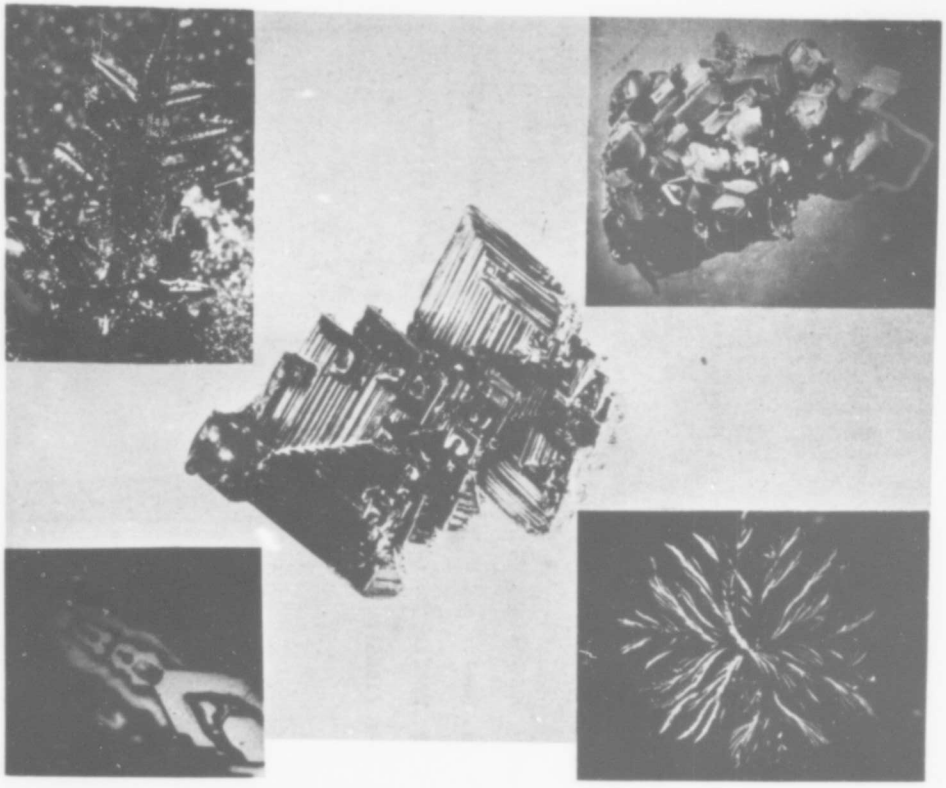

Fig. 1. Photographs of various crystal growth forms:

Center - bismuth hopper crystal grown from the melt

Upper left - chromium dendrite grown from the vapor

Upper right - gallium phosphide crystal grown from an alloy melt

Lower left - silver dendrite grown by electrodeposition

Lower right - spherulite grown from a blend of 40% isotatic polypropylene and 60% atactic polypropylene.

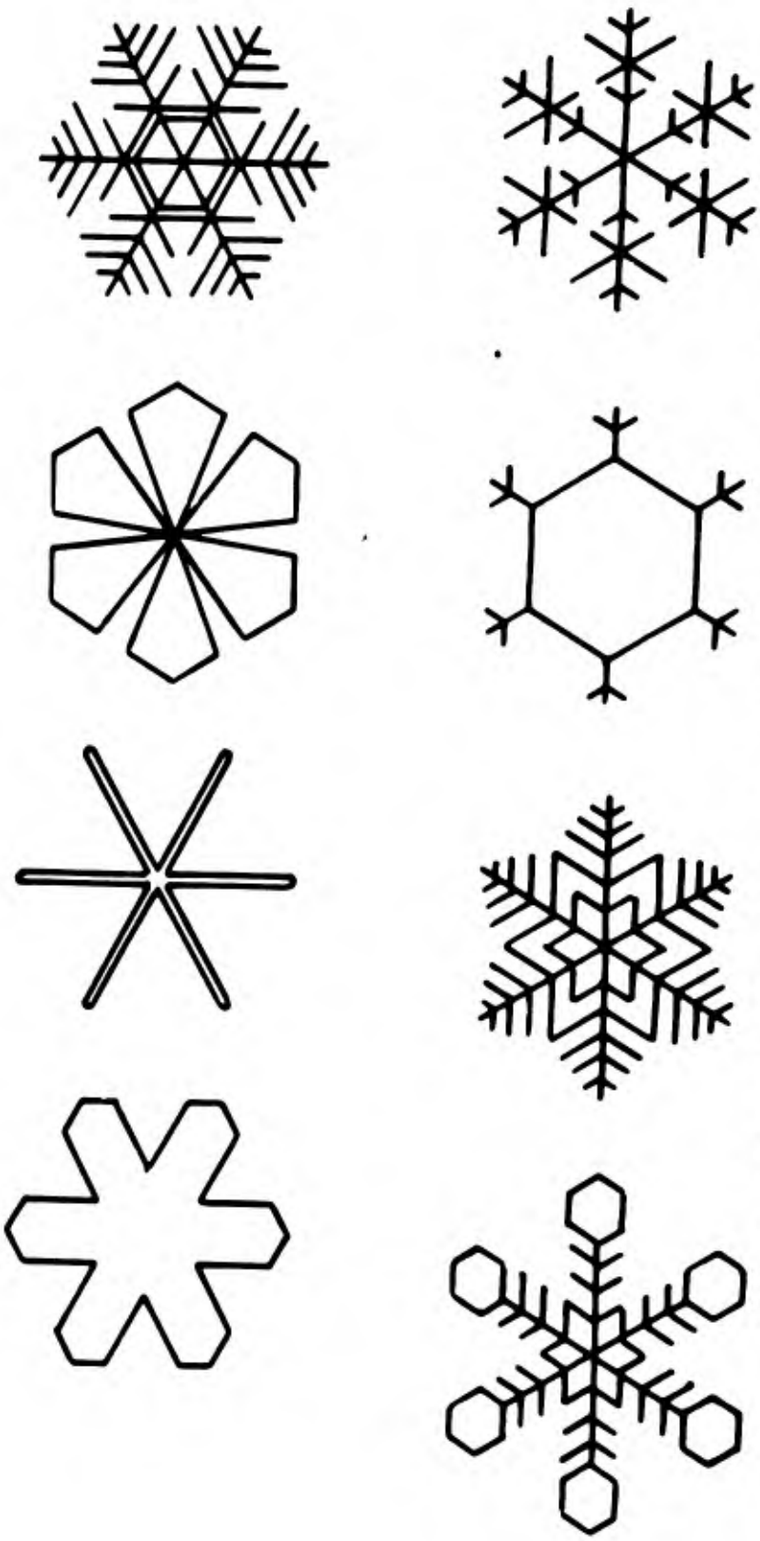

Fig. 2. Schematic illustration of Nakaya's eight snow crystal types.

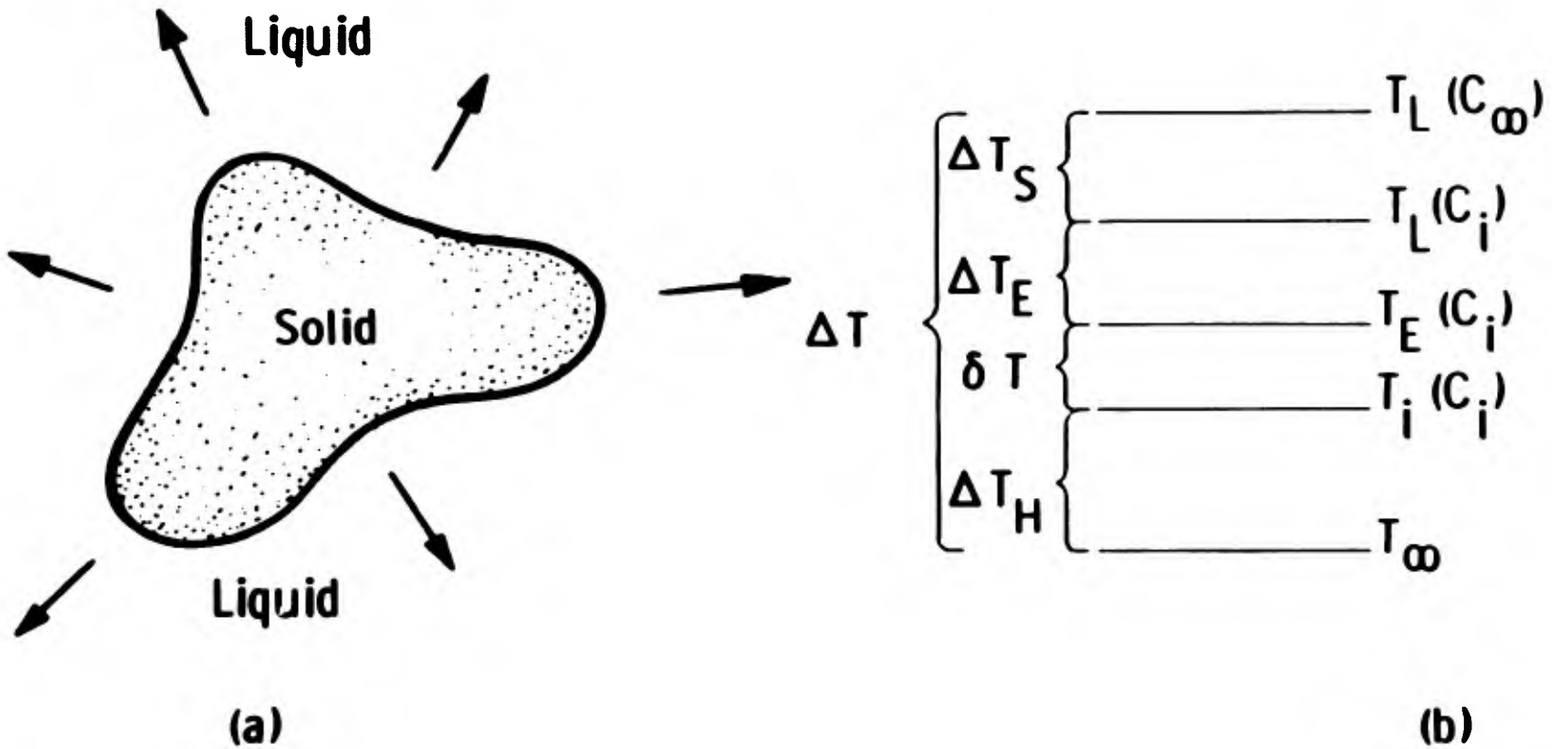

Fig. 3. (a) Illustration of a crystal growing from a supercooled liquid

(b) The important temperatures in a growth process; the magnitudes of the temperature differences indicate the degree of solute diffusion, capillarity, kinetic or heat transport control.

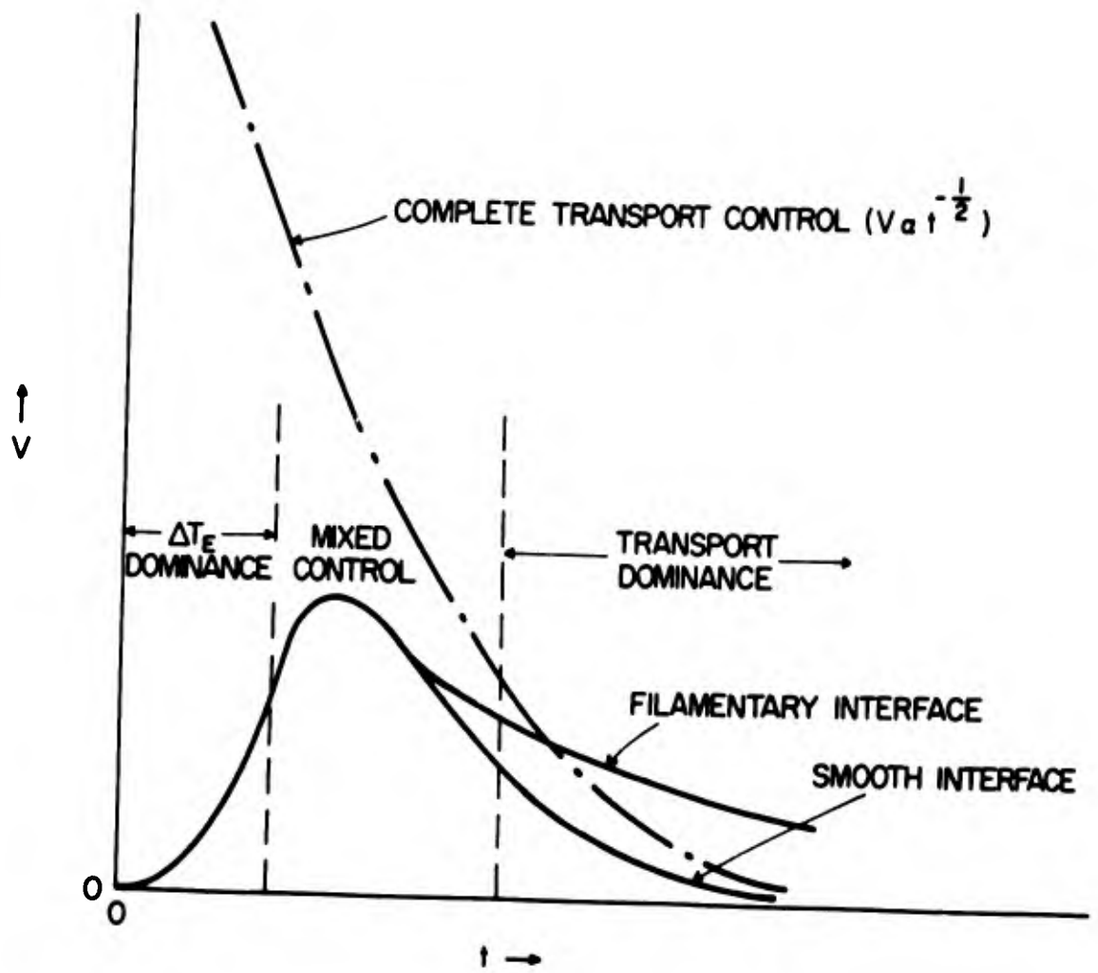

Fig. 4. Schematic of particle growth velocity, V, versus time, t, illustrating the regions where various mechanisms are dominant.

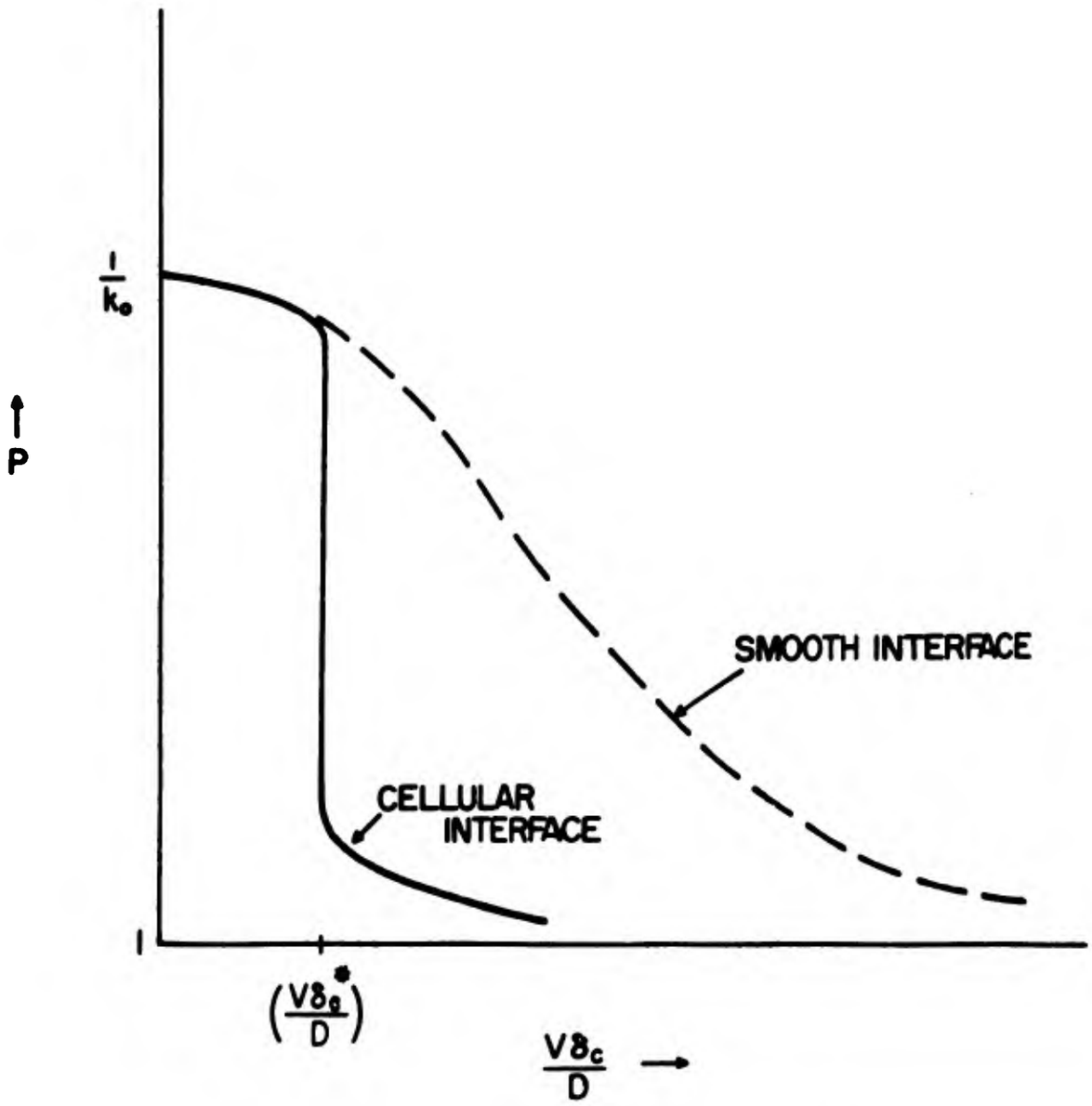

Fig. 5. Schematic variation of purification per pass, P, as a function of the combined stirring and growth parameter $V\delta_C/D$.

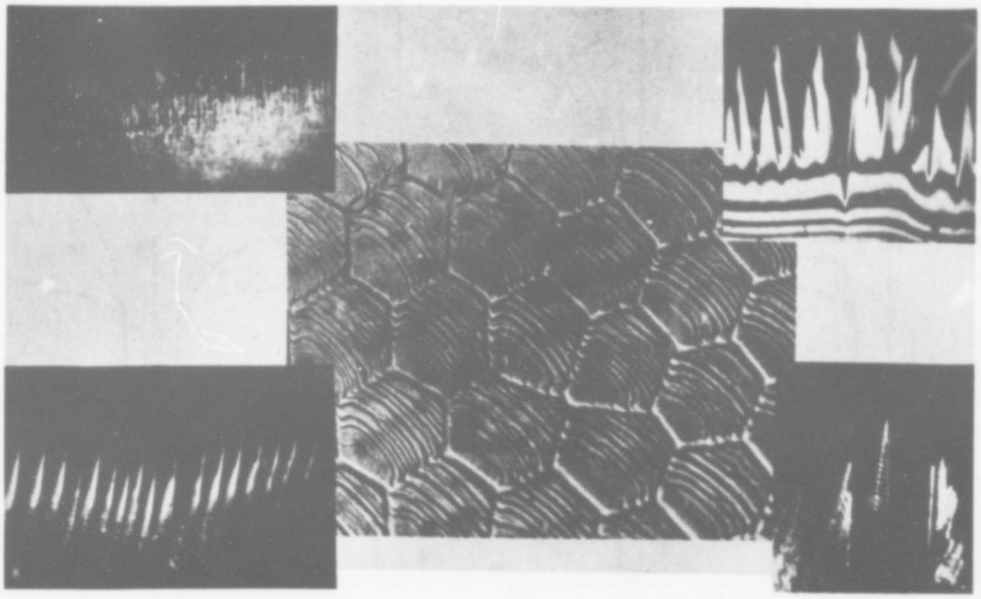

6. Filament and dendrite formation during constrained crystal growth: Center - photomicrograph of a decanted interface of a lead crystal solidifying from a Pb + 5 x 10^{-4} wt % Ag melt; Upper right - ice bicrystal grown from very dilute HCl solution taken with polarized light; Lower right - direction observation of dendrite formation in ice; Upper left - filament growth at an interface (K_2CrO_4 solution); Lower left - onset of side branch development on ice filaments (2 AT % NaCl solution).

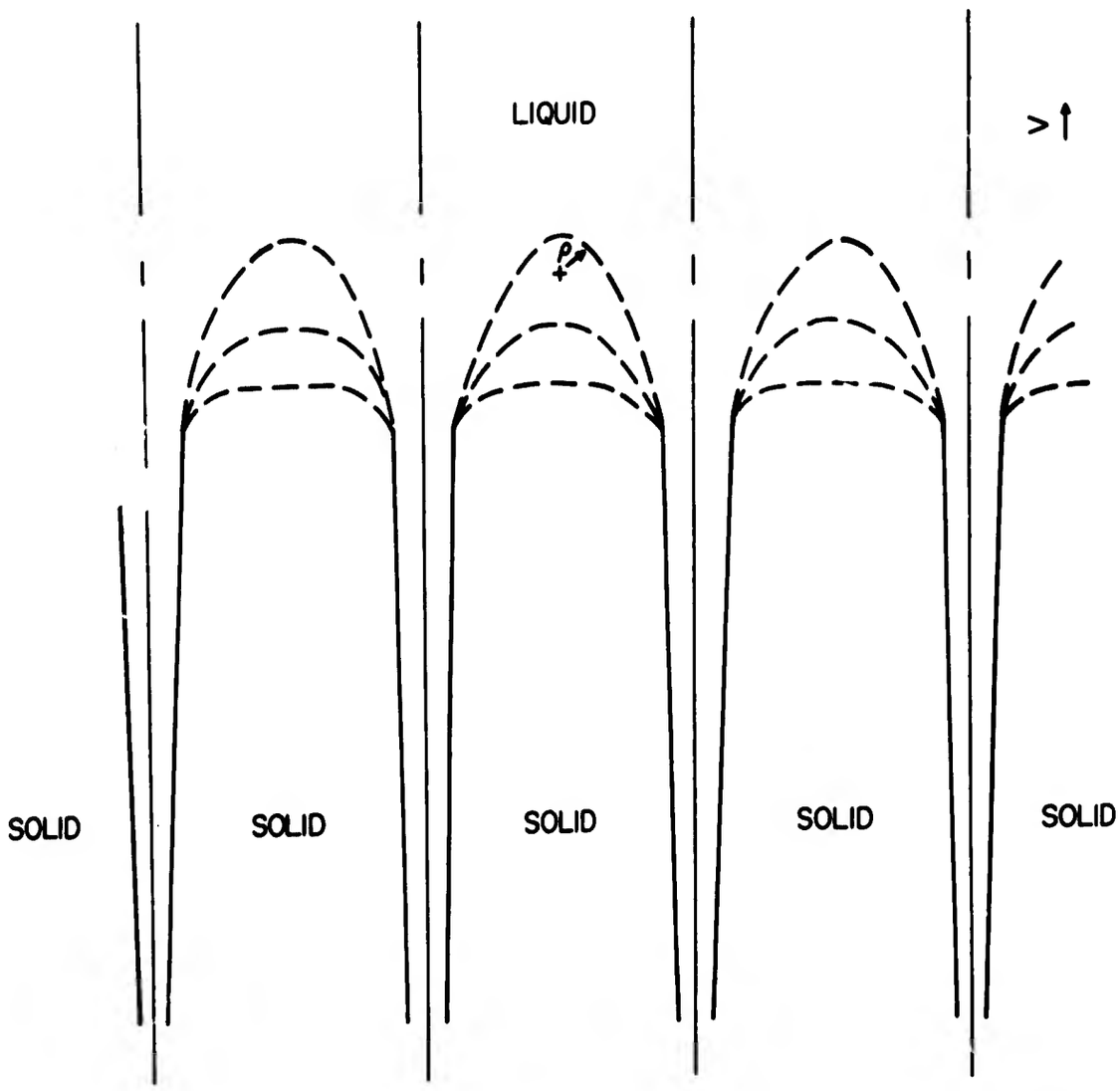

7. Schematic of cell cross-section illustrating the increase in lateral diffusion as the radius of curvature of the tip, ρ, decreases.

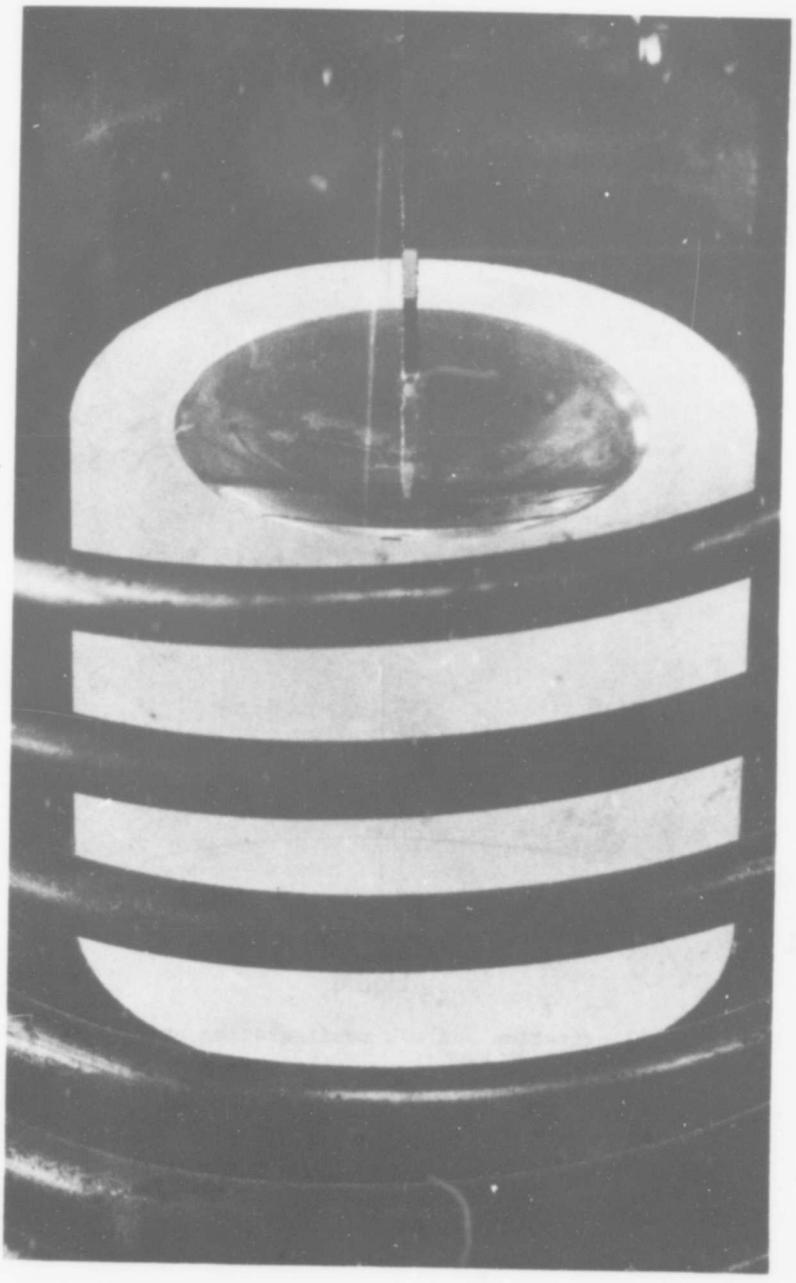

8. Photograph of actual germanium dendrite pulling operation.

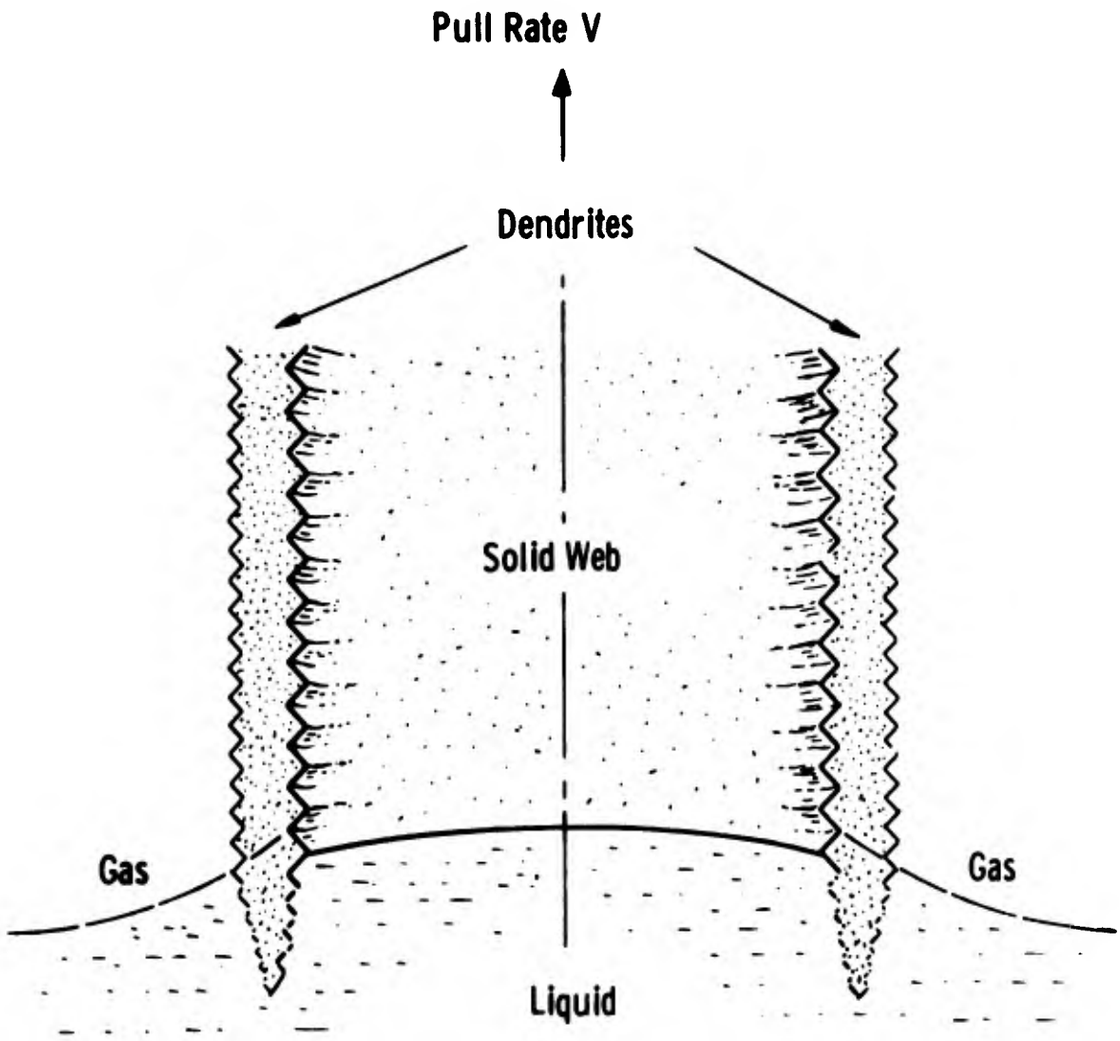

9. Schematic illustration and web configuration utilized in the continuous pulling of web material.

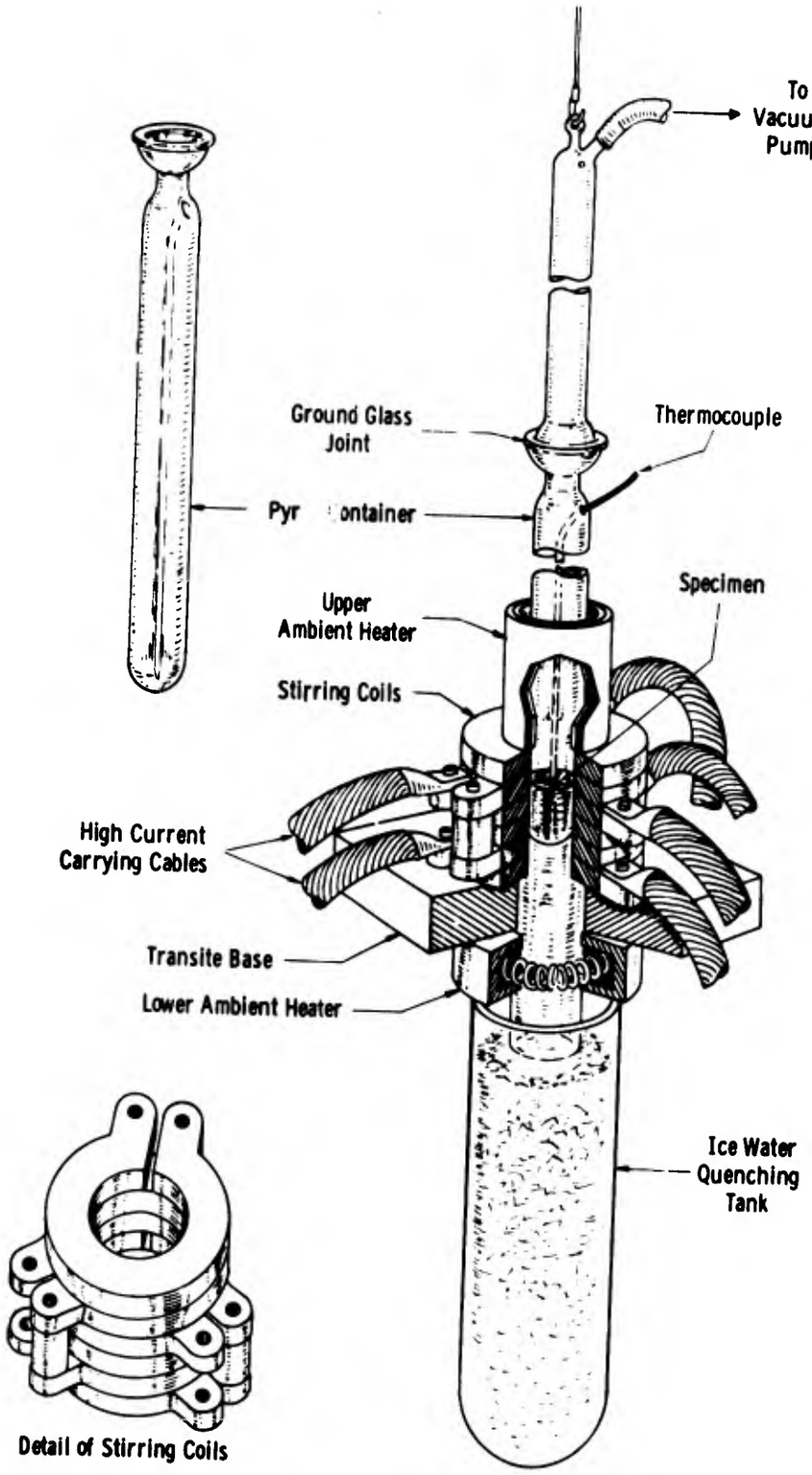

10. Experimental apparatus showing sample container, electromagnetic coil configuration and quenching tank.

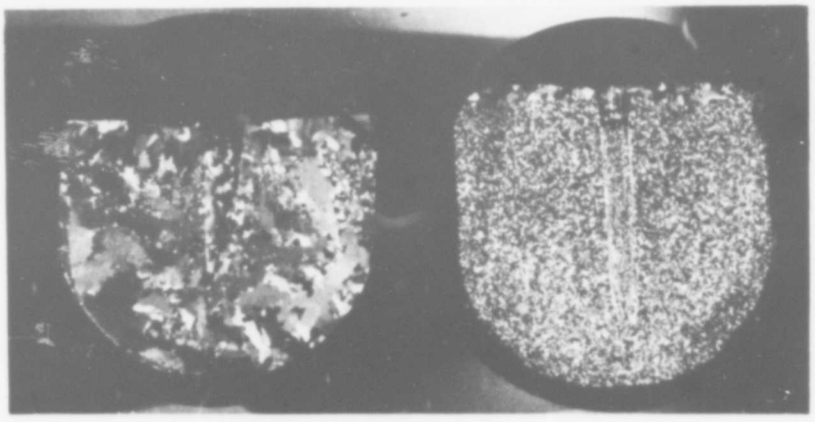

11. (a) Sample of tin alloy, unstirred

(b) Sample of tin alloy, stirred.

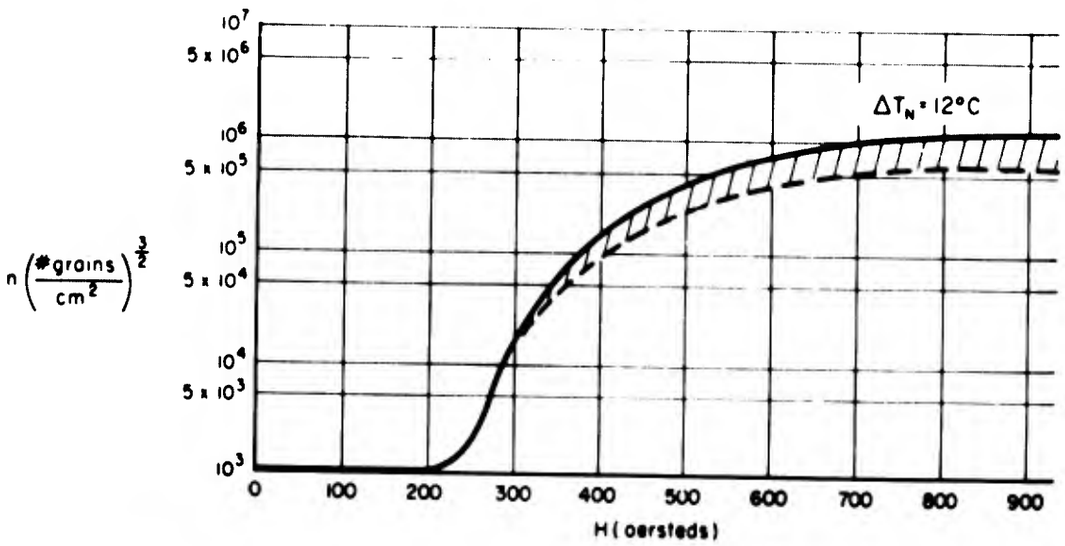

12. The logarithm of the grain number, n, vs the undercooling, ΔT_N, at constant field strength, H.

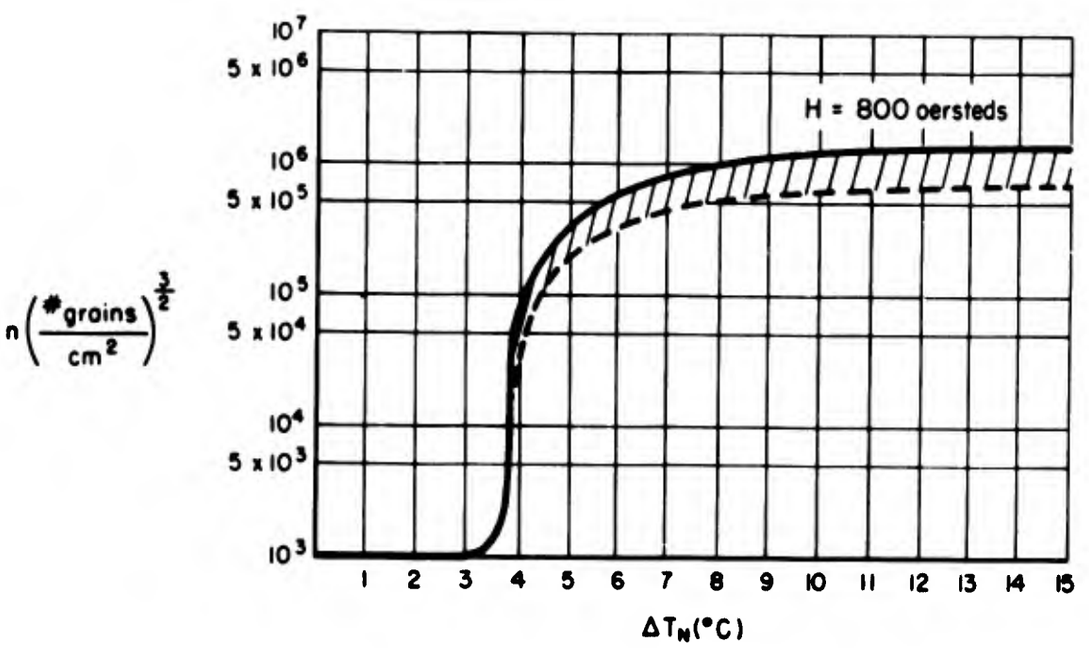

13. The logarithm of the grain number, n, versus the field strength, H, at constant undercooling, ΔT_N.

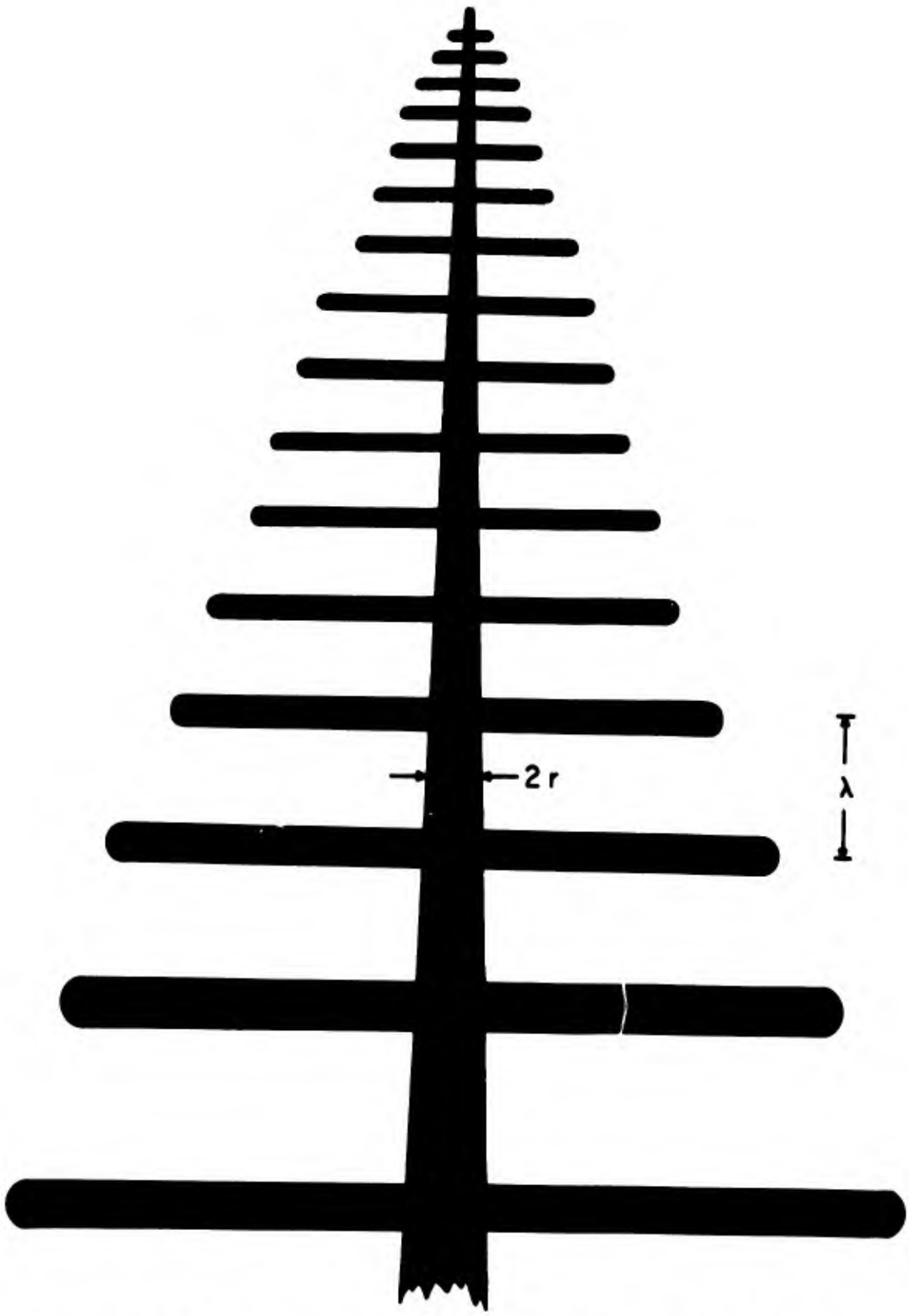

14. Model of a portion of a dendrite raft for an f.c.c. metal.

Dr. Robert G. Dunn is Assistant Director of the Fluid Dynamics Facilities Research Laboratory, Aerospace Research Laboratories, and Chief of the ARL Facilities Research Branch. He is responsible for planning and conducting research involving the investigation of advanced-facilities concepts in the aerosciences area. Dr. Dunn received his B.S. degree in Chemical Engineering from Louisiana State University in 1942, his M.S. degree from Ohio State University in 1949, and his Ph. D. degree from the same university in 1964. He is a member of Phi Lambda Upsilon, Tau Beta Pi, Alpha Chi Sigma, the American Institute of Chemical Engineers, and the American Chemical Society.

(U) SUPERSONIC COMBUSTION SIMULATION

ROBERT G. DUNN
FLUID DYNAMICS FACILITIES RESEARCH LABORATORY
AEROSPACE RESEARCH LABORATORIES
OFFICE OF AEROSPACE RESEARCH
WRIGHT-PATTERSON AIR FORCE BASE, OHIO

ABSTRACT

A facility developed at the Aerospace Research Laboratories for simulating conditions in the combustor region of a high Mach number ramjet engine is described, and the ranges of specific parameters which can be duplicated are discussed. A parallel analytical investigation, made to define the laboratory conditions required for adequate simulation of supersonic combustion for high Mach number flight over a wide range of operation, blanketing the flight corridor in the Mach 10-14 region, is also described. This method of simulation makes possible basic investigation of supersonic combustion for hypersonic flight under conditions approaching those of actual flight. Results obtained in the early experiments are presented.

INTRODUCTION

The fact that supersonic combustion offers a strong potential as a propulsion mode for ramjet operation at hypersonic flight speeds formed the basis for initiation of the work reported here. The recognition that extensive studies in ground-test facilities are necessary if scramjet technology is to advance rapidly provided the real impetus for pushing ahead in this project as fast as possible.

As the flight speed of vehicles in the earth's atmosphere has increased, the problems encountered in providing adequate and realistic ground test facilities have rapidly increased also. For subsonic vehicles and

engines, the solution of these problems represented a relatively small part of the overall task; however, in the supersonic and hypersonic regimes, the technical and scientific efforts needed to create the test equipment have become comparable with those related to the engines themselves.

Existing test facilities are not capable of providing continuously the conditions required for complete duplication of a vehicle's environment at the higher hypersonic Mach numbers. On the other hand, continuous-type test facilities--those providing seconds as opposed to milliseconds of testing time--are required for the investigation of certain time-dependent aspects of supersonic combustion. In order to provide a suitable facility within the present state-of-the-art, therefore, it is necessary to simulate rather than duplicate the appropriate flight parameters.

Investigation of the supersonic combustion simulation problem as related to scramjet operation was undertaken in the Aerospace Research Laboratories in mid-1965. In one phase of this investigation a simulation technique was developed, defining the laboratory conditions required for the simulation of supersonic combustion for high Mach number flight. In a second and parallel phase an experimental facility for conducting laboratory tests based on this simulation technique was developed. Both the simulation technique and the experimental facility are described briefly in this paper.

The first hydrogen-air supersonic combustion experiment in the new ARL simulation facility was conducted in early August 1966. A number of successful tests have been made since that date, although many of these necessarily were "shakedown" runs directed toward solution of facility development problems. Experimental data on auto-ignition limits for hydrogen-air combustion, obtained in the initial series of tests, are presented and discussed.

THE SIMULATION TECHNIQUE

The type of simulation under investigation in ARL is described fully in Reference 1 and summarized below. In this treatment the flow Mach number in the combustor is

not considered to be an important parameter such as is the case in the usual aerodynamic investigation. That is, the combustor entrance Mach number in the laboratory need not be the same as that in the flight case (subject to certain limitations pointed out later in this section).

In the supersonic combustion problem as applied to the scramjet, the chemical composition of the flowing medium, the mixing of the streams of fuel and air, the chemical reactions taking place, and the reaction rates involved are the important factors to be considered. Investigation of the chemical aspects (composition, reactions, reaction rates) requires that the laboratory experiments be run under the same static pressure and temperature conditions as in the flight case, and also that the residence time in the combustor be the same. In the simulation technique described here, the flight parameters not duplicated in the laboratory are the absolute velocities (and hence the Mach numbers also) of the fuel and air streams; however, these velocities may be chosen such that the mixing time in the laboratory is nearly the same as that in flight.

In summary, the primary parameters requiring actual duplication in the laboratory in this technique are the static temperature, static pressure, composition of the gases, residence time in the combustor, and the velocity relationship between the mixing streams. These parameters can be duplicated in the laboratory experiments without necessarily duplicating the absolute values of velocity of the two streams of fuel and air; the length of the combustor and the velocity then become scaling factors.

The flow regions for the flight and laboratory cases are illustrated schematically in Figure 1. With reference to Figure 1a, the airflow at Station 1 relative to the vehicle is hypersonic. The flow is decelerated through the inlet region to a lower but still supersonic Mach number at Station 3, the entrance to the combustor. In Figure 1b, Station 2 represents the laboratory air stagnation region. In this case, the airflow is accelerated in a nozzle from Station 2 to Station 3 to obtain the desired combustor inlet conditions. At this point, the fuel (gaseous hydrogen) is concentrically injected parallel to the airstream.

Certain limitations of this technique should be noted in addition to the requirement indicated above concerning a velocity relationship between the mixing streams. The wall effects in the laboratory will not be identically the same as in flight since the stream velocities are not duplicated. Also, three-dimensional effects in the combustor must be taken into account if the air and fuel streams are not arranged axisymetrically for both the flight and laboratory cases as described in this paper. Even with these limitations, however, it is felt that this simulation technique can provide valuable basic data applicable to the high Mach number flight case.

The flight conditions considered in Reference 1 for simulation in the laboratory are those for continuous flight speeds near Mach number 12. The small circles shown on the curves in Figure 2 indicate the points for which flight conditions were calculated. These points were chosen to blanket the continuous flight corridor in the range of Mach numbers 10 to 14.

Figure 3 shows the isentropic stagnation conditions for the flight case as calculated in Reference 1. These data were needed for the calculation of combustor entrance conditions for the flight case. Also, this graph reveals the extreme values of stagnation pressure and temperature which would be required in a ground test facility for duplication of flight conditions. In Figure 4, typical combustor entrance conditions for the air in the flight case are shown.

By the appropriate choice of combustor entrance Mach number and stagnation conditions in the laboratory, the combustor entrance static conditions for a hypersonic vehicle flying at altitudes of 100,000-200,000 feet can be duplicated. Typical combustor entrance conditions for air in the laboratory case are presented in Figure 5.

For comparison of typical flight and laboratory conditions at the combustor entrance, a numerical example is given in Table 1.

Table I. Comparison of Flight and Laboratory Conditions at the Combustor Entrance

FLIGHT MACH NUMBER = 12 ALTITUDE = 140,000 FEET		
	FLIGHT	LABORATORY
Static Pressure of Air	2.0 Psia	2.0 Psia
Static Pressure of H_2	2.0 Psia	2.0 Psia
Static Temperature of Air	2000°R	2000°R
Static Temperature of H_2	1500°R	1500°R
Mass Fraction (H_2)	0.0108	0.0108
Velocity Difference (H_2-AIR)	1780 Ft/Sec	1780 Ft/Sec
Velocity of Air	11,710 Ft/Sec	5,420 Ft/Sec
Velocity of H_2	13,490 Ft/Sec	7,200 Ft/Sec
Mach Number of Air	5.5	2.5
Mach Number of H_2	1.87	1
Reynolds Number of Air	1.1×10^6/Ft	0.5×10^6/Ft
Reynolds Number of H_2	2.8×10^5/Ft	1.5×10^5/Ft

THE EXPERIMENTAL FACILITY

Paralleling the development of the simulation technique just described, a study was made to determine the feasibility of utilizing the major components of one of ARL's hypersonic wind tunnels for investigations based on this technique. This study led to the development of a flexible experimental facility suitable for basic supersonic combustion investigations applicable to high Mach number flight. A brief description of this new facility, now in operation in ARL, is given below; additional details and discussion of the problems encountered during development are reported in Reference 2.

The initial simulation point for the ARL facility was chosen to be in the high Mach number range of current interest for scramjet operation and at about the middle of the continuous flight corridor. The point selected for simulation is indicated by a double circle in Figure 2 and also in Figure 3 and corresponds to a flight Mach number of 12 at an altitude of 140,000 feet.

The basic facility before modification, known as the 30-Inch Hypersonic Wind Tunnel, is described in detail in Reference 3. It consisted essentially of a 3000-psia air storage system; a methane-gas-fired, ceramic, storage heater for heating air to 4000°R; a hypersonic nozzle; and a pressure recovery system. The latter system is composed of a diffuser, heat exchanger, and three stages of vacuum pumps operable in several configurations.

The modification of the facility for supersonic combustion simulation involved removal of some major components and addition of several new items, with most of the original facility remaining in use. The modified configuration is shown in Figure 6. The original stilling chamber and hypersonic nozzle were removed. New components are the hydrogen storage and control system, hydrogen heater, hydrogen injector and air/hydrogen nozzles, additional air control system, combustion chamber, and modified exhaust system.

Early in the project a decision was made to develop a special hydrogen heater for the facility, capable of heating hydrogen to 2500°R at subatmospheric pressures

and at mass flow rates up to 0.04 lb/sec (power input approximately 300 kw). A study of various heating methods led to the development of an electrical-resistance-type heater with the hydrogen gas passing directly over the elements. The reducing atmosphere of hydrogen permitted the use of molybdenum wire for the heater elements. Complete details and design characteristics are given in Reference 4. Many of the details can be seen in the cross-sectional view presented in Figure 7. A hydrogen temperature of 3100°R at a mass flow rate of 0.016 lb/sec has been achieved with this heater.

The most formidable materials problem was posed by the hydrogen injector, since its outside surface is exposed to air at temperatures up to 4000°R. The solution involved use of a molybdenum injector with the exterior surface coated with molybdenum disilicide, which greatly reduces the oxidation rate.

The external surface of the hydrogen injector and the inner surface of the constant area duct upstream of the combustion chamber (Figs. 7 and 8) form the walls of the air nozzle. The inner surface of the hydrogen injector forms the hydrogen nozzle. The nozzle exit Mach numbers in the initial design are 2.53 for the air and 1.0 for the hydrogen.

The combustion chamber is a constant area duct for the first two feet and then expands thirty percent in area over the remaining three feet. (Figure 8). Material used was 316 stainless steel. The air nozzle and combustion chamber are fitted with static pressure ports and the chamber is also provided with heat transfer gauges and observation ports at intervals along its length. The ports permit the use of optical diagnostics or the insertion of traversing probes for making impact pressure, total temperature and composition surveys. A high-speed computer program developed by the General Applied Science Laboratories, Inc. was utilized for determining the inner contour of the mixing and combustion chamber and for computing conditions expected throughout this section during supersonic combustion experiments. This program takes into account the combined effects

of multi-dimensional aerodynamics, diffusion processes and finite rate chemistry.[5]

One of the prime considerations in developing this simulation facility was the safety hazard involved, particularly with regard to the mixing of hydrogen and air. To eliminate burning downstream of the combustion chamber during operation of the facility, a cold air injection system was installed with the capacity to dilute the mixture below the inflammability limit. This arrangement made the mixture safe for exhausting to the atmosphere through the pressure recovery system.

The hot air flow out of the storage heater is metered by means of a water-cooled orifice flange (Figures 7 and 8) installed at the outlet of the air heater. Typical values of air pressures during an experiment are 162 psia in the storage heater (upstream of the orifice flange) and 38 psia in the air stilling chamber. Temperature and pressure conditions in the airstream at the entrance to the combustor in the ARL facility are shown in Figure 9. Similar data for the hydrogen stream at the combustor entrance is presented in Figure 10.

FIRST EXPERIMENTAL RESULTS--AUTO-IGNITION LIMITS

Only a small amount of experimental data is available at this writing. These results are presented with some reservation at this time, since analysis is far from complete; however, definite trends in the data are indicated. In addition, the successful experiments to date have definitely demonstrated the value of the facility as an experimental tool for supersonic combustion studies.

The initial tests in the ARL supersonic combustion facility were "shakedown" runs using helium throughout the hydrogen supply and control system. Runs were made with heated helium, using the hydrogen heater, as well as with cold helium. These experiments provided a means for checking out most of the instrumentation and operating controls and also resulted in thorough familiarization of operating personnel with the complete facility,

which was considered an absolute necessity before runs with hydrogen were attempted.

The first experiments in the ARL Facility with hydrogen injected into the airstream were conducted on 4 August 1966. At that time, a second series of "shake-down" runs was initiated to investigate temperature limitations, operational characteristics, and peculiarities of the facility under combustion conditions. Procedures for safely handling the combustible hydrogen-air mixtures were also of primary concern in these runs.

It was found that the coated-molybdenum hydrogen injector could withstand exposure to air at temperatures as high as 3500°R for time periods up to 35 seconds without failure. A run duration of 15 seconds at the higher temperatures was established as a normal test procedure in order to extend the life of the hydrogen injector as much as possible.

Auto-ignition limit tests were begun in October 1966. It is the data from these experiments which is being reported here. Experimental investigation of the supersonic combustion process in the combustion chamber, with runs of 15 seconds duration each, will be started in the near future, when additional facility components needed for such tests are completed.

Experimental data on auto-ignition limits for hydrogen-air combustion, obtained in the initial series of tests, are presented in Table II. Shown in the table are the conditions under which the experiments were made; for each run the mass flow rates and stagnation pressures of the air and hydrogen are given as well as the static pressure of the air at the entrance to the combustor. In general, the test procedure involved first establishing a given air temperature then increasing the hydrogen temperature to the point of auto-ignition. Data points were taken at one-tenth second intervals on a magnetic tape data recording system during the period immediately preceeding ignition. Table II shows for each run the stabilized stagnation temperature of the air and also the calculated static temperature of the air at the combustor entrance; finally, the point at which auto-

Table II. Preliminary Experimental Data on Hydrogen-Air Auto-Ignition in a Supersonic Stream

Run No.	$(p_{t2})_{Air}$ Psia	$(p_{t2})_{H_2}$ Psia	$(T_{t2})_{Air}$ °R	$(T_{t2})_{H_2}$ °R	$(p_3)_{Air}$ Psia	$\dot{m}_{Air}$ Lb/Sec	$\dot{m}_{H_2}$ Lb/Sec	$(T_3)_{Air}$ °R (Calc)	$(T_3)_{H_2}$ °R (Calc)	Auto-Ignition Observed
37	39.8	4.64	487	1956	2.17	3.30	.0140	212	1625	Yes
38A	40.7	5.10	858	1977	2.09	2.50	.0140	367	1640	Yes
38B	32.5	5.04	646	1838	1.74	2.40	.0140	280	1525	Yes
39	40.8	4.97	874	1970	1.98	2.50	.0140	369	1620	Yes
41	40.0	4.97	1076	2038	1.92	2.22	.0140	447	1700	Yes
42	64.7	4.90	1162	1827	3.11	3.53	.0130	497	1517	Yes
47	55.0	6.10	1417	1722	2.62	2.75	.0140	614	1435	Yes

ignition occurred in each run is given in terms of the hydrogen stagnation temperature and the hydrogen static temperature at the combustor entrance.

DISCUSSION OF RESULTS

The ignition temperature of hydrogen in air is given in Reference 6 as 585°C (1544°R). Even though this figure may be affected somewhat by such factors as composition, pressure, means of ignition, and degree to which the gases are mixed, it represents a reasonable point for comparison under various conditions and particularly for purposes of the discussion below.

The value of ignition temperature cited above is applied here as a rough guide to auto-ignition temperatures which might be expected in the ARL supersonic combustion experimental facility. Considering the plane at which the hydrogen is injected into the airstream, if the static temperature of either stream is as high as 1544°R, auto-ignition might be expected to occur. Whatever the arguments might be against such a statement, this temperature will be taken to be one possible temperature limit for auto-ignition for purposes of comparison with the experimental data. This "limit" has been applied for both the hydrogen stream and the airstream and is shown in Figure 11 as the upper horizonal dashed line (for hydrogen) and the far right vertical dashed line (for air). In the region where both streams are hot (upper right in the figure), the possible effect of the temperature of one stream on the ignition temperature in the other stream is recognized but will not be considered in this discussion.

Again considering the plane at which the hydrogen is injected into the airstream, if it is assumed that there is full recovery of stagnation temperature for either stream in the boundary along the interface between the two streams, ignition might be expected to occur when the stagnation temperature of this stream reaches 1544°R. As before, whatever the arguments might be against such an assumption, this temperature will also be taken as a possible temperature limit for auto-ignition for pur-

poses of comparison with the experimental data. This "limit" has been applied for both the hydrogen stream and the airstream and is shown in Figure 11 as the lower horizontal dashed line (for hydrogen) and the lefthand vertical dashed line (for air). Again, in the region where both streams are hot, the possible effect of the temperature of one stream on the ignition temperature in the other stream is not considered.

No claim is made that any of the "limits" represented by the dashed lines in Figure 11 are actual auto-ignition limits in a supersonic stream of hydrogen and air; these limits have been included on the graph for purposes of comparison and discussion and have been clearly defined above.

The hydrogen-air auto-ignition limit data obtained in the preliminary ARL experiments and previously cited in Table II have been plotted in Figure 11 (the circled points) for comparison with the "limits" mentioned above. In this group of experiments, at least in the temperature range so far investigated, it is noted that the auto-ignition limits observed in the laboratory are very close to the line representing a hydrogen static temperature of 1544°R. Experiments toward the higher air temperatures are presently underway. It is expected that with changes currently underway, it will be possible to conduct such experiments at air temperatures well in excess of the far right "limit" shown in Figure 11, i.e., an air static temperature of 1544°R or stagnation temperature of 3180°R.

FUTURE PLANS

Plans are to extend the current auto-ignition limit tests to the highest air temperatures attainable in the ARL facility. It is expected that air stagnation temperatures very near to 4000°R can be reached when modifications presently underway have been completed.

As mentioned earlier, experimental investigation

of the supersonic combustion phenomena in the combustion chamber, with runs of 15 seconds duration each, will be started in the very near future. These experiments will also be conducted at temperatures up to near 4000°R as soon as such temperatures can be attained. Computed theoretical data on conditions throughout a burning supersonic stream are expected to be available soon for comparison with the experimental data.

Several additions to the available instrumentation are planned, including shadowgraph and gas sampling stations at the injector exit plane and along the combustor. Plans are being made to conduct experiments with hydrocarbon fuels after the current hydrogen-air supersonic combustion program is completed.

APPLICATIONS

Results of the research reported here are applicable to problems of hypersonic flight at high Mach numbers, specifically in the neighborhood of Mach number 12. The specific type of propulsive system to which the data presented herein applies is that now known as Scramjet, envisioned for application within the earth's atmosphere at flight Mach numbers above approximately 5.

Engines making use of supersonic combustion are expected eventually to be of great potential benefit to the Air Force. This type of engine may, for example, provide the basis for air-breathing reusable spacecraft booster stages or launching vehicles, and also for global non-stop hypersonic flight within the earth's atmosphere, with reasonable operating costs.

One of the objectives of the present work was to demonstrate the feasibility of adequately simulating supersonic combustion in the laboratory without duplicating all of the flight parameters, thus making adequate ground testing possible and considerably reducing research and development costs. Another objective was to provide such a simulation

facility for basic supersonic combustion studies by updating or modifying an existing research facility rather than developing a new one specifically for such investigations.

CONCLUSION

The studies at ARL have shown that supersonic combustion simulation applicable to flight Mach numbers near 12, under prolonged testing conditions (up to 15 seconds), is feasible with ground test facilities presently available.

The method of simulation and type of facility described above make it possible to conduct laboratory supersonic combustion experiments under combustor temperature and pressure conditions duplicating those of actual flight at high hypersonic Mach numbers. The success achieved to date at ARL in this area is due largely to four factors: (1) the invention of a unique hydrogen heater to provide streams of very high temperature hydrogen, (2) demonstration of a means of injecting the hot hydrogen into the center of a very high temperature airstream, using previously untried materials, (3) development of a unique means of safely handling the hydrogen-air exhaust in the existing wind tunnel vacuum system, permitting attainment of low density test conditions, and (4) demonstration of a simulation technique in which only the essential combustion parameters are duplicated.

The ARL facility can be used for basic investigations of supersonic combustion phenomena. Although the configuration of the present facility is limited to simulation of combustion conditions for flight Mach numbers near 12, the range of the facility can be readily extended by modifying the geometries of the air and hydrogen nozzles now in use. The experimental results to be obtained at conditions simulating high Mach number flight are expected to hasten the solution of Scramjet problems.

ACKNOWLEDGEMENTS

The author is deeply indebted to the Director and staff of this Laboratory for numerous individual contributions and for extensive active participation as a research team. In particular the author wishes to express his appreciation to Mr. Emil J. Walk for his part in the development of the simulation technique, to Mr. Norman E. Scaggs who has had direct responsibility for the experimental facility developed and used in this project, and also to personnel of the General Applied Science Laboratories, Inc. for helpful recommendations and discussions particularly with respect to the combustion chamber design.

REFERENCES

1. Dunn, Robert G. and Walk, Emil J., "Supersonic Combustion Simulation for High Mach Number Flight," Paper No. 9, Proceedings of the 13th Annual Air Force Science and Engineering Symposium, Tullahoma, Tennessee, 27-29 September 1966.

2. Scaggs, Norman E. and Dunn, Robert G., "Development of a Facility for Supersonic Combustion Simulation," Paper No. 66-743, presented at the AIAA Aerodynamics Testing Conference, Los Angeles, California, 21-23 September 1966.

3. Scaggs, Norman E., Burggraf, W., and Gregorek, G. M., "The ARL Thirty-Inch Hypersonic Wind Tunnel Initial Calibration and Performance," ARL 63-225, Aerospace Research Laboratories, Wright-Patterson Air Force Base, Ohio, December 1963.

4. Prete, Ralph, "On the Design of an Electrical Resistance Hydrogen Heater," presented at the Twenty-Fourth Meeting of the Supersonic Tunnel Association, Hawthorne, California, 1-2 November 1965.

5. Ferri, A., Moretti, G., and Slutsky, S., "Mixing Processes in Supersonic Combustion," J. Soc. Indust. Appl. Math., 13, 229-258, March 1965.

6. Coward, H. F. and Jones, G. W., "Limits of Flammability of Gases and Vapors," Bureau of Mines Bulletin 503, 1952.

NOMENCLATURE

A	Area
$\dot{m}$	Mass Flow
M	Mach number
p	Pressure[1]
T	Temperature[1]

Subscripts

H_2	Hydrogen
t	Total conditions
1	Conditions in the ambient region (flight) or air heater (laboratory)
2	Conditions in the inlet region (flight) or stilling chamber (laboratory)
3	Conditions at the combustor inlet (flight and laboratory)

Superscripts

$()'$	(prime) Pertains tc free-flight condition
	(no prime) Pertains to laboratory test condition
*	Pertains to conditions where the local speed is equal to the local speed of sound

[1] When used without the subscript t, the symbols p and T denote static conditions.

a. FLIGHT CASE

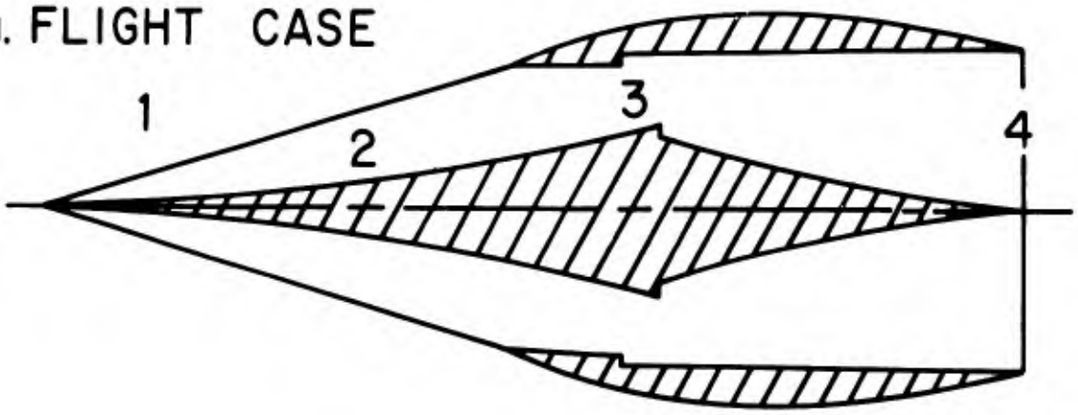

b. LABORATORY CASE

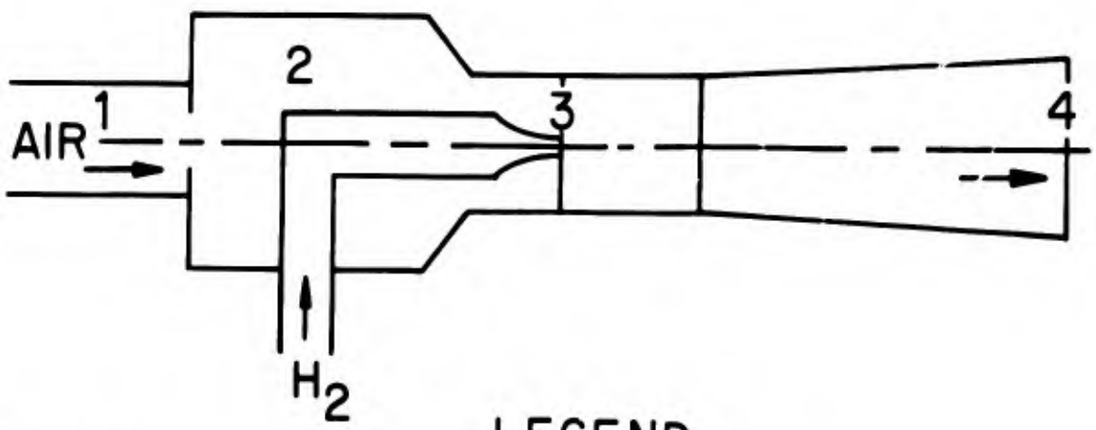

LEGEND

Station

1 Ambient region (flight) or air heater (laboratory)
2 Inlet region (flight) or stilling chamber (laboratory)
3 Combustor inlet (flight and laboratory)
4 Combustor discharge (flight and laboratory)

Figure 1. Typical Geometries for Flight and Laboratory Cases

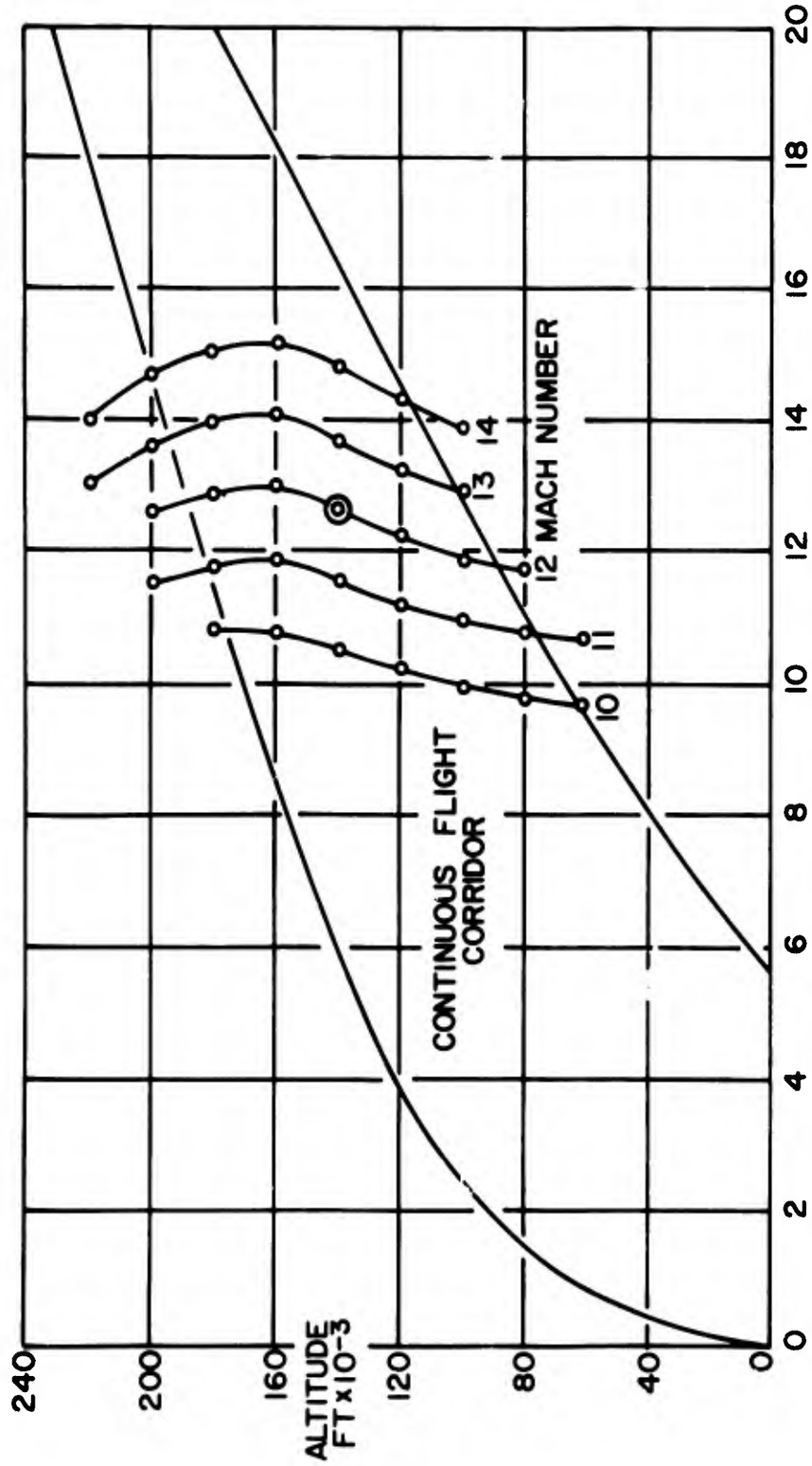

Figure 2. Flight Regime Under Study for Simulation

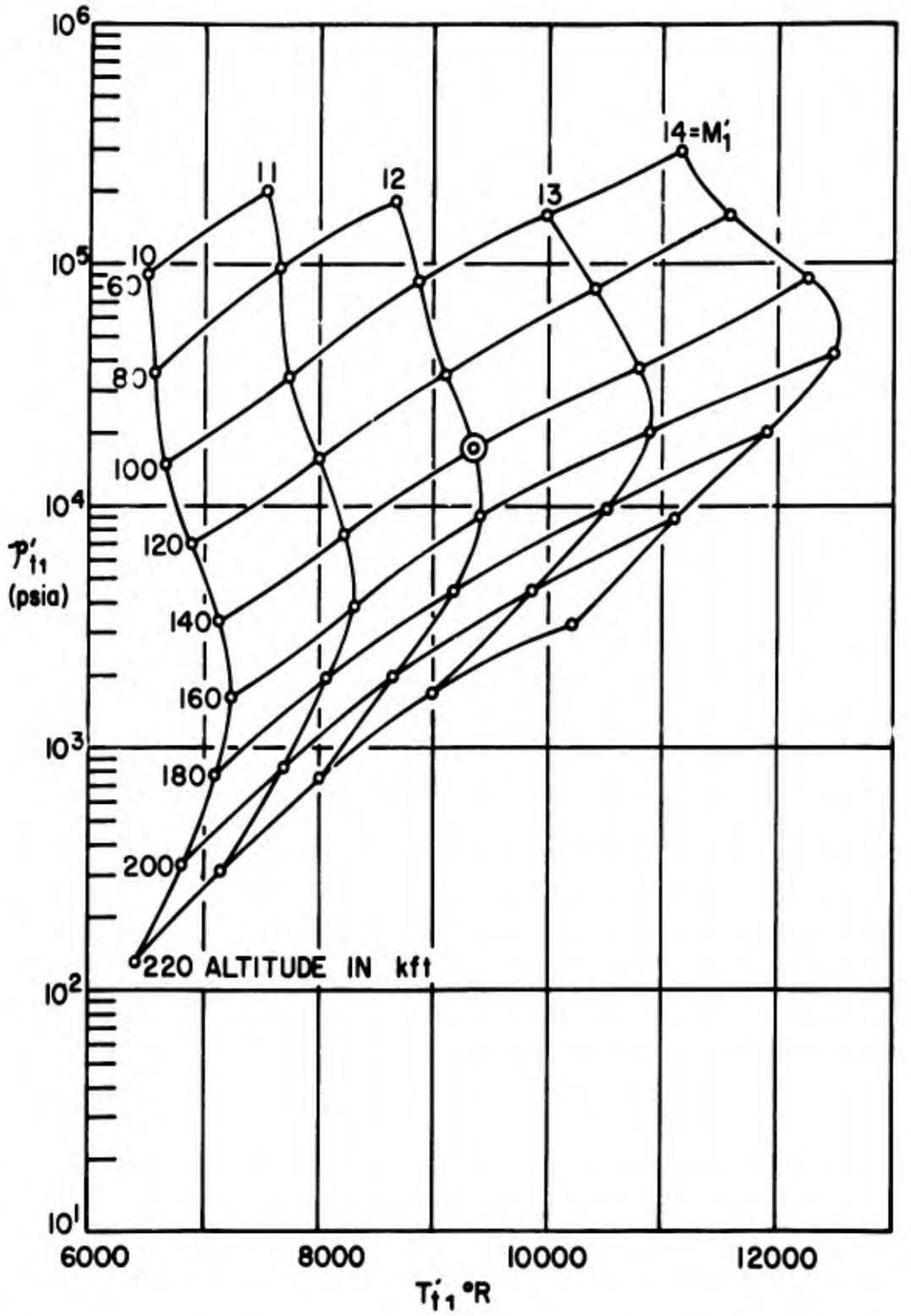

Figure 3. Stagnation Conditions in the Flight Case

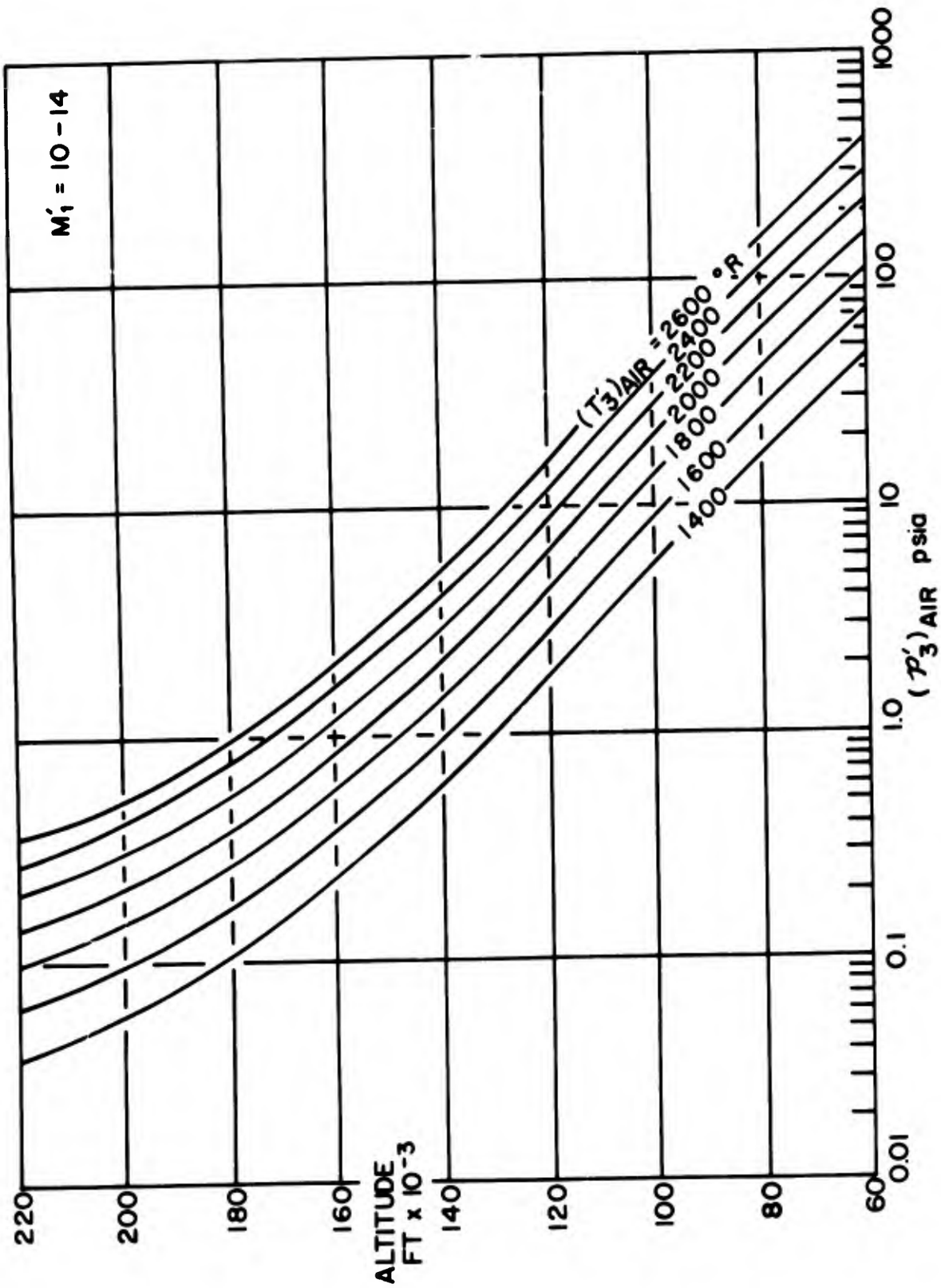
$M_1' = 10-14$
$(T_3')_{AIR}$ = 2600 °R
2400
2200
2000
1800
1600
1400
ALTITUDE
FT x 10^{-3}
220
200
180
160
140
120
100
80
60
0.01
0.1
1.0
10
100
1000
$(P_3')_{AIR}$ psia

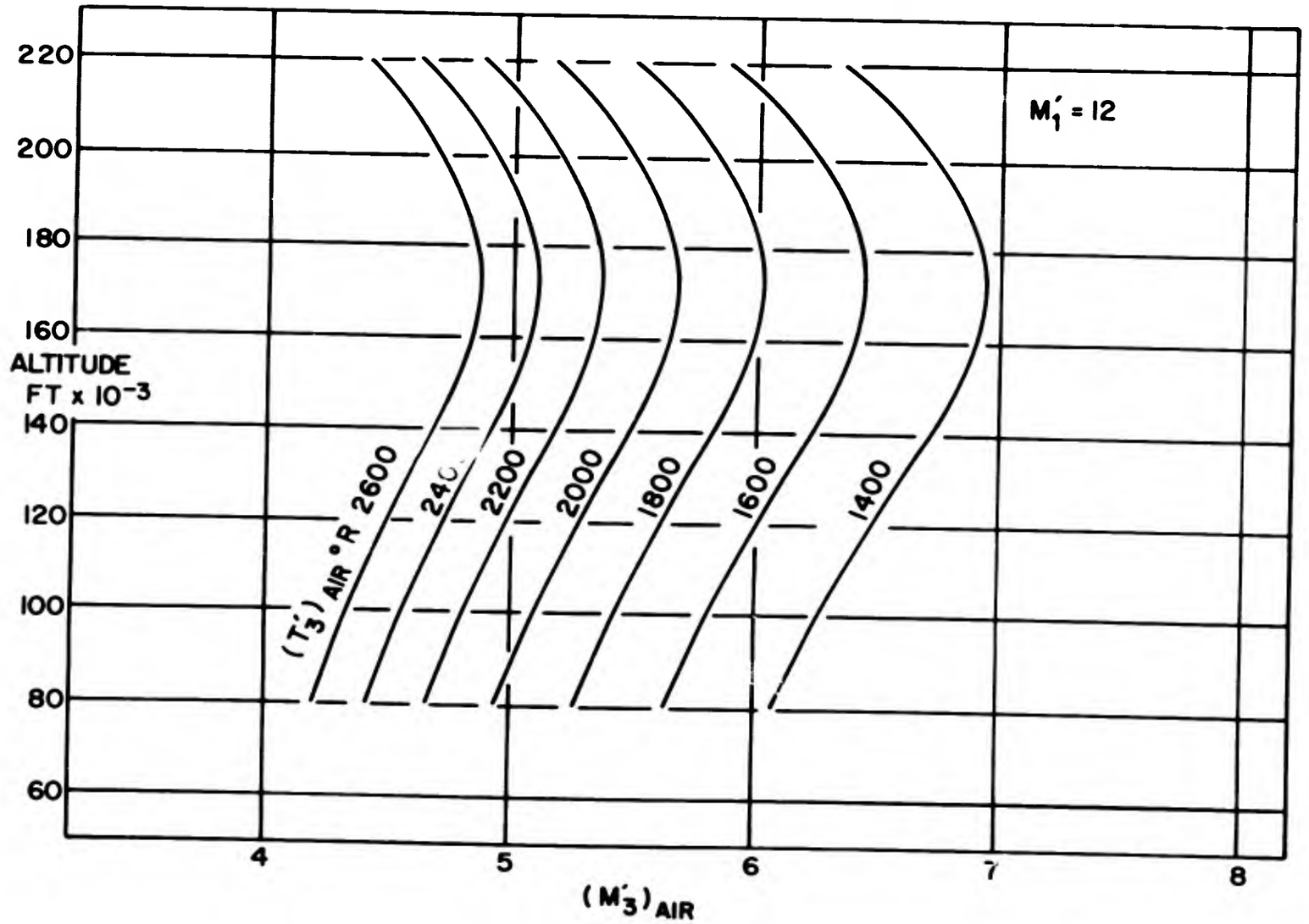

Figure 4. Typical Combustor Entrance Conditions in Flight

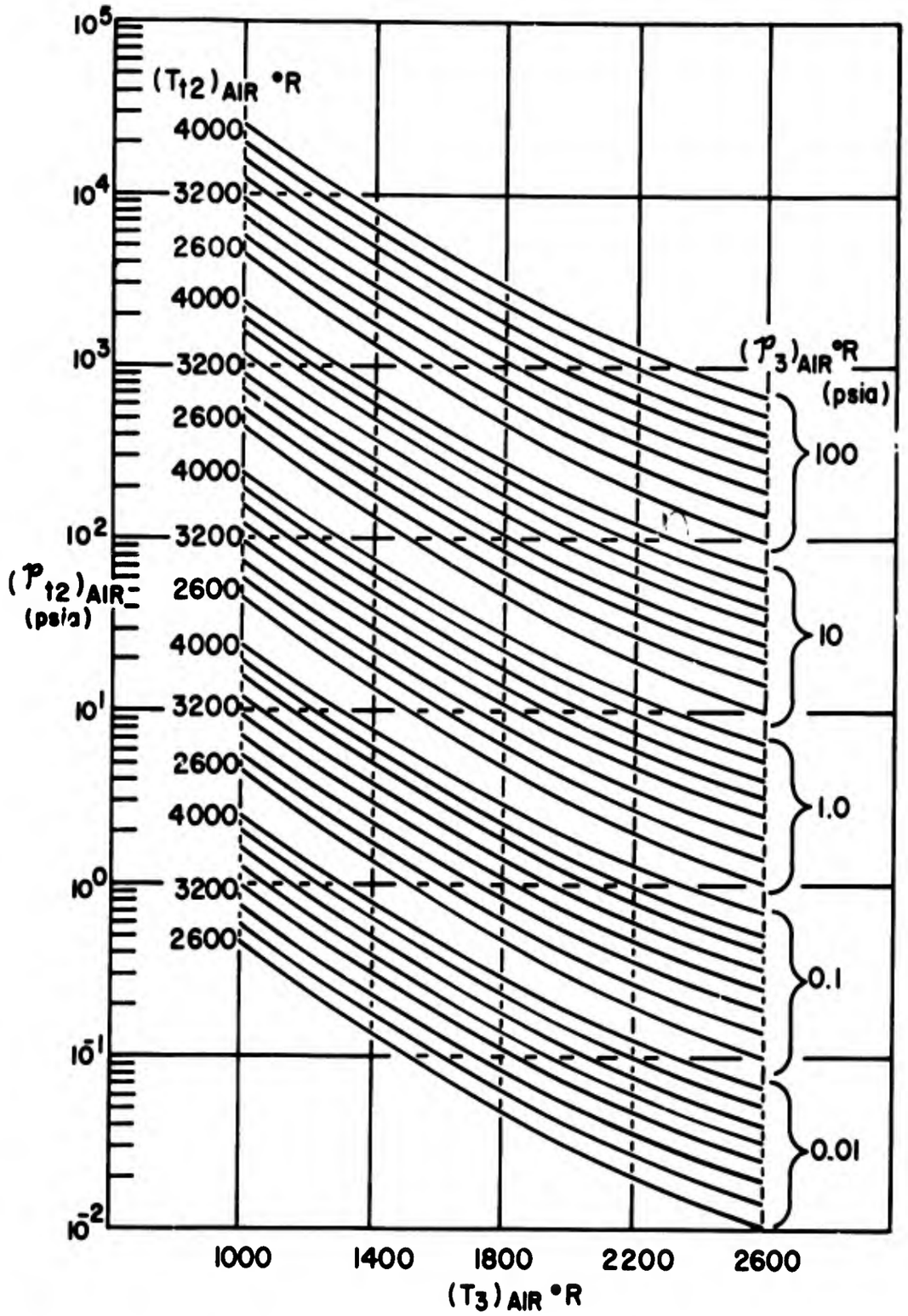
10^5
10^4
10^3
10^2
10^1
10^0
10^{-1}
10^{-2}
$(T_{t2})_{AIR}$ °R
4000
3200
2600
4000
3200
2600
4000
3200
2600
4000
3200
2600
$(P_{t2})_{AIR}$ (psia)
$(P_3)_{AIR}$ °R (psia)
100
10
1.0
0.1
0.01
1000
1400
1800
2200
2600
$(T_3)_{AIR}$ °R

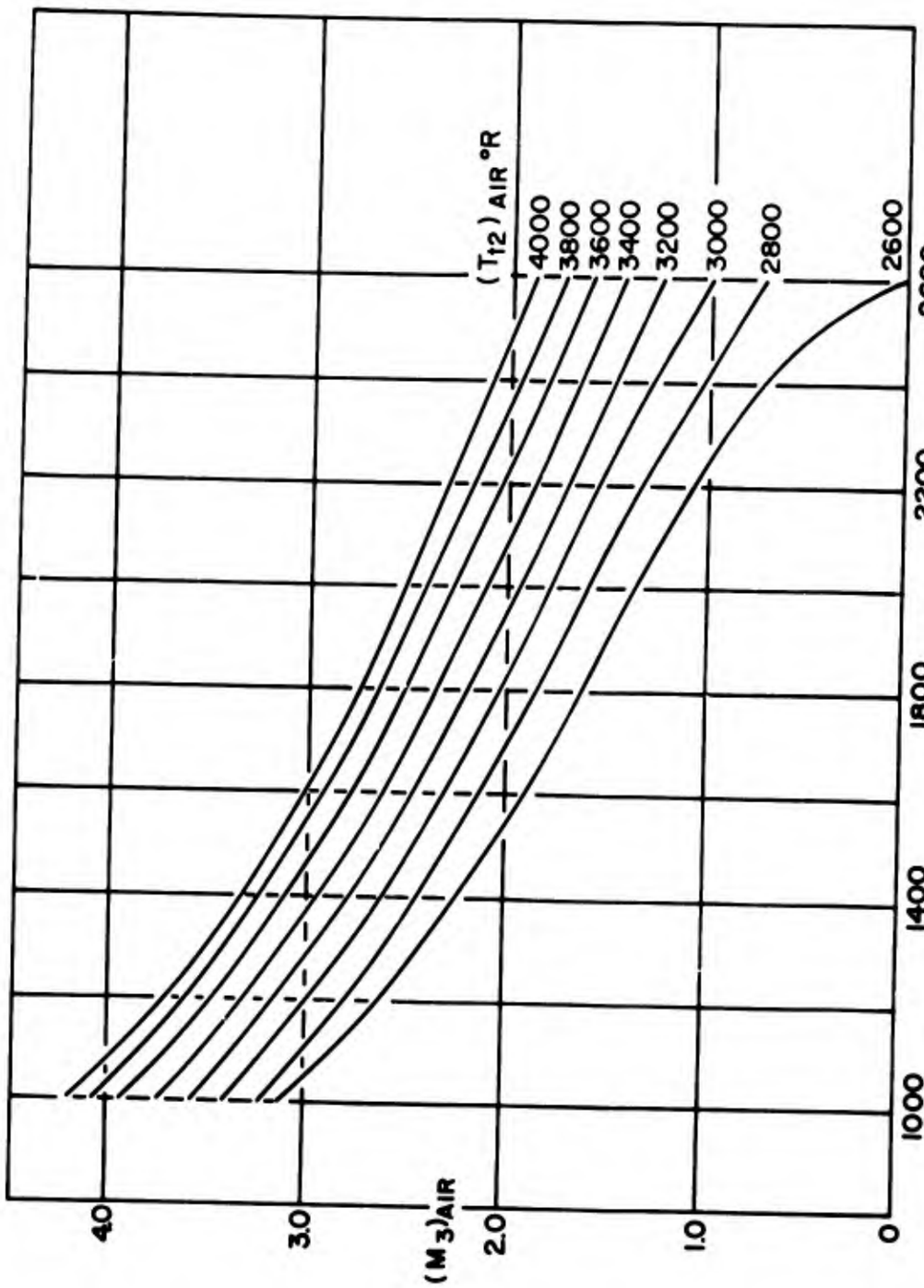

Figure 5. Typical Combustor Entrance Conditions in the Laboratory

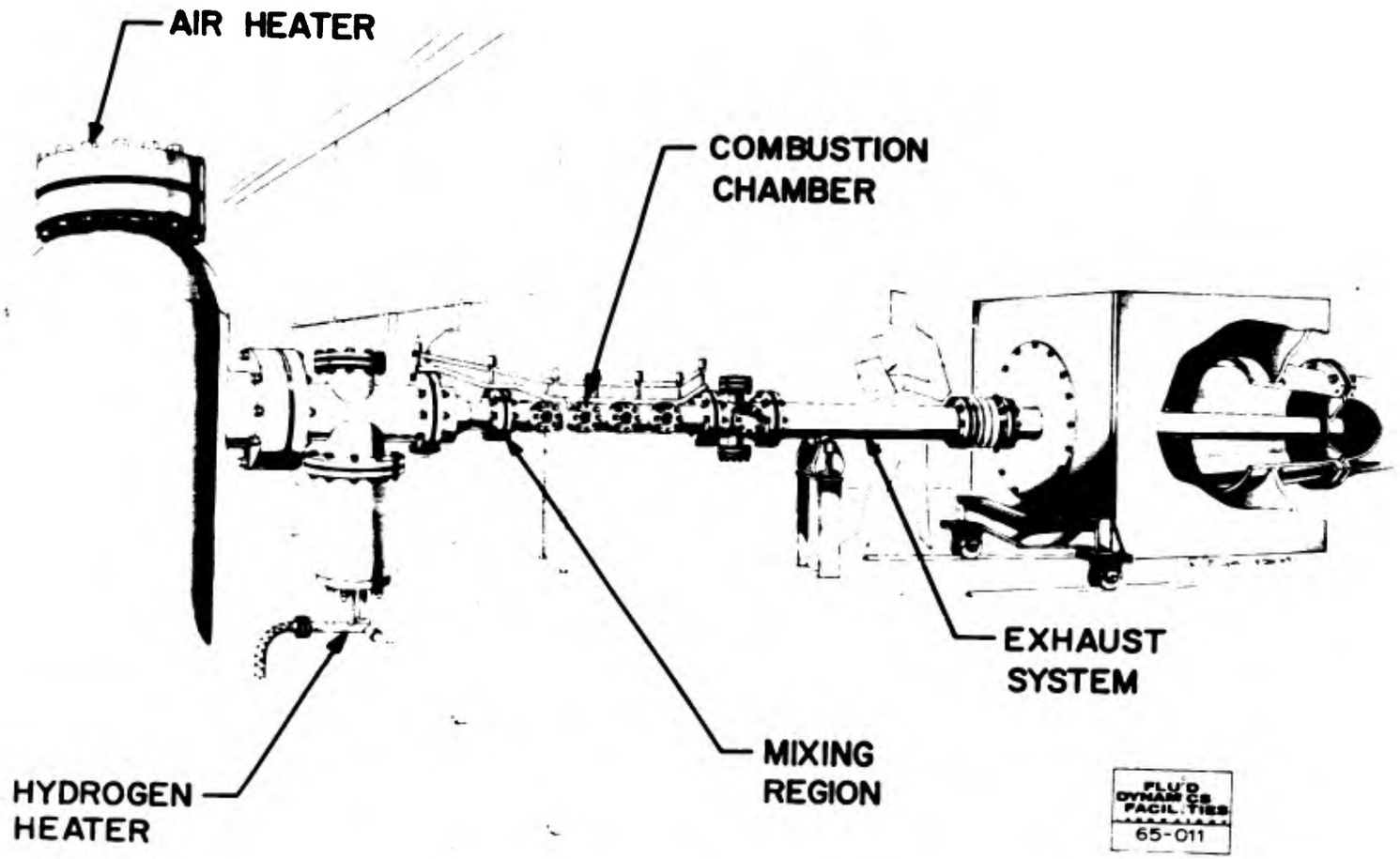

Figure 6. The ARL Supersonic Combustion Facility

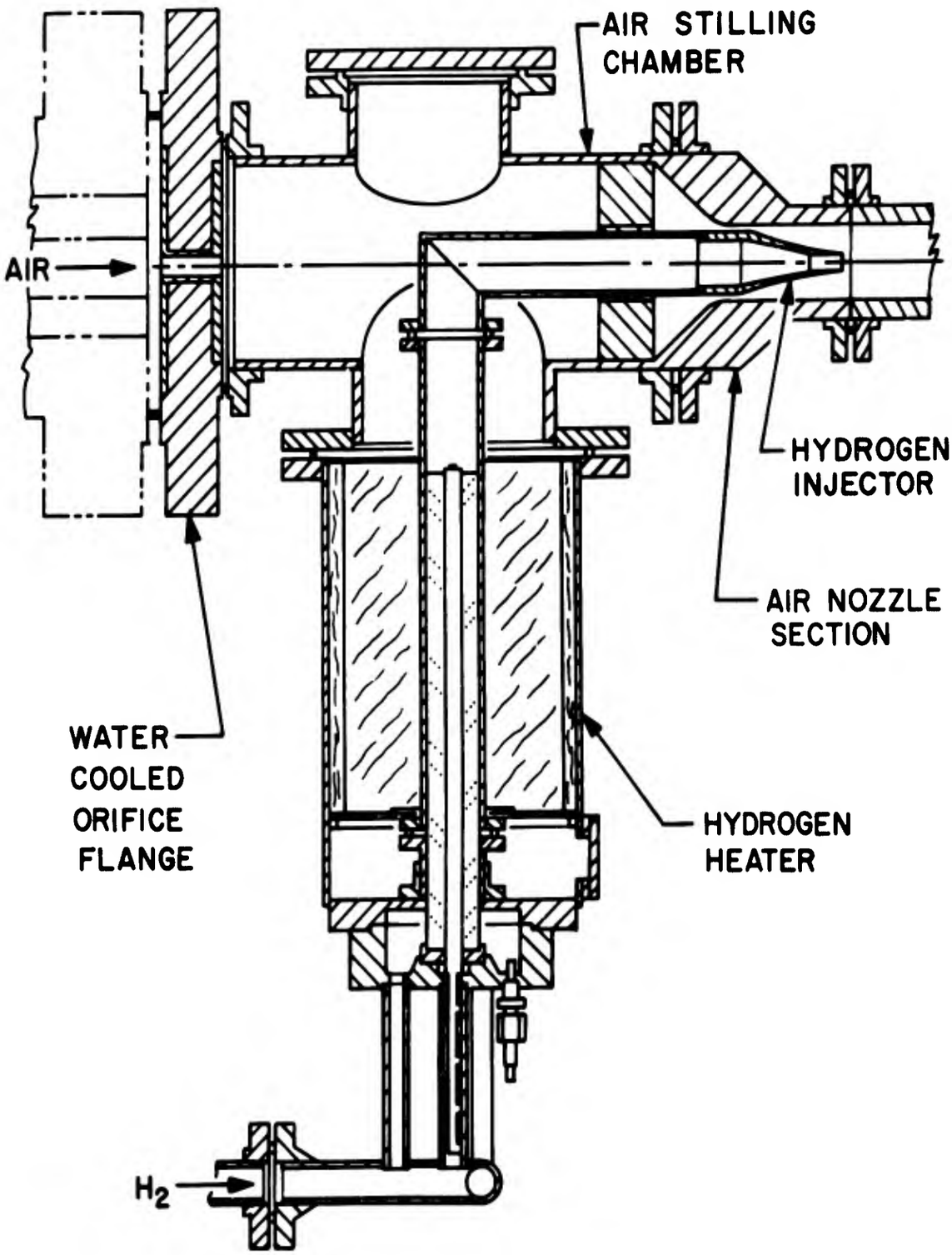

Figure 7. Hydrogen Heater and Injector in the ARL Facility

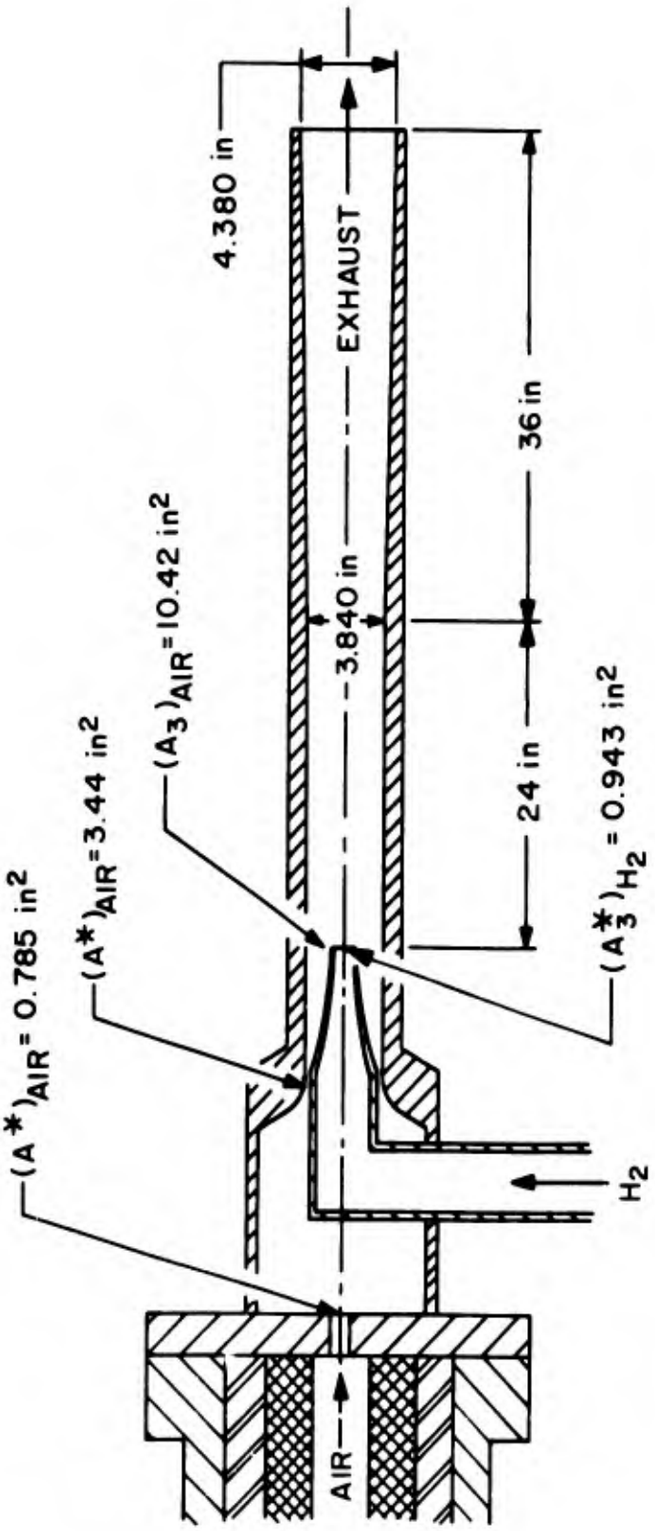

Figure 8. Mixing Region and Combustion Chamber in the ARL Facility

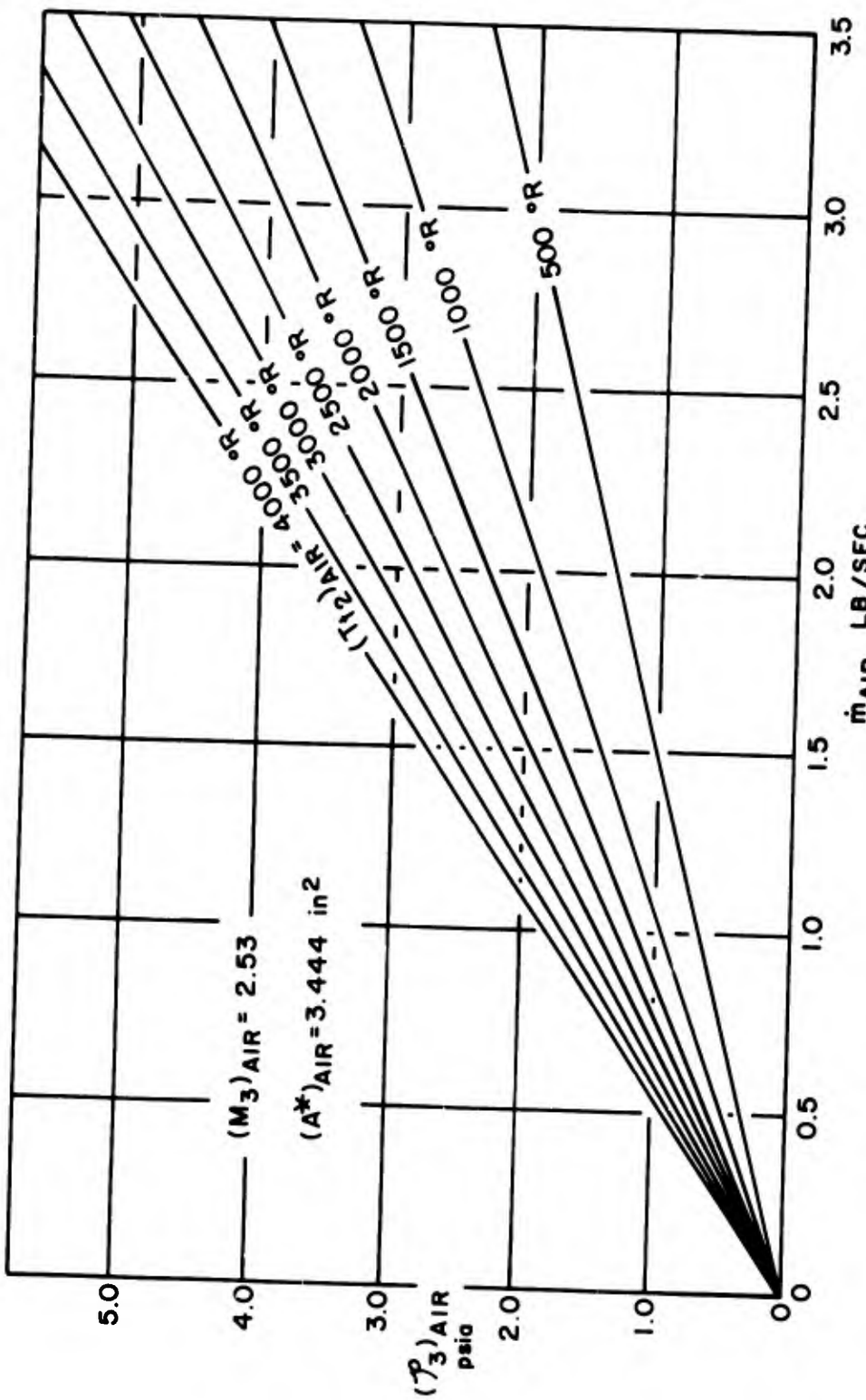

Figure 9. Static Pressure and Temperature of Air at Combustor Entrance in the ARL Facility

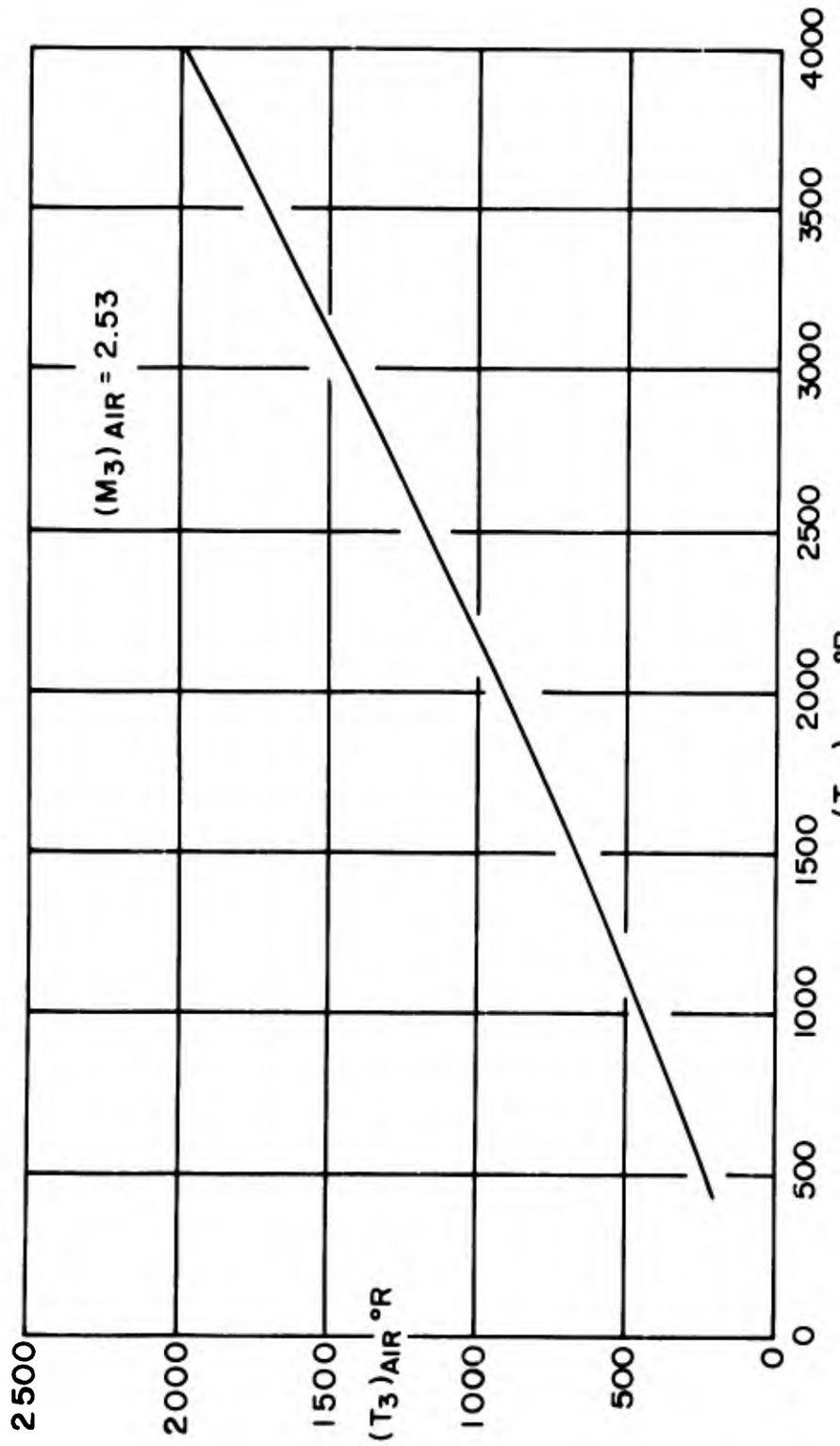

Static Pressure and Temperature of Air
at Combustor Entrance in the ARL Facility (Cont.)

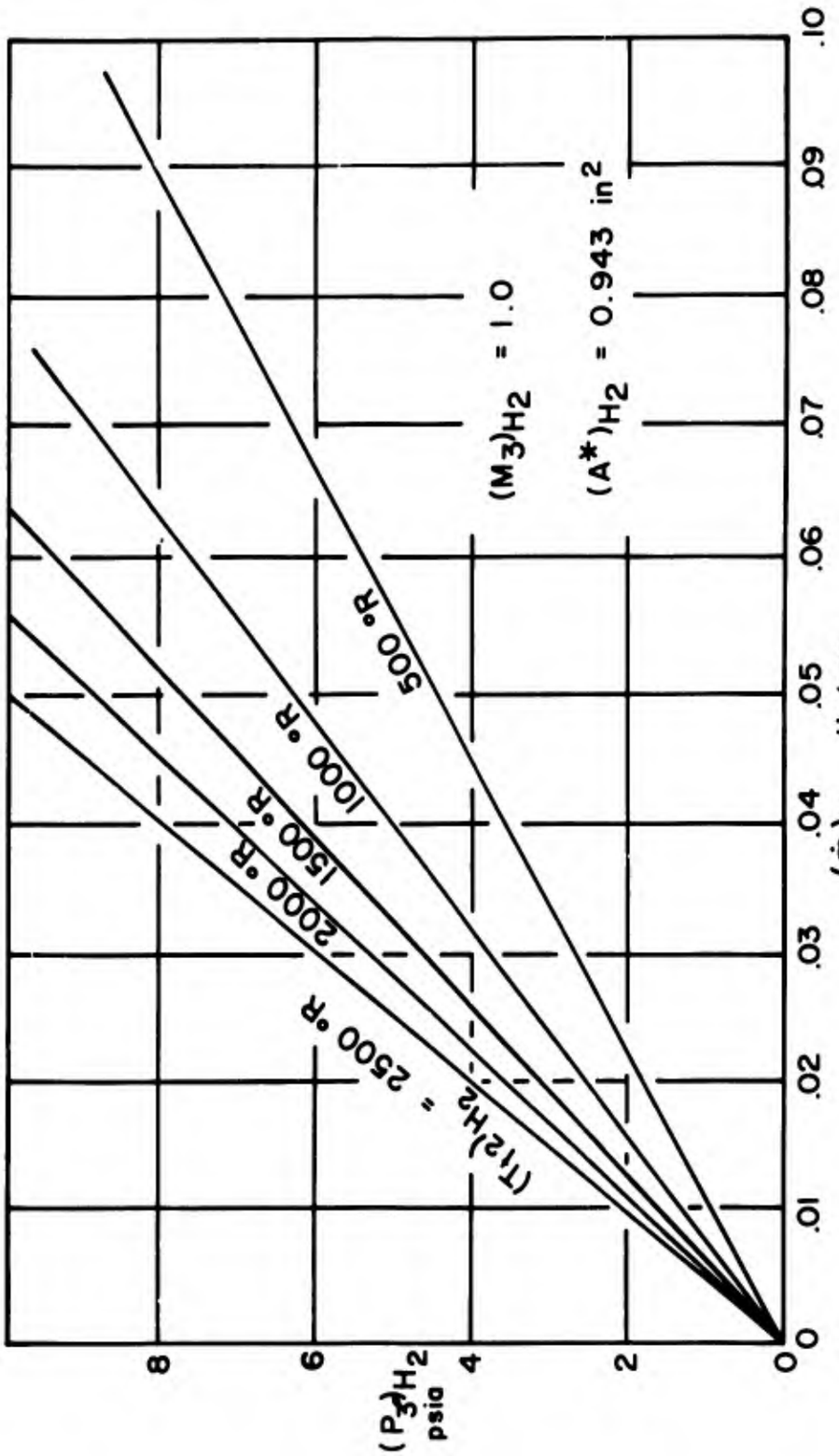

Figure 10. Static Pressure and Temperature of Hydrogen at Combustor Entrance in the ARL Facility

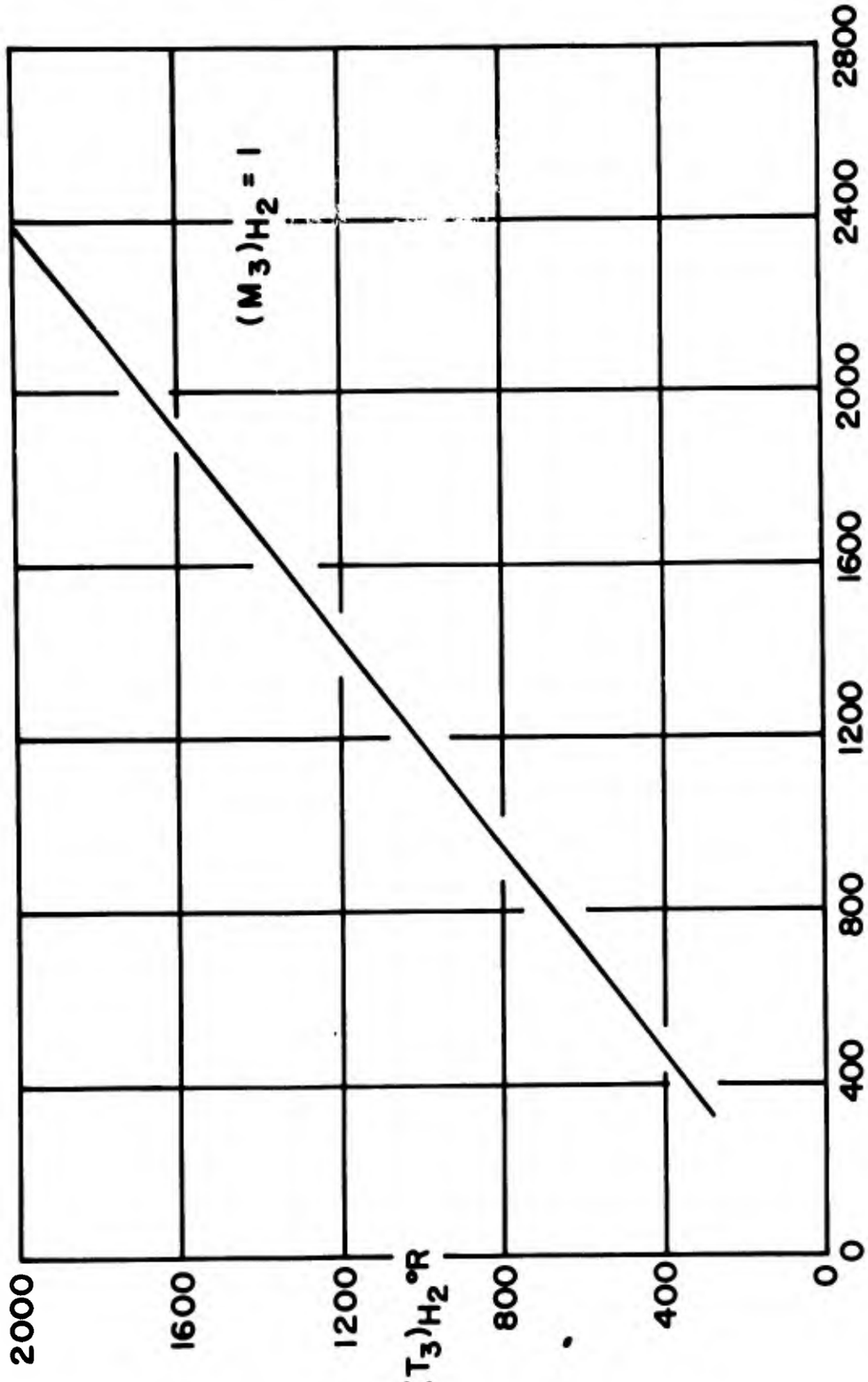

Figure 10. (Cont.) Static Pressure and Temperature of Hydrogen at Combustor Entrance in the ARL Facility

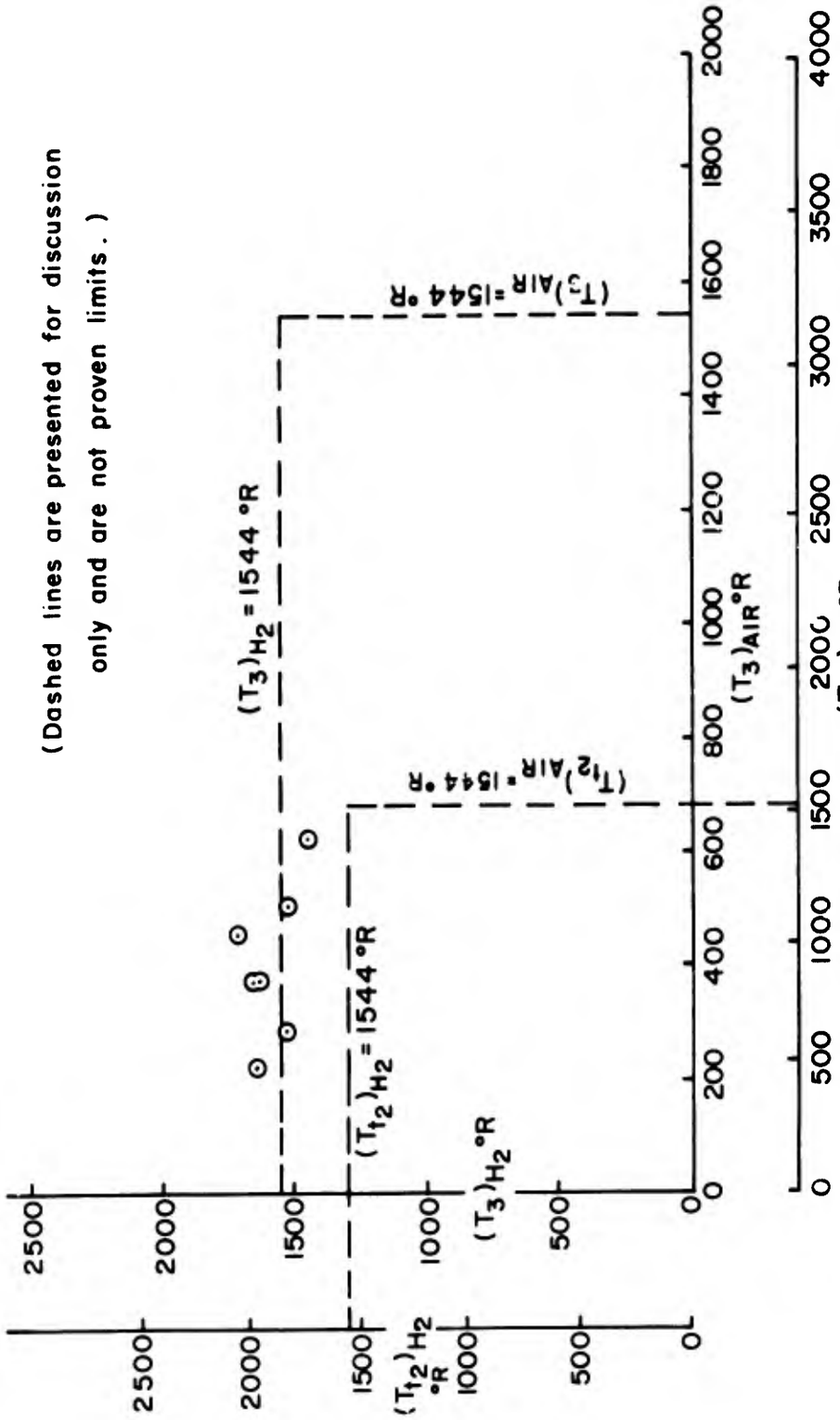

Figure 11. Auto-Ignition Limits for Hydrogen-Air Supersonic Combustion

1st Lt. Brian P. Quinn is an aerospace research engineer with the Hypersonic Research Laboratory, Aerospace Research Laboratories. He obtained his B.S. and M.S. degrees in Aeronautical Engineering from the University of Notre Dame in 1959 and 1962, respectively, and his Docteur de L'Université from the University of Paris, France, in 1964. Lt. Quinn is author of several scientific publications, winner of scientific awards, and a member of the Institute of Aerospace Sciences and the Sigma Xi Society.

PREDICTION OF THE DYNAMIC STABILITY OF NOSE CONES

By

BRIAN P. QUINN*

ABSTRACT

The flow around a blunted slender cone performing pitching oscillations is theoretically analyzed by means of Chernyi's blast-wave piston analogy. Stationary and transient shock shapes and pressure distributions are presented in power series form. Within the region of convergence, the stationary pressure agrees well with Chernyi's numerical integration. Normal force and pitching moment coefficient derivatives are presented and the results are plotted for a 10° cone. The theoretical static and dynamic stability derivatives agree satisfactorily with recent experiments in a Mach 14 wind tunnel. It is concluded that the experimentally observed reduction in static and dynamic stability due to increased nose bluntness may be attributed to blast wave effects.

INTRODUCTION

The delivery of a given payload to a prescribed location is the final mission objective of any missile system. The attainment of this objective requires that the system be capable of correcting any deviation from the planned trajectory during all phases of its flight. With particular reference to the vehicle's performance in an atmosphere, completion of the mission demands that the configuration be aerodynamically stable both statically and dynamically.

At the same time, however, the vehicle must be provided with some means for accommodating the severe aerodynamic heating which it encounters during re-entry. This can be accomplished by several techniques, one of which is blunting the nose of the missile. However, blunting the nose of the vehicle also changes the flow field around it, and this in turn alters its stability characteristics. The problem

* 1stLt, USAF, Hypersonic Research Laboratory, Aerospace Research Laboratories, Wright-Patterson Air Force Base, Ohio

facing the missile designer is to balance the opposing effects of heating and stability. Moreover, this is a fundamental problem which will persist as long as trajectories include atmospheric flight. For this reason, research into the stability of re-entry vehicles continues to play a timely role in the Air Force' s missile program.

Recognizing this need, a program of continuing research on the basic fluid mechanics of stability at hypersonic speeds was begun by the Hypersonic Research Laboratory at the Aerospace Research Laboratories several years ago when it became clear that dynamic stability was indeed a problem during re-entry. The study of reference (1) represents one of the major results of this effort. Walchner and Clay therein presented conclusive experimental evidence of the destabilization provoked by blunting the nose of circular cones, a configuration of obvious practical importance. Their semiempirical analysis was based on the method of tangent cones applied to Griffith and Lewis' [2] correlation of experimental pressure distributions along blunted cones at zero lift. The results of their analytical study agreed with their measured static pitching moment derivatives over the entire range of nose bluntnesses investigated. However, the apparent limitations of the tangent cone technique in such a complicated flow field were illustrated by the divergence of their analytical and experimental dynamic stability curves at rather large values of the nose bluntness ratio.

This paper is a theoretical study concerned with the influence of marked nose bluntness on the hypersonic stability derivatives of slender nose cones. As a complement to the work of reference (1), the explicit objective is to determine if the trend of experimental dynamic stability data can be explained through the blast wave analogy.

NOMENCLATURE

$C_m = \dfrac{\text{Pitching Moment}}{\frac{1}{2}\rho V^2 S \ell}$, pitching moment coefficient

$C_N = \dfrac{\text{Normal Force}}{\frac{1}{2}\rho V^2}$, normal force coefficient

$$( )_\alpha = \lim_{\alpha \to 0} \frac{\partial ( )}{\partial \alpha}$$

$$\left(\frac{q\ell}{V}\right) = 0$$

$$( )_q = \lim_{\alpha = 0} \frac{\partial}{\partial \left(\frac{q\ell}{V}\right)}$$

$$\left(\frac{q\ell}{V}\right) \to 0$$

C_{D_n} = $\dfrac{\text{Nose Drag}}{\frac{1}{2}\rho\, V^2 \pi\, r_N^2}$, nose drag coefficient

C_p = $\dfrac{P_{surface} - P_\infty}{\frac{1}{2}\rho\, V^2}$, pressure coefficient

C_p' = $\dfrac{P_{surface\ perturbation}}{\frac{1}{2}\rho\, V^2}$, perturbation pressure coefficient

E = energy released by explosion, related to nose drag of blunt cone

I = impulse imparted by explosion

K = $M_\infty \tan \Theta$, hypersonic similarity parameter

L = $\left(\dfrac{E}{\pi\, \rho\, U^2}\right)^{1/2}$, characteristic length

ℓ = body length

M_∞ = free stream Mach number

P = $\dfrac{C_p}{2\Theta^2}$, dimensionless pressure

$p = \frac{C_p'}{2\Theta^2}$, dimensionless perturbation pressure

$R(\xi)$ = dimensionless shock shape or shock radius

$R_p(\xi)$ = dimensionless piston radius

$r(\xi)$ = dimensionless shock perturbation

$r_p(\xi)$ = dimensionless piston perturbation

r_N = nose radius of body

r_B = base radius of body

$S = \pi r_B^2$

$T = \frac{L}{U}$, characteristic time

t = time

$U = V \tan \Theta$

V = free stream speed

x = distance from nose in flow direction

x_{cg} = distance of pitch axis from nose

y = body fixed ordinate

Greek symbols

$\alpha = |\alpha| \sin \omega t$, pitch angle

$|\alpha|$ = amplitude of α

γ = ratio of specific heats

$\epsilon = -\frac{|\alpha|}{\Theta} \cos \phi$

η = $\frac{r_N}{r_B}$, nose bluntness ratio

Θ = cone half angle

λ = $\left(\frac{\Theta\,(1-\eta)}{2\eta}\right)^{1/2}$, a correlation parameter

ξ = $\frac{t}{T} = \sqrt{\frac{2}{C_D}}\ \Theta^2\ \frac{x}{r_N}$, dimensionless time

ρ_∞ = free stream density

ϕ = peripheral angle (see fig. 3)

ω = circular pitching frequency

subscript $(\ )_0$ = { stationary shock shape and pressure or pitch axis through nose

$(\dot{\ })$ = $\frac{d(\ )}{d\xi}$

ANALYSIS

1. Equations of Motion

Blunted leading edges on hypersonic vehicles are responsible for a host of fluid dynamic complications including detached and curved shock waves, rotational flow, chemical effects, existence of subsonic and supersonic speed regimes, and many others. Although it is sometimes necessary to account for all or most of these complexities in a theoretical study, expediency and efficiency frequently suggest that a simplified model, retaining only the global aspects of the flow, serve as the foundation of the analysis. Chernyi[3] has proposed such a model for the hypersonic flow over blunted cones. By virtue of the equivalence principle, he treats the blunted cone problem indirectly by considering an analogous problem in piston theory. The analogy is represented schematically in figure 1. In the piston plane, a cylindrical charge of unit depth explodes at time t = 0 and releases a quantity of energy into fluid which is initially at rest. At the same instant, a cylindrical piston is formed at the point of the explosion and

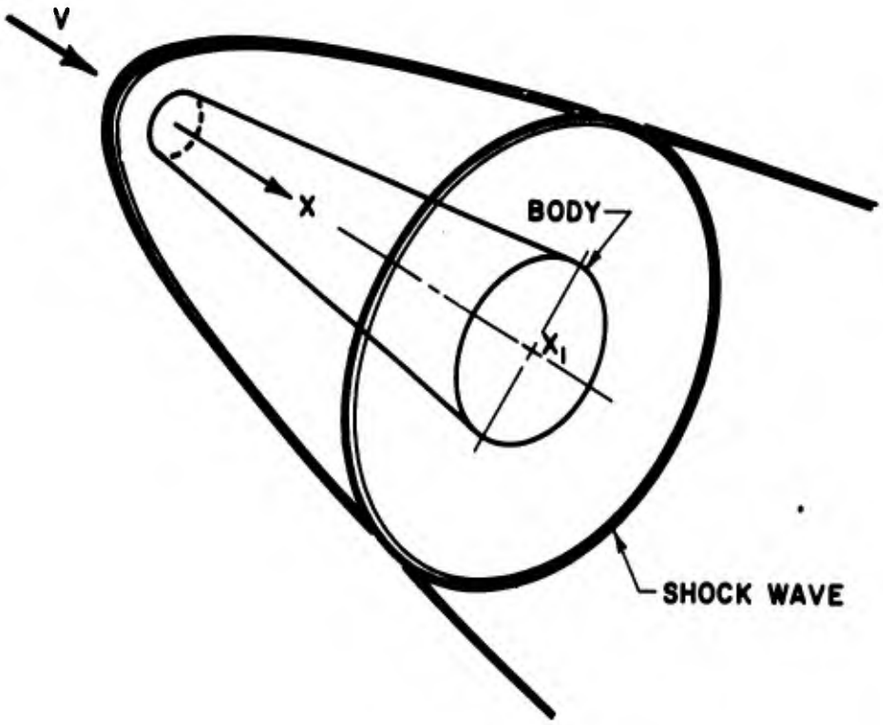

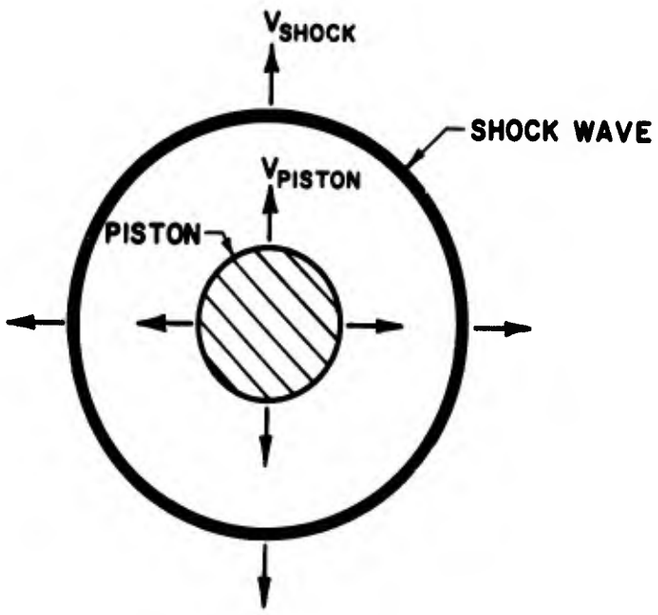

$$0 < t_1 = \frac{X_1}{V}$$

FIGURE 1

begins to move outwards toward the shock wave produced by the explosion. The analogy is related to the hypersonic flow over a blunted cone by equating the energy released by the explosion with the work done by the nose drag in moving a unit distance.

Conservation of energy requires that the fluid's energy at any instant be equal to the sum of the energy released by the explosion, the initial energy of the gas and the work done by the piston. In like manner, the momentum of the fluid at any instant is equal to the sum of the impulses imparted by the explosion and by the piston. In view of these considerations, Chernyi has deduced that the equations expressing conservation of energy and momentum may be approximated by the following dimensionless equations:

$$\frac{1}{2}\left(\frac{2}{\gamma+1}\right)^2\left(\dot{R}R\right)^2+\frac{1}{\gamma-1}\left(R^2-R_p{}^2\right)P=1+2\int_0^{\xi}PR_p\,dR_p(\xi) \qquad (1)$$

and

$$\left(\frac{2}{\gamma+1}\right)\dot{R}R^2=\frac{IU}{E}+2\int_0^{\xi}PR\,d\xi \qquad (2)$$

where characteristic length and time have been chosen as $L=(E/\pi\rho_\infty U^2)^{1/2}$ and $T=L/U$, respectively. The term IU/E in equation (2) is generally considered to be negligibly small for slender cones.

The above equations differ somewhat from those set down by Chernyi in that the initial pressure of the fluid has been neglected. This implies an infinite value for the hypersonic similarity parameter, $K=M_\infty\tan\Theta$. The deletion of the initial pressure brings to question the applicability of equations (1) and (2) to physical problems wherein K is finite. This simplification is, however, consistent with the fact that equations (1) and (2) were not derived from consideration of the physical flow about a blunted cone but from a very simplified model. More than qualitative information should not be expected from their solution. Moreover, we note that Chernyi's pressure expression does not approach true cone surface pressures for large ξ, but it does tend toward the Newtonian value $P=1$ for all K. This is a consequence of certain approximations used in the formulation of the model, such as the constancy of the speed of the gas in the region bounded by the piston and the shock wave, and the concentration of mass near the shock wave. These approximations become realistic in the double

limit $K \to \infty$, $\gamma \to 1$, and for this reason Chernyi's equations may be considered as limiting equations for large K. In this sense, deletion of the initial pressure from the energy and momentum equations, as has been done in equations (1) and (2), should not influence their qualitative validity.

2. Solution of the Steady Problem

The approximate equations (1) and (2) serve as the point of departure for this study. Before proceeding to the case of a pitching cone, it is first necessary to solve the governing equations for the case of hypersonic flow over a stationary blunt cone.

Eliminating the pressure terms from equations (1) and (2), and noting that $R_{p_0} = \Theta x / L = \xi$, results in the shock shape being governed by the following equation:

$$\frac{1}{2}\left(\frac{2}{\gamma+1}\right)^2\left(\dot{R}_0 R_0\right)^2 + \frac{R_0^2 - \xi^2}{\gamma^2 - 1}\,\frac{1}{R_0}\,\frac{d}{d\xi}\left(R_0^2\dot{R}_0\right) = 1 + \frac{2}{\gamma+1}\int_0^{\xi}\frac{\xi}{R_0}\,\frac{d}{d\xi}\left(R_0^2\dot{R}_0\right)d\xi \tag{3}$$

where subscript zero indicates a nonpitching condition.

For the bluntness ratios of interest, that is for $\eta = r_N / r_B$ more than around 10 percent and for small cone angles Θ, the entire body will generally be contained in the interval

$$0 \leqq \xi \leqq 1 \tag{4}$$

For such small values of ξ and in view of the asymptotic form of R_0 established by Chernyi, the solution of equation (3) has been approximated by a power series of the form

$$R_0 = A\xi^{1/2} + B\xi^{3/2} + C\xi^{5/2} + \ldots \tag{5}$$

which is convergent in the interval (4). Expressions for the coefficients A, B, C may be found by substituting the series expansion (5) into equation (3). Representative numerical values are given in Table I.

	$\gamma = 1.4$	$\gamma = 1.6667$
A	1.3027	1.4756
B	.0741	.0791
C	.0153	.0140

TABLE I

The pressure distribution over slender blunted cones whose shock shape is given by equation (5) is found from equation (2) to be

$$P_0 = \frac{1}{4(\gamma + 1)} \left[A^2 \xi^{-1} + 14AB + (21B^2 + 34AC)\, \xi + \ldots \right] \quad (6)$$

Figure (2) compares Chernyi's numerical solution of the system of equations (1) and (2) with the above result.

3. The Pitching Problem

The approach used herein to formulate the problem of hypersonic flow around a blunted cone performing small pitching oscillations about zero angle of attack consists of a perturbation technique. Thus, corresponding to a piston whose radius is perturbed an amount $r_p(\xi)$ such that the piston radius may be expressed as

$$R_p(\xi) = R_{p_0}(\xi) + r_p(\xi) \quad (7)$$

The shock radius and pressure may be represented by similar expressions.

With reference to figure (3), the piston radius is, in general, given by $R_p = \Delta y / L$, so that at zero incidence $\Delta y = \Theta x$ and $R_{p_0} = \xi$. The piston perturbation r_p appears only under conditions of non-zero incidence and can be deduced from figure (3) through the law of cosines. Thus, after neglecting the higher order terms we find that

$$r_p(\xi) = -\frac{a}{\Theta} \cos\phi\, \xi \quad (8)$$

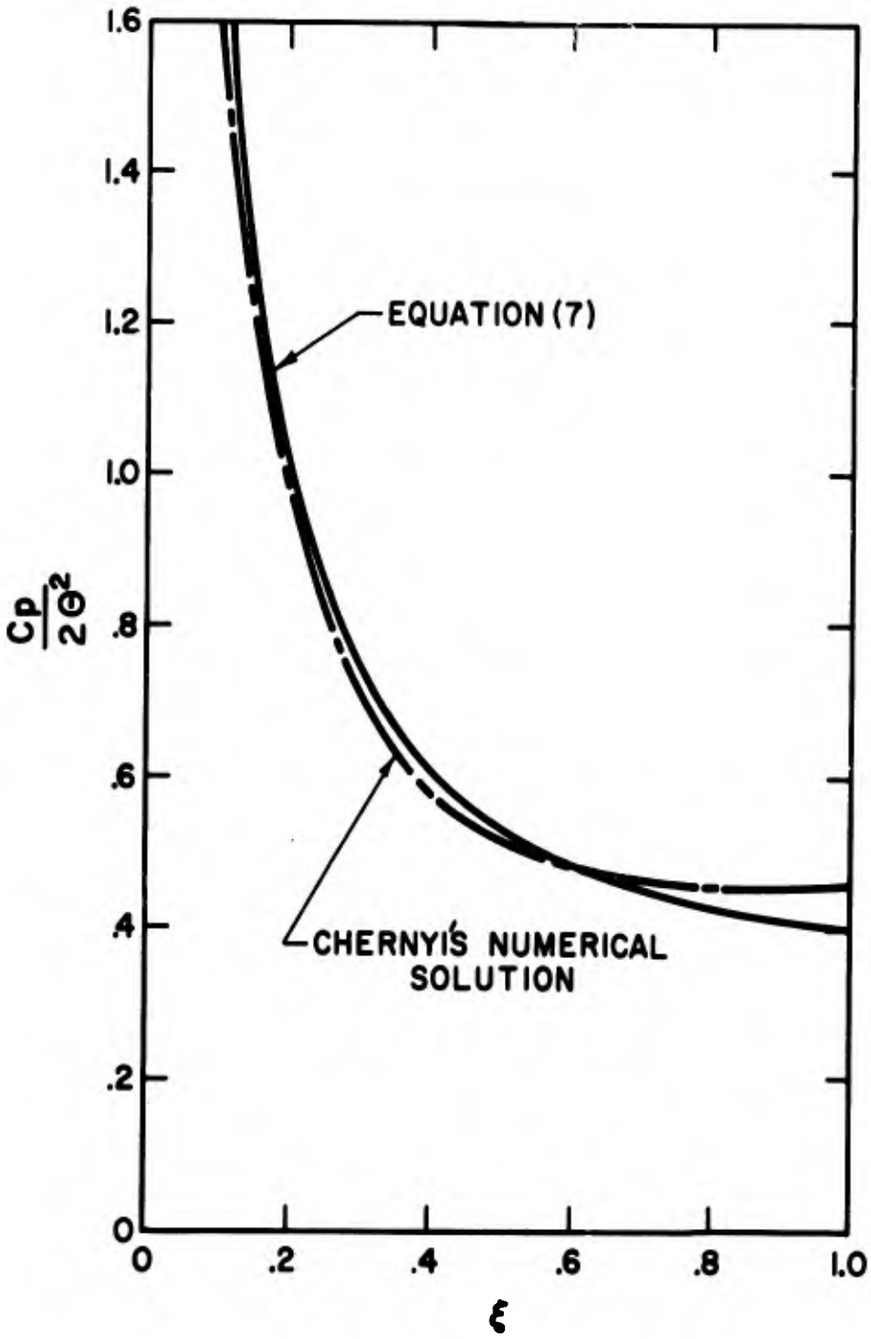
1.6
1.4
1.2
1.0
.8
.6
.4
.2
0
0
.2
.4
.6
.8
1.0
$\frac{C_p}{2\Theta^2}$
ξ
EQUATION (7)
CHERNYI'S NUMERICAL SOLUTION

FIGURE 2

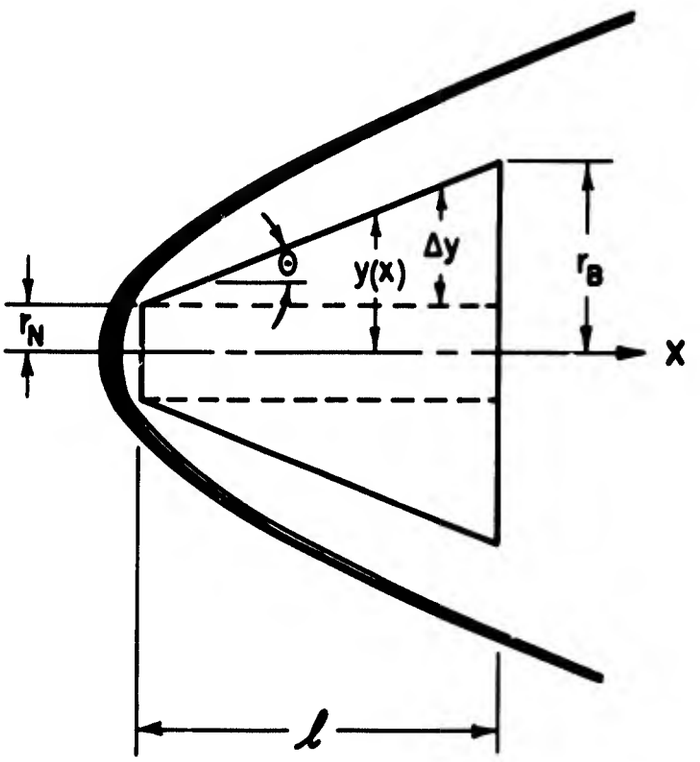

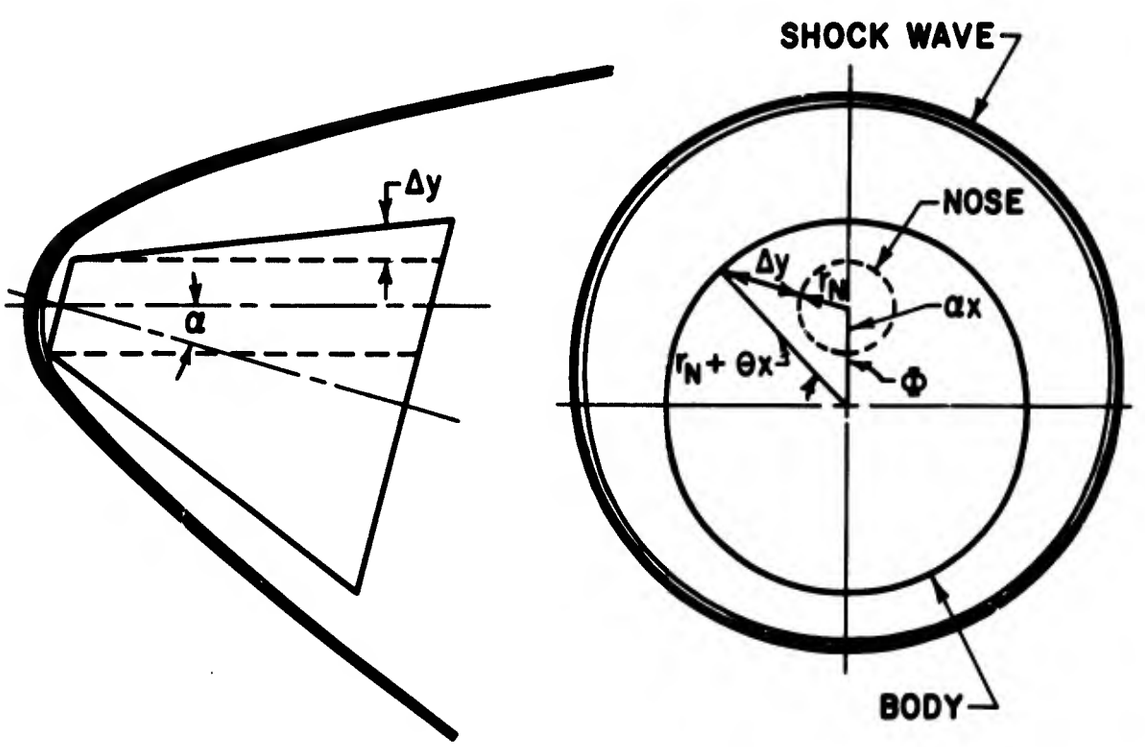

FIGURE 3

Strictly speaking, equation (8) is not compatible with the equations of motion (1) and (2) because of its dependence on the peripheral angle ϕ. The $\cos\phi$ term will introduce cross flows into the model for which no account has been taken. However, since the stability derivatives are to be evaluated under the limiting conditions of vanishing incidence and vanishing pitch rate, it is assumed that cross-flow components may be neglected

Expressing α as $|\alpha| \sin \omega t$, where $|\alpha|$ and ω are the amplitude and circular frequency of the oscillation, respectively, and noting that for small values of its argument $\sin \omega t = \omega t = (\omega L / U)\, \xi$, the piston perturbation becomes

$$r_p(\xi) = \epsilon \frac{\omega L}{U} \xi^2 \tag{9}$$

thereby defining ϵ. When this piston perturbation is introduced into the equations of motion together with the appropriate boundary conditions, there results a well-defined system of equations from which the shock and pressure perturbations may be determined. The shock perturbation is represented by the following expansion:

$$r(\xi) = (a\xi^{3/2} + b\xi^{5/2} + c\xi^{7/2} + \ldots) \sin \omega t \tag{10}$$

The coefficients may be found from direct substitution into the equation of motion and are given in table II for representative values of γ.

	$\gamma = 1.4$	$\gamma = 1.6667$
$\bar{a}$	.04607	.04304
$\bar{b}$	.20355	.21320
$\bar{c}$	.22705	.16355

$$\bar{a} = \frac{a}{\epsilon} \qquad \bar{b} = \frac{b}{\epsilon} \qquad \bar{c} = \frac{c}{\epsilon}$$

TABLE II

Direct substitution of the shock perturbation into the pressure-shock shape relation (2) results in the perturbation pressure being given by

$$p = \frac{1}{\gamma+1}\left\{\left[\frac{7}{2}Aa + \left(\frac{17}{2}Ab + \frac{21}{2}Ba\right)\xi + \left(\frac{31}{2}Ac + \frac{39}{2}Bb + \frac{39}{2}Ca\right)\xi^2\right]\sin\omega t + \frac{\omega L}{U}\left[5Aa\xi + \left(7Ab + 9Ba\right)\xi^2 + \left(9Ac + 11Bb + 13Ca\right)\xi^3\right]\cos\omega t\right\} \qquad (11)$$

Notice that the perturbation pressure is the sum of two components: the first, which is in phase with the piston displacement, is associated with the oscillation frequency, while the second, which is ninety degrees out of phase, is associated with the damping of the oscillation. Each component is plotted in figure (4).

4. Forces and Moments

Using the notation of figure (3), it has been shown[4] that the normal force and pitching moment coefficients can be determined from the following relations:

$$C_N = -\frac{2\ell^2}{S}\int_0^1 \frac{y(x)}{\ell}\, d\left(\frac{x}{\ell}\right)\int_\pi^0 C_p \cos\phi \, d\phi \qquad (12)$$

$$C_m = \frac{2\ell^2}{S}\int_0^1 \left(\frac{xy(x)}{\ell^2} + \frac{6y^2(x)}{\ell^2}\right) d\left(\frac{x}{\ell}\right)\int_\pi^0 C_p \cos\phi \, d\phi \qquad (13)$$

where the pitching axis has been taken through the nose of the body and the small angle approximations have been assumed.

The pressure integrand which is common to both equations (12) and (13) is, of course, the sum of two terms; the stationary pressure at zero angle of attack and the perturbation pressure. Due to symmetry, the integrated contribution of the former is null so the pressure integral depends only on the perturbation components and may be integrated around the periphery of the body very easily. By introducing the nose bluntness ratio η, which is the ratio of the body's nose radius to its base radius, the expressions (12) and (13) may be

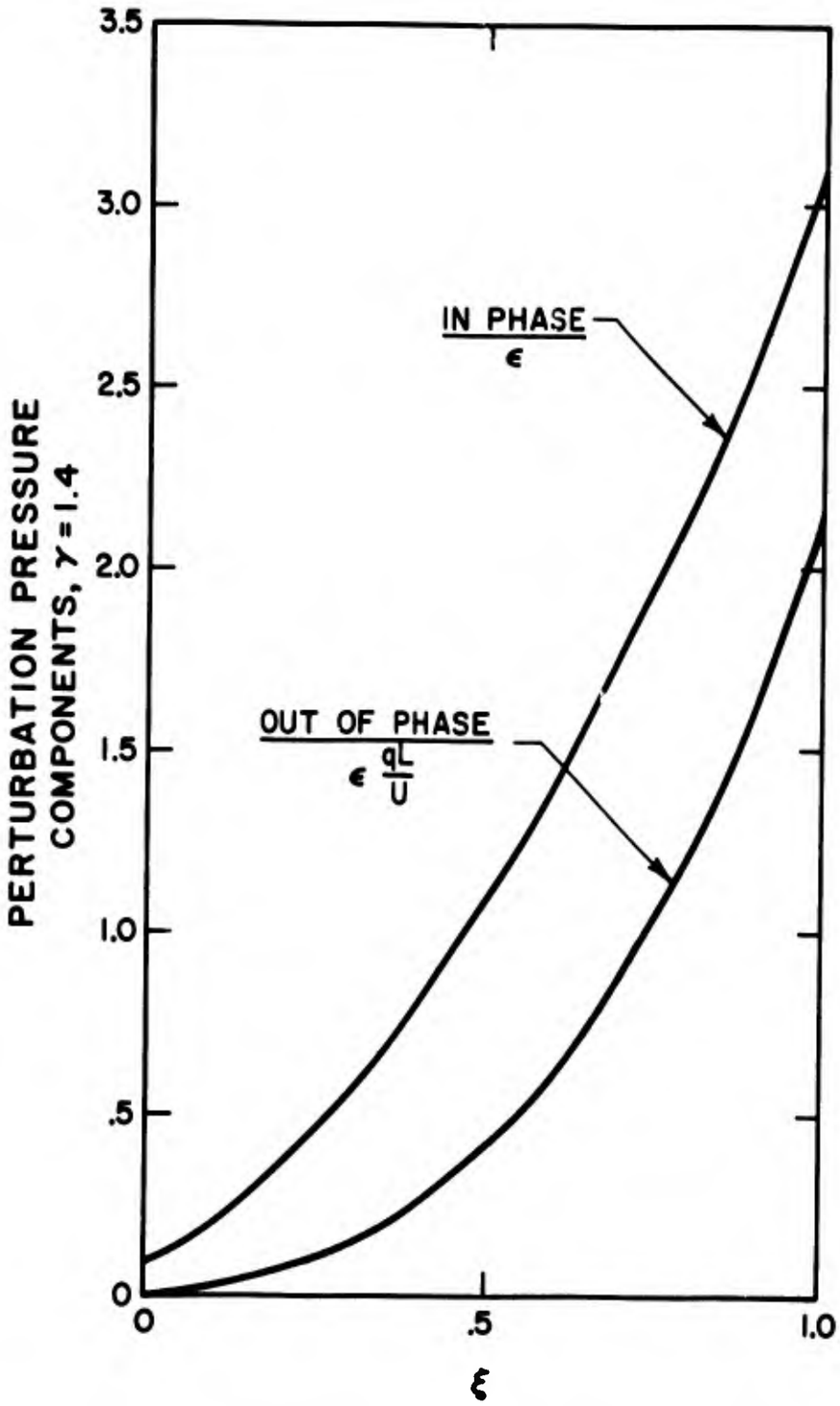
PERTURBATION PRESSURE COMPONENTS, γ = 1.4
3.5
3.0
2.5
2.0
1.5
1.0
.5
0
0
.5
1.0
ξ
IN PHASE
ε
OUT OF PHASE
ε qL/U

FIGURE 4

integrated along the length of the cone by elementary techniques once it is recognized that the variable ξ may be written as

$$\sqrt{\frac{2}{C_D}}\ \theta\ \frac{1-n}{n}\ \frac{x}{l}$$

This may be deduced from the geometry of figure (3).

The integrated values of the normal force and pitching moment coefficients (12) and (13) may then be differentiated with respect to either α or ql/V to give either the static or dynamic stability derivatives, as the case may be.

The stability derivatives for a 10° cone pitching about an axis through its nose in an atmosphere where the ratio of specific heats has a value of 1.4 are plotted in figure (5) as a function of the bluntness parameter, η. The destabilizing influence of increased nose bluntness is apparent.

COMPARISON WITH EXPERIMENT

The experimental values for C_{m_α} and C_{m_q} which were established over a broad range of nose bluntness ratios and pitching frequencies in reference (1) serve as the basis of comparison with the preceding analysis. For the configurations with larger nose bluntness ratios (greater than approximately 10 percent) these experiments found a slight and linear increase in the dynamic derivatives $C_{m_q} + C_{m_{\dot\alpha}}$, with increasing pitch frequencies, although the static derivatives were insensitive to changes in the frequency. Insofar as C_{m_q} is defined under the limiting process of frequency tending to zero, the experimental values of $C_{m_q} + C_{m_{\dot\alpha}}$ extrapolated to zero frequency have been plotted in figure (5). Frequency effects, if they exist in C_{m_q}, are of a higher order and would require a greater degree of precision in the power series expansions (5) and (9) in order to be delineated theoretically.

The stability derivatives discussed above and graphed in figure (5) are only valid for blunted cones performing pitching oscillations about an axis through the nose of the body. This unlikely circumstance, however, presents no serious limitation to the applicability of these results to bodies pitching about another axis location, in view of the axis transfer relations established by Tobak and Wehrand[4]. In

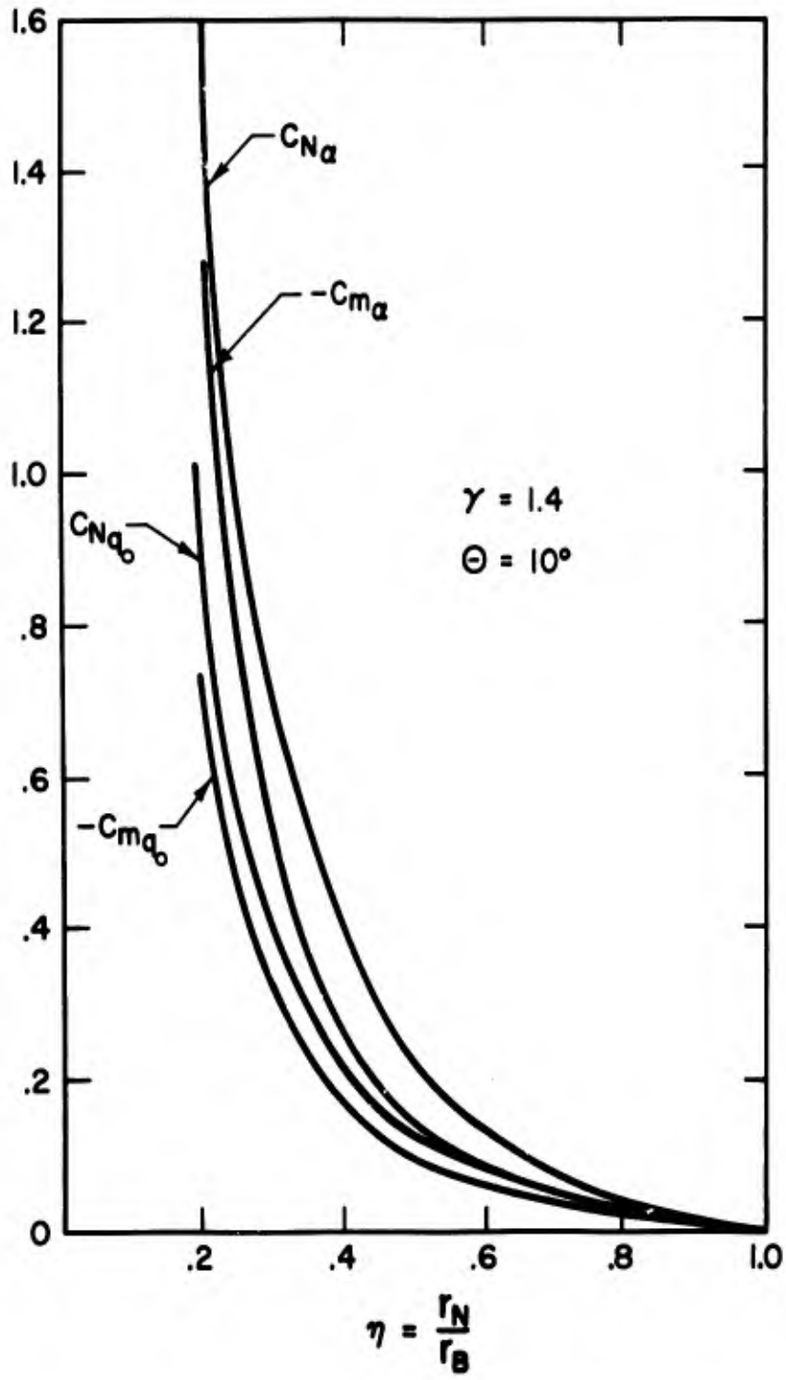
1.6
1.4
1.2
1.0
.8
.6
.4
.2
0
.2
.4
.6
.8
1.0
C_{N_α}
$-C_{m_\alpha}$
$C_{N_{q_0}}$
$-C_{m_{q_0}}$
$\gamma = 1.4$
$\Theta = 10°$
$\eta = \frac{r_N}{r_B}$

FIGURE 5

brief, if the pitch axis is located a distance x_{cg} from the nose, the normal force and pitching moment derivatives may be expressed as functions of x_{cg}/ℓ and the stability derivatives evaluated with the pitch axis through the nose of the body, with the exception of C_{N_α} which remains unchanged.

With the values of η and x_{cg}/ℓ corresponding to the experimental model of reference 1, C_{m_α} and C_{m_q} have been computed from the above expression and plotted in figure (6).

In view of the restriction (4) on ξ, the region of valid comparison in figure (6) extends up to values of the correlation parameter of reference 1, $\lambda = [\Theta (1-\eta)/2\eta]^{1/2}$ equal to around one-half. Within this range, the experimental and analytical values of C_{m_α} agree very well although there is an obvious discrepancy in the dynamic derivative $C_{m_q} + C_{m_{\dot\alpha}}$. This quantitative discordance might be attributable to the analysis' tacit assumption that the shock wave responds immediately to piston perturbations. With such a model, $C_{m_{\dot\alpha}}$ is zero since phase lags in the perturbations do not exist. On the other hand, the inability to separate the experimental C_{m_q} and $C_{m_{\dot\alpha}}$ unfortunately necessitates comparing the C_{m_q} of the theory with the $C_{m_q} + C_{m_{\dot\alpha}}$ of the experiment. It is also noted that the experiments were run at a Mach number of fourteen which corresponds to a value of 1.37 for the hypersonic similarity parameter K, while the theory has assumed that K is infinite. In view of the approximate nature of the model, the overall agreement is considered qualitatively satisfactory.

SUMMARY

An analysis of the effects of bluntness on the static and dynamic pitching moment derivatives of a slender cone has been presented. The theory was founded on Chernyi's approximate model of the flow around a blunted cone and analyzed the unsteady flow around the pitching body by perturbing its analogous piston problem.

The solution to the integrodifferential equation which describes the stationary flow field was approximated by a power series, as was the solution to the linearized perturbation equation. Equations for the stationary and perturbation shock shapes and pressure distributions have been presented while a comparison, over a defined range,

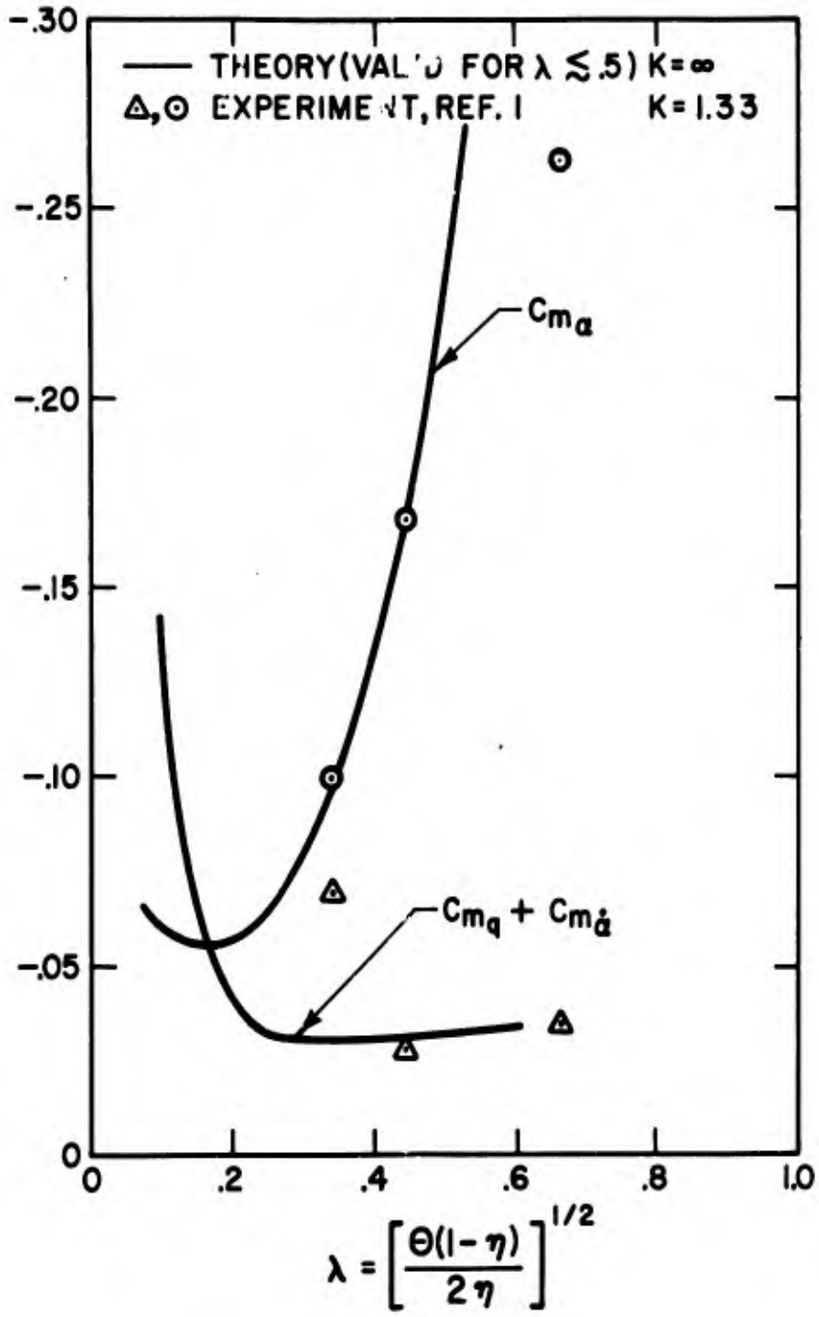
THEORY(VALID FOR λ ≲ .5) K=∞
EXPERIMENT, REF. 1 K=1.33
C_{m_α}
$C_{m_q} + C_{m_{\dot\alpha}}$
-.30
-.25
-.20
-.15
-.10
-.05
0
0
.2
.4
.6
.8
1.0
$\lambda = \left[\frac{\Theta(1-\eta)}{2\eta}\right]^{1/2}$

FIGURE 6

between the present stationary pressure distribution and Chernyi's numerical solution confirmed the accuracy of the power series technique.

It was found that the expression for the perturbation pressure distribution contained a component which was in phase with the displacement and a component which was in phase with the displacement speed. From this perturbation pressure, static and dynamic normal force and pitching moment derivatives were calculated with graphic results presented for a 10° half-angle cone.

With the aid of already existing axis transfer equations, the theoretical stability derivatives were compared with recent experimental results; and within the framework of such an approximate analysis, the agreement was satisfactory. In view of this, it can be concluded that the experimentally observed reduction in dynamic stability with increasing nose bluntness may be attributed to so-called blast wave effects.

In view of the results of this study, the prediction of dynamic stability derivatives for nose cones flying at hypersonic speeds is now possible across the whole gamut of nose bluntness: for negligibly small bluntness, Newtonian theory may be used; Walchner and Clay's empirical analysis may be used up to moderate nose bluntness; and then, the present blast wave theory may be used to predict the stability derivatives for cones of large nose bluntness.

ACKNOWLEDGEMENT

Grateful appreciation is extended to Mr. Otto Walchner for his continuing encouragement and advice during the course of this work.

REFERENCES

1. Walchner, O. and Clay, J. T., "Transactions of the Second Technical Workshop on Dynamic Stability Testing" (Sponsored by AEDC and ARO, Inc.), Volume I, Paper 8, (1965).

2. Griffith, B. J. and Lewis, C. H., "A Study of Laminar Heat Transfer to Spherically Blunted Cones and Hemisphere Cylinders at Hypersonic Conditions," AEDC TDR 63-102 (June 1963).

3. Chernyi, G. G., "Introduction to Hypersonic Flow," Translated by R. F. Probstein, Academic Press, New York (1961).

4. Tobak, M. and Wehrand, W. R., "Stability Derivatives of Cones at Supersonic Speeds," NACA TN 3788, (September 1956).

BLANK PAGE

Dr. Aleksandar Golubovic is a research chemist with the Energetics Branch, Space Physics Laboratory, Air Force Cambridge Research Laboratories. He is presently doing research on the utilization of organic materials in light-sensitive devices and for the generation of electrical power. Prior to joining AFCRL in 1964, he was senior research scientist with Tyco Laboratories, Inc., Waltham, Mass. From 1956 to 1962, he was a research associate at the Massachusetts Institute of Technology. Dr. Golubovic has a B.S. degree and a Ph. D. degree in Chemistry from the University of Zagreb, Yugoslavia, and is author or coauthor of several scientific papers.

(U) ORGANIC PHOTOVOLTAIC DEVICES

by

Aleksandar Golubovic

Space Physics Laboratory
Air Force Cambridge Research Laboratories (OAR)
L. G. Hanscom Field, Bedford, Massachusetts

Photovoltaic effects in inorganic materials are well known and have been studied extensively.[1] Voluminous research on their characteristics and properties has led to the development of operational solar cells. On the other hand, research on electrical properties of organic materials has been sporadic and inconclusive in spite of the fact that interesting electrical phenomena were observed more than sixty years ago.[2-4] Although most of the compounds are insulators ($< 10^{-13}$ mho), organic materials of nearly metallic conductivity ($< 10^{-1}$ mho) have been synthesized recently.[5] Although the electronic properties of organic semiconductors bear some resemblance to those of inorganic materials, there would appear to be fundamental differences in the mechanism of conduction resulting from the fact that organic compounds are molecular crystals whereas the inorganic semiconducting compounds are valence bonded. There are other important differences in physical and chemical properties between inorganic and organic solids. The greater thermal instability and molecular complexity of most organic materials are major factors discouraging their utilization in electronic devices. On the other hand, a wide variety of organic molecular structures is available and there is the possibility that by subtle variation of functional group substituents on a basic molecular framework, one can "custom tailor" desirable properties.

When an irradiated photoconductor is sandwiched between two different metallic electrodes a photovoltage is generated. Absolute voltages are a function of the metals used as the electrodes. In organic materials the phenomena were first studied in cells prepared from photosensitizing dyes. An open circuit photovoltage of 10 mV and a photocurrent of 10^{-8} amperes was observed in a photocell made from pinacyanol.[6] Also, systems such as gold (or aluminum) polycyclic aromatic hydrocarbon-alkali metal generated photovoltages of up to 1 volt and power as high as 10^{-8} watts.[7] The development of inorganic p-n junction solar cells inspired attempts to make organic p-n junctions from similar configurations. Meier[8] constructed cells from p-conductive merocyanines and n-conductive malachite green and recorded a maximum open circuit voltage of 100 mV and photocurrents of 10^{-8} to 10^{-9} amperes. Nelson[9] prepared surface cells with junctions between dyes and cadmium sulfide and observed a maximum photopotential of 200 mV across platinum electrodes. Meier,[10] using the same materials, obtained comparable photovoltages with sandwich cells and with silver bromide and rhodamin-B

layers[11] he observed photovoltages of up to 350 mV. Calvin and Kearns[12] obtained open circuit photovoltages of 200 mV in cells prepared from a combination of oxidized tetramethyl-p-phenylenediamine and magnesium phthalocyanine. Needler[13] recently reported photovoltages up to 3 volts from sandwich cells containing thin layers of sensitizing dye and an arylamine.

Unfortunately, none of the above systems generates currents greater than 10^{-8} amperes and hence the power output is severely restricted. In the following work, we have examined different materials and cell parameters in an attempt to increase the power output of cells made from organic thin films by decreasing the internal resistance.

EXPERIMENTAL

Thin film cells were fabricated as follows: Aluminum electrodes (average transparency 20%) are deposited by high vacuum sublimation on a pyrex glass plate (25 by 18 mm). The organic compound and a second electrode of gold are deposited in turn on the aluminum electrode. By the same method, one can deposit adjacent organic layers of different materials. The construction of the cell is shown in Figure 1. The deposition assembly, shown in Figure 2, allows the preparation of four separate cells simultaneously. Organic materials are sublimed from tantalum or stainless steel cups at 200 to 300°C at a pressure of 1 to 2×10^{-6} mm Hg. It was found that the quality of the gold electrode depends on the smoothness of the organic layer. Best results are obtained when organic compounds are sublimed through a distance of 10 cm.

Two classes of organic materials were used in the present work: (a) Photoconductive compounds (See Table 1); (b) Nonphotoconductive materials such as electron acceptors (7,7,8,8- tetracyanoquinodimethan (TCNQ), chloranil, and so forth), ion-radical salts (TCNQ-triethylammonium anion-radical complex), and the free radical $\alpha_1 \alpha'$ - diphenyl-β-picrylhydrazyl (DPPH). Two kinds of cells were fabricated: cells utilizing photoconductive material in the form of a single layer, and cells utilizing materials of type a and b in the form of a double layer. The photoconductor was deposited on the aluminum electrode in the double layer cells.

Commercially available batches of anthracene, tetracene, and pentacene were purified by crystallization, chromatography, and sublimation. Phthalocyanine was purified by high vacuum sublimation. Aceanthraquinoxaline was synthesized from the condensation reaction between aceanthraquinone and o-phenylenediamine. The yellow product was purified by chromatography and crystallization (mp 250°). Analytic results are: (Calcd for $C_{22}H_{12}N_2$: C, 86.82; H, 4.1; N, 9.22. Found: C, 86.64; H, 4.19; N, 8.96%). The sample of 2, 7 dinitrofluoren -$\Delta^{9\alpha}$-malononitrile (DFM) was kindly furnished by Dr. T. K. Mukherjee.[14]

TABLE 1. Representative Values of Resistivity, Dark Activation Energy, and Carrier Type for the Organic Photoconductors Used in the Present Work.

Compound	Structural Formulae	Resistivity ohm-cm	Activation Energy eV	Carrier Type
Anthracene[a]	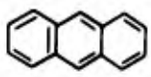	1.3×10^{14}	1.94	Hole
Tetracene[a]	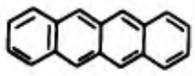	1.0×10^{15}	1.69	Hole
Pentacene[a]	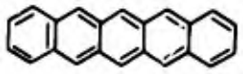	1.0×10^{14}	1.50	Hole
Aceanthra-quinoxaline[b]	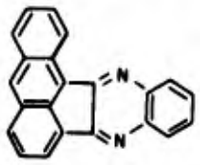	1.8×10^{15}	1.98	Hole
Phthalocya-nine[c]	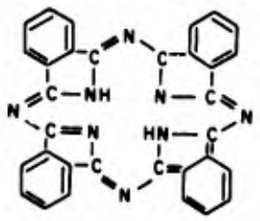	1.0×10^{12}	1.70	Hole
2,7 dinitro-fluoren -$\Delta^{9\alpha}$-malononitrile (DFM)[d]	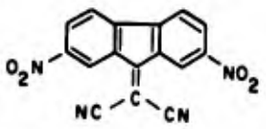	2.0×10^{15}	2.28	Electron

a. D.C. Northrop and O. Simpson, Proc. Ray. Soc. (London) A 234:124 (1956).

b. A. Golubovic, Unpublished results.

c. J. Kaufhold and K. Haufe, Z. Elektrochem., Ber. Bunsenges. Physik. Chem., 69: 168 (1965).

d. T.K. Mukherjee, J. Phys. Chem. (in press).

ELECTRICAL MEASUREMENTS

The cell was illuminated through the semitransparent aluminum electrode by a 500 watt quartz-iodine lamp. Measurements of voltage (V_O) and current (I_O) were taken with a Keithley model 150A voltmeter (input resistance 10^{11} ohms) and a Keithley model 610A electrometer respectively, both connected to a Moseley X-Y recorder model 135 AM. The light intensity was varied by using Kodak neutral-density filters. The energy of the incident light was determined with the YSE-Kettering Radiometer model 65. The spectral dependence of the photocurrents was measured in the visible region by scanning with a Bausch and Lomb grating monochromator with a 900-watt xenon lamp as the light source. The entrance slit of the monochromator was set at 5 mm and the exit slit at 2 mm. The absorption spectra of the organic films were determined from a Cary 14 spectrophotometer. The film thickness was measured by means of a Sloan interferometer model M-100.

RESULTS AND DISCUSSION

The results of the measurements are summarized in Table 2. The parameter L is the intensity of monochromatic light incident on the organic material after passage through the glass and the semitransparent aluminum electrode. The photovoltage (V_r) is the voltage read when the cell is connected in series to the 10^6 ohm input resistor of the Moseley X-Y recorder model 135 AM. The final column lists the efficiency defined as the ratio in percent of power output (P) to input light intensity (L). In all experiments the aluminum electrode was negative with respect to the gold electrode indicating the transfer of electrons from the organic material to the aluminum electrode. The polarity was uninfluenced by the direction of illumination.

In general, the power output of the cells is improved upon addition of a second layer of an electron acceptor or an ion-radical complex. For example, with tetracene as the starting material, the efficiency increases by the factors 1.2, 1.4, 1.5, and 2.5 upon addition of a second layer of DFM (cell No. 14), TEA^+TCNQ^-TCNQ (cell No. 4), chloranil (cell No. 7), and TCNQ (cell No. 5), respectively. This finding confirms previous observations 15, 16, 17 that both the dark current and the photocurrent in p-type organic photoconductors can be enhanced substantially by doping with electron-acceptors. The power output of the tetracene cell is improved by adding a layer of the anion radical salt TEA^+TCNQ^-TCNQ, whereas the use of the neutral free radical (DPPH) has a detrimental effect.

The relationship between photocurrent and light intensity for a number of the cells (Figures 3, 4, and 5) follows the equation $I_O = KL^n$ where I_O is the photocurrent, L the light intensity, and K is a constant. The exponents n of these plots vary from 0.86 to 1.6. For $n \leq 1$,

TABLE 2. Results of Electrical Measurements on Organic Photovoltaic Cells. System: Aluminum - organic material(s) - gold

Cell Number	Organic Material	Light Intensity (L) Milliwatts	Cell Resistance Ohms	Open Circuit Photovoltage (V_o) Volts	Photovoltage Under Load (V_r) Millivolts	Photocurrent (I_o) Microamperes	Power (P) Microwatts	Efficiency $\left(\frac{P}{L}\right)$ Percent
1	Anthracene	23	1.0×10^7	1.08	36	0.04	0.04	1.92×10^{-4}
2	Anthracene + TEA^+TCNQ^-TCNQ	35	2.0×10^5	1.00	125	0.13	0.13	3.93×10^{-4}
3	Tetracene	20	7.0×10^6	1.02	390	0.71	0.71	3.55×10^{-3}
4	Tetracene + TEA^+TCNQ^-TCNQ	55	1.3×10^5	0.75	575	3.75	2.80	5.05×10^{-3}
5	Tetracene + TNCQ	28	2.0×10^5	1.10	760	2.30	2.50	8.92×10^{-3}
6	Tetracene + DPPH	86	1.5×10^5	1.00	360	.63	.63	7.27×10^{-4}
7	Tetracene + Chloranil	30	1.3×10^5	1.10	480	1.50	1.60	5.33×10^{-3}
8	Pentacene	25	1.5×10^5	.75	326	.54	0.40	1.60×10^{-3}
9	Pentacene + TEA^+TCNQ^-TCNQ	31	8.0×10^4	.77	355	.68	0.51	1.65×10^{-3}
10	Pentacene + TCNQ	14	2.0×10^4	.59	323	.49	0.29	2.10×10^{-3}

TABLE 2. Results of Electrical Measurements on Organic Photovoltaic Cells. System: Aluminum - organic material(s) - gold (Continued)

Cell Number	Organic Material	Light Intensity (L) Milliwatts	Cell Resistance Ohms	Open Circuit Photovoltage (V_o) Volts	Photovoltage Under Load (V_r) Millivolts	Photocurrent (I_o) Microamperes	Power (P) Microwatts	Efficiency $\left(\frac{P}{L}\right)$ Percent
11	Aceanthraquinoxaline	37	1.5×10^6	1.06	84	.35	0.37	1.00×10^{-3}
12	Aceanthraquinoxaline + TEA^+TCNQ^-TCNQ	41	1.6×10^5	.79	420	.75	.59	1.44×10^{-3}
13	DFM	22	1.0×10^4	.21	12.5	.02	0.003	1.54×10^{-5}
14	Tetracene + DFM	45	3.0×10^4	.85	437	2.25	1.94	4.30×10^{-3}
15	Phenanthrenequinone[a]	19	4.0×10^6	.69	7.1	.008	0.005	2.80×10^{-5}
16	Phthalocyanine	54	2.0×10^4	.70	255	.29	0.20	3.70×10^{-4}
17	Phthalocyanine + TCNQ	32	2.3×10^4	.51	195	.64	0.33	1.00×10^{-3}
18	Phthalocyanine + TEA^+TCNQ^-TCNQ	28	2.0×10^4	0.60	306	2.85	1.71	6.18×10^{-3}
19	Phthalocyanine + DPPH	30	3.0×10^4	0.60	234	0.67	0.42	1.30×10^{-3}

a. Cell No. 15 using nonphotoconductor included for comparison.

Almeleh and Harrison[18] have postulated that the charge carriers are either generated by a single exciton process and recombine by a monomolecular mechanism or that they are generated by a double exciton process and recombine via a bimolecular process. For $n > 1$, these authors speculate that a double exciton process and a monomolecular recombination mechanism are dominant.

The spectral dependence of the photocurrent for tetracene cells Nos. 3 and 5 is shown in Figure 6. Both cells followed the optical absorption spectrum of tetracene itself. In other cells, although the main absorption peaks of the photoconductors are retained in the curves of photocurrent versus wavelength, the poor resolution in the 300 to 500 $m\mu$ range made detailed comparison difficult. In all cases, the photoconductivity threshold nearby coincides with the threshold for optical absorption.

The activation energies for photoconductivity of a number of cells were determined from the relationship between photocurrent and temperature which followed the equation $I_o = A \exp [-\Delta E_{ph}/kT]$ where A is a constant, k the Boltzmann constant, T is absolute temperature, and ΔE_{ph} the photoactivation energy. The results shown in Table 3 are all close to the typical value of 0.2 eV for photoactivation in organic materials.

TABLE 3. Activation Energies of Photocurrents Measured over the Temperature Range 298 to 363°K

Cell No.	Materials	ΔE_{ph} in eV
3	Tetracene	0.124
4	Tetracene + TEA^+TCNQ^-TCNQ	0.267
5	Tetracene + TCNQ	0.195
8	Pentacene	0.144
9	Pentacene + TEA^+TCNQ^-TCNQ	0.197

SUMMARY AND CONCLUSION

Photovoltaic cells containing organic materials have been prepared. The fabrication of such cells involved a sublimed layer of an organic photoconductor sandwiched between aluminum and gold electrodes.

The photocurrent output in the above cells has been enhanced by secondary layers of electron-acceptors. There is some indication that the efficiency of the photovoltaic cell can be improved further by suitable choice of more powerful acceptors.

It is evident that the power output of the present cells is still quite inferior to that of conventional photovoltaic devices. These cells however, mark a distinct improvement in the efficiency with which light energy can be converted into useful electrical energy by use of organic materials. Research on the phenomenological aspects of photovoltage in organic materials, in conjunction with the development of new materials, supports the premise that organic photovoltaic cells will prove to be practical devices for energy conversion.

ACKNOWLEDGMENTS

The author wishes to thank Dr. Tapan K. Mukherjee for many fruitful discussions and suggestions and Miss Noreen A. Dimond for very able assistance with the measurements.

EFERENCES

1. Moss, T.S. Reports Progr. Phys., 28: 15 (1965).
2. Pocchettino, A. Acad. Lincei. Rend., 15: 355 (1906).
3. Zcodro, N. Bull. Acad., St. Petersburg, 6: 727 (1919).
4. Byk, A. and Borck, H. Ber. Deut. Physik. Ges., 8: 621 (1910).
5. Acker, D.S. et al., J. Am. Chem. Soc. 82: 6408 (1960).
6. Noddack, W. and Meier, H. Z. Elektrochem. Ber. Bunsenges. Physik. Chem., 57: 691 (1953).
7. Inokuchi, H. and Akamatu, H. Solid State Physics, 12: 93 (1961).
8. Meier, H. J. Phys. Chem., 69: 719 (1965).
9. Nelson, R.C. J. Opt. Soc. Am., 46: 13 (1956).
10. Meier, H. and Albrecht, W. Z. Elktrochem., Ber. Bunsenges. Physik. Chem., 67: 838 (1963); 68: 64 (1964).
11. Meier, H. and Albrecht, W. Z. Elektrochem. Ber. Bunsenges. Physik. Chem., 69: 160 (1965).

12. Calvin, M. and Kearns, D. J. Chem. Phys. 29: 950 (1958).

13. Needler, W.C. J. Chem. Phys., 42: 2972 (1965).

14. Mukherjee, T.K. J. Phys. Chem. (in press).

15. Hoegl, H. J. Phys. Chem., 69: 755 (1965).

16. Kearns, D.M., Tollin, G.M., and Calvin, M. J. Chem. Phys., 32: 1020 (1960).

17. Meier, H. and Albrecht, W. Z. Physik. Chem. N.F., 39: 249 (1963).

18. Almeleh, N. and Harrison, S.E. J. Phys. Chem. Solids. Pergamon Press, 26: 1571 (1965).

DETAILS OF CELL DESIGN

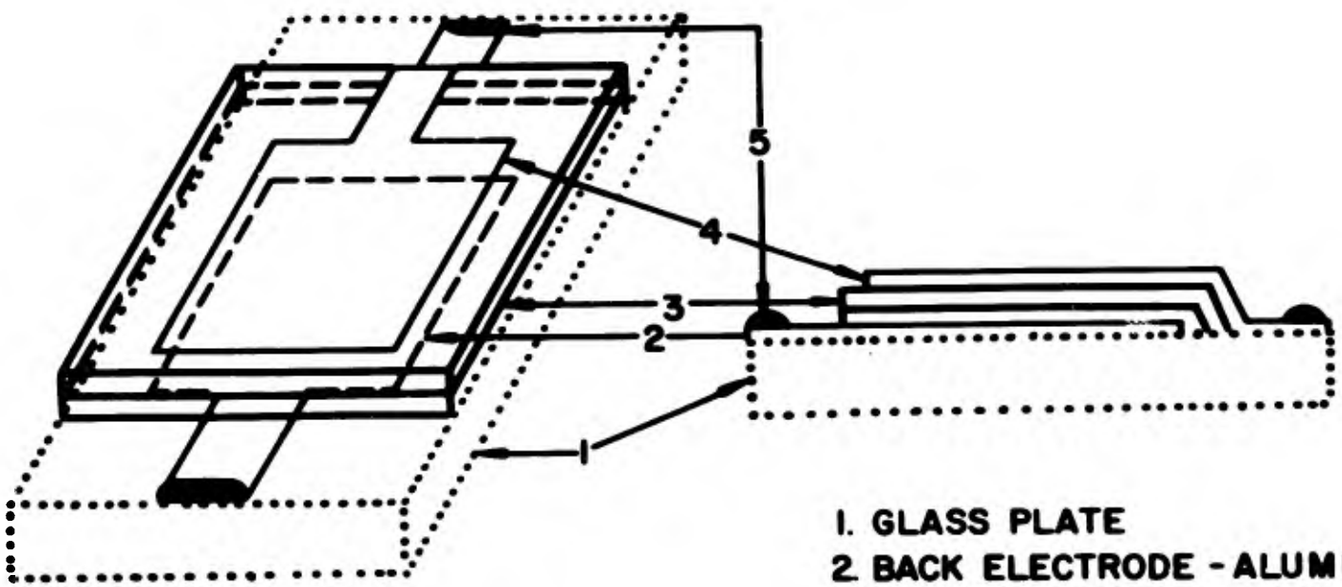

1. GLASS PLATE
2. BACK ELECTRODE - ALUMINUM
3. SINGLE OR MULTIPLE LAYER OF ORGANIC MATERIAL
4. FRONT ELECTRODE
5. SILVER PASTE CONTACT

Figure 1. Details of Cell Design

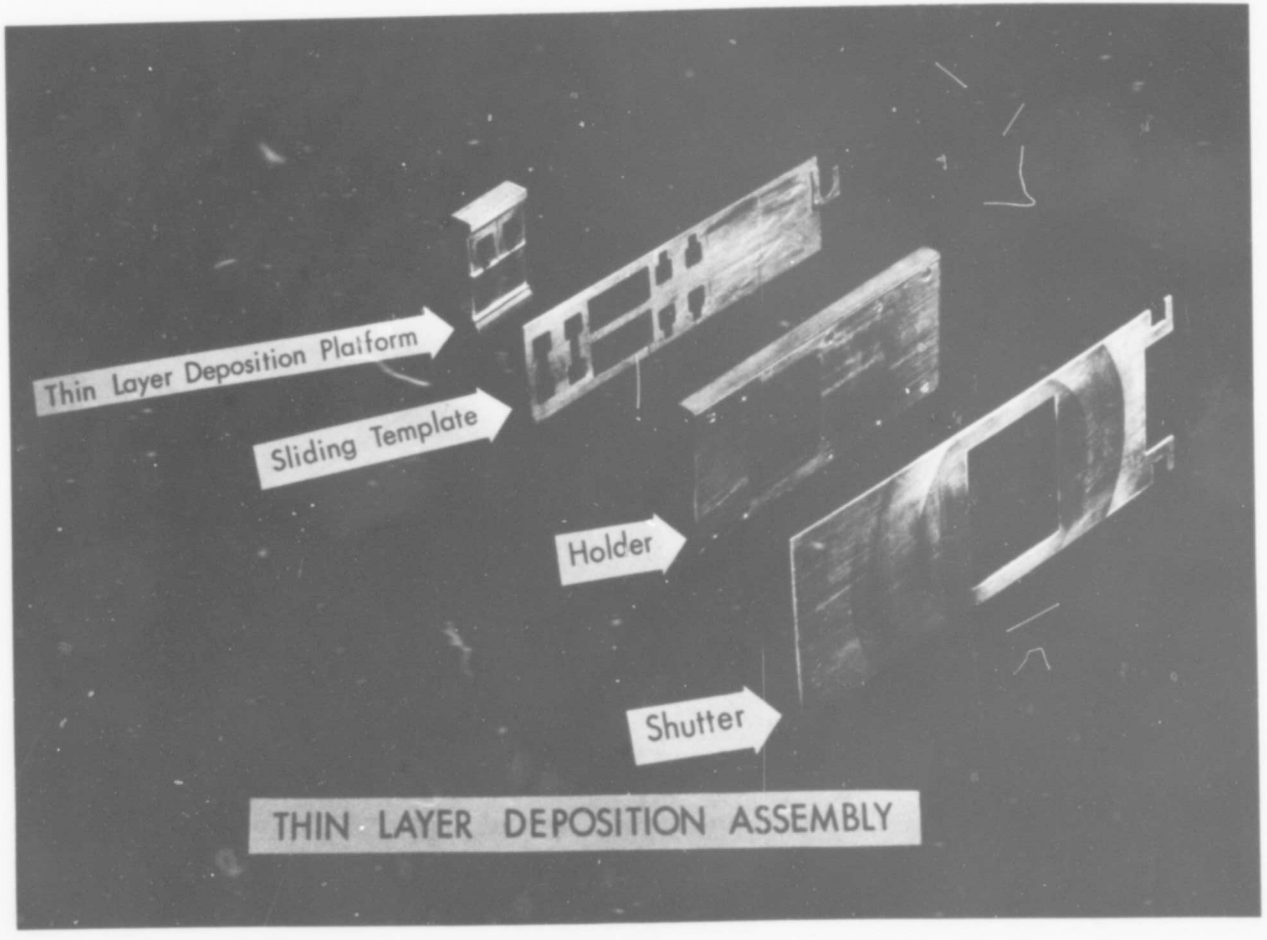

Figure 2. The Thin Layer Deposition Assembly

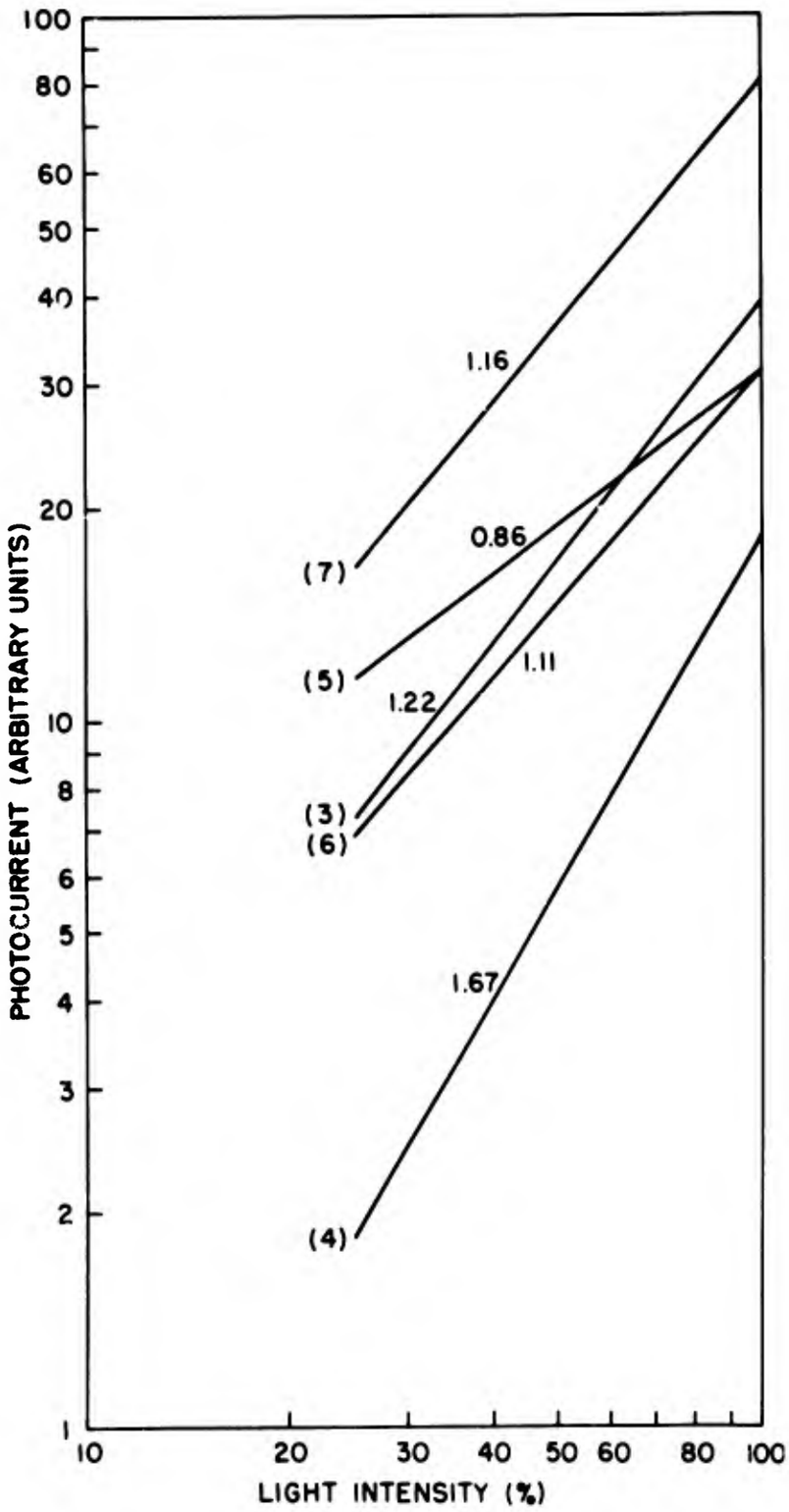

Figure 3. Photocurrent – Light Intensity Relationship of Tetracene Photocells. The numbers in parenthesis represent the cells in Table 2

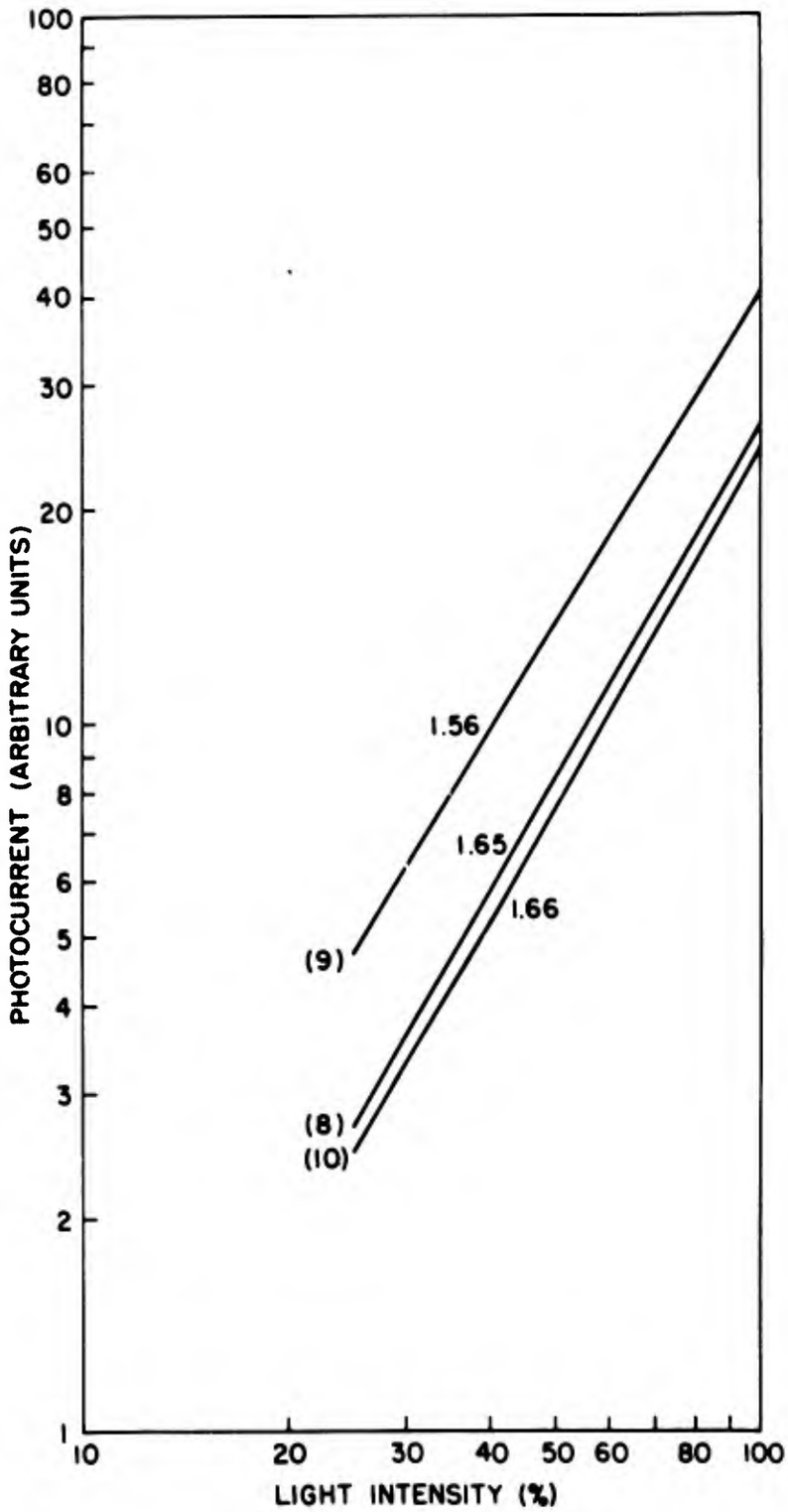

Figure 4. Photocurrent — Light Intensity Relationship of Pentacene Photocells. The numbers in parenthesis represent the cells in Table 2.

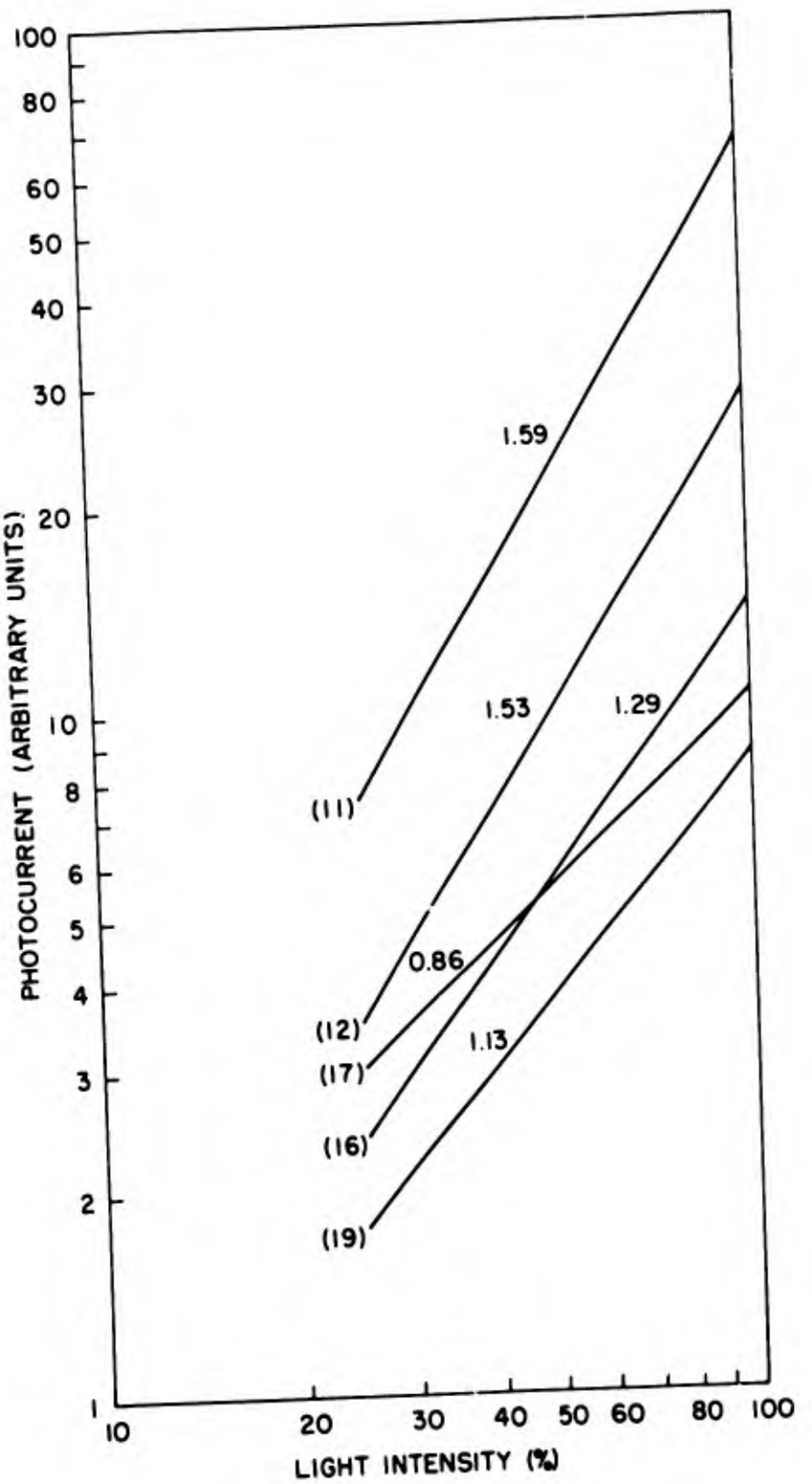

Figure 5. Photocurrent – Light Intensity Relationship of Phthalocyanine and Aceanthraquinoxaline Photocells. The numbers in parenthesis represent the cells in Table 2.

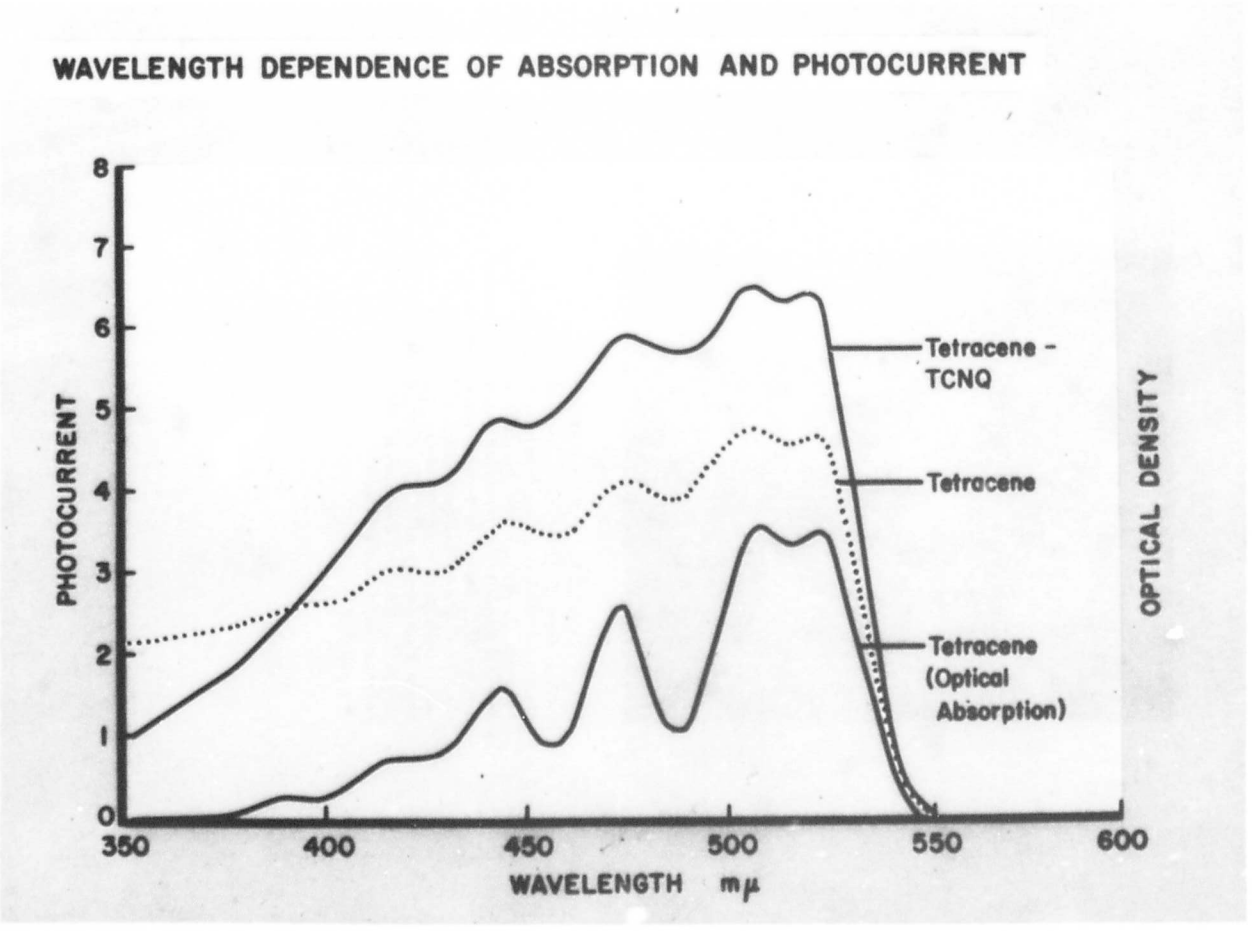

Figure 6. Wavelength Dependence of Absorption and Photocurrent

Capt. Dirk H. deDoes is assigned to the Aerospace Mechanics Division, the Frank J. Seiler Research Laboratory. He received his B.S. degree in Aeronautical Engineering from San Diego State College, and his M.S. degree in Aerospace Engineering from the University of Southern California. He has also completed course requirements for a Ph. D. in Aerospace Engineering at USC. Capt. deDoes was assigned to the Air Force Institute of Technology before coming to FJSRL.

(U) TIME-OPTIMAL ATTITUDE CONTROL OF A SPINNING VEHICLE

Dirk H. de Does, Captain, USAF
FJSRL, OAR, USAF Academy, Colorado, 80840

The design of efficient attitude control systems for extra-atmospheric vehicles is of considerable importance. The basic functions of a spacecraft attitude control system are those of maneuvering the vehicle in a prescribed manner and stabilizing it when a desired orientation has been acquired. One important attitude control problem is that of maneuvering a spin stabilized vehicle where various performance criteria are considered. For example the performance of a space vehicle attitude control system may be evaluated in terms of the amount of fuel consumed during a specified maneuver or the time required to re-orient a vehicle from some initial position to a desired final position.

The research discussed in this paper is directed to the problem of re-orienting a spinning vehicle in minimum time. Such a maneuver is important in certain military and scientific missions. For example, consider the problem of making rapid corrections in the orientation of a spinning re-entry vehicle during the extra-atmospheric portion of an intercontinental trajectory. During the latter phase of such trajectories the vehicle's attitude influences a variety of parameters including aerodynamic forces during initial contact with the atmosphere. Thus minimum time attitude control may be an important consideration for such mission requirements.

The problem considered, a time-optimal control problem, is one of properly orienting a spinning vehicle with respect to specified reference directions, starting from known initial conditions of the vehicle's attitude and nutation rates. This problem has been studied extensively by the author [1]. As a result:

1. Mathematical techniques for computing the time-optimal control law for a wide class of vehicles in which small changes in attitude are required were obtained.

2. The influence of spin rate, vehicle geometry, control magnitude, and thruster configuration (Figure 1) on the time required to optimally re-orient a spinning vehicle was demonstrated.

3. True time-optimal solutions which may be useful in conjunction with feedback control or as a reference in the evaluation of nearly time-optimal schemes were obtained.

Discussion of the Problem

In several respects, the analytic and computational aspects of the optimal attitude control problem are very difficult. When confronted with such situations one must often rely on some type of idealized model. Such models often provide significant insight as to the behavior of the actual system. For the purpose of this analysis it was assumed that the system could be represented mathematically as a rigid body with a single axis of symmetry. This choice represents a realistic compromise between analytic models which are exceedingly simple to analyze and in turn provide relatively little insight as to the behavior of the actual physical system and models that closely represent the physical system but are very difficult to handle from a computational standpoint.

The problem specifications must also include a statement as to the type of control device employed (i.e., reaction jets, reaction wheels, etc.). For the problem considered in this text it was assumed that control is provided by various combinations of thrust-limited reaction jets or small rockets; the controller configurations considered are shown in Figure 1. Case (a) corresponds to a basic 4-jet configuration. Cases (b) and (c) represent the situation where two or three thrusters of the basic configuration, case(a), have failed respectively. Case (d) corresponds to a single gimballed jet which may be oriented arbitrarly in a plane normal to the vehicle's spin axis. In case(e), the basic spacecraft consists of two separate sections which are connected at the axis of symmetry by a bearing; the aft section (which houses the attitude sensors and four body fixed reaction jets) has a zero spin rate about the vehicle's axis of symmetry.

Figure 1 Control Jet Configurations

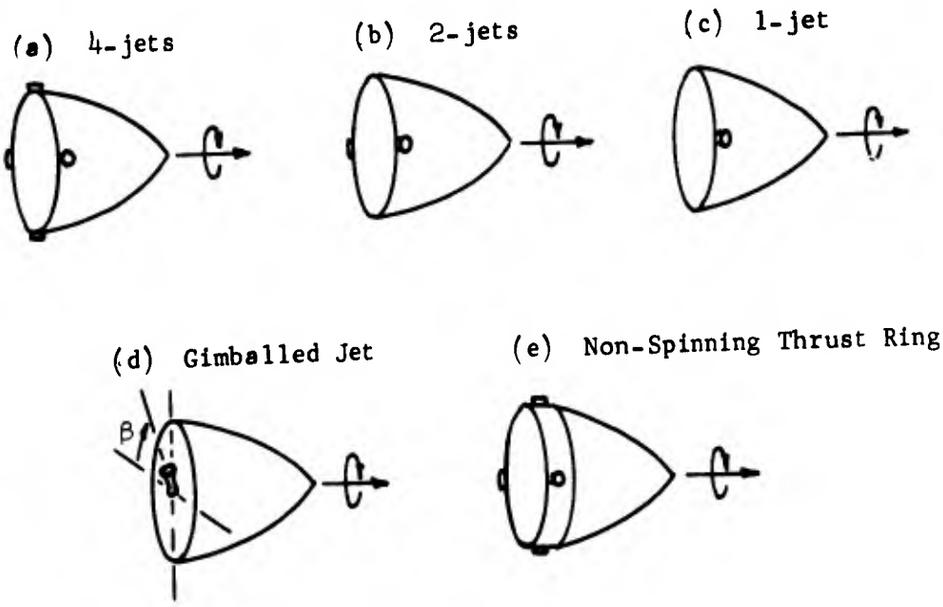

The system under investigation was represented mathematically by a set of linear differential equations of the form

$$\dot{\vec{x}}(t) = A(t)\,\vec{x}(t) + B(t)\,\vec{u}(t)$$

These equations relate angular velocity and position, forces and accelerations, nutation rates and time, etc. In the above system of equations $\vec{x}(t)$ represents a vector whose components are the state variables. These give the state of the system at any time and thus represent the angular position and velocities of the system. The components of the vector $\vec{u}(t)$ represent control variables that one may use to control the system. For the system described in the previous section, these controls correspond to control jet angle, thrust magnitude, and jet "off-on" times. The primary objective is then to determine a minimum time maneuver from all possible control sequences which will cause a specified change in the state of the system.

For systems described mathematically by the preceding equation it is possible to obtain the necessary conditions for the time-optimal control law by the application of a mathematical technique known as the maximum principle, [2]. If the maximum principle is applied to the equation representing a system with a gimballed jet, case (d), one obtains the optimal steering law as a continuous function of time. However, when applied to equations representing the remaining configurations, cases (a), (b), (c), (e) it is found that the control jets must operate discontinuously or in an "on-off" mode. The maximum principle thus gives only the qualitative nature of the control law. To obtain a control law that quantitatively satisfies all the conditions of the physical system it is necessary to determine the initial amount of thrust, the time the engine is to be turned on or off and the final time when the optimum maneuver is to be completed. This results in the requirement to solve a two point boundary value problem, the satisfying of specified values for the initial and final states.

Solution to the Time-Optimal Control Problem

For systems of fourth order and greater, a solution to the two point boundary value problem usually requires a computational scheme which involves the use of a high speed digital or analog computer. However the author has succeeded in generating closed form solutions for case (d) and for specific situations arising in cases (a) and (b). These significant results will be discussed in more detail in the following paragraphs.

The first step toward the results discussed earlier involved normalizing the set of differential equations which describe the motion of the vehicle. Thus, all information essential to the problem (i.e., spin rate, vehicle geometry, thrust level, initial nutation rates, etc.) may be condensed into a minimum number of physical parameters which

completely describe the system. This procedure has three important advantages: the number of cases which must be considered and in turn the computer time required to investigate the control problem are greatly reduced; the influence of system parameters on the control law and the terminal time can be readily determined; and, the control law for a wide range of problems may be conveniently described in terms of these physical parameters. This entire procedure is unique in that a family of solutions is generated for each analytic or numerical solution to the two point boundary value problem. The utility and uniqueness of these solutions are discussed in the following paragraphs.

In the case where control is provided by a gimballed jet, case (d), the author [1] has found closed form solutions to the attitude control problem. In this case, symplifying assumptions are held to a minimum in that the initial and final values of the state variables were chosen to be as realistic as possible and yet retain solvability of the system in closed form. Solutions of this type are very useful in that one may readily determine both the jet steering angle β (see Figure 1) as a function of time and the optimum maneuver for a wide range of problems which are specified in terms of the physical parameters. Thus if a control problem lies within the scope of this analysis one is able to readily determine how an ideal control system must operate in order to carry out a given maneuver in minimum time. In addition, the characteristics of the optimal control law and the minimum time required to reorient a spinning vehicle can be determined. These concepts will be demonstrated by an example problem at the end of this text.

In cases (a, b, c, e) the control jets must operate in an "on-off" or discontinuous mode and therefore it is more difficult to generate closed form solutions as was the case in the preceding paragraph. In most instances where the control must operate in a discontinuous mode the two point boundary value problem must be solved on a high speed digital computer. Many of the modern computational procedures which are used for solving boundary value problems of this type employ mathematical schemes which require an initial estimate of the steering or control law and the terminal time. An algorithm or computing rule is then used to systematically modify the steering law and the terminal time until a specific set of boundary conditions is satisfied. The computer time required to carry out this process depends upon how close the initial "guess" is to be actual optimal control law. If the results of an analysis are to be useful in terms of evaluating the effect of vehicle geometry, spin rate, thrust level, etc., then the two point boundary value problem must be solved repeatedly for a wide range of system parameters. This would become very inefficient in terms of computer usage unless a systematic method was developed for reducing the error between the initial "guess" and the correct optimal control law. The significant result of this study is the development of a method which overcomes the computational difficulties described previously and greatly reduces the computer time required.

Two concepts are essential to the success of the method and actually increase its power and versatility. The first demands that all information essential to the problem (i.e., spin rate, thrust level, initial nutation rates, etc.) must be combined into a minimum number of physical parameters which completely describe the system. This procedure was described in a previous paragraph. The second is that the algorithm's utility is directly related to the choice of the mathematical model for the system. For an appropriate mathematical representation of the system, exact analytic solutions have been found. These solutions are based on specific sets of values of the physical parameters for a particular system. The computational scheme which was employed makes use of these exact solutions in that variations are made in the physical parameter space, starting from the known solutions. The result is a technique which is efficient in terms of computer usage in that the error between the "starting" and actual control laws is very small. In addition, exact analytic solutions have been found for cases (a, b) for a range of parameters where the time required to complete a maneuver is small compared to the vehicle's spin rate.

The advantage of this computational scheme compared to those employed by others to solve the optimal attitude control problem is that families of solutions are generated and plotted as graphs with a minimum expenditure of computer time. From the resulting graphs one can readily determine the control law, the optimal maneuver, and the minimum time required to re-orient a spinning spacecraft. Thus true time-optimal solutions are provided which may be used in conjunction with feedback control or as reference in the evaluation of nearly time-optimal control schemes. These concepts can be understood more readily and the utility of the method may be demonstrated by considering as an example the optimal control for a typical re-orientation maneuver.

Example

Consider the problem of re-orienting a spinning spacecraft in minimum time where control is provided by a gimballed reaction jet, case (d). Hence the minimum time required to maneuver the spacecraft thru a prescribed angle θ is sought. (For this particular problem the author has been able to find closed form solutions provided the initial nutation rate is zero. [1]) To be of practical value, applicable to many sizes and types of vehicles, the minimum time should be specified in terms of the physical parameters. The method discussed earlier provides such a representation of the minimum time for re-orientation. It provides a dimensionless angle of re-orientation, in terms of the moments of inertia about the vehicle's principal axis, the spin rate, the maximum torque, and the actual angle of re-orientation. It also provides a dimensionless minimum final time, T_f, in terms of the actual final time, the vehicle's geometry, and the spin rate. Figure 2 shows a plot of the dimensionless minimum final time versus the dimensionless angle of re-orientation. Thus if the terminal attitude is changed, the

spin rate increased or decreased, the vehicle's mass altered, or a smaller or larger control jet used, the new terminal time may be determined directly from Figure 2. Similar curves have been determined from which the optimal control laws have been found. Use of these curves is illustrated in Figure 4, where the terminal time is given for various combinations of spin rate and thrust level. The corresponding vehicle configuration and re-orientation angle are given in Figure 3.

Figure 2 Dimensionless Minimum Final Time vs. Dimensionless Re-orientation Angle

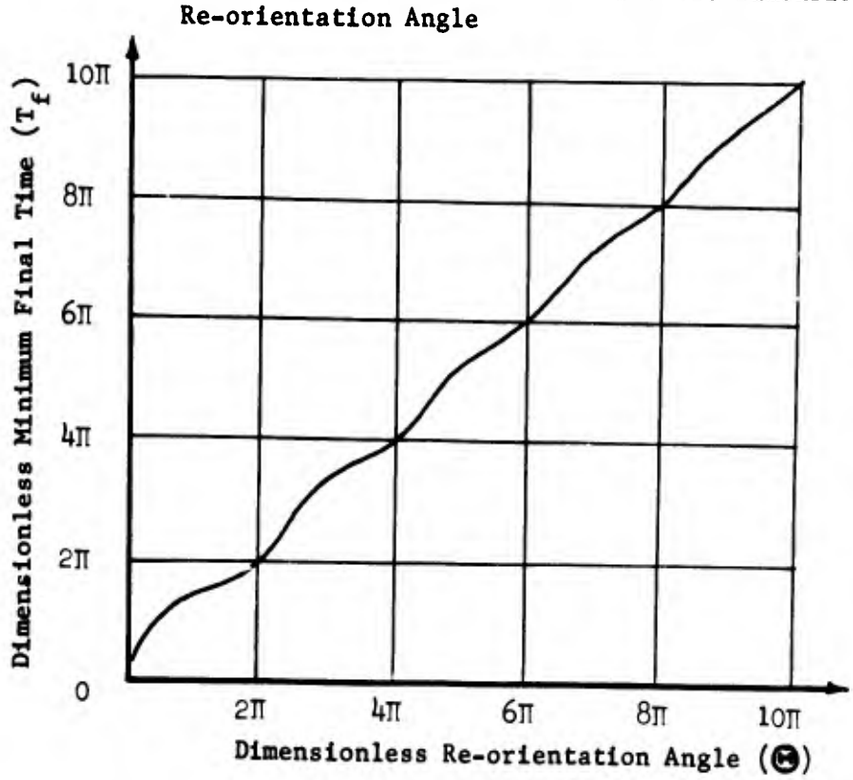

Legend:

t_f = final time (seconds)

θ = defined in Figure 3

I_z = moment of inertia about spin axis

$I = I_x = I_y$ = transverse moment of inertia

ω_z = spin rate

T_{max} = maximum torque

$$T_f = \frac{I_z \omega_z}{I} t_f \qquad \Theta = \frac{\theta I_z^2 \omega_z^2}{I T_{max}}$$

Figure 3 Coordinate System and Vehicle Specifications

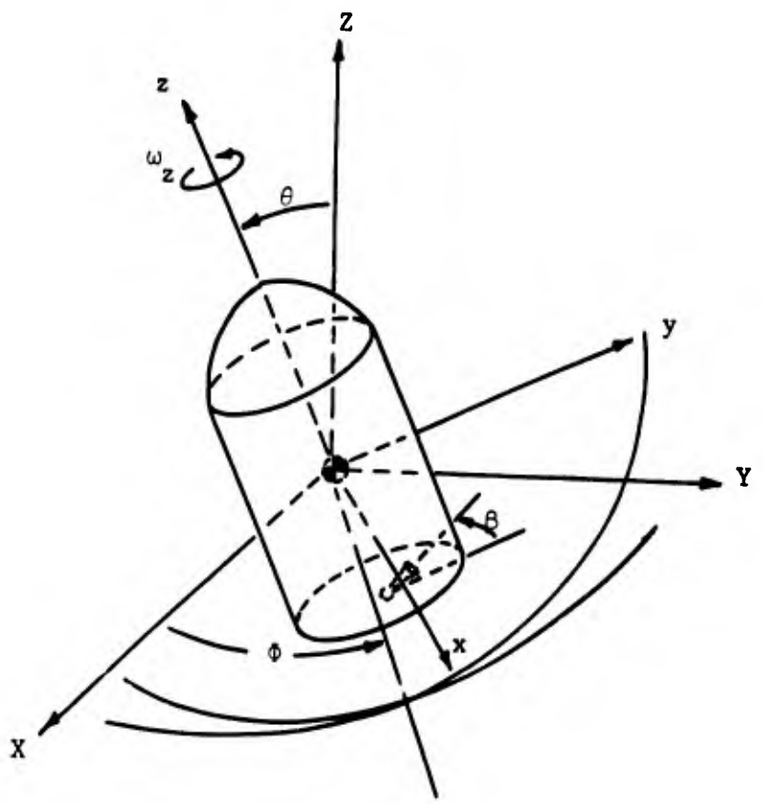

Legend:

I_z = 25 slugs . ft^2

$I_x = I_y$ = 80 slugs . ft^2

ω_z = 1000, 500 RPM

Vehicle Weight = 1000 lbs

β Position of Gimballed Jet

X, Y, Z Space Fixed Coordinate System

x, y, z Body Fixed Coordinate System

Figure 4 Thrust vs Time for Spin Rates of 1000 and 500 RPM

	Time (seconds)	
Thrust (lbs)	Spin Rate 1000 RPM	Spin Rate 500 RPM
50	4.20	2.10
100	2.00	1.10
150	1.30	0.73
200	1.00	0.57
250	0.80	0.43
300	0.66	0.36
350	0.57	0.33
400	0.51	0.30
450	0.45	0.28
500	0.40	0.25

Applications

As discussed earlier, an important military problem is one of re-orienting a spin stabilized payload in minimum time. The methods previously described are directly applicable to this problem and can be used in the design of the control system required to maneuver the vehicle. In addition one can use the results of this study in the design of attitude control systems required for spinning spacecraft used for meteorological and communication missions. As a design tool, the method has an important advantage in that answers to the following questions are readily available. For a given vehicle configuration what is the minimum time required to carry out a specified change in attitude? How do the system parameters affect the minimum re-orientation time? What are the characteristics of the optimal control law in terms of the system parameters? How do the controller configurations shown in Figure 1 compare with one another in terms of efficiency?

The method also provides a reference for evaluating the performance of nearly time-optimal control schemes. As such it provides both the time-optimal control law and the terminal time for a wide range of problems which are specified in terms of the physical parameters.

References

1. deDoes, D., "Time-Optimal Attitude Control of a Spinning Vehicle", American Astronautical Society Science and Technology Series, Vol 11, January 1967.

2. Pontryagin, L.S., et al., The Mathematical Theory of Optimal Processes, Interscience Publishers, New York, 1962.

3. Athans, M., Falb, P.L., Lacross, R.T., "Time-Optimal Velocity Control of a Spinning Space Body", IEEE Transactions on Applications and Industry, July 1963.

Dr. Manuel Ballester is Head of the Physical Organic Chemistry Section of the Higher Council for Scientific Research (Consejo Superior de Investigaciones Cientificas), and Professor at the University of Barcelona, Spain. Since 1958 he has been directing research in aromatic and alkaromatic chlorocarbons at the University of Barcelona under the sponsorship of the Aerospace Research Laboratories. Dr. Ballester was a 1944 "premio extraordinario" graduate in Chemistry from the University of Barcelona. A few years later, he received his Dr. Sc. in Organic Chemistry from the same university. In 1949 he was appointed Research Fellow in Chemistry at Harvard University and, in 1961, a Visiting Research Associate at ARL under arrangement with Ohio State University. Since 1951 he has been Scientific Investigator of the Spanish Higher Council for Scientific Investigations and, since 1953, Professor of Physical Organic Chemistry at the University of Barcelona. Dr. Ballester's scientific work includes research in the condensation of esters, mechanisms of the Darzens and aldol condensations, the chlorination of aromatic substances, the ultraviolet spectrum of benzene derivatives, and stable free radicals. He is author of some 50 papers, and recipient of several Spanish and international honors and medals for his work in chemistry.

UNCLASSIFIED

Security Classification

DOCUMENT CONTROL DATA - R & D

(Security classification of title, body of abstract and indexing annotation must be entered when the overall report is classified)

1 ORIGINATING ACTIVITY *(Corporate author)*

Hq OAR (RRO)
1400 Wilson Blvd.
Arlington, Va. 22209

2a. REPORT SECURITY CLASSIFICATION

UNCLASSIFIED

2b. GROUP

3 REPORT TITLE

Proceedings of the OAR Research Applications Conference, Volumn I

4 DESCRIPTIVE NOTES *(Type of report and inclusive dates)*

Scientific Recurring

5 AUTHOR(S) *(First name, middle initial, last name)*

None

6 REPORT DATE	7a. TOTAL NO. OF PAGES	7b. NO. OF REFS
14 March 1967	248	

8a CONTRACT OR GRANT NO N/A	9a. ORIGINATOR'S REPORT NUMBER(S)
b. PROJECT NO N/A	
c. N/A	9b. OTHER REPORT NO(S) *(Any other numbers that may be assigned this report)*
d N/A	OAR 607-2

10 DISTRIBUTION STATEMENT

Distribution of this document is unlimited.

11 SUPPLEMENTARY NOTES	12 SPONSORING MILITARY ACTIVITY
PROCEEDINGS: OAR Rsch Application Conference, V 1, 14 Mar 1967	Hq OAR (RRO) 1400 Wilson Blvd. Arlington, Va. 22209

13 ABSTRACT

These are the titles of the papers presented at the conference:

Positive Ion-Sensing System for the Measurement of Spacecraft Attitude by Rita C. Sagalyn and Dr. Michael Smiddy
Investigation of Optimum Lifting Bodies by Dr. W.L. Hankey
Gasdynamics of Explosions and its Relevence to Propulsion by Dr. Anthony K. Oppenheim
The OV-1-Promoter of Timely Space Research by Lt Col Clyde A. Northcott, Jr.
Computer-Aided Circuit Design by Dr. Donald A. Calahan
A Family of Novel Antennas: The "Backfire" Antenna by Dr. H.H. Ehrenspeck
The Generation of Science-Based Technology in the Field of Crystallization by Dr. William A. Tiller
Supersonic Combustion Simlulation by Dr. Robert G. Dunn
Prediction of the Dynamic Stability of Nose Cones by 1st Lt Brian P. Quinn
Organic Photovoltaic Devices by Dr. Aleksandar Golubovic
Time Optimal Attitude Control of a Spinning Vehicle by Capt Dirk H. de Does
The Alkaromatic Chlorocarbons by Prof. Manuel Ballester.

DD FORM 1 NOV 65 1473

UNCLASSIFIED

Security Classification

14 KEY WORDS	LINK A		LINK B		LINK C	
	ROLE	WT	ROLE	WT	ROLE	WT
Ion-Sensing System						
Spacecraft Attitude						
Optimum Lifting Bodies						
Gasdynamics						
Explosions						
Propulsion						
Space Research						
Computer-Aided Circuit Design						
"Backfire" Antenna						
Crystallization						
Supersonic						
Combustion Simlulation						
Dynamic Stability						
Nose Cones						
Organic Photovoltaic Devices						
Optimal Attitude Control						
Spinning Vehicle						
Alkaromatic Chlorocarbons						